Synthesis and Surface Modification of Formamidinium Tin Iodide Perovskite Crystals

(ホルムアミジニウムヨウ化錫ペロブスカイト結晶の合成と表面修飾)

Jiakai CHEN

Graduate School of Chemical Sciences and Engineering

Hokkaido University

2024

Content

Abstract

Lead halide perovskites have aroused intense scientific attention in recent years owing to their low cost and outstanding optoelectronic properties, which lead them to applications in high-efficiency solar cells, light-emitting diodes, single-photon sources, lasers, and so on. A major application limit for lead halide perovskites is the presence of the highly toxic lead element, raising critical concerns of environmental pollution and health problems. To address this issue, developing lead-free halide perovskites have been in the forefront of the current research. Tin halide perovskites thus have come under the spotlight by virtue of their low toxicity and eco-friendly merit and tantalizing photophysical properties.

Organic-inorganic hybrid tin halide perovskites, especially formamidine tin iodide ($FASnI_3$), have emerged as a promising semiconductor material for a range of optoelectronic applications. For example, the power conversion efficiency of solar cells based on $FASnI_3$ as light-absorber has reached over 14%, gradually narrowing the gap with their lead counterpart. However, the structure-photophysical property relationship remains ambiguous owing to the ready occurrence of structural defects in the fragile lattice of $FASnI_3$, and the synthesis of highly luminescent colloidal nanocrystals (NCs) is still a long-standing challenge due to the lack of a fundamental understanding of how to rationally suppress the formation of intrinsic as well as surface structural defects.

To address the above issues, this thesis aims at getting insight into the defect behaviors in the photophysical properties of $FASnI_3$ crystals, and developing effective synthesis routes, including judiciously adopting Sn-rich reaction condition as well as regulating surface conditions by appropriative ligands, for obtaining high-quality $FASnI_3$ crystals with great optical properties.

Chapter 1 provides a general background about metal halide perovskites. Particularly, I critically summarize and assess the latest advances in the synthesis approaches of tin halide perovskite NCs. The state-of-the-art preliminary studies in modulating their

photophysical properties and in enhancing the stability with a variety of strategies are also concluded. In addition, the remaining challenges that need to be overcome to attain high-quality tin halide perovskite NCs are also highlighted. Finally, the purposes regarding my research and the framework of whole research topic are clarified.

Chapter 2 shows the defect behaviors in the photophysical properties of $FASnI_3$. Using $FASnI_3$ microcrystals synthesized with tailored reaction conditions as the model systems, I unveil that structural defects can induce bandgap widening and abnormal photoluminescence. Based on combined analysis of X-ray photoelectron spectroscopy, solid nuclear magnetic resonance, and optical spectroscopy, I propose that bandgap widening could stem from defect-mediated lattice distortion. Temperature-dependent photoluminescence measurements lead me to the discovery of a new near-infrared photoluminescence band between 185 and 10 K and negative thermal quenching in a broad range of 110~200 K, both of which are associated with structural defects.

Chapter 3 develops an innovative surface capping ligand, zwitterionic phosphatidylcholine, replacing traditional amine ligands for the synthesis of colloidal $FASnI_3$ NCs. By introducing a small amount of phosphatidylcholine in the reaction, the particle size of $FASnI_3$ crystals could be reduced from several hundred nanometers to around 30 nanometers. Three phosphatidylcholines with different chain lengths were studied, and all of them could produce small-size, uniform-morphology $FASnI_3$ NCs. A maximum PLQY of 1.2% was achieved by reasonably tuning the reaction parameters. Importantly, stability tests reveal that phosphatidylcholine-capping $FASnI_3$ NCs have excellent long-time colloidal stability and structural stability in glovebox, indicating that as-prepared NCs could serve as an ideal platform for the future exploration of their potential optoelectronic applications.

Chapter 4 proposes a general one-pot surface modification strategy for highly luminescent organic-inorganic hybrid tin iodide perovskite NCs. Guided by density functional theory (DFT) calculations, I predict that, highly luminescent $FASnI_3$ NCs could be obtained through meeting three important factors: Sn-rich reaction condition; quasi-

AI-terminated surface; suppression of surface iodine vacancies. After creating a Sn-rich reaction condition through simply tuning the reactant ratio, large-sized organic ammonium and alkali metals are used for constructing a quasi-AI-terminated surface. By this means, high-efficiency near-infrared emitting $FASnI_3$ NCs with a maximum PLQY of 36.9±0.7%, which is over 50 times larger than those previously reported, can be obtained. A wide range of optical and structural characterizations, coupled with DFT calculations, clarify that NC surface is modified by organic ammonium and alkali metal ions. Finally, I showcase the generalizability of our concept by further demonstrating the synthesis of highly luminescent $FA_{0.9}Cs_{0.1}SnI_3$ and $FA_{0.8}Cs_{0.2}SnI_3$ NCs which have better tolerance factors, benefiting the future application explorations.

Chapter 5 summarizes the above research findings, and provides an outlook on the unresolved challenges for tin halide perovskites, as well as offers my perspective on how to achieve stabler, higher-quality, device-applicable $FASnI_3$ crystals.

In conclusion, this thesis focuses on the synthesis chemistry, surface modification, and structural characterization of $FASnI_3$ crystals, uncovering the relationship between defect and photophysical properties, offering feasible synthetic roadmap to prepare high-quality $FASnI_3$ crystals. The knowledge gained here may help others better understand the structural properties of tin halide perovskites, and inspire their explorations on related high-performance optoelectronic devices.

Chapter 1: Introduction

1.1 Perovskite materials

In 1830, Gustav Rose firstly discovered a calcium titanium oxide mineral composed of calcium titanate, $CaTiO_3$.[1] After that, Russian mineralogist Lev Perovski named this kind of material as perovskite which has the same type of crystal structure as $CaTiO_3$.[2] Many traditional oxide perovskites are well-known classical ferroelectrics, like $BaTiO_3$, $SrTiO_3$, and so on. Instead of it, oxide perovskites also have great performance in the photocatalyst field.[2]

Different with oxide perovskites, metal halide perovskites have superior properties, such as facile synthesis, outstanding optoelectronic properties, that makes them become star materials in recent years.[3] In the next part, I will focus on introducing the properties of metal halide perovskites and their applications.

1.2 Metal halide perovskites

The development of metal halide perovskites started several decades ago, and is still flourishing because of their outstanding optoelectronic properties, including tunable band gaps, narrow emission bands, high absorption cross sections, and high carrier mobilities.[4-6] The structure of metal halide perovskites is analogous to $CaTiO_3$, with a general formula of AMX_3, where A is a monovalent cation, M is a divalent cation, and X is a halide anion (Cl, Br, or I). In their structures, M^{2+} cations and halide ions form corner-sharing $[MX_6]^{4-}$ octahedra, in which M^{2+} ions are in the center. The $[MX_6]^{4-}$ octahedra are interconnected to form three-dimensional (3D) structure, where A^+ cations occupy the large cavity between octahedra to stabilize the crystal structure (**Figure 1.1**).[7]

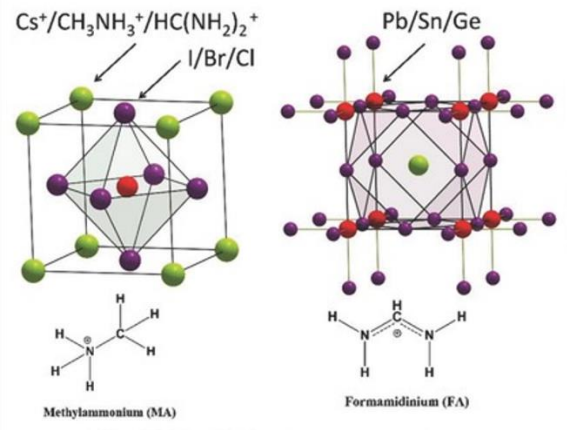

Figure 1.1 The basic unit of AMX_3 (X=Cr, Br, or I) halide perovskite structure.[7]

The formation of perovskite structure is restricted to the Goldschmidt tolerance factor (t), which is dependent on the ionic radii of A^+, M^{2+} and X^-, as given in the following formula:[8]

$$t = \frac{R_A + Rx}{\sqrt{2}(R_M + R_X)} \quad (1)$$

The suitable elements for M^{2+} metal cation in halide perovskites are from group 14 elements, like Pb^{2+}, Sn^{2+}, and Ge^{2+} with the ionic radii of 1.19 Å,[9] 1.18 Å,[10] and 0.73 Å,[9] respectively. For A-site ions, up to now, there are three cations that can stabilize 3D halide perovskite structure, i.e., inorganic Cs^+ (1.88 Å), as well as organic $CH_3NH_3^+$ (MA, 2.17 Å) and $HC(NH_2)_2^+$ (FA, 2.53 Å),[9, 11] that have appropriate ionic radii meeting the Goldschmidt tolerance factor.

1.2.1 The development of lead halide perovskite NCs

Among all metal halide perovskites, lead halide perovskites (LHPs) get the most attention, since the stable chemical valence state of Pb^{2+} compared with Sn^{2+} or Ge^{2+}, and more excellent optical properties.[5] LHPs in the form of polycrystalline films were adopted as main active layers for these applications at the early stage of research, and the rapid increase of power conversion efficiencies (PCE) of solar cells from 3.8% to 26.1%,[12, 13]

and of external quantum efficiencies (EQE) of LEDs from <1% to over 20% has been achieved.[14-16]

The research history of conventional colloidal semiconductor nanocrystals (NCs) such as CdSe and InP suggests that an excellent direct-bandgap semiconductor commonly demonstrates outstanding photophysical properties when their sizes are down to the nanometer scale and nonradiative recombination channels are perfectly suppressed.[17] Inspired by this lesson, materials scientists, chemists, and physicists have devoted a lot of effort on the synthesis, characterization, and application of colloidal LHP NCs soon after the realization of high-efficiency perovskite solar cells, with the intention of not only boosting the photoluminescence quantum yields (PLQYs) but also accessing unusual optical properties in the quantum-confinement size regime.[5, 18-20]

In 2015, Protesescu *et al*. firstly reported the synthesis of colloidal all-inorganic cesium lead halide ($CsPbX_3$) perovskite NCs by hot-injection method.[21] 4-15 nm $CsPbX_3$ NCs with cubic shape and cubic crystal structure were achieved. Through changing the halogen, the photoluminescence (PL) can include entire visible spectral region of 410-700 nm (**Figure 1.2 a, Figure 1.2 b, Figure 1.2 c**). High PLQYs (50-90%) (**Figure 1.2 d**) could also be achieved by this easy synthesis method. After that, many further efforts like doping heterogeneous ions, surface treatment, ligand passivation, have been adopted to boost the PLQYs of LHP NCs. So far, LHP NCs with near-unity PLQYs across the visible and near infrared have been achieved, and tantalizing optical properties have been discovered.[22-31]

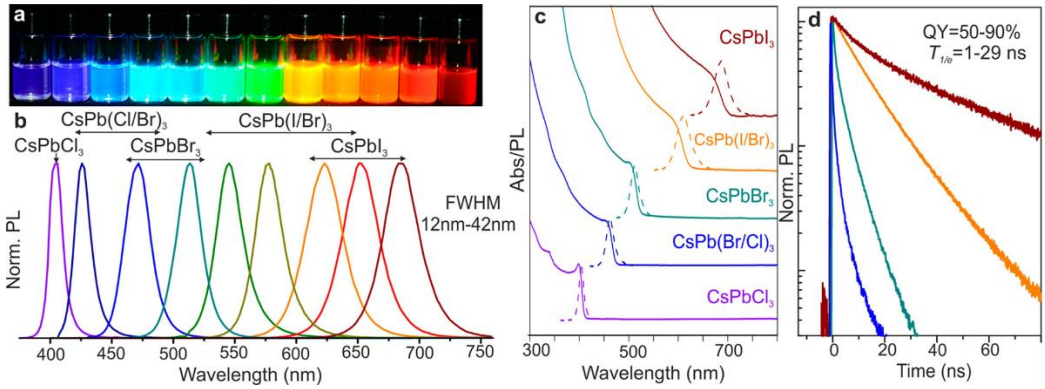

Figure 1.2 Colloidal perovskite $CsPbX_3$ (X=Cl, Br, I) NCs exhibit composition-tunable bandgap energies.[21] (a) Photos of $CsPbX_3$ NCs under UV light. (b) Emission peaks of $CsPbX_3$ NCs. (c) Optical absorption and PL spectra of $CsPbX_3$ NCs. (d) Time-resolved PL decays of $CsPbX_3$ NCs.

The excellent optical properties of LHP NCs result from their high defect tolerance. Conventional semiconductors, like Si, CdTe, GaAs, requires ultralow concentrations of impurities and crystalline defects, typically at ppb levels, that all act as dopants or traps causing excitonic nonradiative recombination. Likewise, optoelectronic properties of LHP NCs are highly tolerant to the material's structural defects. As shown in **Figure 1.3**, out of a large variety of conceivable point defects, only A-sit or X-site vacancies are characterized by low formation energies and are therefore exclusively observed.[18] For $CsPbBr_3$ or $CsPbI_3$, the energy levels of these point defects are close to the valence band maximum (VBM) or conduction band minimum (CBM). These shallow trap states have few effects on the optoelectronic properties of LHPs. Interstitial and antisite defects, which would form deep trap states in the electronic structure, are almost absent, since their very high formation energies.[18] Specially, Cl vacancies in $CsPbCl_3$ can bring about in-gap states, which act as nonradiative traps for the photogenerated charge carriers.[24] However, some strategies have been developed to suppress the formation of Cl vacancies, and boost the PLQY of $CsPbCl_3$ NCs to near unity.[24, 30, 32]

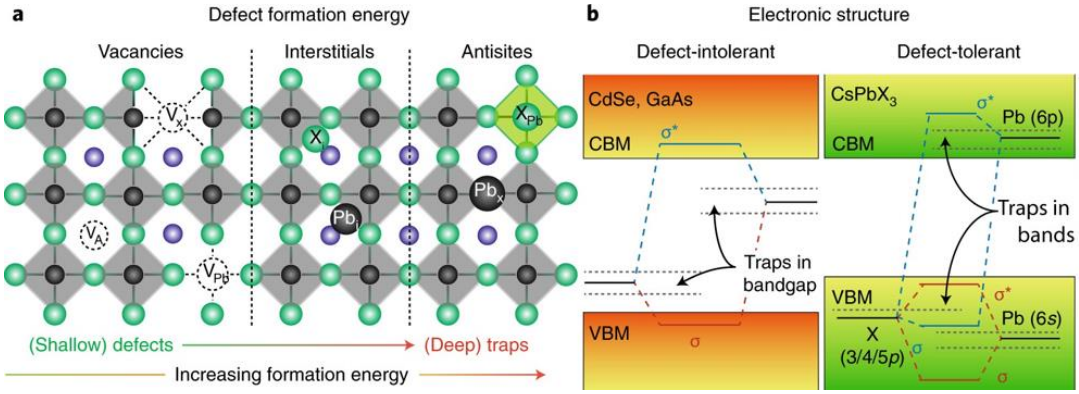

Figure 1.3 (a) Defect formation energies of different defects in LHPs, including point vacancies, interstitials, and antistites, and their depths in the bandgap.[18] (b) Schematic representation of electronic structures for defect-intolerant conventional semiconductors, like CdSe, GAS, and defect-tolerant LHPs.[18]

Table 1.1 compares the physical and electronic properties of conventional NCs and LHP NCs. For optical properties and synthesis methods, LHP NCs show multiple superiorities compared with conventional NCs. The main limitations for LHP NCs are poor thermal stability and poor compatibility in polar solvents. Recently, some materials scientists, chemists, and physicists are devoting themselves to address the stability problem of LHP NCs, and develop the potential commercial applications of LHP NCs.[33-36]

Table 1.1 Comparison of the physical, chemical, optical properties of LHP NCs with conventional NCs.[18]

	Metal chalcogenide (II–VI) and pnictide (InP) core-only NCs	**Metal chalcogenide and pnictide core-shell NCs**	**LHP NCs**
Crystal structure	Wurtzite, zinc-blende	Wurtzite, zinc-blende	Perovskite
Composition	CdSe, ZnSe, InP	CdSe/CdS, CdSe/CdZnS, InP/ZnS	(Cs, FA, MA)PbX_3 (X=Cl, Br, I)

Spectral range	400-700 nm for metal chalcogenide; 520-700 nm for InP	510-650 nm	400-700 nm
PLQY	Low (0-10%)	High (up to 95%)	High (near unity)
PL FWHM	Narrow for metal chalcogenide (<100 meV), but limited for InP		Narrow (<100 meV)
Synthesis	High-temperature, High-purity precursors, air-free	High-temperature, long-time	Facile synthesis, possible under ambient conditions, Multiple methods
Post-synthesis tunability	Only cation exchange		Both cation and anion exchange; ligand exchange
Thermal stability	Stable	Stable	Limited
Ambient stability and photostability	Limited	High	High
Solvent compatibility	Nonpolar solvents and polar solvents	Nonpolar solvents and polar solvents	Only nonpolar solvents; Dissolved in polar solvents
Commercial applications	None	LCD TV	Under development for LCD TV, LED

1.2.2 Photoelectric applications

As discussed above, lead halide perovskite NCs possess some arresting optoelectronic properties including strong light-absorption, tunable band gap, narrow emission line width, and high PLQY, which make them be widely used as light absorber in solar cells or as light emitters in a range of optoelectronic devices such as solar cell, light-emitting diodes (LEDs), single-photo sources, lasers, and X-ray scintillators.[37-45]

The first report of the use of LHP in solar cells came in 2006. Miyasaka et al. used $MAPbBr_3$ as a sensitizer in a dye-sensitized solar cell, and they achieved a 2.2% powder conversion efficiency (PCE).[46] After that, perovskite photovoltaic technology achieved a rapid and break-through development. Until now, using LHP in the form of polycrystalline films as light absorber, the champion PCE is 26.14%,[13] placing them on

par with the capabilities of alternative photovoltaic technologies such as copper indium gallium selenide (23.35%), crystalline silicon (26.8%), and GaAs SCs (29.1%).[47] However, using LHP NCs as light absorber, the PCE still cannot achieve 20%. In 2019, Zhao et al. reported a layer-by-layer deposition process to achieve high-performance, heterostructure perovskite NC solar cells.[48] As shown in **Figure 1.4a**, a perovskite film contains different layers of nanocrystals. In this layer-by-layer assembly, methyl acetate (MeOAc) is used to remove the native oleate ligands and to render the deposited nanocrystals insoluble in the solvent. **Figure 1.4b** shows the device structure, in which they controlled the thickness ratio of $Cs_{0.25}FA_{0.75}PbI_3$ layer to $CsPbI_3$ layer in the perovskite QD absorber, and they achieved a high PCE of 17.39% when the ratio is 1:3. The J-V curves of different devices with different light absorber layers are shown in **Figure 1.4c-f**. Until now, 17.39% is still the maximum PCE for perovskite NC solar cells.

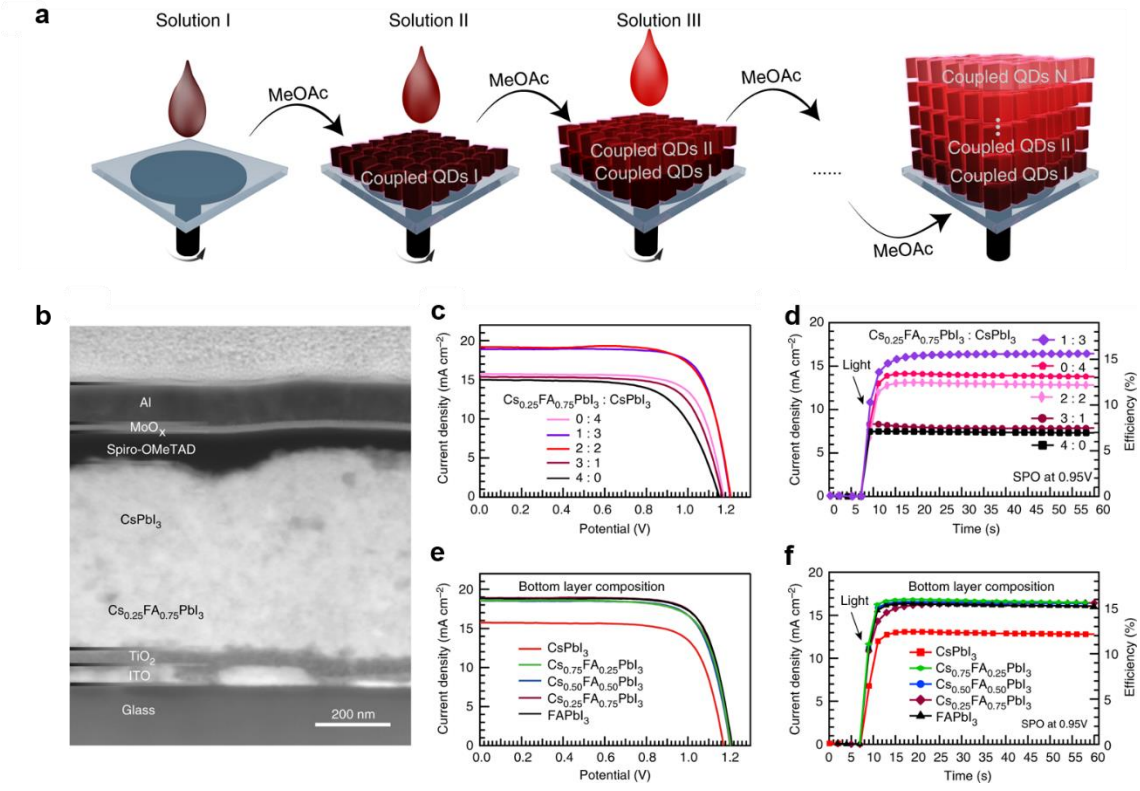

Figure 1.4 (a) Schematic representation of layer-by-layer assembly process. (b) Cross-sectional STEM-HAADF image of the device structure. (d-f) J-V curves of perovskite

NC solar cells with different light absorber layers.[48]

The second main optoelectronic application of LHP NCs is LED. In the past few years, wurtzite, or zinc blende Cd-based quantum dots (QDs), like CdS, CdSe, CdTe, and InP@ZnSeS are widely studied for quantum dot-based light emitting diodes (QLEDs). The commercial product, QLED television, has already been well know now. Compared with the traditional QDs, LHP NCs have higher brightness and color purity which make them become the better substitute for QLEDs. In 2014, Friend et al. highlighted the fact that an efficient solar cell material is generally also a good light emitter, and they firstly fabricated high-brightness LEDs based on solution-processed organometal halide perovskites.[49] By tuning the halide compositions in the perovskite, near-infrared, green, and red LEDs were achieved, and their external quantum efficiencies (EQEs) are 0.76%, 0.1%, and 0.018% respectively. After that, more and more scientists devote themselves to fabricating high-performance perovskite LEDs. Up to now, perovskite LEDs show excellent efficiencies during total visible region. For example, the record EQEs are 12.2% for white;[50] 18.65% for blue;[51] 25.85% for red;[52] and 30.84% for green.[53] It is noted that the high-performance LEDs are mainly based on polycrystalline perovskite films, instead of perovskite NCs, which is as same as perovskite solar cells. In 2015, Zeng et al. firstly reported the perovskite QLEDs using inorganic perovskite $CsPbX_3$ NCs, but they achieved poor EQEs (0,07% for blue; 0.12% for green; 0.09% for red).[54] Surface modification is an effective strategy to improve the optical and/or structural properties of NCs, and optimize the performance of their optoelectronic devices. Sargent's group report a bipolar-shell resurfacing strategy for $CsPbBr_3$ QDs, and got effective blue LEDs.[16] As shown in **Figure 1.5**, they choose isopropylammonium (IPA) Br and NaBr to post-treat the CsPbBr3 NCs, and successfully got a less long-chain ligands and bipolar-shell surface. From the ζ potential (**Figure 1.5a-d**), we can see that after post-treatment, the NCs' surface has positive charge which confirms the formation of bipolar-shell. This surface

treatment enables a high EQE of 22% for green LEDs and 12.3% for blue LEDs.

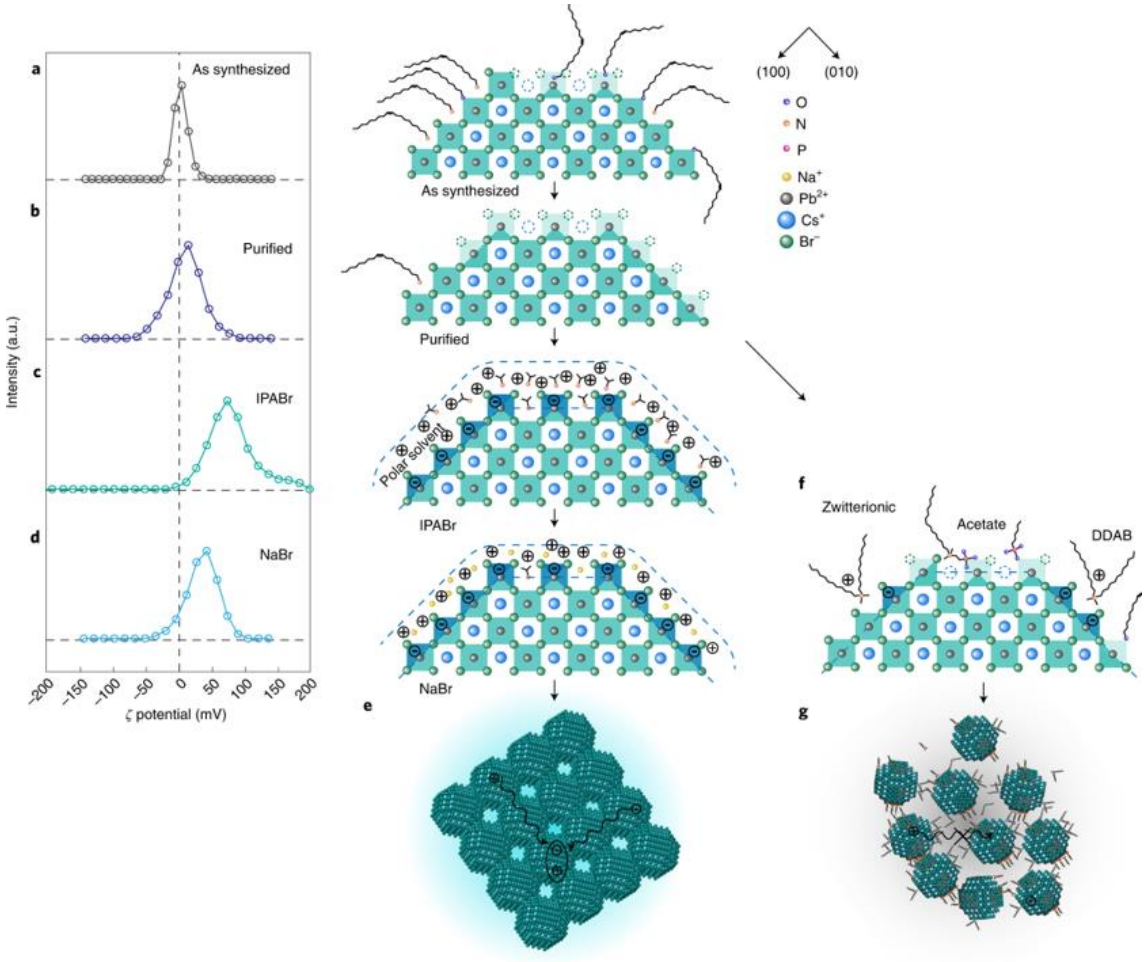

Figure 1.5 (a-d) ζ potentials (left) and schematics (right) of as-synthesized, purified, IPABr-passivated, and NaBr-passivated QD surfaces. (e) Solids formed with resurfaced QDs. (f) Schematic of QD surface with long-chain ligands. (g) Film cast from QDs with long-chain ligands. Because of the ligand effect, there is a larger interdot spacing.[16]

Whether solar cells or LEDs, there are two main challenges in how to fabricate excellent NC devices: 1). How to make a dense, smooth NCs films. Especially for solar cells, larger-sized crystals are good for current transmission, but large-sized crystals are hardly to be spin-coated into a dense film. 2). How to remove the insulative capping ligands on the NCs' surface. The most reported LHP NCs are capped by oleic acid and/or oleylamine which are detrimental to the optoelectronic devices. Ligand exchange process

is necessary when constructing NC devices, but it is difficult to maintain the properties of NCs after ligand exchange. Except solar cells and LEDs, LHP NCs also show great potential in lasers and single-photon sources. For example, Sun et al. firstly reported the vertical cavity surface emitting lasers based on colloidal $CsPbX_3$ NCs with low threshold (9 μJ cm^{-2}).[42] By changing the halide elements, the lasing wavelength could be tuned across red, green, and blue regions. Klimov el at. highlighted that $CsPbX_3$ NCs can serve as room-temperature sources of quantum light, because they exbibit strong photo antibunching that could be detected by single-dot photoluminescence measurements.[40]

1.2.3 Toxicity issue of lead halide perovskites

Despite the advancements mentioned above, the presence of lead in LHPs has aroused the concerns of environmental pollution and health problems due to the toxicity of Pb. It should be pointed out that Pb's toxicity results from its high ability to mimic other metals and interfere with biological functions.[55] Examples include blocking N-methyl-D-aspartate receptors and inhibiting the formation of haem, leading to neuron damage and anaemia, respectively.[55] Currently, the use of hazardous heavy metals, including lead, in electronic devices is regulated in the European Union, with many other countries expected to introduce similar regulations soon.[56]

Abate's group recently studied the bioavailability of Pb from LHPs, and the Pb uptake ability in the plants.[57] As shown in **Figure 1.6a-c**, the plants grown in LHP-contaminated soil have high Pb concentration both in roots, stems, and leaves. Especially in roots, the concentration of Pb can be 130.4 mg kg^{-1} when the added Pb amount is 35 mg kg^{-1}. Notably, the bioavailability of Pb from lead halide perovskite is strongly higher than other Pb source, like PbI_2. The calculated Pb uptake ability for mint plants is above 300% as shown in **Figure 1.6d**. To address this problem, developing some lead-free halide perovskites has been of primary importance.

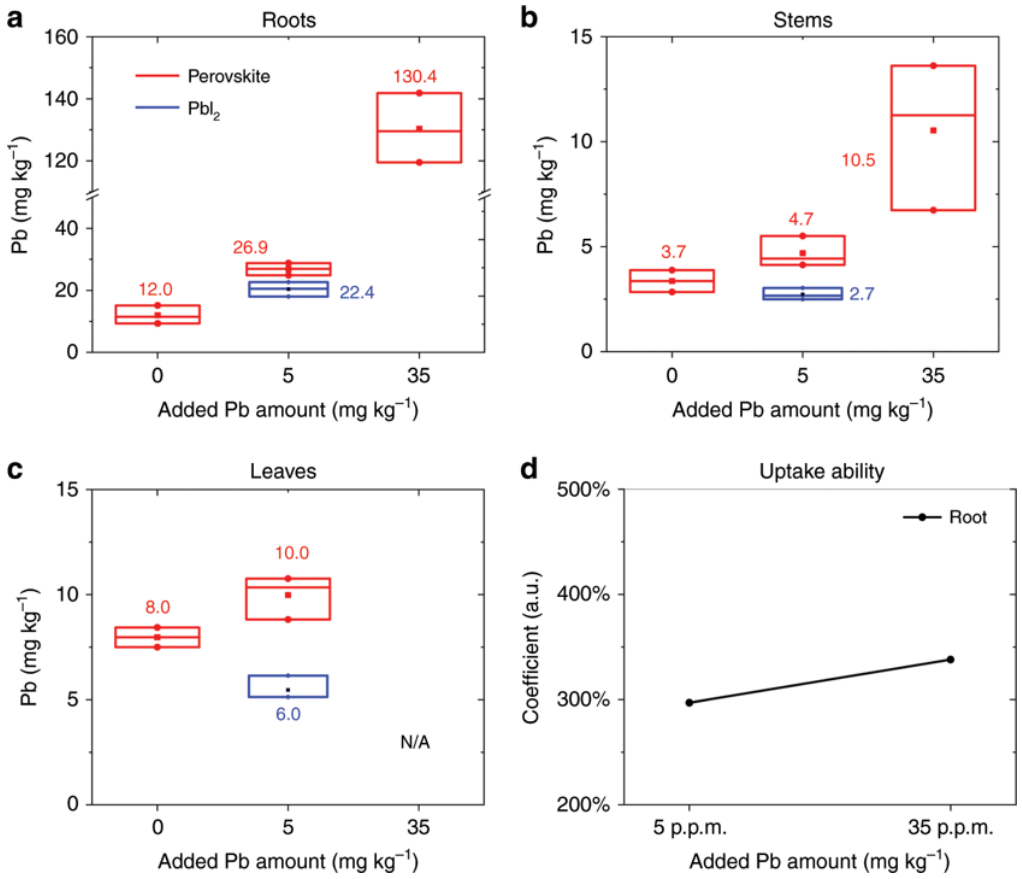

Figure 1.6 The concentrations of Pb in different parts of mint plants:[57] (a) roots; (b) stems; and (c) leaves. (d) Pb uptake ability for mint plants.

1.2.4 Lead-free halide perovskites

Considering the similarity in size, charge, chemical reactivity, properties, and structural tolerance, different nontoxic elements have been developed to replace lead in halide perovskites. **Figure 1.7** lists potential elements forming three different lead-free perovskites, including $AB^{II}X_3$ structure; $A_2B^IB^{III}X_6$ double perovskite structure; and vacancy-ordered $A_2B^{IV}X_6$ structure.[58] Among these elements, the ideal elements are in the same group (group 14) as Pb, like tin (Sn) and germanium (Ge), which can form stable ABX_3 perovskite structure. Recent studies have reported the preparation of Sn and Ge based halide perovskites, and emphasized their potential in various optoelectronic devices.[59, 60] In addition, combination of a monovalent cation and a trivalent cation can form a double perovskite structure.[61, 62] The monovalent cation B^I can be Li, Na, K, Rb,

Cs, Ag (**Figure 1.7 d**, green color), and the trivalent cation B^{III} can be Al, Ga, In, Sb, Bi (**Figure 1.7 d**, yellow color).[63, 64] Among them, Cs_2AgBiX_6 has been widely studied because of its outstanding stability, good optical properties, and long charge carrier lifetime.[65] However, most double perovskites are indirect bandgaps that it inferior for LED applications. Another interesting structure is vacancy-ordered double perovskites, in which, B^{I} and B^{III} ions are replaced by B^{IV} ions (Zr, Hf, Te) and a vacancy, while strictly speaking, it does not belong to the perovskite family based on its crystal structure (**Figure 1.7c**).[66]

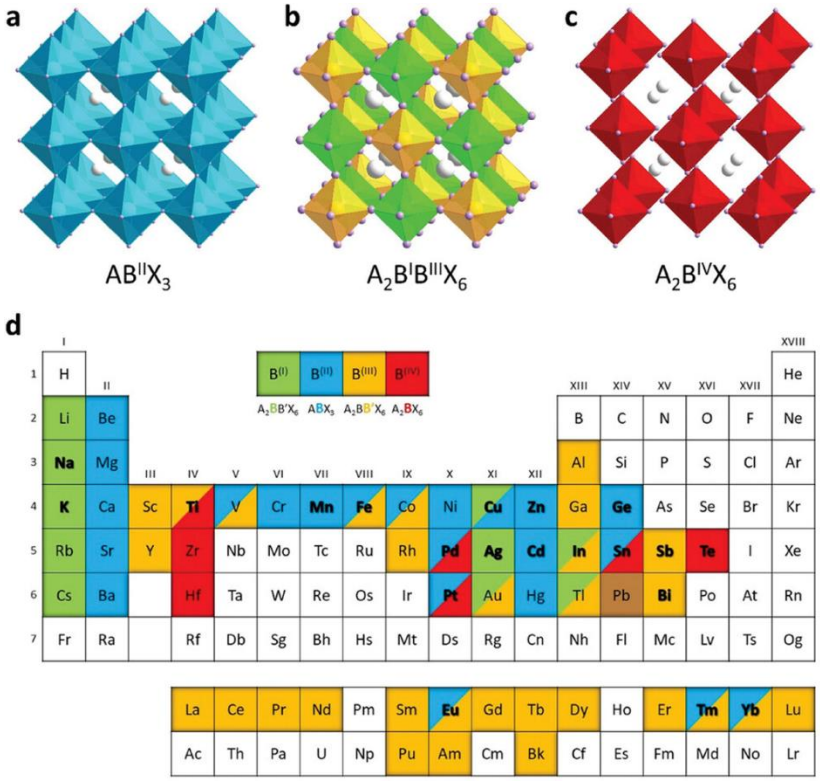

Figure 1.7 Crystal structures of three different lead-free perovskites:[58] (a) $AB^{II}X_3$; (b) $A_2B^{I}B^{III}X_6$ double perovskite; (c) vacancy-ordered $A_2B^{IV}X_6$ perovskites. (d) The possible elements that can form three crystal structures shown in (a-c).

In particular, Sn-based halide perovskites (THPs) have come under the spotlight by virtue of their low toxicity and outstanding electrical and optical properties.[60] Compared

to Pb, Sn has the same type of valence electron configuration (ns^2sp^2) and close ionic radii (i.e., 1.19 and 1.18 Å for six-coordinated Pb^{2+} and Sn^{2+} ions, respectively).[9, 10] Thus, Sn has been considered to be ideal element to fully or partially replace Pb, leading to research on Pb-Sn alloyed perovskites with enhanced stability.[67] Although Sn is not fully non-toxic for human beings, a negligible bioavailability of Sn from Sn-based perovskites was confirmed because of the low water solubility of related Sn compounds.[57] Furthermore, tin iodide perovskites show a band gap of 1.3–1.4 eV, high carrier mobilities, and long carrier diffusion lengths, all of which favor the attainment of high-efficiency solar cells.[68, 69] In light of these advantages, THPs are becoming one of the research focuses in the domain of halide perovskites.

1.3 Crystal and electronic structures of THP NCs

The structure of THPs is characterized as $ASnX_3$, in which one Sn^{2+} cation coordinate with 6 X anions, forming corner-sharing $[SnX_6]^{4-}$ octahedra cavities embedding the A cations. There are many similarities in the crystal structures between Pb-based and THP perovskites. The ideal structural phase of THPs is cubic, while octahedral tilting induces the transition to lower-symmetry tetragonal and orthorhombic phases.[70, 71] Like Pb-based perovskites, THPs crystallize in the cubic phase at a higher temperature, since the larger formation energy of the cubic lattice; cooling can induce the phase transformation to octahedrally tilled variants.[69, 72] As shown in **Figure 1.8a**, bulk $CsSnI_3$ stabilizes at the cubic phase at 227 ℃, and transforms to tetragonal and orthorhombic structures at 107 and 27 ℃, respectively.[73] In addition to temperature-induced phase transformation, it has revealed that other external stimuli, like pressure and light illumination, can trigger the structural transition of Pb-based perovskites but similar effects remain underexplored in the THP system.[74, 75] Compared with three perovskite polymorphs for $CsSnI_3$, the yellow non-perovskite phase is more stable at room temperature (**Figure 1.8a**), which is as similar as $CsPbI_3$. The lower Goldschmidt

tolerance factors of iodine-based perovskites may contribute to the easy formation of optically inactive yellow phase.[76] The calculated Goldschmidt tolerance factors of $CsPbI_3$ and $CsSnI_3$ are both about 0.85, which is not within the optimal range of 0.9-1.[76] Previous works have uncovered that the crystal structure of Pb-based perovskites is of great relevance with the intrinsic defects, NC size, dopants, alloying, and external stimuli, which is a variety of measurement techniques.[77] By contrast, so far there are few reports about the structures of THP NCs. In this respect, our knowledge is only limited to the reported cubic phase for $CsSnCl_3$ NCs and orthorhombic phase for $CsSnBr_3$ and $CsSnI_3$ NCs at room temperature, but their exact phase transition temperature remains unclear.[78]

To date, the electronic structures of THPs have been studied theoretically and experimentally.[79-81] Generally, their positions of valence band maximum (VBM) are mainly determined by the antibonding hybridized Sn s and X p orbitals, whereby the X p orbital has a major contribution. The conduction band minimum (CBM) instead consists of the Sn p and X p orbitals, and Sn p orbital plays the major role.[82] Goyal *et al.* compared the electronic structures of $MAPbI_3$, $MASnI_3$, and $MA(Pb_{1-x}Sn_x)I_3$ alloys (**Figure 1.8b**). Since the binding strength of Sn s and Sn p orbitals is significantly less than the corresponding Pb atomic orbitals, the band edges in pure $MASnI_3$ are less strongly bound than those in pure $MAPbI_3$, which results in the smaller bandgaps of THPs than Pb-based perovskites.[83] For instance, the calculated bandgaps of $MASnI_3$ (1.24 eV) and $CsSnI_3$ (1.25 eV) are much smaller than their Pb-based cousins (1.59 eV for $MAPbI_3$ and 1.72 eV for $CsPbI_3$, respectively).[82] Changing the halide ions from I to Br to Cl causes an enhanced binding strength of X p, which significantly induces the downward shift of the VBM and contributes to the tunability of bandgaps of THPs. Although A-site cation does not directly contribute to the VBM and CBM of THPs, it can lead to the lattice distortion or enlarged lattice volume caused by introducing a large A-site cation, such as MA^+ or FA^+; this can indirectly influence the hybridization of Sn and X orbitals, leading to the shift of VBM and CBM.[82] **Figure 1.8c** shows the bandgaps of all-inorganic and organic-inorganic hybrid THPs. We can see that the bandgap varies from 3.55 to 1.24 eV through

compositional engineering.

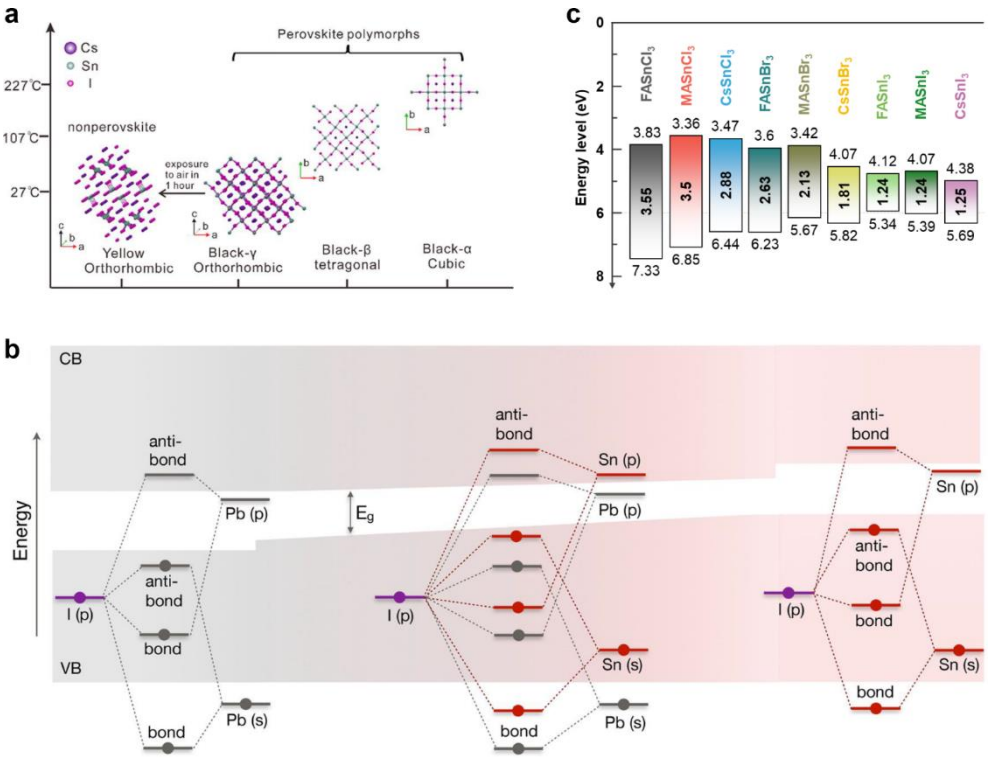

Figure 1.8 (a) Crystal structures and temperature-dependent phase transitions of various $CsSnI_3$ polymorphs.[73] (b) Schematic of electronic band structures of $MAPbI_3$, $MASnI_3$, and $MA(Pb_{1-x}Sn_x)I_3$ alloys. Shaded regions show the valence band (VB) and conduction band (CB), and the thick lines represent the molecular orbital picture.[83] (c) Schematic of energy level diagrams of 9 typical THPs. The bandgaps are extracted from the UV-vis measurements, while the ionization energy (IE) and electron affinity (EA) are extracted from the inverse photoelectron spectroscopy.[82]

1.4 Synthetic method of THP NCs

The synthesis of semiconducting NCs typically relies on the "top-down" or "bottom-up" approaches. The "top-down" approach includes the fragmentation and restructuring of bulk solids, such as the mechanically ball-milling and chemically etching methods.[84, 85] Some studies have been conducted to prepare perovskite NCs based on these methods,

which usually produce NCs with the nonuniform shape and particle size, as well as the unsatisfactory optical properties.[86, 87] By contrast, the "bottom-up" approach involves the crystal nucleation and growth from molecular building blocks in the liquid- or gas-phase, such as liquid-phase soft-chemical synthesis and chemical vapor deposition (CVD).[88, 89] The soft-chemical approach has been widely employed for the synthesis of high-quality colloidal Pb-based NCs with near-perfect optical properties, controlled morphologies and sizes.[5] Up to now, the approaches used for the synthesis of Pb-based perovskites NCs, including the hot-injection, ligand-assisted reprecipitation (LARP), and solvothermal reaction, have been adopted for synthesizing THP NCs.[78, 90-96] Besides, the well-developed gas-phase "bottom-up" synthesis is CVD, through which epitaxial growth of perovskite nanowires (NWs) were successfully achieved on crystalline substrates.[97, 98] Recently, this method has been used to produce $CsSnX_3$ NWs, which will be discussed in the following section.[73, 99]

1.4.1 Hot injection method

The hot-injection approach to synthesizing colloidal perovskite NCs was firstly developed by Kovalenko *et al.* in 2015.[21] The as-prepared $CsPbX_3$ NCs have uniform morphology and excellent optical properties. Inspired by this work, for the first time, Jellicoe *et al.* reported the synthesis of $CsSnX_3$ NCs via a similar air-free hot-injection approach.[78] In their synthesis, a weakly reducing solvent, tri-n-octylphosphine (TOP) was used to dissolve the SnX_2 powder, and the resulting Sn-X-TOP precursor solution was then injected into the Cs-oleate precursor solution containing oleic acid (OA) and oleylamine (OAm) ligands at a temperature of 170 ℃. The reaction was finished within 1 min, followed by an ice-water bath for quick termination. Through compositional engineering, colloidal $CsSnX_3$ NCs with various halide components (X=Cl, $Cl_{0.5}Br_{0.5}$, Br, $Br_{0.5}I_{0.5}$, I) were successfully prepared, and the optical bandgap of these NCs varies from visible to the near-infrared region (**Figure 1.9a**). The morphology of the as-prepared NCs, particularly for $CsSnI_3$ NCs, is cubic with a size of less than 20 nm (**Figure 1.9b**). OAm

and OA were chosen as surface capping ligands to stabilize the structure and morphology of $CsSnX_3$, but the stability of as-prepared NCs is extremely poor (e.g., the NCs were degraded within several minutes in the ambient condition). The PLQY of the obtained $CsSnI_3$ NCs is less than 1%, suggesting the existence of a high density of structural defects contributing to the nonradiative recombination. In addition, one disadvantage of this synthetic approach is the use of a large amount of expensive TOP. A possible alternative to TOP is trioctylphosphine oxide (TOPO) that has been proven to be effective for preparing Pb-based counterparts.[100] Further investigation shows that the judicious mixing of long-chain OAm, short-chain octylamine and octanoic acid can tune the morphology of $CsSnI_3$ from nanocubes to nanoplates (**Figure 1.9c**).[91]

Li et. al. recently synthesized red-emitting $CsSnI_3$ NCs with cubic phase.[101] They also used TOP as solvent to dissolve SnI_2, meanwhile added Sn(0) power to suppress the oxidation of Sn^{2+}. They selected a high ratio of Sn/Cs (6.7/1) to achieve high-quality $CsSnI_3$ NCs. As shown in **Figure 1.9d**, the sample with introduction of Sn(0) powder has brighter red-emitting (PLQY=~6.3%), and narrower PL peak compared with the sample without Sn(0) power (PLQY=~0.1%). An interesting finding is that the as-prepared $CsSnI_3$ NCs have an ultralong carrier lifetime (278.30 ns) surpassing all of the previously reported $CsSnI_3$ NCs' lifetimes (**Figure 1.9d**). We note that their emission peak is at ~725 nm (~1.7eV) that seemingly shows a strong quantum confinement effect of small-size $CsSnI_3$ NCs (~9 nm) since the bandgap of bulk $CsSnI_3$ is just 1.3eV. A large difference of ~0.3eV in bandgap is hard to be understanded because the calculated diameter for the Wannier–Mott exciton of $CsSnI_3$ is only 4.4 nm.[102] This abnormal quantum confinement effect for $CsSnI_3$ NCs need to be further confirmed.

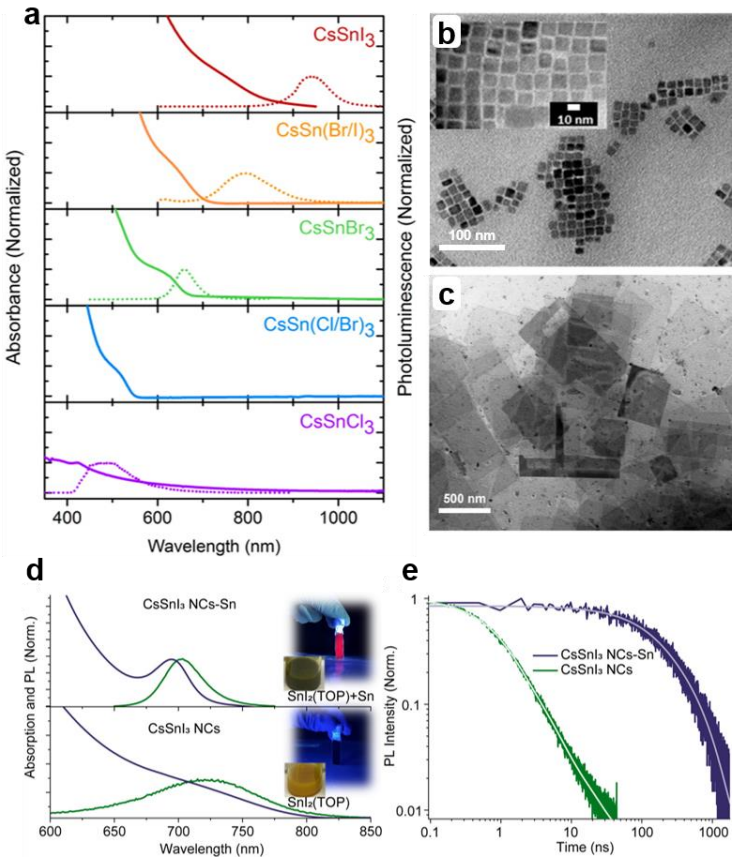

Figure 1.9 (a) Absorbance and steady-state PL spectra of $CsSnX_3$ NCs (X=Cl, Cl/Br, Br, Br/I, I) synthesized through the hot-injection approach.[78] (b) TEM image of $CsSnI_3$ NCs.[78] (c) TEM image of $CsSnI_3$ nanoplates.[91] (d) Absorbance and steady-state PL spectra of $CsSnI_3$ NCs with and without Sn (0) powder treat. The inset provides digital photographs of the SnI_2(TOP) precursors with and without Sn (0) powder and the resulting NCs. (e) Normalized PL kinetics of $CsSnI_3$ NCs-Sn and $CsSnI_3$ NCs.[101]

The hot injection approach was also used for the synthesis of organic-inorganic hybrid $FASnI_3$ NCs with a uniform particle size of ~ 10 nm.[103] Compared with the bulk material, $FASnI_3$ NCs exhibit a 190 meV increase of the bandgap, which is attributed to a highly disordered lattice. In addition, another interesting finding shows when the size of $FASnI_3$ NCs is down to several nanometers, in addition to the occurrence of a strong quantum-confinement effect, the conduction band can evolute from a continuous band structure to separate energy levels.[104] This leads to slow carrier relaxation, suggesting its

potential for high-efficiency photovoltaic devices that could break the Shockley-Queisser limit.

1.4.2 Ligand-assisted reprecipitation

An alternative approach for synthesizing halide perovskite NCs is the LARP strategy, wherein a polar solvent (DMF or DMSO) containing respective ions is quickly mixed with a nonpolar solvent (hexane or toluene), bursting the nucleation and growth of perovskite NCs.[105, 106] The driven force of this process comes from the huge difference of the solubilities for ions in polar and nonpolar solvents. A highly supersaturated state of the ionic solution in the nonpolar solvent is greatly destabilized, which induces the rapid crystallization within a few seconds even at room temperature.

In 2016, Weidman *et al.* prepared the $L_2[ABX_3]_{n-1}BX_4$ perovskite nanoplatelets via LARP, wherein L represents the long-chain ligands, butylammonium (BA) or octylammonium; A is the Cs, FA, or MA; B is the Pb or Sn; N represents the thickness of the nanoplatelets.[93] In particular, L_2SnI_4 (n=1) and $L_2[FASnI_3]SnI_4$ (n=2) nanoplatelets were successfully synthesized by dropwise mixing the BAI, CsI, and SnI_2 ionic solution in DMF with toluene. The thickness of the nanoplatelets can be adjusted by changing the precursor ratio. As shown in **Figure 1.10a, c**, long-chain butylammonium ligand occupies the site of FA^+, terminating the growth of NCs along one dimension, which thus induces the nanoplatelet morphology (**Figure 1.10b, d**). The average d-spacing of n=1 and n=2 nanoplatelets can be calculated as ~1.7 and 2.3 nm, respectively. Subtracting the length of the butylammonium ligand (~0.5 nm), the exact thickness of the perovskite layer is ~0.6 nm and ~1.2 nm for n=1 and n=2 nanoplatelets, respectively, in consistence with the one and two perovskite unit cells. In addition to the butylammonium ligand, recent reports showed that some linear π-conjugated ligands can be incorporated into the perovskite lattice, resulting in the improved stability, enhanced charge carrier mobility, and inhibited ion diffusion of THP films. We point out that such ligands might be used for surface passivation of THP NCs.[107-109] Recently, Chen et al. reported to use LARP method to

prepare FASnI3 NCs.[110] They tried different polar solvents, like DMF, DMSO, GBL and NMP, and different nonpolar solvent, like CB, CF, Pxylene, hexane, MeOAc, octane, and DE. Small sized $FASnI_3$ NCs were successfully obtained (~7.1 nm), but the morphology and optical properties are poor. One remaining challenge for LARP is the rapid reaction rate in this crystallization process, making it difficult to control the shape and quality of NCs.

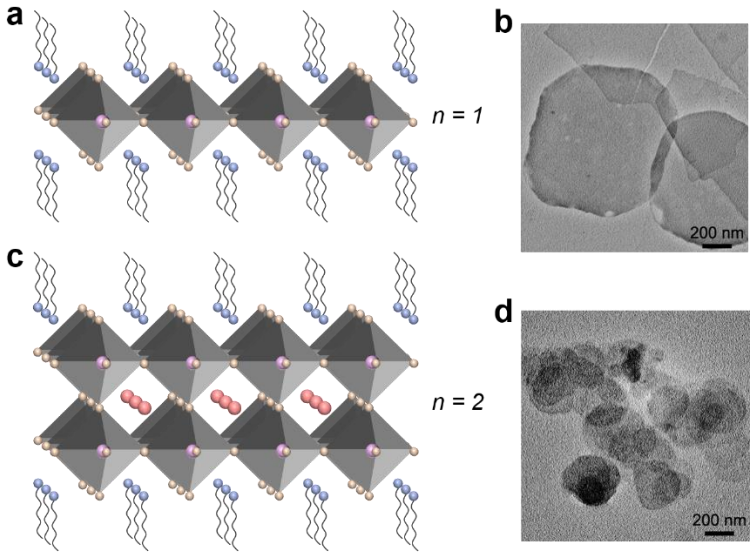

Figure 1.10 (a) Structural model of $L_2[ASnI_3]_{n-1}SnI_4$ nanoplates for n=1. (b) TEM image of $L_2[ASnI_3]_{n-1}SnI_4$ nanoplates for n=1. (c) Structural model of $L_2[ASnI_3]_{n-1}SnI_4$ nanoplates for n=2. (d) TEM image of $L_2[ASnI_3]_{n-1}SnI_4$ nanoplates for n=2.[93]

1.4.3 Chemical vapor deposition

Different from the solution-phase synthetic approaches, the CVD process needs a higher temperature, longer reaction time, and precise control of gas flow rate and vapor pressure. Normally, this process enables the epitaxial growth of low-dimensional perovskite NCs, like NWs, nanosheets, and so on.[97, 111, 112] The use of CVD approach for perovskite NCs dates back to 2015. High-quality $MAPbI_3$ NWs were successfully synthesized by a two-step reaction process, using PbI_2 and MAI salts as the precursors.[113] Thereafter, the low-dimensional perovskite NCs prepared by CVD have attracted much

attention owing to their high stability, excellent crystallinity, and great performance in various optoelectronic applications. The synthesis of THP NWs via CVD was firstly reported in 2019 by Chen *et al.* They used $CsSnX_3$ ingots prepared at 550 ℃ as the precursor, and fluorophlogopite mica as the substrate for epitaxial growth.[73] $CsSnX_3$ ingots were placed in the middle of a special tube-in-tube reactor, and heated at a high temperature of 280 ℃ for generating evaporated precursors, which were then carried by the controlled flowing argon gas to the mica substrate for crystallization **(Figure 1.11 a)**. Normally, the crystallization and growth of THPs are highly dependent on the purity of Sn^{2+} reagent, because trace Sn^{4+} impurity can impact the quality of the crystals. However, the CVD route can avoid this obstacle since the SnI_4 can decompose to SnI_2 and I_2 at a high temperature. As shown in **Figure 1.11 b**, even using CsI+SnI_4 as the starting reagents to prepare $CsSnI_3$ ingots, the XRD results indicate that the as-synthesized $CsSnI_3$ NWs still hold pure orthorhombic $CsSnI_3$ perovskite phase, consistent with that of $CsSnI_3$ NWs prepared using CsI+SnI_2 reagents. The optical microscopy images confirm the formation of $CsSnI_3$ NWs, and display their unique shapes relevant to growth times (**Figure 1.11 c, e**). After 1 h, the diameters of NWs range from a few hundred nanometers to several micrometers, and the length of NWs is several hundred micrometers (**Figure 1.11 c**). The Cs, Sn, and I elements are uniformly distributed over the NWs, as well as the ratio of these elements is near 1:1:3 (**Figure 1.11 d**). After 2 h reaction time, longer and wider NWs are produced, which are interconnected to form hexagonal networks (**Figure 1.11 e)**. Besides the $CsSnI_3$ NWs, well-oriented and high-crystalline $CsSnBr_3$ NWs can also be produced using $CsSnBr_3$ ingots as the precursor. It was found that the growth of $CsSnBr_3$ NWs is also tolerant for Sn^{4+} impurity; even using $SnBr_4$ agent can lead to phase-pure $CsSnBr_3$ NWs. The CVD approach thus not only provides a new route to control the morphology of THP NCs, but also can eliminate the deleterious effect of trace Sn^{4+} impurity, which is beneficial for optoelectronic applications.

A subsequent work reported the syntheses of $CsSnCl_3$, $CsSnBr_3$, $CsSnI_3$, and

$CsSnBrI_2$ NWs through a modified CVD process.[99] Instead of using the $CsSnX_3$ ingots, they directly used CsX and SnX_2 as the precursors to grow $CsSnX_3$ NWs. A possible growth mechanism for $CsSnX_3$ NWs is that the decomposed Cs, Sn, and X atoms from their precursors at high temperatures were carried by argon gas to the mica substrate for epitaxial growth. Owing to the lattice mismatch between the mica substrate and $CsSnX_3$, the crystallization process is restricted along two dimensions, producing high-orientated one-dimension $CsSnX_3$ NWs. The peculiar morphology of $CsSnX_3$ NWs makes $CsSnX_3$ NWs attractive for use in photodetectors. For instance, the $CsSnI_3$ NW photodetector showed a responsivity of 54 mA/W, a detectivity of 3.85×10^5 J, and fast response rise/decay times of 83.8 ms/243.4ms,[99] which hold promise for medical imaging, night vision, environmental sensing, and so on. Of note, until now there are only two studies concerning the synthesis of THP NCs by CVD, and only THP NWs arrays can be achieved on the mica substrate. Thanks to the slower and more controlled crystallization rate compared with solution synthesis routes, CVD ought to be suitable for the growth of THP NCs with other uniform, highly ordered morphology, which might be accomplished by changing the substrate, precursors, growth temperature and pressure, and so forth.

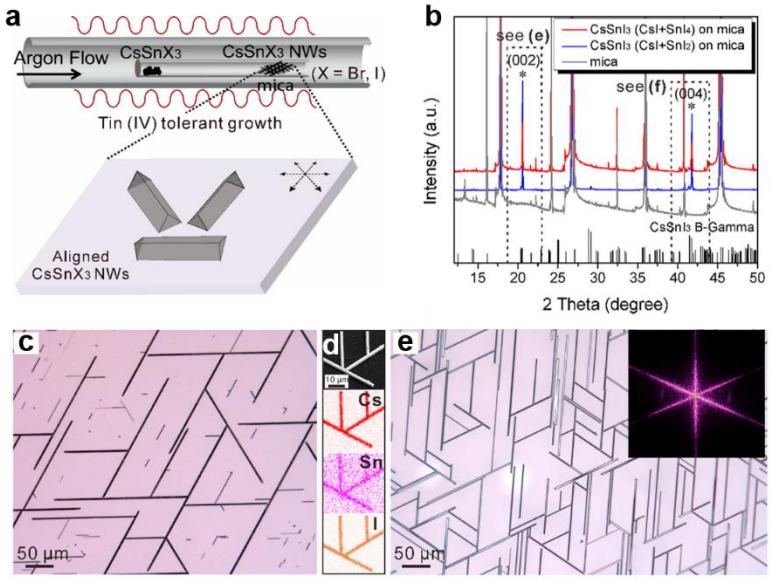

Figure 1.11. (a) Schematic illustration of the Sn^{4+}-tolerant CVD epitaxial growth of $CsSnX_3$ NWs. (b) XRD patterns of $CsSnI_3$ NWs prepared by SnI_2 and SnI_4 regents,

respectively. (c) Optical microscopy image of $CsSnI_3$ NWs grown at 280 °C for 1 h. (d) EDS mapping of a $CsSnI_3$ NW network. (e) Optical microscopy image of $CsSnI_3$ NWs grown at 280 °C for 2 h.[73]

So far, various approaches have been proposed to synthesize THP NCs, but each has pros and cos. At present, the hot-injection approach seems to be the most suitable for the synthesis of high-quality THP NCs with a relatively high PLQY and uniform size.[90] However, it requires a high temperature to promote the nucleation and growth of NCs, and is hard to scale up for a large-scale synthesis. By contrast, the LARP approach can be realized at room temperature and is easier to yield NCs in large quantities. Thanks to the high polarity of good solvents (DMF or DMSO), some potential additives that have poor solubility in nonpolar solvents can be attempted in the LARP synthesis, which leads to additional levers for improving NCs' quality. Nevertheless, controlling the reaction rate is challenging, because the reprecipitation process is finished within several seconds that makes it difficult to control the morphology or crystal quality of NCs. The CVD approach can produce high-oriented THP NCs based on the epitaxial growth, but requires a higher temperature, longer reaction time, and precise control of gas flow rate and vapor pressure.

Apart from the aforementioned synthesis approaches, the soft ionic crystal structure of halide perovskite NCs makes them readily get access to other facile synthetic approaches, like solvothermal reaction,[114] microwave-assisted synthesis,[115] and sonication-assisted reaction,[116] which have been developed for preparing Pb-based NCs but are not extended to the THP system. We believe that concentrated efforts in this direction may aid in developing new synthetic routes to obtain THP NCs with controlled size, morphology, and outstanding photophysical properties.

1.5 Approaches to enhancing the photophysical properties and stability of THP NCs

The excellent defect tolerance nature of Pb-based perovskite NCs makes them show

outstanding optical properties even without any surface modification, but THP NCs seem not to hold this merit. DFT calculations revealed that the Sn vacancy has a very low formation energy and can contribute the electronic state between the CB and VB, behaving as a deep trap for electronic or holes.[90] Therefore, suppressing the formation of Sn vacancies is an effective approach to enhancing the optical properties of THP NCs. In addition, the easy oxidization of Sn^{2+} to Sn^{4+} is another crucial factor causing low PLQY and poor stability of THP NCs, on account of the lattice deformation induced by Sn^{4+} self-doping effect.[117] In the past five years, some approaches have been provided to retarding this oxidization process during the preparation of THP films, such as using reducing atmosphere, antioxidative additive, and ligand protection, some of which, as we consider, could be extended to the synthesis of THP NCs.[118-120] In the following sections, I will discuss the recent efforts on enhancing the optical properties and stability of THP NCs.

1.5.1 Precursor engineering

To better understand the defect nature in $CsSnI_3$ NCs, and to effectively suppress the formation of detrimental structural defects contributing to nonradiative recombination, Liu *et al.* carried out detailed DFT calculations and molecular dynamics simulations to gain deep insight into the characteristics of various point defects and their impact on the photophysical properties.[90] The calculated formation energies of three vacancies (V_{Cs}, V_{Sn}, and V_I), two antisites (Cs_{Sn} and Sn_I), and one interstitial (I_i) show that V_{Sn} has the lowest formation energy and is the dominant defect under the Sn-poor condition (**Figure 1.12a**). A distinct trend is that increasing the chemical potential of Sn can increase the formation energies of V_{Sn}, V_{Cs}, Cs_{Sn}, and I_i, but decrease the formation energies of V_I and Sn_I. Notably, V_{Sn} induces the deep trap level between the VB and CB (at 0.21 eV above the VBM), while other defects contribute to the shallow levels near the VB or VB (**Figure 1.12b**). As a result, only V_{Sn} can exert a significant impact on the charge-carrier recombination in $CsSnI_3$. Using the molecular dynamics simulations, the vibrations of the

VBM and CBM were tracked (**Figure 1.12c, d**). Compared with the pristine $CsSnI_3$, a larger variation in the bandgap for the V_{sn}-containing cousin signifies that the distortion caused by V_{Sn} leads to the change in its crystal geometry and therefore broadening of the emission of $CsSnI_3$. These computational results suggest that suppressing the formation of V_{sn} can not only increase the PLQY but also result in a narrow-band emission from $CsSnI_3$.

For $CsPbCl_3$ NCs, increasing the Cl concentration in the synthesis via precursor engineering has been successfully conducted to decrease the density of Cl vacancies and enhance the NC's optical properties.[28] The key point for the synthesis is the precise control of the ratio of precursors. Being in this regime, Liu *et al.* judiciously employed Cs-oleate, tin (II) 2-ethylhexanote ($Sn(Oct)_2$), and trimethylsilyl iodide (TMSI) as Cs, Sn, and I precursors, respectively (**Figure 1.12e**). Notably, increasing the chemical potential of Sn via changing the precursor ratio of Cs:Sn:I from 0.25:3:3 to 0.25:4.8:3 enhances the PLQYs of $CsSnI_3$ NCs from 4.3% to 18.4%. The full width at half-maximum (fwhm) of the emission decreases from 93 to 77 nm with changing the precursor ratio from 0.25:3:3 to 0.25:4.2:3 (**Figure 1.12f**). The experimental results are consistent with the theoretical prediction.[90] However, for the sample of 0.25:4.8:3, the fwhm increases to 79 nm because of the formation of large crystals and some by-products. Solid-state ^{133}Cs magic angle spinning (MAS) NMR spectra show that the sample synthesized under the Sn-rich condition has a narrower Cs signal compared with those synthesized under the Sn-poor condition, indicating the improved crystal quality. It is interesting to note that the ligand densities of OA/OAm and TOP are extremely low, 1.8 nm^{-2} for OA/OAm and 2.0 nm^{-2} for TOP. It is also noted that imperfect passivation of NC surface by capping ligands may cause the occurrence of certain surface trap states that could significantly influence optical properties. It is thus believed that ligand engineering can be used as an effective strategy to further boost the PLQY of $CsSnI_3$ NCs. The concept of theory-guided synthesis in this work may be applicable to other THP NCs.[108]

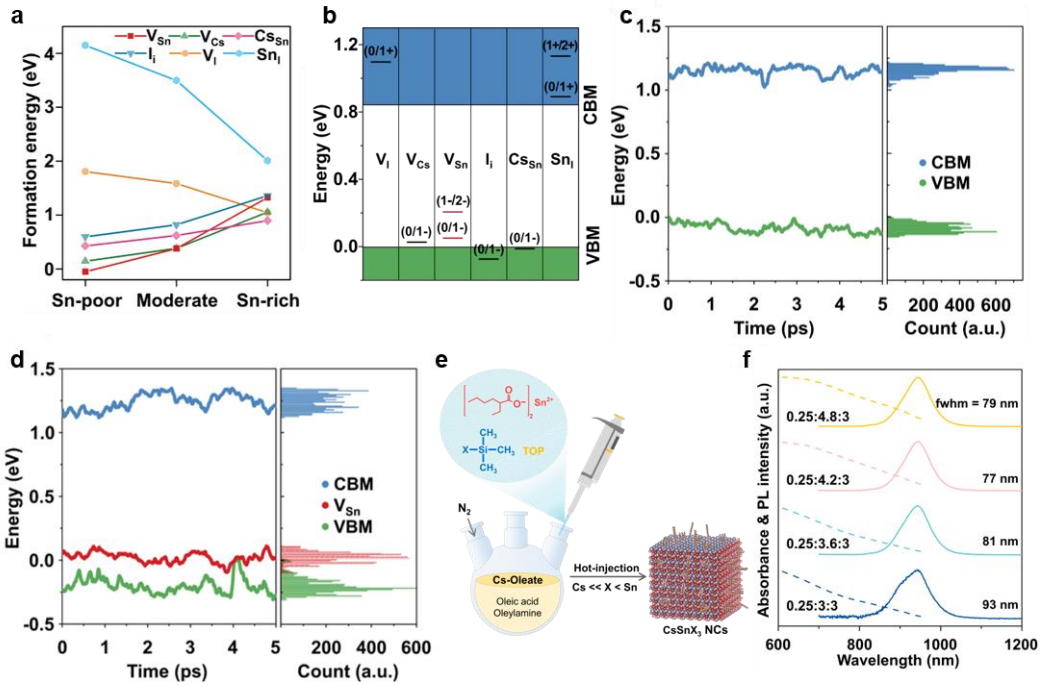

Figure 1.12. (a) Calculated defect formation energies of for 2 × 2 × 2 orthorhombic $CsSnI_3$ supercell at Sn-poor, moderate, and Sn-rich conditions. (b) Defect charge-transition levels of $CsSnI_3$. (c, d) Time evolution of the valence band maximum (VBM), conduction band minimum (CBM), and defect state calculations for non-defect $CsSnI_3$ (c), and V_{sn}-containing $CsSnI_3$ (d), at 300 K. (e) Schematic illustration of the colloidal synthesis of $CsSnX_3$ NCs via precursor engineering. (f) Absorbance and steady-state PL spectra of $CsSnI_3$ NCs with different Cs:Sn:I ratios.[90]

1.5.2 Ligand engineering

Surface capping ligands always have been considered to play an important role in determining the photophysical properties of semiconducting NCs. The traditional ligands for colloidal halide perovskite NCs are long-chain OAm and OA, which maintain the cubic morphology as well as crystal structure of NCs, while some short-chain ligands like octylamine and octanoic acid could induce the low-dimensional morphologies such as nanosheets.[121] In addition, other appropriate ligands can also passivate surface defects, resulting in highly luminescent perovskite NCs and/or notable enhancement of structural stability.[25, 122] Besides, some application-minded scientists and engineers are always

committed to finding appropriate conductive ligands to enhance their performance in solar cells or LED devices.[123, 124] To address the structural instability of THP NCs, it is necessary to exchange the OAm and OA with some peculiar ligands that can effectively protect NCs. For example, perfluorooctanoic acid (PFOA) with a strong electron-withdrawing group was reported to act as an effective ligand to stabilize Sn^{2+} species in THP NCs.[92] The obtained $CsSnBr_3$ NCs show decent stability under ambient environment and light illumination.

Recently, Kang *et al.* used antioxidative oxalate ligand to improve the stability of THP NCs.[125] They chose stannous oxalate (SnC_2O_4), Cs_2CO_3, and NH_4I as the precursors of Sn, Cs, and I, respectively, to prepare $CsSnI_3$ NCs via the hot-injection approach. The yielded $CsSnI_3$ NCs (denoted as SnC_2O_4-$CsSnI_3$) maintain their perovskite structure after reaction and centrifugation process. After storing the SnC_2O_4-$CsSnI_3$ NCs solution in N_2 for 20 days (**Figure 1.13a**), no color change was observed, suggesting superior stability. It was found that these NCs can maintain their original perovskite structure for almost 15 days in the N_2 and 12 h in the air. With further prolonging the storage time in the air, SnC_2O_4-$CsSnI_3$ NCs undergo a phase transition from $CsSnI_3$ to Cs_2SnI_6 (**Figure 1.13b**). In addition, stable $CsSnCl_3$ and $CsSnBr_3$ NCs can also be obtained by this means. The origin of improved stability can be considered as two aspects. One is the strong antioxidative capability of the SnC_2O_4 precursor, possibly suppressing the in-situ oxidation process during the synthesis. The other is the strong coordination of the oxalate ligand with Sn ions forming stable chelates (**Figure 1.13c**), hence preventing the decomposition of NCs. Kang *et al*. also used SnO and SnI_2 to replace SnC_2O_4 as the Sn source. For the case of SnO, it was found that the color of the rude solution changes from black to colorless within several seconds after injecting the Cs_2CO_3 stock solution, indicating the quick degradation of NCs. When using SnI_2 as the precursor, the obtained sample decomposed quickly when exposed to air; even under N_2 environment, the degradation occurs within 40 min (**Figure 1.13a)**. It is noted that the PLQY of $CsSnX_3$ NCs is extremely low, suggesting the existence of a high density of defects leading to

strong nonradiative recombination. We envision that employing other antioxidative and conductive ligands, like phenolsulfonic acid and 2-aminophenol-4-sulfonic acid, deserve to be explored to produce THP NCs with enhanced stability and decent optical property.[126]

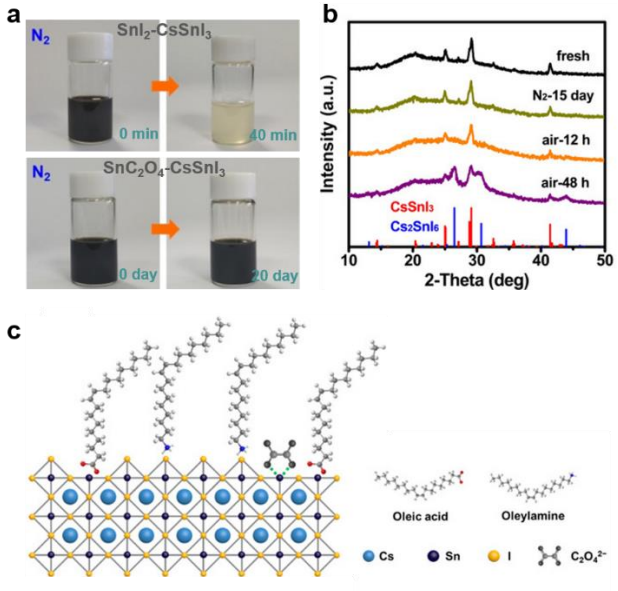

Figure 1.13. (a) Stability comparison between the SnI_2-$CsSnI_3$ NCs and SnC_2O_4-$CsSnI_3$ NCs stored in the N_2. (b) XRD patterns of SnC_2O_4-$CsSnI_3$ NCs after storage in the N_2 and air for different times. (c) Schematic illustration of the surface ligands for SnC_2O_4-$CsSnI_3$ NCs.[125]

1.5.3 Alloyed structure

Alloyed structure construction is another widely employed strategy to regulate the optoelectrical properties and enhance the stability of halide perovskite NCs. For instance, in the Pb-based perovskite category, alloyed $CsPb_{0.64}Zn_{0.36}I_3$ NCs show near-unity PLQY and maintain the α perovskite phase for 70 days;[127] alloying Cd^{2+} into the lattice of perovskite NCs can tune the bandgap and influence crystal structures of NCs.[128, 129] For THPs, the most studied alloyed structure is the SnPb alloyed perovskite films, showing not only enhanced device efficiency, but also bandgap tunability and better structural stability.[67] Recently, SnPb alloyed halide perovskite NCs were also synthesized, which display superior stability compared with pure Sn- and Pb-based perovskite

counterparts.[130, 131]

The first synthesis of alloyed $CsSn_{1-x}Pb_xI_3$ NCs was reported in 2017, using TOP to dissolve SnI_2 and PbI_2 precursors.[130] Increasing the feeding ratio of PbI_2/SnI_2 can tune x from 0 to 3, with the decrease of the bandgaps. Among all alloyed NCs, $CsSn_{0.6}Pb_{0.4}I_3$ NCs are of the most interest because of the less content of Pb and the widest range of light absorption. The extremely poor stability of pure $CsSnI_3$ NCs is always an important challenge, which can be seen in the **Figure 1.14a**. In the air, the color of the prepared $CsSnI_3$ NCs changes from black to clear within 10 min, indicating the fast degradation of NCs. Even under the N_2 atmosphere, the degradation also happens within 40 min. By contrast, the color of alloyed $CsSn_{0.6}Pb_{0.4}I_3$ NCs almost does not change up to 150 days in air. It was found that the structure of $CsSn_{0.6}Pb_{0.4}I_3$ NC films remain unchanged for one month when exposed in air (**Figure 1.14c**), whereas pure $CsSnI_3$ NC films gradually degrade into the yellow non-perovskite phase within 3 days (**Figure 1.14b**). Liu *et al.* proposed a plausible mechanism for the improved stability of SnPb perovskite NCs: compared with $CsSnI_3$ NCs, the introduction of Pb^{2+} gives rise to the change in the ionic charge at the B site, resulting in a decreased Coulomb energy, then leading to a more stable structure; compared with pure $CsPbI_3$ NCs, the improved phase stability could be rationalized by the increase in the Goldschmidt tolerance factor owing to the smaller ionic radius of Sn^{2+} than Pb^{2+}.[131] Despite with enhanced stability, $CsSn_{1-x}Pb_xI_3$ NCs show low PLQYs of only 0.3%~3% (x=0.4-0.8). With increasing the concentration of Sn, the PLQY becomes lower, which may result from the increased intrinsic Sn vacancies. Hence, the suppression of Sn vacancies may be essential not only for pure $CsSnI_3$ NCs but also for SnPb perovskite NCs.

Interestingly, it was found that the PLQY of alloyed $CsSn_{0.6}Pb_{0.4}I_3$ NCs can be increased from ~0.3% to ~28% via sodium (Na) doping (**Figure 1.14d**).[132] X-ray photoelectron spectroscopy (XPS) measurement shows that the binding energies of Cs, Sn, and I all shift to higher energies after Na doping, indicating the enhanced chemical interactions between Cs^+, Sn^{2+}, and I^-. As a result, the diffusion and dissociation of these

ions are strongly restrained, mitigating the formation of some point defects. Detailed theoretical calculations reveal that Na ions prefer to locate at the surface of $CsSn_{0.6}Pb_{0.4}I_3$ NCs, and occupy the interstitial sites because of their small ionic size.[133] Upon Na doping, the newly formed Na-I bonding on the surface layer can induce a decrease in the covalent bonding between the surface I^- and central Sn^{2+} ions. As a result, this charge redistribution promotes the enhancement in the covalent bonding of the surface Sn-I bonds, therefore suppressing the formation of Sn and/or I vacancies. Besides, the binding energies of OAm and OA ligands are also enhanced upon the incorporation of Na ions, contributing to passivate the surface dangling bonds of NCs. However, the optical stability of Na-doped $CsSn_{0.6}Pb_{0.4}I_3$ NCs is poor. The PLQY degrades from ~28% to 4% after 24 h, which may result from the easy migration of the small-sized Na dopant. We believe that employing other kinds of dopants to passivate structural defects of SnPb perovskite NCs could also be considered,[134] since doping engineering is a traditional wisdom to enhance the photophysical properties of semiconducting NCs.

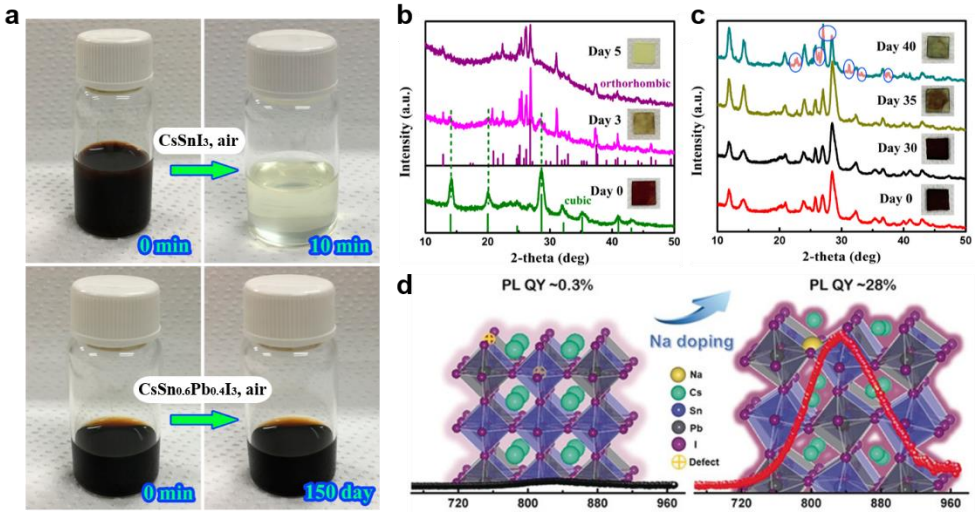

Figure 1.14. (a) Stability comparison between the $CsSnI_3$ NCs and $CsSn_{0.6}Pb_{0.4}I_3$ NCs stored in the air. (b, c) XRD patterns of $CsSnI_3$ NC film (b) and $CsSn_{0.6}Pb_{0.4}I_3$ NC film (c) after storage in air for different times.[130] (d) Schematic illustration of the increase in PLQY for Na-doped $CsSn_{0.6}Pb_{0.4}I_3$ NCs.[132]

It is obvious that the introduction of Pb in the perovskite lattice is not a wise choice on account of the environmental impact. The recently developed SnGe alloyed perovskite NCs can avoid the toxicity issue.[135] The synthetic route is followed the traditional hot-injection approach by mixing equal-ratio SnI_2 and GeI_2. The as-prepared $CsSn_{0.6}Ge_{0.4}I_3$ NCs, with a size of ~9.4 nm, have an orthorhombic structure. Optical characterizations show that the absorption onset and PL peak from $CsSn_{0.6}Ge_{0.4}I_3$ NCs have a clear blue shift compared with that of pure $CsSnI_3$ NCs, indicating a wider bandgap upon the incorporation of Ge into the $CsSnI_3$ lattice (**Figure 1.15a**). However, two different emission peaks, centered at 725 and 782 nm, are observed (**Figure 1.15b**). The main emission peak at 782 nm is derived from the $CsSn_{0.6}Ge_{0.4}I_3$ nanocubes with uniform morphology, while the other PL sub-peak at 725 nm may be ascribed to the formed some nanorods with a smaller diameter of ~4.5 nm. Strong quantum confinement effect in the nanorods results in the blue shift of the PL peak, which also has been observed in the pure $CsSnI_3$ nanorods.[95] A slight increase in PLQY from 0.16% for pure $CsSnI_3$ NCs to 0.95% for $CsSn_{0.6}Ge_{0.4}I_3$ NCs indicates partial suppression of Sn vacancies in NCs. In addition, the stability of $CsSn_{0.6}Ge_{0.4}I_3$ NCs is much higher than unalloyed ones. As shown in **Figure 1.15c**, the PLQYs of pure $CsSnI_3$ NCs decreased to below 30% of the initial value after 30 min in air, while $CsSn_{0.6}Ge_{0.4}I_3$ NCs still maintain about 80 % of the initial PLQY after 30 min. **Figure 1.15d** illustrates the possible alloying effect of Ge^{2+} ions in the perovskite lattice. Apart from the partial replacement of Sn^{2+} with Ge^{2+}, Ge^{2+} ions also could fill in the Sn vacancies, therefore improve the optical properties of NCs. The enhanced stability of alloyed SnGe perovskite NCs can be rationalized as two aspects: (*i*) the increased Goldschmidt tolerance factor upon the involvement of Ge is beneficial for the structural stability; (*ii*) the activation barrier towards water or oxygen penetration of alloyed SnGe perovskite is higher than pure Sn perovskite, indicating the better protection against ambient environment of Ge related termination layer on the NC surface (**Figure 1.15d**). Alloyed $CsSn_{0.6}Ge_{0.4}I_3$ NCs also have been applied in the preparation of solar cells as a light-absorbing material, and the resultant device displays a high PCE of 4.9%,

much better than using $CsSnI_3$ NCs.[135]

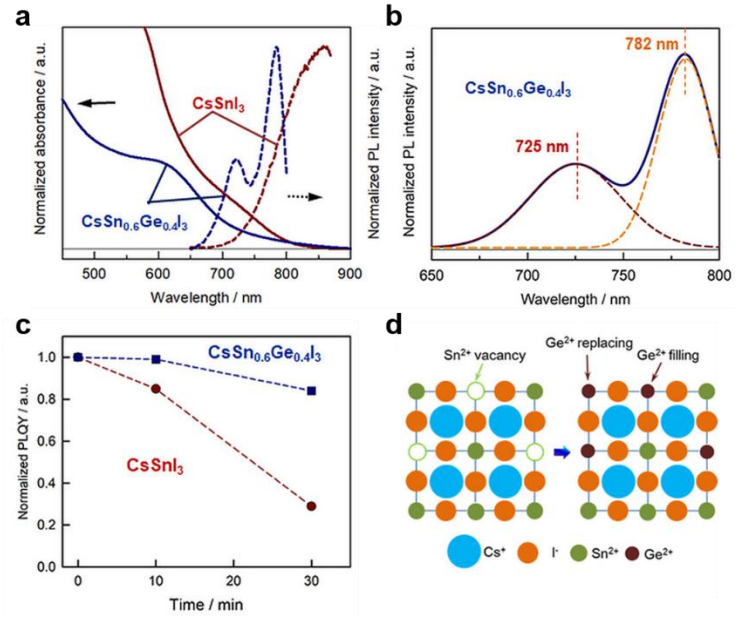

Figure 1.15. (a) Absorption (solid lines) and PL (dash lines) of $CsSnI_3$ and $CsSn_{0.6}Ge_{0.4}I_3$ NCs. (b) Deconvolution of the PL profile of $CsSn_{0.6}Ge_{0.4}I_3$ NCs. (c) Time-dependent PLQYs of $CsSnI_3$ and $CsSn_{0.6}Ge_{0.4}I_3$ NCs stored in the air. (d) Schematic illustration of the Ge filling effect in the Sn vacancies and the replacement of Sn by Ge in the NC structure.[135]

However, both alloyed SnPb and SnGe perovskite NCs show much lower PLQYs than their Pb-based analogues, which is the dominant obstacle for their optoelectronic applications, especially for light-emitting devices, suggesting the necessity to further in-depth investigation of defect chemistry in these alloyed structures. Furthermore, considering the facts that alloyed SnPb NCs cannot avoid the use of toxic Pb and Ge-related reagents are highly expensive, exploring environmental benign, low-cost metal-containing chemicals for the synthesis of alloyed Sn-based perovskites might lead to the discovery of more attractive materials.[127, 136]

I point out that THP NCs synthesized by each approach are still much inferior to Pb-based counterparts. To improve both the photophysical properties and stability of THP

NCs, I believe that it is necessary to combine the aforementioned strategies. For example, precursor engineering enables minimizing the occurrence of V_{Sn} in the $CsSnX_3$ NCs but cannot simultaneously results in perfect surface passivation by ligands used in the reaction,[90] which could be overcome via ligand engineering to cap NCs or by exploiting alloyed structures to increase the defect formation energy.

1.6 Challenges in THP NCs

1.6.1 Synthetic chemistry of THP NCs

At present, the scope of THP NCs that can be synthesized is still limited owing to our poor understanding of their synthetic chemistry. Most studies are related to the synthesis of all-inorganic $CsSnX_3$ NCs, while organic-inorganic hybrid THP NCs are seldom reported. In the perovskite community, the investigations of some fundamental issues in terms of material chemistry and physics are intimately linked to the optoelectronic applications, either for the benchmark energy conversion efficiencies or the enhanced environmental and operational stability. Although it still remains unclear which is the best choice for devices among all-inorganic and hybrid THPs, previous experiments evidences that solar cells constructed by hybrid THPs, especially $FASnI_3$ or its derivatives, show much higher power conversion efficiencies than those based on $CsSnX_3$.[130, 131, 135, 137, 138] It is noted that when the size of $FASnI_3$ NCs is down to several nanometers, in addition to the occurrence of a strong quantum-confinement effect, the conduction band can evolute from a continuous band structure to separate energy levels.[104] This leads to slow carrier relaxation, suggesting its potential for high-efficiency photovoltaic devices that could break the Shockley-Queisser limit. We thus believe that extending the synthesis of tin-based NCs to hybrid ones could not only enrich the library of halide perovskite NCs but also lead to a comprehensive understanding of synthetic chemistry of THP NCs. Besides, the knowledge gained in three-dimensional THP NCs might be applied to low-dimensional hybrid counterparts or low-dimensional/three-dimensional hybrid structures.[139]

Of note, the present synthetic routes to THP NCs are still limited, which is in sharp contrast to those to Pb-based counterparts. The hot-injection approach, which is the only way to highly luminescent THP NCs, is not convenient enough compared with room-temperature synthesis strategies.[5, 116] Developing more facile synthetic methods, like those successfully used in Pb-based NCs such as LARP and sonication strategies, can facilitate the large-scale and low-cost production of THP NCs. Furthermore, the rapid nucleation and growth of THPs, as met in the preparation of Sn-based films, also exists in the synthesis of NCs. Therefore, gaining a deep understanding of the underlying crystallization kinetics and thermodynamics of crystal nucleation, as well as rationally screening the approaches to regulating the nucleation and growth process becomes increasingly important for obtaining THP NCs with outstanding physical and chemical properties. Beyond this, addressing this issue may aid in precise control over defect states in THP NCs. We also underscore that, other synthetic strategies, especially CVD and epitaxial growth, are worthwhile deeply pursuing to grow THP NCs in the form of nanowires and nanoplatelets, which might lead to interesting nanostructures such as heterojunctions.

1.6.2 Sn oxidation

Like the case in THP polycrystalline films, the trace amount of Sn^{4+} may cause self-doping of Sn^{4+} into the lattice of THP NCs, and then destroy the perovskite structure. As a result, Sn^{4+} self-doping is an important factor influencing the optical and physical properties of THP NCs. How to avoid in-situ oxidation of Sn^{2+} moieties during the synthesis and purification process of THP NCs is an important issue needed to be soundly resolved. Even under nitrogen atmosphere, it is still hard to restrain oxidation eventually, as recent findings point out the oxidation of THP in the absence of oxygen.[140] Motivated by the successful routes in the preparation of THP films, we highlight that introducing some reductive additives could be tested to realize in-situ reduction of Sn^{4+}, which may be beneficial for synthesizing high-quality THP NCs.

Previous work shows that the quality of the $FASnI_3$ is of fundamental importance in order to study the real electrical property of Sn-based perovskites, as the neat material showed a PL and absorption characteristic dominated by the high self-doping related to the oxidation of Sn.[141] At present, efficient and reliable tuning of carrier density remains much more challenging in THP NCs than that in Pb halide perovskite NCs, because of a limited understanding of their defect states. We believe that there can be no doubt that THP NCs represent a fertile playground for further investigating electrical properties of Sn-based perovskites, which could lead to reliable and efficient tuning of charge-carrier density.[142]

1.6.3 Surface states and structure of THP NCs

In ABX_3 perovskites, the larger and polarizable ionic components, as well as the lower charge on the X site, result in weaker coulombic interactions and softer ionic bonding within THP NCs, which could enable the occurrence of a mobile and sensitive surface that favors atomic reconstruction and irregularities.[143] In the domain of Pb-based perovskites from nano to bulk, the surface often plays a key role in determining the physical and chemical properties, thus motivating intensive studies in the understanding of perovskite surface and surface strategies towards boosting the efficiency and stability of optoelectronic devices.[143] In marked contrast, our knowledge on the origins of surface states in THP NCs is rather limited. This emphasizes the importance of making efforts in identifying surface defect states for rationally developing surface passivation strategies without laborious trial and error. We believe that THP NCs can be used model systems for the surface study of Sn-based perovskites owing to the large surface-to-volume ratio. In addition to surface states, our understanding of the long-range structure and defect states in the inner part of NCs remains almost blank. We envision that future works in this regard can refer to excellent demonstrations in Pb-based NCs.[77, 144, 145] The benefits in this direction will not only enrich the knowledge bank of defects and structure in halide perovskite NCs but also aid in intentionally tuning them to endow with near-perfect

optoelectronic properties.

1.6.4 Stability of THP NCs

Like Pb-based counterparts, the soft and ionic nature of THP NCs renders them susceptible to larger lattice deformations upon external stimuli. The poor stability of THP NCs against heat, light, oxygen, and humidity is the primary challenge that needs to be addressed to pave the way for technological applications, although this is not a problem at the level of experimental testing. The dominating reason for the poor stability is the easy oxidization of Sn^{2+} into Sn^{4+}. We envision that two concepts can be adopted to boost the stability of THP NCs. Since the conversion of Sn^{2+} to Sn^{4+} preferentially takes place at the surface of NCs, developing perfect surface passivation approaches that can make the surface immune from the interaction with O_2/H_2O should be the first priority. To this end, appropriate ligand protection is one effective method. Recently, the reported cross-linked $MAPbBr_3$ NCs have achieved excellent stability un-der harsh environments over 1.5 years.[146] It is reasonable to expect that similar ligand engineering could also make THP NC's surface almost immune to external stimuli when perfect coordination of surface atoms with ligands is realized. In addition, the design of core-shell structure is also possible to enhance the NC's stability.[147] For instance, previous works have shown that SiO_2-encapsulated LHP NCs possess great stability against air or water.[148, 149] Construction of core-shell THP perovskite NCs may not only improve their structural and optical stabilities but also enhance their performance in NC optoelectronic devices. The second concept, reconstructing the perovskite lattice via introducing foreign elements, can be considered, because this could increase the defect formation energy and thus decrease the density of detrimental structural defects. This could be achieved by doping engineering or forming alloyed structures.

1.6.5 PLQYs of THP NCs

It is noted that, although the THP NCs were first synthesized in 2016,[78] their

relatively high PLQY was not realized yet.[90] Although the reported theory-guided precursor engineering is an effective strategy to suppress the formation of V_{Sn} during the synthesis of THP NCs, the highest PLQY is only 18.4%, still far from nearly 100% as demonstrated in the Pb-based perovskites. There hence exists much room for further improvement of the photophysical properties of THP NCs. We believed that, even under the Sn-rich synthetic condition, the formation of structural defects like V_{Sn} in the $CsSnX_3$ NCs is inevitable because of the features of their fast nucleation and growth and the dynamic change in the precursor ratios in the synthesis process. Only regulating the chemical potential of Sn might not eliminate the V_{Sn} completely. One plausible strategy is to choose appropriate dopant to fill Sn vacancies. Metal doping is a powerful and widely used in Pb-based perovskites to either increase the defect formation energy or endow NCs with new photophysical properties.[134] Recently, Wu *et al.* successfully doped Mn^{2+} and In^{3+} in the bulk $CsSnCl_3$, and obtain stable crystals with ~2% PLQY,[150] but related strategies have not been reported in the NCs. We point out that metal doping could be fully explored in the domain of THP NCs, which may boost their optical properties and stability. Of note, although computational screening could provide more suggestions and guidance for the judicious choice of optimal synthetic conditions, the predictions should be experimentally verified as thermodynamic equilibrium growth conditions are typically considered for a given material.[90]

1.7 Thesis motivations and organization

Lead halide perovskites contain highly toxic lead element, raising critical concerns of environmental pollution and health problems. To address this issue, tin halide perovskites have been pushed to the forefront of the perovskite research owing to their eco-friendly merit and tantalizing photophysical properties. Among them, organic-inorganic tin halide perovskites show better application prospect compared with all-inorganic tin halide perovskites, since the power conversion efficiencies of solar cells based on formamidinium tin iodide ($FASnI_3$) are higher than those based on all-inorganic

cousins. However, instead of the research progress on polycrystalline $FASnI_3$ films, studies on $FASnI_3$ micro/nano crystals much lag than lead halide perovskites.

Different with lead halide perovskites, $FASnI_3$ has poor defect-tolerance, impeding the preparation of high-quality crystals. Some interesting photophysical properties of $FASnI_3$ were observed, such as bandgap widening by structural distortion; slow carrier relaxation for small-sized NCs. Notably, the objects they used for studying the structure-photophysical properties feature massive defect concentrations that lead to extremely low PLQYs. To better understand the structure-photophysical properties of $FASnI_3$ crystals, it is necessary to develop a novelty synthesis route for highly luminescent $FASnI_3$ crystals. In addition, researches regarding the $FASnI_3$ NCs are much limited. Poor stability and poor optical properties of $FASnI_3$ NCs are present challenges. How to choose appropriate ligands and design a general synthesis route for high-quality $FASnI_3$ NCs will pay the way for varied tin halide perovskite optoelectronic applications.

In Chapter 2, I developed a precursor strategy for getting both low-quality and high-quality $FASnI_3$ microcrystals. Under Sn-rich reaction condition, the PLQY of $FASnI_3$ microcrystals could be increased to 8.0%, while that of $FASnI_3$ microcrystals synthesized under Sn-poor reaction condition was only 3.8%, suggesting the controlled structural defects by rationally tuning the reactant ratios. An unconventional bandgap widening by 0.23 eV for the low-quality $FASnI_3$ microcrystals was observed, which is caused by defect-induced structural distortion based on the analysis of X-ray photoelectron spectroscopy, solid-state nuclear magnetic resonance, and optical characterizations. Air-induced degradation of $FASnI_3$ microcrystals also lead to the widened bandgap because of the generated structural defects. Finally, temperature-dependent photoluminescence measurements lead me to the discovery of a new near-infrared photoluminescence band between 185 K and 10 K and the negative thermal quenching in a broad range of 110-200 K, both of which originate from structural defects. The knowledge gained in this research may not only offer a plausible roadmap to prepare high-quality organic-inorganic tin halide perovskite crystals but can also deepen our understanding on the relationship

between defects and photophysical properties of tin-based perovskites.

In Chapter 3, I innovatively develop a new kind of zwitterionic capping ligand, phosphatidylcholine, for $FASnI_3$ NCs. The motivations for me to develop new ligand are two-fold. Firstly, traditional anionic and cationic surface ligands, such as oleate (OA^-), oleylammonium (OAm^+), highly dynamic binding exists between the surface capping ligands and the oppositely charged NC surface ions, together with a mutual equilibrium between the ionized and molecular forms of these ligands, resulting in the poor colloidal and structural stability of tin halide perovskite NCs. Secondly, during the nucleation and growth, amine-related Ruddlesden-Popper (RP) 2D perovskite phases, such as OAm_2SnI_4, usually crystallize as impurities in the final products. To get stable $FASnI_3$ NCs and avoid the crystallization of RP 2D perovskites, I chose zwitterionic phosphatidylcholine as surface capping ligands. The phosphatidylcholine-capped $FASnI_3$ NCs had a mean edge size of ~30 nm and ~1.2% PLQY. Stability tests show that they have excellent colloidal stability in glovebox for 30 days, and great structural stability for 14 days. Temperature-dependent synthesis also suggests that phosphatidylcholine-capped $FASnI_3$ NCs could be synthesized during a wide temperature range from 25 ºC to 150 ºC. My research here provides a new synthesis route for stable $FASnI_3$ NCs that could be beneficial for further structural modification or optoelectronic applications.

In Chapter 4, based on the research in Chapter 3, I develop a surface modification strategy to greatly improve the optical properties of $FASnI_3$ NCs. I started with the theoretical calculations which suggests that creating a Sn-rich reaction condition and achieving quasi-AI-terminated surface is a necessary route for highly luminescent $FASnI_3$ NCs. A novelty synthesis was then provided, in which, the precursor ratio of FA: Sn: I was controlled to 0.2: 1.4: 1, and 2-thiophenemethylammonium (TEA^+) as well as sodium (Na^+) was introduced for realizing TEAI/NaI-terminated surface. This effort led to a record PLQY of 36.9±0.7%, highly larger than all reported tin halide perovskite NCs. Detailed analysis, including X-ray photoelectron spectra, inductively coupled plasma optical emission spectrometry, energy-dispersive X-ray spectroscopy, and ζ-potential

elucidates the surface modification effect by TEA^+ and Na^+. Additionally, my synthesis concept could be extended for FA/Cs alloying NCs that also exhibited high PLQYs. The synthesis route here for highly luminescent $FASnI_3$ NCs could accelerate the research progress regarding tin halide perovskite NCs not only in understanding the structural-photophysical properties of organic-inorganic hybrid tin halide perovskites but also in constructing high-efficiency tin halide perovskite optoelectronic devices.

In Chapter 5, conclusions as well as outlook for further investigations on the topic of the thesis are presented.

Reference:

1. Buttner, R. H.; Maslen, E. N. Electron difference density and structural parameters in CaTiO3. *Acta Crystallographica Section B* **1992,** *48*, 644-649.

2. Lemanov, V. V.; Sotnikov, A. V.; Smirnova, E. P.; Weihnacht, M.; Kunze, R. Perovskite CaTiO3 as an incipient ferroelectric. *Solid State Communications* **1999,** *110*, 611-614.

3. Wang, K.; Yang, D.; Wu, C.; Sanghadasa, M.; Priya, S. Recent progress in fundamental understanding of halide perovskite semiconductors. *Progress in Materials Science* **2019,** *106*, 100580.

4. Sutherland, B. R.; Sargent, E. H. Perovskite photonic sources. *Nature Photonics* **2016,** *10*, 295-302.

5. Shamsi, J.; Urban, A. S.; Imran, M.; De Trizio, L.; Manna, L. Metal Halide Perovskite Nanocrystals: Synthesis, Post-Synthesis Modifications, and Their Optical Properties. *Chemical Reviews* **2019,** *119*, 3296-3348.

6. Yin, W.-J.; Shi, T.; Yan, Y. Unique Properties of Halide Perovskites as Possible Origins of the Superior Solar Cell Performance. *Advanced Materials* **2014,** *26*, 4653-4658.

7. Stoumpos, C. C.; Kanatzidis, M. G. The Renaissance of Halide Perovskites and Their Evolution as Emerging Semiconductors. *Accounts of Chemical Research* **2015,** *48*, 2791-2802.

8. Bartel, C. J.; Sutton, C.; Goldsmith, B. R.; Ouyang, R.; Musgrave, C. B.; Ghiringhelli, L. M.; Scheffler, M. New tolerance factor to predict the stability of perovskite oxides and halides. *Science Advances* **2019,** *5*, eaav0693.

9. Shannon, R. Revised effective ionic radii and systematic studies of interatomic distances in halides and chalcogenides. *Acta Crystallographica Section A* **1976,** *32*, 751-767.

10. van der Stam, W.; Geuchies, J. J.; Altantzis, T.; van den Bos, K. H. W.; Meeldijk, J. D.; Van Aert, S.; Bals, S.; Vanmaekelbergh, D.; de Mello Donega, C. Highly Emissive Divalent-Ion-Doped Colloidal CsPb1–xMxBr3 Perovskite Nanocrystals through Cation

Exchange. *Journal of the American Chemical Society* **2017,** *139*, 4087-4097.

11. Kieslich, G.; Sun, S.; Cheetham, A. K. Solid-state principles applied to organic–inorganic perovskites: new tricks for an old dog. *Chemical Science* **2014,** *5*, 4712-4715.

12. Correa-Baena, J.-P.; Saliba, M.; Buonassisi, T.; Grätzel, M.; Abate, A.; Tress, W.; Hagfeldt, A. Promises and challenges of perovskite solar cells. *Science* **2017,** *358*, 739-744.

13. Cao, F.; Bian, L.; Li, L. Perovskite solar cells with high-efficiency exceeding 25%: a review. *Energy Materials and Devices* **2024**.

14. Chiba, T.; Hayashi, Y.; Ebe, H.; Hoshi, K.; Sato, J.; Sato, S.; Pu, Y.-J.; Ohisa, S.; Kido, J. Anion-exchange red perovskite quantum dots with ammonium iodine salts for highly efficient light-emitting devices. *Nature Photonics* **2018,** *12*, 681-687.

15. Lin, K.; Xing, J.; Quan, L. N.; de Arquer, F. P. G.; Gong, X.; Lu, J.; Xie, L.; Zhao, W.; Zhang, D.; Yan, C.; Li, W.; Liu, X.; Lu, Y.; Kirman, J.; Sargent, E. H.; Xiong, Q.; Wei, Z. Perovskite light-emitting diodes with external quantum efficiency exceeding 20 per cent. *Nature* **2018,** *562*, 245-248.

16.Dong, Y.; Wang, Y.-K.; Yuan, F.; Johnston, A.; Liu, Y.; Ma, D.; Choi, M.-J.; Chen, B.; Chekini, M.; Baek, S.-W.; Sagar, L. K.; Fan, J.; Hou, Y.; Wu, M.; Lee, S.; Sun, B.; Hoogland, S.; Quintero-Bermudez, R.; Ebe, H.; Todorovic, P.; Dinic, F.; Li, P.; Kung, H. T.; Saidaminov, M. I.; Kumacheva, E.; Spiecker, E.; Liao, L.-S.; Voznyy, O.; Lu, Z.-H.; Sargent, E. H. Bipolar-shell resurfacing for blue LEDs based on strongly confined perovskite quantum dots. *Nature Nanotechnology* **2020,** *15*, 668-674.

17. Yang, J.; Choi, M. K.; Yang, U. J.; Kim, S. Y.; Kim, Y. S.; Kim, J. H.; Kim, D.-H.; Hyeon, T. Toward Full-Color Electroluminescent Quantum Dot Displays. *Nano Letters* **2021,** *21*, 26-33.

18. Akkerman, Q. A.; Rainò, G.; Kovalenko, M. V.; Manna, L. Genesis, challenges and opportunities for colloidal lead halide perovskite nanocrystals. *Nature Materials* **2018,** *17*, 394-405.

19. Kovalenko, M. V.; Protesescu, L.; Bodnarchuk, M. I. Properties and potential

optoelectronic applications of lead halide perovskite nanocrystals. *Science* **2017,** *358*, 745-750.

20. Weidman, M. C.; Goodman, A. J.; Tisdale, W. A. Colloidal Halide Perovskite Nanoplatelets: An Exciting New Class of Semiconductor Nanomaterials. *Chemistry of Materials* **2017,** *29*, 5019-5030.

21. Protesescu, L.; Yakunin, S.; Bodnarchuk, M. I.; Krieg, F.; Caputo, R.; Hendon, C. H.; Yang, R. X.; Walsh, A.; Kovalenko, M. V. Nanocrystals of Cesium Lead Halide Perovskites (CsPbX3, X = Cl, Br, and I): Novel Optoelectronic Materials Showing Bright Emission with Wide Color Gamut. *Nano Letters* **2015,** *15*, 3692-3696.

22. Zhang, F.; Zhong, H.; Chen, C.; Wu, X.-g.; Hu, X.; Huang, H.; Han, J.; Zou, B.; Dong, Y. Brightly Luminescent and Color-Tunable Colloidal CH3NH3PbX3 (X = Br, I, Cl) Quantum Dots: Potential Alternatives for Display Technology. *ACS Nano* **2015,** *9*, 4533-4542.

23. Mondal, N.; De, A.; Samanta, A. Achieving Near-Unity Photoluminescence Efficiency for Blue-Violet-Emitting Perovskite Nanocrystals. *ACS Energy Letters* **2019,** *4*, 32-39.

24. Yong, Z.-J.; Guo, S.-Q.; Ma, J.-P.; Zhang, J.-Y.; Li, Z.-Y.; Chen, Y.-M.; Zhang, B.-B.; Zhou, Y.; Shu, J.; Gu, J.-L.; Zheng, L.-R.; Bakr, O. M.; Sun, H.-T. Doping-Enhanced Short-Range Order of Perovskite Nanocrystals for Near-Unity Violet Luminescence Quantum Yield. *Journal of the American Chemical Society* **2018,** *140*, 9942-9951.

25. Pan, J.; Shang, Y.; Yin, J.; De Bastiani, M.; Peng, W.; Dursun, I.; Sinatra, L.; El-Zohry, A. M.; Hedhili, M. N.; Emwas, A.-H.; Mohammed, O. F.; Ning, Z.; Bakr, O. M. Bidentate Ligand-Passivated CsPbI3 Perovskite Nanocrystals for Stable Near-Unity Photoluminescence Quantum Yield and Efficient Red Light-Emitting Diodes. *Journal of the American Chemical Society* **2018,** *140*, 562-565.

26. Li, Z.; Kong, L.; Huang, S.; Li, L. Highly Luminescent and Ultrastable CsPbBr3 Perovskite Quantum Dots Incorporated into a Silica/Alumina Monolith. *Angewandte*

Chemie International Edition **2017,** *56*, 8134-8138.

27. Liu, F.; Zhang, Y.; Ding, C.; Kobayashi, S.; Izuishi, T.; Nakazawa, N.; Toyoda, T.; Ohta, T.; Hayase, S.; Minemoto, T.; Yoshino, K.; Dai, S.; Shen, Q. Highly Luminescent Phase-Stable CsPbI3 Perovskite Quantum Dots Achieving Near 100% Absolute Photoluminescence Quantum Yield. *ACS Nano* **2017,** *11*, 10373-10383.

28.Imran, M.; Caligiuri, V.; Wang, M.; Goldoni, L.; Prato, M.; Krahne, R.; De Trizio, L.; Manna, L. Benzoyl Halides as Alternative Precursors for the Colloidal Synthesis of Lead-Based Halide Perovskite Nanocrystals. *Journal of the American Chemical Society* **2018,** *140*, 2656-2664.

29. Almeida, G.; Infante, I.; Manna, L. Resurfacing halide perovskite nanocrystals. *Science* **2019,** *364*, 833-834.

30. Dutta, A.; Behera, R. K.; Pal, P.; Baitalik, S.; Pradhan, N. Near-Unity Photoluminescence Quantum Efficiency for All CsPbX3 (X=Cl, Br, and I) Perovskite Nanocrystals: A Generic Synthesis Approach. *Angewandte Chemie International Edition* **2019,** *58*, 5552-5556.

31. Pradhan, N. Tips and Twists in Making High Photoluminescence Quantum Yield Perovskite Nanocrystals. *ACS Energy Letters* **2019,** *4*, 1634-1638.

32. Chen, J.-K.; Ma, J.-P.; Guo, S.-Q.; Chen, Y.-M.; Zhao, Q.; Zhang, B.-B.; Li, Z.-Y.; Zhou, Y.; Hou, J.; Kuroiwa, Y.; Moriyoshi, C.; Bakr, O. M.; Zhang, J.; Sun, H.-T. High-Efficiency Violet-Emitting All-Inorganic Perovskite Nanocrystals Enabled by Alkaline-Earth Metal Passivation. *Chemistry of Materials* **2019,** *31*, 3974-3983.

33. Wu, Y.; Li, X.; Zeng, H. Highly Luminescent and Stable Halide Perovskite Nanocrystals. *ACS Energy Letters* **2019,** *4*, 673-681.

34. Li, H.; Lin, H.; Ouyang, D.; Yao, C.; Li, C.; Sun, J.; Song, Y.; Wang, Y.; Yan, Y.; Wang, Y.; Dong, Q.; Choy, W. C. H. Efficient and Stable Red Perovskite Light-Emitting Diodes with Operational Stability >300 h. *Advanced Materials* **2021,** *33*, 2008820.

35. Seth, S.; Ahmed, T.; De, A.; Samanta, A. Tackling the Defects, Stability, and Photoluminescence of CsPbX3 Perovskite Nanocrystals. *ACS Energy Letters* **2019,** *4*,

1610-1618.

36. Aggarwal, P.; Ahlawat, M.; Govind Rao, V. Engineering Water Stable Perovskite and Plasmonic-Perovskite Nanocomposites: A Step toward Unleashing the True Potential of Perovskite Catalysis. *Advanced Materials Interfaces* **2023,** *10*, 2202029.

37. Song, J.; Li, J.; Li, X.; Xu, L.; Dong, Y.; Zeng, H. Quantum Dot Light-Emitting Diodes Based on Inorganic Perovskite Cesium Lead Halides (CsPbX3). *Adv Mater* **2015,** *27*, 7162-7167.

38. Wang, H.-C.; Bao, Z.; Tsai, H.-Y.; Tang, A.-C.; Liu, R.-S. Perovskite Quantum Dots and Their Application in Light-Emitting Diodes. *Small* **2018,** *14*, 1702433.

39. Nong, Y.; Yao, J.; Li, J.; Xu, L.; Yang, Z.; Li, C.; Song, J. Boosting External Quantum Efficiency of Blue Perovskite QLEDs Exceeding 23% by Trifluoroacetate Passivation and Mixed Hole Transportation Design. *Advanced Materials n/a*, 2402325.

40. Park, Y.-S.; Guo, S.; Makarov, N. S.; Klimov, V. I. Room Temperature Single-Photon Emission from Individual Perovskite Quantum Dots. *ACS Nano* **2015,** *9*, 10386-10393.

41. Utzat, H.; Sun, W.; Kaplan, A. E. K.; Krieg, F.; Ginterseder, M.; Spokoyny, B.; Klein, N. D.; Shulenberger, K. E.; Perkinson, C. F.; Kovalenko, M. V.; Bawendi, M. G. Coherent single-photon emission from colloidal lead halide perovskite quantum dots. *Science* **2019,** *363*, 1068-1072.

42. Wang, Y.; Li, X.; Nalla, V.; Zeng, H.; Sun, H. Solution-Processed Low Threshold Vertical Cavity Surface Emitting Lasers from All-Inorganic Perovskite Nanocrystals. *Advanced Functional Materials* **2017,** *27*, 1605088.

43. Chen, Q.; Wu, J.; Ou, X.; Huang, B.; Almutlaq, J.; Zhumekenov, A. A.; Guan, X.; Han, S.; Liang, L.; Yi, Z.; Li, J.; Xie, X.; Wang, Y.; Li, Y.; Fan, D.; Teh, D. B. L.; All, A. H.; Mohammed, O. F.; Bakr, O. M.; Wu, T.; Bettinelli, M.; Yang, H.; Huang, W.; Liu, X. All-inorganic perovskite nanocrystal scintillators. *Nature* **2018,** *561*, 88-93.

44. Liu, C.; Zeng, Q.; Wei, H.; Yu, Y.; Zhao, Y.; Feng, T.; Yang, B. Metal Halide Perovskite Nanocrystal Solar Cells: Progress and Challenges. *Small Methods* **2020,** *4*,

2000419.

45. Akkerman, Q. A.; Gandini, M.; Di Stasio, F.; Rastogi, P.; Palazon, F.; Bertoni, G.; Ball, J. M.; Prato, M.; Petrozza, A.; Manna, L. Strongly emissive perovskite nanocrystal inks for high-voltage solar cells. *Nature Energy* **2016,** *2*, 16194.

46. Kojima, A.; Teshima, K.; Miyasaka, T.; Shirai, Y. Novel Photoelectrochemical Cell with Mesoscopic Electrodes Sensitized by Lead-Halide Compounds (2). *ECS Meeting Abstracts* **2006,** *MA2006-02*, 397-397.

47. Green, M. A.; Dunlop, E. D.; Yoshita, M.; Kopidakis, N.; Bothe, K.; Siefer, G.; Hao, X. Solar cell efficiency tables (Version 63). *Progress in Photovoltaics: Research and Applications* **2024,** *32*, 3-13.

48. Zhao, Q.; Hazarika, A.; Chen, X.; Harvey, S. P.; Larson, B. W.; Teeter, G. R.; Liu, J.; Song, T.; Xiao, C.; Shaw, L.; Zhang, M.; Li, G.; Beard, M. C.; Luther, J. M. High efficiency perovskite quantum dot solar cells with charge separating heterostructure. *Nature Communications* **2019,** *10*, 2842.

49. Tan, Z.-K.; Moghaddam, R. S.; Lai, M. L.; Docampo, P.; Higler, R.; Deschler, F.; Price, M.; Sadhanala, A.; Pazos, L. M.; Credgington, D.; Hanusch, F.; Bein, T.; Snaith, H. J.; Friend, R. H. Bright light-emitting diodes based on organometal halide perovskite. *Nature Nanotechnology* **2014,** *9*, 687-692.

50. Chen, Z.; Li, Z.; Chen, Z.; Xia, R.; Zou, G.; Chu, L.; Su, S.-J.; Peng, J.; Yip, H.-L.; Cao, Y. Utilization of Trapped Optical Modes for White Perovskite Light-Emitting Diodes with Efficiency over 12%. *Joule* **2021,** *5*, 456-466.

51. Zhou, W.; Shen, Y.; Cao, L.-X.; Lu, Y.; Tang, Y.-Y.; Zhang, K.; Ren, H.; Xie, F.-M.; Li, Y.-Q.; Tang, J.-X. Manipulating Ionic Behavior with Bifunctional Additives for Efficient Sky-Blue Perovskite Light-Emitting Diodes. *Advanced Functional Materials* **2023,** *33*, 2301425.

52. Jiang, J.; Chu, Z.; Yin, Z.; Li, J.; Yang, Y.; Chen, J.; Wu, J.; You, J.; Zhang, X. Red Perovskite Light-Emitting Diodes with Efficiency Exceeding 25% Realized by Co-Spacer Cations. *Advanced Materials* **2022,** *34*, 2204460.

53. Bai, W.; Xuan, T.; Zhao, H.; Dong, H.; Cheng, X.; Wang, L.; Xie, R.-J. Perovskite Light-Emitting Diodes with an External Quantum Efficiency Exceeding 30%. *Advanced Materials* **2023,** *35*, 2302283.

54. Song, J.; Li, J.; Li, X.; Xu, L.; Dong, Y.; Zeng, H. Quantum Dot Light-Emitting Diodes Based on Inorganic Perovskite Cesium Lead Halides (CsPbX3). *Advanced Materials* **2015,** *27*, 7162-7167.

55. T. Sanders; Y. Liu; V. Buchner; P.B. Tchounwou Neurotoxic Effects and Biomarkers of Lead Exposure: A Review. *Reviews on Environmental Health* **2009,** *24*, 15-46.

56. Fan, Q.; Biesold-McGee, G. V.; Ma, J.; Xu, Q.; Pan, S.; Peng, J.; Lin, Z. Lead-Free Halide Perovskite Nanocrystals: Crystal Structures, Synthesis, Stabilities, and Optical Properties. *Angewandte Chemie International Edition* **2020,** *59*, 1030-1046.

57. Li, J.; Cao, H.-L.; Jiao, W.-B.; Wang, Q.; Wei, M.; Cantone, I.; Lü, J.; Abate, A. Biological impact of lead from halide perovskites reveals the risk of introducing a safe threshold. *Nature Communications* **2020,** *11*, 310.

58. López-Fernández, I.; Valli, D.; Wang, C.-Y.; Samanta, S.; Okamoto, T.; Huang, Y.-T.; Sun, K.; Liu, Y.; Chirvony, V. S.; Patra, A.; Zito, J.; De Trizio, L.; Gaur, D.; Sun, H.-T.; Xia, Z.; Li, X.; Zeng, H.; Mora-Seró, I.; Pradhan, N.; Martínez-Pastor, J. P.; Müller-Buschbaum, P.; Biju, V.; Debnath, T.; Saliba, M.; Debroye, E.; Hoye, R. L. Z.; Infante, I.; Manna, L.; Polavarapu, L. Lead-Free Halide Perovskite Materials and Optoelectronic Devices: Progress and Prospective. *Advanced Functional Materials* **2024,** *34*, 2307896.

59. Ke, W.; Kanatzidis, M. G. Prospects for low-toxicity lead-free perovskite solar cells. *Nature Communications* **2019,** *10*, 965.

60. Chen, J.-K.; Zhang, B.-B.; Liu, Q.; Shirahata, N.; Mohammed, O. F.; Bakr, O. M.; Sun, H.-T. Advances and Challenges in Tin Halide Perovskite Nanocrystals. *ACS Materials Letters* **2021,** *3*, 1541-1557.

61. Dey, A.; Ye, J.; De, A.; Debroye, E.; Ha, S. K.; Bladt, E.; Kshirsagar, A. S.; Wang, Z.; Yin, J.; Wang, Y.; Quan, L. N.; Yan, F.; Gao, M.; Li, X.; Shamsi, J.; Debnath, T.; Cao,

M.; Scheel, M. A.; Kumar, S.; Steele, J. A.; Gerhard, M.; Chouhan, L.; Xu, K.; Wu, X.-g.; Li, Y.; Zhang, Y.; Dutta, A.; Han, C.; Vincon, I.; Rogach, A. L.; Nag, A.; Samanta, A.; Korgel, B. A.; Shih, C.-J.; Gamelin, D. R.; Son, D. H.; Zeng, H.; Zhong, H.; Sun, H.; Demir, H. V.; Scheblykin, I. G.; Mora-Seró, I.; Stolarczyk, J. K.; Zhang, J. Z.; Feldmann, J.; Hofkens, J.; Luther, J. M.; Pérez-Prieto, J.; Li, L.; Manna, L.; Bodnarchuk, M. I.; Kovalenko, M. V.; Roeffaers, M. B. J.; Pradhan, N.; Mohammed, O. F.; Bakr, O. M.; Yang, P.; Müller-Buschbaum, P.; Kamat, P. V.; Bao, Q.; Zhang, Q.; Krahne, R.; Galian, R. E.; Stranks, S. D.; Bals, S.; Biju, V.; Tisdale, W. A.; Yan, Y.; Hoye, R. L. Z.; Polavarapu, L. State of the Art and Prospects for Halide Perovskite Nanocrystals. *ACS Nano* **2021,** *15*, 10775-10981.

62. Lei, H.; Hardy, D.; Gao, F. Lead-Free Double Perovskite Cs2AgBiBr6: Fundamentals, Applications, and Perspectives. *Advanced Functional Materials* **2021,** *31*, 2105898.

63. Kieslich, G.; Sun, S.; Cheetham, A. K. An extended Tolerance Factor approach for organic–inorganic perovskites. *Chemical Science* **2015,** *6*, 3430-3433.

64. Travis, W.; Glover, E. N. K.; Bronstein, H.; Scanlon, D. O.; Palgrave, R. G. On the application of the tolerance factor to inorganic and hybrid halide perovskites: a revised system. *Chemical Science* **2016,** *7*, 4548-4556.

65. Delor, M.; Slavney, A. H.; Wolf, N. R.; Filip, M. R.; Neaton, J. B.; Karunadasa, H. I.; Ginsberg, N. S. Carrier Diffusion Lengths Exceeding 1 μm Despite Trap-Limited Transport in Halide Double Perovskites. *ACS Energy Letters* **2020,** *5*, 1337-1345.

66. Bhumla, P.; Jain, M.; Sheoran, S.; Bhattacharya, S. Vacancy-Ordered Double Perovskites Cs2BI6 (B = Pt, Pd, Te, Sn): An Emerging Class of Thermoelectric Materials. *The Journal of Physical Chemistry Letters* **2022,** *13*, 11655-11662.

67. Xi, J.; Loi, M. A. The Fascinating Properties of Tin-Alloyed Halide Perovskites. *ACS Energy Letters* **2021,** *6*, 1803-1810.

68. Diau, E. W.-G.; Jokar, E.; Rameez, M. Strategies To Improve Performance and Stability for Tin-Based Perovskite Solar Cells. *ACS Energy Letters* **2019,** *4*, 1930-1937.

69. Chung, I.; Song, J.-H.; Im, J.; Androulakis, J.; Malliakas, C. D.; Li, H.; Freeman, A. J.; Kenney, J. T.; Kanatzidis, M. G. CsSnI3: Semiconductor or Metal? High Electrical Conductivity and Strong Near-Infrared Photoluminescence from a Single Material. High Hole Mobility and Phase-Transitions. *Journal of the American Chemical Society* **2012,** *134*, 8579-8587.

70. Glazer, A. The classification of tilted octahedra in perovskites. *Acta Crystallographica Section B* **1972,** *28*, 3384-3392.

71. Yamada, K.; Funabiki, S.; Horimoto, H.; Matsui, T.; Okuda, T.; Ichiba, S. Structural Phase Transitions of the Polymorphs of CsSnI3 by Means of Rietveld Analysis of the X-Ray Diffraction. *Chemistry Letters* **2006,** *20*, 801-804.

72. Stoumpos, C. C.; Malliakas, C. D.; Kanatzidis, M. G. Semiconducting Tin and Lead Iodide Perovskites with Organic Cations: Phase Transitions, High Mobilities, and Near-Infrared Photoluminescent Properties. *Inorganic Chemistry* **2013,** *52*, 9019-9038.

73. Chen, J.; Luo, Z.; Fu, Y.; Wang, X.; Czech, K. J.; Shen, S.; Guo, L.; Wright, J. C.; Pan, A.; Jin, S. Tin(IV)-Tolerant Vapor-Phase Growth and Photophysical Properties of Aligned Cesium Tin Halide Perovskite (CsSnX3; X = Br, I) Nanowires. *ACS Energy Letters* **2019,** *4*, 1045-1052.

74. Xiao, G.; Cao, Y.; Qi, G.; Wang, L.; Liu, C.; Ma, Z.; Yang, X.; Sui, Y.; Zheng, W.; Zou, B. Pressure Effects on Structure and Optical Properties in Cesium Lead Bromide Perovskite Nanocrystals. *Journal of the American Chemical Society* **2017,** *139*, 10087-10094.

75. Kirschner, M. S.; Diroll, B. T.; Guo, P.; Harvey, S. M.; Helweh, W.; Flanders, N. C.; Brumberg, A.; Watkins, N. E.; Leonard, A. A.; Evans, A. M.; Wasielewski, M. R.; Dichtel, W. R.; Zhang, X.; Chen, L. X.; Schaller, R. D. Photoinduced, reversible phase transitions in all-inorganic perovskite nanocrystals. *Nature Communications* **2019,** *10*, 504.

76. Yao, H.; Zhao, J.; Li, Z.; Ci, Z.; Jin, Z. Research and progress of black metastable phase CsPbI3 solar cells. *Materials Chemistry Frontiers* **2021,** *5*, 1221-1235.

77. Chen, J.-K.; Zhao, Q.; Shirahata, N.; Yin, J.; Bakr, O. M.; Mohammed, O. F.; Sun, H.-T. Shining Light on the Structure of Lead Halide Perovskite Nanocrystals. *ACS Materials Letters* **2021,** *3*, 845-861.

78. Jellicoe, T. C.; Richter, J. M.; Glass, H. F. J.; Tabachnyk, M.; Brady, R.; Dutton, S. E.; Rao, A.; Friend, R. H.; Credgington, D.; Greenham, N. C.; Böhm, M. L. Synthesis and Optical Properties of Lead-Free Cesium Tin Halide Perovskite Nanocrystals. *Journal of the American Chemical Society* **2016,** *138*, 2941-2944.

79. Lefebvre, I.; Lippens, P. E.; Lannoo, M.; Allan, G. Band structure of $CsSnBr_3$. *Physical Review B* **1990,** *42*, 9174-9177.

80. Huang, L.-y.; Lambrecht, W. R. L. Electronic band structure, phonons, and exciton binding energies of halide perovskites $CsSnCl_3$, $CsSnBr_3$, and $CsSnI_3$. *Physical Review B* **2013,** *88*, 165203.

81. Padmavathy, R.; Amudhavalli, A.; Rajeswarapalanichamy, R.; Iyakutti, K. Electronic structure and optical properties of $CsSnI_{3-y}Br_y$ (y = 0, 1, 2, 3) perovskites. *International Journal of Modern Physics B* **2019,** *33*, 1950003.

82. Tao, S.; Schmidt, I.; Brocks, G.; Jiang, J.; Tranca, I.; Meerholz, K.; Olthof, S. Absolute energy level positions in tin- and lead-based halide perovskites. *Nature Communications* **2019,** *10*, 2560.

83. Goyal, A.; McKechnie, S.; Pashov, D.; Tumas, W.; van Schilfgaarde, M.; Stevanović, V. Origin of Pronounced Nonlinear Band Gap Behavior in Lead–Tin Hybrid Perovskite Alloys. *Chemistry of Materials* **2018,** *30*, 3920-3928.

84. Fecht, H. J.; Hellstern, E.; Fu, Z.; Johnson, W. L. Nanocrystalline metals prepared by high-energy ball milling. *Metallurgical Transactions A* **1990,** *21*, 2333-2337.

85. Naguib, M.; Kurtoglu, M.; Presser, V.; Lu, J.; Niu, J.; Heon, M.; Hultman, L.; Gogotsi, Y.; Barsoum, M. W. Two-Dimensional Nanocrystals Produced by Exfoliation of Ti3AlC2. *Advanced Materials* **2011,** *23*, 4248-4253.

86. Protesescu, L.; Yakunin, S.; Nazarenko, O.; Dirin, D. N.; Kovalenko, M. V. Low-Cost Synthesis of Highly Luminescent Colloidal Lead Halide Perovskite Nanocrystals by

Wet Ball Milling. *ACS Applied Nano Materials* **2018,** *1*, 1300-1308.

87. Hintermayr, V. A.; Richter, A. F.; Ehrat, F.; Döblinger, M.; Vanderlinden, W.; Sichert, J. A.; Tong, Y.; Polavarapu, L.; Feldmann, J.; Urban, A. S. Tuning the Optical Properties of Perovskite Nanoplatelets through Composition and Thickness by Ligand-Assisted Exfoliation. *Advanced Materials* **2016,** *28*, 9478-9485.

88. Cargnello, M.; Gordon, T. R.; Murray, C. B. Solution-Phase Synthesis of Titanium Dioxide Nanoparticles and Nanocrystals. *Chemical Reviews* **2014,** *114*, 9319-9345.

89. Swihart, M. T. Vapor-phase synthesis of nanoparticles. *Current Opinion in Colloid & Interface Science* **2003,** *8*, 127-133.

90. Liu, Q.; Yin, J.; Zhang, B.-B.; Chen, J.-K.; Zhou, Y.; Zhang, L.-M.; Wang, L.-M.; Zhao, Q.; Hou, J.; Shu, J.; Song, B.; Shirahata, N.; Bakr, O. M.; Mohammed, O. F.; Sun, H.-T. Theory-Guided Synthesis of Highly Luminescent Colloidal Cesium Tin Halide Perovskite Nanocrystals. *Journal of the American Chemical Society* **2021,** *143*, 5470-5480.

91. Wong, A. B.; Bekenstein, Y.; Kang, J.; Kley, C. S.; Kim, D.; Gibson, N. A.; Zhang, D.; Yu, Y.; Leone, S. R.; Wang, L.-W.; Alivisatos, A. P.; Yang, P. Strongly Quantum Confined Colloidal Cesium Tin Iodide Perovskite Nanoplates: Lessons for Reducing Defect Density and Improving Stability. *Nano Letters* **2018,** *18*, 2060-2066.

92. Wang, A.; Guo, Y.; Muhammad, F.; Deng, Z. Controlled Synthesis of Lead-Free Cesium Tin Halide Perovskite Cubic Nanocages with High Stability. *Chemistry of Materials* **2017,** *29*, 6493-6501.

93. Weidman, M. C.; Seitz, M.; Stranks, S. D.; Tisdale, W. A. Highly Tunable Colloidal Perovskite Nanoplatelets through Variable Cation, Metal, and Halide Composition. *ACS Nano* **2016,** *10*, 7830-7839.

94. Chen, M.-Y.; Lin, J.-T.; Hsu, C.-S.; Chang, C.-K.; Chiu, C.-W.; Chen, H. M.; Chou, P.-T. Strongly Coupled Tin-Halide Perovskites to Modulate Light Emission: Tunable 550–640 nm Light Emission (FWHM 36–80 nm) with a Quantum Yield of up to

6.4%. *Advanced Materials* **2018,** *30*, 1706592.

95. Chen, L.-J.; Lee, C.-R.; Chuang, Y.-J.; Wu, Z.-H.; Chen, C. Synthesis and Optical Properties of Lead-Free Cesium Tin Halide Perovskite Quantum Rods with High-Performance Solar Cell Application. *The Journal of Physical Chemistry Letters* **2016,** *7*, 5028-5035.

96. Wang, Y.; Tu, J.; Li, T.; Tao, C.; Deng, X.; Li, Z. Convenient preparation of CsSnI3 quantum dots, excellent stability, and the highest performance of lead-free inorganic perovskite solar cells so far. *Journal of Materials Chemistry A* **2019,** *7*, 7683-7690.

97.Wang, Y.; Sun, X.; Shivanna, R.; Yang, Y.; Chen, Z.; Guo, Y.; Wang, G.-C.; Wertz, E.; Deschler, F.; Cai, Z.; Zhou, H.; Lu, T.-M.; Shi, J. Photon Transport in One-Dimensional Incommensurately Epitaxial CsPbX3 Arrays. *Nano Letters* **2016,** *16*, 7974-7981.

98. Chen, J.; Fu, Y.; Samad, L.; Dang, L.; Zhao, Y.; Shen, S.; Guo, L.; Jin, S. Vapor-Phase Epitaxial Growth of Aligned Nanowire Networks of Cesium Lead Halide Perovskites (CsPbX3, X = Cl, Br, I). *Nano Letters* **2017,** *17*, 460-466.

99. Han, M.; Sun, J.; Peng, M.; Han, N.; Chen, Z.; Liu, D.; Guo, Y.; Zhao, S.; Shan, C.; Xu, T.; Hao, X.; Hu, W.; Yang, Z.-x. Controllable Growth of Lead-Free All-Inorganic Perovskite Nanowire Array with Fast and Stable Near-Infrared Photodetection. *The Journal of Physical Chemistry C* **2019,** *123*, 17566-17573.

100. Almeida, G.; Ashton, O. J.; Goldoni, L.; Maggioni, D.; Petralanda, U.; Mishra, N.; Akkerman, Q. A.; Infante, I.; Snaith, H. J.; Manna, L. The Phosphine Oxide Route toward Lead Halide Perovskite Nanocrystals. *Journal of the American Chemical Society* **2018,** *140*, 14878-14886.

101. Li, Y.; Wang, D.; Yang, Y.; Ding, C.; Hu, Y.; Liu, F.; Wei, Y.; Liu, D.; Li, H.; Shi, G.; Chen, S.; Li, H.; Fuchimoto, A.; Tosa, K.; Hiroki, U.; Hayase, S.; Wei, H.; Shen, Q. Stable Inorganic Colloidal Tin and Tin–Lead Perovskite Nanocrystals with Ultralong Carrier Lifetime via Sn(IV) Control. *Journal of the American Chemical Society* **2024,**

146, 3094-3101.

102. Gahlot, K.; de Graaf, S.; Duim, H.; Nedelcu, G.; Koushki, R. M.; Ahmadi, M.; Gavhane, D.; Lasorsa, A.; De Luca, O.; Rudolf, P.; van der Wel, P. C. A.; Loi, M. A.; Kooi, B. J.; Portale, G.; Calbo, J.; Protesescu, L. Structural Dynamics and Tunability for Colloidal Tin Halide Perovskite Nanostructures. *Advanced Materials* **2022,** *34*, 2201353.

103. Dirin, D. N.; Vivani, A.; Zacharias, M.; Sekh, T. V.; Cherniukh, I.; Yakunin, S.; Bertolotti, F.; Aebli, M.; Schaller, R. D.; Wieczorek, A.; Siol, S.; Cancellieri, C.; Jeurgens, L. P. H.; Masciocchi, N.; Guagliardi, A.; Pedesseau, L.; Even, J.; Kovalenko, M. V.; Bodnarchuk, M. I. Intrinsic Formamidinium Tin Iodide Nanocrystals by Suppressing the Sn(IV) Impurities. *Nano Letters* **2023,** *23*, 1914-1923.

104. Dai, L.; Deng, Z.; Auras, F.; Goodwin, H.; Zhang, Z.; Walmsley, J. C.; Bristowe, P. D.; Deschler, F.; Greenham, N. C. Slow carrier relaxation in tin-based perovskite nanocrystals. *Nature Photonics* **2021,** *15*, 696-702.

105. Li, X.; Wu, Y.; Zhang, S.; Cai, B.; Gu, Y.; Song, J.; Zeng, H. CsPbX3 Quantum Dots for Lighting and Displays: Room-Temperature Synthesis, Photoluminescence Superiorities, Underlying Origins and White Light-Emitting Diodes. *Advanced Functional Materials* **2016,** *26*, 2435-2445.

106. Wei, S.; Yang, Y.; Kang, X.; Wang, L.; Huang, L.; Pan, D. Room-temperature and gram-scale synthesis of CsPbX3 (X = Cl, Br, I) perovskite nanocrystals with 50–85% photoluminescence quantum yields. *Chemical Communications* **2016,** *52*, 7265-7268.

107. Gao, Y.; Wei, Z.; Yoo, P.; Shi, E.; Zeller, M.; Zhu, C.; Liao, P.; Dou, L. Highly Stable Lead-Free Perovskite Field-Effect Transistors Incorporating Linear π-Conjugated Organic Ligands. *Journal of the American Chemical Society* **2019,** *141*, 15577-15585.

108. Shi, E.; Yuan, B.; Shiring, S. B.; Gao, Y.; Akriti; Guo, Y.; Su, C.; Lai, M.; Yang, P.; Kong, J.; Savoie, B. M.; Yu, Y.; Dou, L. Two-dimensional halide perovskite lateral epitaxial heterostructures. *Nature* **2020,** *580*, 614-620.

109. Wang, K.; Jin, L.; Gao, Y.; Liang, A.; Finkenauer, B. P.; Zhao, W.; Wei, Z.; Zhu, C.; Guo, T.-F.; Huang, L.; Dou, L. Lead-Free Organic–Perovskite Hybrid Quantum Wells for Highly Stable Light-Emitting Diodes. *ACS Nano* **2021,** *15*, 6316-6325.

110. Chen, Z.; Dhakal, T. P. Room temperature synthesis of lead-free FASnI3 perovskite nanocrystals with improved stability by SnF2 additive. *Applied Physics Reviews* **2023,** *10*.

111. Wu, Z.; Chen, J.; Mi, Y.; Sui, X.; Zhang, S.; Du, W.; Wang, R.; Shi, J.; Wu, X.; Qiu, X.; Qin, Z.; Zhang, Q.; Liu, X. All-Inorganic CsPbBr3 Nanowire Based Plasmonic Lasers. *Advanced Optical Materials* **2018,** *6*, 1800674.

112. Zheng, Z.; Wang, X.; Shen, Y.; Luo, Z.; Li, L.; Gan, L.; Ma, Y.; Li, H.; Pan, A.; Zhai, T. Space-Confined Synthesis of 2D All-Inorganic CsPbI3 Perovskite Nanosheets for Multiphoton-Pumped Lasing. *Advanced Optical Materials* **2018,** *6*, 1800879.

113. Xing, J.; Liu, X. F.; Zhang, Q.; Ha, S. T.; Yuan, Y. W.; Shen, C.; Sum, T. C.; Xiong, Q. Vapor Phase Synthesis of Organometal Halide Perovskite Nanowires for Tunable Room-Temperature Nanolasers. *Nano Letters* **2015,** *15*, 4571-4577.

114. Zhai, W.; Lin, J.; Li, Q.; Zheng, K.; Huang, Y.; Yao, Y.; He, X.; Li, L.; Yu, C.; Liu, C.; Fang, Y.; Liu, Z.; Tang, C. Solvothermal Synthesis of Ultrathin Cesium Lead Halide Perovskite Nanoplatelets with Tunable Lateral Sizes and Their Reversible Transformation into Cs4PbBr6 Nanocrystals. *Chemistry of Materials* **2018,** *30*, 3714-3721.

115. Pan, Q.; Hu, H.; Zou, Y.; Chen, M.; Wu, L.; Yang, D.; Yuan, X.; Fan, J.; Sun, B.; Zhang, Q. Microwave-assisted synthesis of high-quality “all-inorganic” CsPbX3 (X = Cl, Br, I) perovskite nanocrystals and their application in light emitting diodes. *Journal of Materials Chemistry C* **2017,** *5*, 10947-10954.

116. Tong, Y.; Bladt, E.; Aygüler, M. F.; Manzi, A.; Milowska, K. Z.; Hintermayr, V. A.; Docampo, P.; Bals, S.; Urban, A. S.; Polavarapu, L.; Feldmann, J. Highly Luminescent Cesium Lead Halide Perovskite Nanocrystals with Tunable Composition

and Thickness by Ultrasonication. *Angewandte Chemie International Edition* **2016,** *55*, 13887-13892.

117. Gupta, S.; Cahen, D.; Hodes, G. How SnF2 Impacts the Material Properties of Lead-Free Tin Perovskites. *The Journal of Physical Chemistry C* **2018,** *122*, 13926-13936.

118. Song, T.-B.; Yokoyama, T.; Aramaki, S.; Kanatzidis, M. G. Performance Enhancement of Lead-Free Tin-Based Perovskite Solar Cells with Reducing Atmosphere-Assisted Dispersible Additive. *ACS Energy Letters* **2017,** *2*, 897-903.

119. Nakamura, T.; Yakumaru, S.; Truong, M. A.; Kim, K.; Liu, J.; Hu, S.; Otsuka, K.; Hashimoto, R.; Murdey, R.; Sasamori, T.; Kim, H. D.; Ohkita, H.; Handa, T.; Kanemitsu, Y.; Wakamiya, A. Sn(IV)-free tin perovskite films realized by in situ Sn(0) nanoparticle treatment of the precursor solution. *Nature Communications* **2020,** *11*, 3008.

120. Song, T.-B.; Yokoyama, T.; Logsdon, J.; Wasielewski, M. R.; Aramaki, S.; Kanatzidis, M. G. Piperazine Suppresses Self-Doping in CsSnI3 Perovskite Solar Cells. *ACS Applied Energy Materials* **2018,** *1*, 4221-4226.

121. Shamsi, J.; Dang, Z.; Bianchini, P.; Canale, C.; Di Stasio, F.; Brescia, R.; Prato, M.; Manna, L. Colloidal Synthesis of Quantum Confined Single Crystal CsPbBr3 Nanosheets with Lateral Size Control up to the Micrometer Range. *Journal of the American Chemical Society* **2016,** *138*, 7240-7243.

122. Park, J.; Jang, H. M.; Kim, S.; Jo, S. H.; Lee, T.-W. Electroluminescence of Perovskite Nanocrystals with Ligand Engineering. *Trends in Chemistry* **2020,** *2*, 837-849.

123. Dai, J.; Xi, J.; Li, L.; Zhao, J.; Shi, Y.; Zhang, W.; Ran, C.; Jiao, B.; Hou, X.; Duan, X.; Wu, Z. Charge Transport between Coupling Colloidal Perovskite Quantum Dots Assisted by Functional Conjugated Ligands. *Angewandte Chemie International Edition* **2018,** *57*, 5754-5758.

124. Zhang, L.; Zhang, Q.; Xing, X.; Jiang, Y.; He, T.; Huang, Y.; Ma, Z.; Yang, J.; Yuan, M. Conjugated Alkylamine by Two-Step Surface Ligand Engineering in CsPbBr3 Perovskite Nanocrystals for Efficient Light-Emitting Diodes. *ChemNanoMat*

2019, *5*, 318-322.

125. Kang, C.; Rao, H.; Fang, Y.; Zeng, J.; Pan, Z.; Zhong, X. Antioxidative Stannous Oxalate Derived Lead-Free Stable CsSnX3 (X=Cl, Br, and I) Perovskite Nanocrystals. *Angewandte Chemie International Edition* **2021,** *60*, 660-665.

126. Tai, Q.; Guo, X.; Tang, G.; You, P.; Ng, T.-W.; Shen, D.; Cao, J.; Liu, C.-K.; Wang, N.; Zhu, Y.; Lee, C.-S.; Yan, F. Antioxidant Grain Passivation for Air-Stable Tin-Based Perovskite Solar Cells. *Angewandte Chemie International Edition* **2019,** *58*, 806-810.

127. Shen, X.; Zhang, Y.; Kershaw, S. V.; Li, T.; Wang, C.; Zhang, X.; Wang, W.; Li, D.; Wang, Y.; Lu, M.; Zhang, L.; Sun, C.; Zhao, D.; Qin, G.; Bai, X.; Yu, W. W.; Rogach, A. L. Zn-Alloyed CsPbI3 Nanocrystals for Highly Efficient Perovskite Light-Emitting Devices. *Nano Letters* **2019,** *19*, 1552-1559.

128. Guo, J.; Fu, Y.; Lu, M.; Zhang, X.; Kershaw, S. V.; Zhang, J.; Luo, S.; Li, Y.; Yu, W. W.; Rogach, A. L.; Zhang, L.; Bai, X. Cd-Rich Alloyed CsPb1-xCdxBr3 Perovskite Nanorods with Tunable Blue Emission and Fermi Levels Fabricated through Crystal Phase Engineering. *Advanced Science* **2020,** *7*, 2000930.

129. Imran, M.; Ramade, J.; Di Stasio, F.; De Franco, M.; Buha, J.; Van Aert, S.; Goldoni, L.; Lauciello, S.; Prato, M.; Infante, I.; Bals, S.; Manna, L. Alloy CsCdxPb1–xBr3 Perovskite Nanocrystals: The Role of Surface Passivation in Preserving Composition and Blue Emission. *Chemistry of Materials* **2020,** *32*, 10641-10652.

130. Liu, F.; Ding, C.; Zhang, Y.; Ripolles, T. S.; Kamisaka, T.; Toyoda, T.; Hayase, S.; Minemoto, T.; Yoshino, K.; Dai, S.; Yanagida, M.; Noguchi, H.; Shen, Q. Colloidal Synthesis of Air-Stable Alloyed CsSn1–xPbxI3 Perovskite Nanocrystals for Use in Solar Cells. *Journal of the American Chemical Society* **2017,** *139*, 16708-16719.

131. Liu, F.; Zhang, Y.; Ding, C.; Kawabata, K.; Yoshihara, Y.; Toyoda, T.; Hayase, S.; Minemoto, T.; Wang, R.; Shen, Q. Trioctylphosphine Oxide Acts as Alkahest for SnX2/PbX2: A General Synthetic Route to Perovskite ASnxPb1–xX3 (A = Cs, FA, MA; X = Cl, Br, I) Quantum Dots. *Chemistry of Materials* **2020,** *32*, 1089-1100.

132. Liu, F.; Jiang, J.; Zhang, Y.; Ding, C.; Toyoda, T.; Hayase, S.; Wang, R.; Tao, S.; Shen, Q. Near-Infrared Emission from Tin–Lead (Sn–Pb) Alloyed Perovskite Quantum Dots by Sodium Doping. *Angewandte Chemie International Edition* **2020,** *59*, 8421-8424.

133. Jiang, J.; Liu, F.; Shen, Q.; Tao, S. The role of sodium in stabilizing tin–lead (Sn–Pb) alloyed perovskite quantum dots. *Journal of Materials Chemistry A* **2021,** *9*, 12087-12098.

134. Zhou, Y.; Chen, J.; Bakr, O. M.; Sun, H.-T. Metal-Doped Lead Halide Perovskites: Synthesis, Properties, and Optoelectronic Applications. *Chemistry of Materials* **2018,** *30*, 6589-6613.

135. Liu, M.; Pasanen, H.; Ali-Löytty, H.; Hiltunen, A.; Lahtonen, K.; Qudsia, S.; Smått, J.-H.; Valden, M.; Tkachenko, N. V.; Vivo, P. B-Site Co-Alloying with Germanium Improves the Efficiency and Stability of All-Inorganic Tin-Based Perovskite Nanocrystal Solar Cells. *Angewandte Chemie International Edition* **2020,** *59*, 22117-22125.

136. Akkerman, Q. A.; Meggiolaro, D.; Dang, Z.; De Angelis, F.; Manna, L. Fluorescent Alloy CsPbxMn1–xI3 Perovskite Nanocrystals with High Structural and Optical Stability. *ACS Energy Letters* **2017,** *2*, 2183-2186.

137. Cui, D.; Liu, X.; Wu, T.; Lin, X.; Luo, X.; Wu, Y.; Segawa, H.; Yang, X.; Zhang, Y.; Wang, Y.; Han, L. Making Room for Growing Oriented FASnI3 with Large Grains via Cold Precursor Solution. *Advanced Functional Materials* **2021,** *31*, 2100931.

138. Zheng, Y.; Fang, Z.; Shang, M.-H.; Du, Z.; Yang, Z.; Chou, K.-C.; Yang, W.; Wei, S.; Hou, X. Enhancing the Stability of Orthorhombic CsSnI3 Perovskite via Oriented π-Conjugated Ligand Passivation. *ACS Applied Materials & Interfaces* **2020,** *12*, 34462-34469.

139. Shao, S.; Liu, J.; Portale, G.; Fang, H.-H.; Blake, G. R.; ten Brink, G. H.; Koster, L. J. A.; Loi, M. A. Highly Reproducible Sn-Based Hybrid Perovskite Solar Cells with 9% Efficiency. *Advanced Energy Materials* **2018,** *8*, 1702019.

140. Awais, M.; Kirsch, R. L.; Yeddu, V.; Saidaminov, M. I. Tin Halide

Perovskites Going Forward: Frost Diagrams Offer Hints. *ACS Materials Letters* **2021,** *3*, 299-307.

141. Kahmann, S.; Shao, S.; Loi, M. A. Cooling, Scattering, and Recombination—The Role of the Material Quality for the Physics of Tin Halide Perovskites. *Advanced Functional Materials* **2019,** *29*, 1902963.

142. Euvrard, J.; Yan, Y.; Mitzi, D. B. Electrical doping in halide perovskites. *Nature Reviews Materials* **2021,** *6*, 531-549.

143. Xue, J.; Wang, R.; Yang, Y. The surface of halide perovskites from nano to bulk. *Nature Reviews Materials* **2020,** *5*, 809-827.

144. Ma, J.-P.; Yin, J.; Chen, Y.-M.; Zhao, Q.; Zhou, Y.; Li, H.; Kuroiwa, Y.; Moriyoshi, C.; Li, Z.-Y.; Bakr, O. M.; Mohammed, O. F.; Sun, H.-T. Defect-Triggered Phase Transition in Cesium Lead Halide Perovskite Nanocrystals. *ACS Materials Letters* **2019,** *1*, 185-191.

145. Ma, J.-P.; Chen, J.-K.; Yin, J.; Zhang, B.-B.; Zhao, Q.; Kuroiwa, Y.; Moriyoshi, C.; Hu, L.; Bakr, O. M.; Mohammed, O. F.; Sun, H.-T. Doping Induces Structural Phase Transitions in All-Inorganic Lead Halide Perovskite Nanocrystals. *ACS Materials Letters* **2020,** *2*, 367-375.

146. Jang, J.; Kim, Y.-H.; Park, S.; Yoo, D.; Cho, H.; Jang, J.; Jeong, H. B.; Lee, H.; Yuk, J. M.; Park, C. B.; Jeon, D. Y.; Kim, Y.-H.; Bae, B.-S.; Lee, T.-W. Extremely Stable Luminescent Crosslinked Perovskite Nanoparticles under Harsh Environments over 1.5 Years. *Advanced Materials* **2021,** *33*, 2005255.

147. Ahmed, G. H.; Yin, J.; Bakr, O. M.; Mohammed, O. F. Successes and Challenges of Core/Shell Lead Halide Perovskite Nanocrystals. *ACS Energy Letters* **2021,** *6*, 1340-1357.

148. Kumar, P.; Patel, M.; Park, C.; Han, H.; Jeong, B.; Kang, H.; Patel, R.; Koh, W.-G.; Park, C. Highly luminescent biocompatible CsPbBr3@SiO2 core–shell nanoprobes for bioimaging and drug delivery. *Journal of Materials Chemistry B* **2020,** *8*, 10337-10345.

149. Ding, N.; Zhou, D.; Sun, X.; Xu, W.; Xu, H.; Pan, G.; Li, D.; Zhang, S.; Dong, B.; Song, H. Highly stable and water-soluble monodisperse CsPbX3/SiO2 nanocomposites for white-LED and cells imaging. *Nanotechnology* **2018,** *29*, 345703.

150. Wu, Z.; Zhang, Q.; Li, B.; Shi, Z.; Xu, K.; Chen, Y.; Ning, Z.; Mi, Q. Stabilizing the CsSnCl3 Perovskite Lattice by B-Site Substitution for Enhanced Light Emission. *Chemistry of Materials* **2019,** *31*, 4999-5004.

Chapter 2: Defect-induced Bandgap Widening and Abnormal Photoluminescence in Formamidinium Tin Iodide Perovskite Microcrystals

2.1 Introduction

Recent years have witnessed substantial research efforts and rapid technological development of lead (Pb) halide perovskites in a range of optoelectronic devices, such as solar cells, light-emitting diodes, and photodetectors.[1-5] Nevertheless, one of the remaining challenges for their commercialization is the toxicity issue of Pb element that can cause neuron damage and anemia.[6] The ideal element replacing Pb is tin (Sn) owing to its similarity in ionic radius (i.e. 1.19 and 1.18 Å for six-coordinated Pb^{2+} and Sn^{2+} ions, respectively) and valence electronic configuration (ns^2sp^2) with Pb,[7] as well as its lower toxicity and negligible bioavailability.[8] In the past decade, thanks to the intensive efforts of chemists, material scientists, and engineers, the efficiency gap of tin halide perovskite based optoelectronic devices with that of their Pb-based counterparts is gradually narrowing.[9-13] For example, the external quantum efficiency of red-light emitting diodes based on tin halide perovskite has exceeded 20%;[14] and the power conversion efficiency of tin halide perovskite based solar cells has reached over 14%.[15]

Among all-inorganic and organic-inorganic tin halide perovskites, the power conversion efficiencies of solar cells based on formamidinium (FA) tin triiodide ($FASnI_3$) are higher than those based on all-inorganic cousins.[15-19] $FASnI_3$ exhibits an ideal bandgap of ~1.41 eV close to the optimum bandgap (1.34 eV) of single junction solar cell that can approach the Shocklet-Queisser efficient limit (33%).[20] Interestingly, a recent finding reveals that when the size of $FASnI_3$ crystals is down to several nanometers, strong quantum confinement results in separate energy levels in band structure, slowing down the relaxation of hot carriers.[21] This effect can alleviate the energy loss of hot carriers via phonon emission, leading to a higher theoretical solar conversion efficiency up to 66%.[22]

Despite steady research progress of optoelectronic applications based on polycrystalline films and synthetic chemistry of high-quality crystals,[11, 23] it still lacks deep understanding of the structure-photophysical property relationship of $FASnI_3$ perovskites. An unusual large blue shift of photoluminescence (PL) with increasing excitation power was observed, which was attributed to slow hot carrier relaxation and state filling of the band edge state.[24] Previous work has revealed that $FASnI_3$ perovskite displays bandgap widening upon raising temperature, which is opposite to the normal trend in traditional semiconductors; this was attributed to the overcome of the classical thermal broadening of electronic bands by the emphanitic Sn^{2+} displacement.[25] Kahmann et al. observed similar bandgap widening phenomena and found negative thermal quenching of PL for a high-quality crystal.[26] Additionally, Ozaki et al. found that incorporating SnF_2 into the precursors can lead to polycrystalline $FASnI_3$ perovskite film with a smaller bandgap.[27] However, it was found that the introduction of SnF_2 reduces the doping and passivates Sn^{4+} trap states but conversely introduces additional non-radiative decay channels in the bulk that fundamentally limit the radiative efficiency.[28] We note that tin halide perovskites used for the study of structure-photophysical properties were commonly prepared by solution casting process or solid-state reaction and feature massive defect concentrations that leads to extremely low PLQYs.

Previous work has shown that defects can impact the structure and the photophysical properties of Pb halide perovskites.[29-31] Compared with Pb-based cousins, $FASnI_3$ suffers from a soft ionic lattice and easy oxidation of Sn^{2+}. Although the crystal quality of $FASnI_3$ films can be optimized by various strategies including the use of additives, reducing agents, and solvent engineering,[32] it still remains challenging to obtain microcrystals with a measurable PLQY. Theoretical calculations suggest the low formation energies of some structural defects in $FASnI_3$, such as Sn vacancy (V_{Sn}) and FA vacancy (V_{FA}).[33] These defects might not only act as trap states influencing the recombination of photo-generated carriers, but also could change the lattice symmetry in $FASnI_3$. We therefore hypothesized that the existence of defects could make the structure of $FASnI_3$ different and thus could

lead to the change of the photophysical properties. If we could develop a strategy to synthesize $FASnI_3$ crystals with tailored defect states, we could use them as model systems for gaining deep insight into the relationship between the structure and photophysical properties.

Inspired by our previous work in cesium tin iodide ($CsSnI_3$) nanocrystals (NCs),[34] here I rationally tune the reactant ratio of the precursors to create a tin-rich reaction condition for the synthesis of a series of $FASnI_3$ microcrystals with PLQYs ranging from 3.8% to 8.0%. Interestingly, I uncover an unconventional bandgap widening by 0.23 eV for the sample with a low PLQY. Based on detailed structural characterizations including X-ray photoelectron spectroscopy (XPS) and ^{199}Sn solid-state nuclear magnetic resonance (NMR), I show that structural defects, such as Sn^{4+} impurities and/or point defects could lead to the structural distortion and bandgap widening. I also demonstrate that degradation in air can also augment abundant structural defects leading to luminescence quenching and slightly larger bandgap. Importantly, I discover a near-infrared PL band between 185 and 10 K and negative thermal quenching in a broad range of 110~200 K, both of which are associated with structural defects.

2.2 Experimental section

2.2.1 Chemicals

Formamidine acetate (FA-acetate, Sigma, ≥99%), tin 2-ethylhexanoate ($Sn(Oct)_2$, Sigma, 92.5-100.0%), tin(II) iodide (SnI_2, Sigma, 99.99% trace metals basis), 1-octadecene (ODE, Sigma, 95%), oleic acid (OA, Sigma, 90%), tri-n-octylphosphine (TOP, Thermo, 90%), n-hexane (Sigma, ≥99%), Toluene (Wako, 99%) were used without purification unless otherwise noted.

Table 2.1. List of the manufacturer, batch number, and purity from certificate of analysis (COA) of all used chemicals for synthesis.

Chemical	Manufacturer	Batch number	Purity from COA
FA-acetate	Sigma-Aldrich	BCBZ7461	100%
$Sn(Oct)_2$	Sigma-Aldrich	SLCM1306	96.9%
SnI_2	Sigma-Aldrich	0000303819	99.99%
ODE	Sigma-Aldrich	BCCH1566	98.9%
OA	Sigma-Aldrich	MKCR9052	94.9%
TOP	ThermoFisher	L15744	99.99%
n-hexane	Sigma-Aldrich	STBL2142	99.3%
Toluene	FUJIFILM Wako	KSP2915	99.9%

2.2.2 Experiments

Preparation of FA-oleate solution. 0.2603 g FA-acetate was mixed with 10 ml 1-octadecene (ODE) and 3.39 ml oleic acid in 100 ml three-necked flask in an argon-filled glovebox. The mixture was then degassed for half hour at 80 ºC, then heated under nitrogen to 120 ºC for half hour, yielding a clear FA-oleate solution. After that, the as-prepared FA-oleate was cooled to room temperature, and transferred to glovebox for the further use.

Preparation of the SnI_2-TOP stock solution. The mixture of 0.1105 g SnI_2 and 0.3 ml TOP was vigorously stirred at 120 ºC on a hot plate for 20 min, yielding a yellow stock solution.

Synthesis of $FASnI_3$ microcrystals. 5 ml toluene was heated to 120 ºC in a 20 ml vial on a hot plate, followed by the addition of SnI_2-TOP stock solution (50 µl for FA:SnI_2=1:1.3; 80 µl for FA:SnI_2=1:2.1; 120 µl for FA:SnI_2=1:3.2; 135 µl for FA:SnI_2=1:3.5) under vigorous stirring for 5 min. Then, 0.2 ml FA-oleate solution was swiftly injected into the reaction solution. After reaction for 10 s, the crude solution was taken off from the hot plate, and centrifugated at 12000 r.p.m. for 5 min to remove the supernatant solution.

2.2.3 Characterizations

XRD, TEM measurements. Powder XRD data were recorded on a MiniFlex 600 diffractometer (Rigaku) with a Cu Kα X-ray source (λ = 1.5418 Å). The $FASnI_3$ microcrystals were dispersed in hexane to form a concentrated solution which was then dropped on a silicon substrate for XRD measurements. TEM images were collected by a JEM-2100F (JEOL) microscope operated at 200 kV. TEM samples were prepared by dropping a dilute microcrystals-hexane solution onto a TEM copper grid and dried in glovebox.

Optical characterizations. PL spectra were measured by a NanoLog Horiba Jovin Yvon spectrofluorometer with a continuous 450 W xenon lamp. The excitation wavelength is 500 nm. To measure the temperature-dependent PL spectra, the sample was placed inside a cryostat holder connected to a Gifford-Mcmahon cooler and controlled by a Mercury iTC temperature controller. Before the PL measurement, the sample was stored under vacuum overnight. Absolute PLQYs were measured by a standardized integrating sphere method using a C9920-03G system equipped with a 150-W xenon lamp (Hamamatsu Photonics). The PL decays were obtained with a time-correlated single photon counting lifetime spectroscopy system (NanoLog, Horiba Jovin Ybon), equipped with a pulse laser (λem = 726 nm). UV-vis-NIR absorption spectra were recorded by using a SolidSpec-3700 DUV spectrophotometer. The data was collected in reflectance model and then converted to absorbance curves by Kubelka-Munk function. The powder forms of the microcrystals were used for the characterizations of PL and absorption.

XPS and ^{119}Sn solid NMR characterization. XPS spectra were measured using a dual scanning X-ray photoelectron microprobe equipped with hard X-ray photoelectron spectroscopy (HAX-PES/XPS; ULVAC-PHI, Inc., Japan). A concentrated microcrystal-hexane solution was dropped on the Si substrate. To avoid the oxidation in the air, an anaerobic hold was used in the Ar-filled glovebox. ^{119}Sn solid NMR spectra were performed on a 11.75 T JEOL-ECZ 500 spectrometer. The instrument was equipped with a 3.2 mm sample tube operating at 20 KHz MAS. Spectra were acquired using a Hahn-echo (π/2-tau-π-tau-echo) sequence. Tau (echo-delay time) is rotor synchronized (tau=50 μs). π/2 pulse length is 3 μs. Pulse delay time is 4 s. The spectra were referenced to $SnMe_4$.

2.3 Results and discussion

I synthesized $FASnI_3$ microcrystals by a simple solvent-thermal method, in which four reactant ratios of FA-oleate to SnI_2 (1:1.3, 1:2.1, 1:3.2, and 1:3.5) were used. The samples are denoted by these ratios. Powder X-ray diffraction (PXRD) patterns of the as-prepared four products match the cubic perovskite structure, in accordance with ever reported $FASnI_3$ bulk and NCs (gray line),[21, 26] without additional crystalline phases (**Figure 2.1a**). Transmission electron microscopy (TEM) images show the particle size up to several hundred nanometers (**Figure 2.2)**. Considering the large particle size, we classify them to microcrystals instead of NCs. Obvious agglomeration of $FASnI_3$ microcrystals can be found because of the lack of capping ligands.

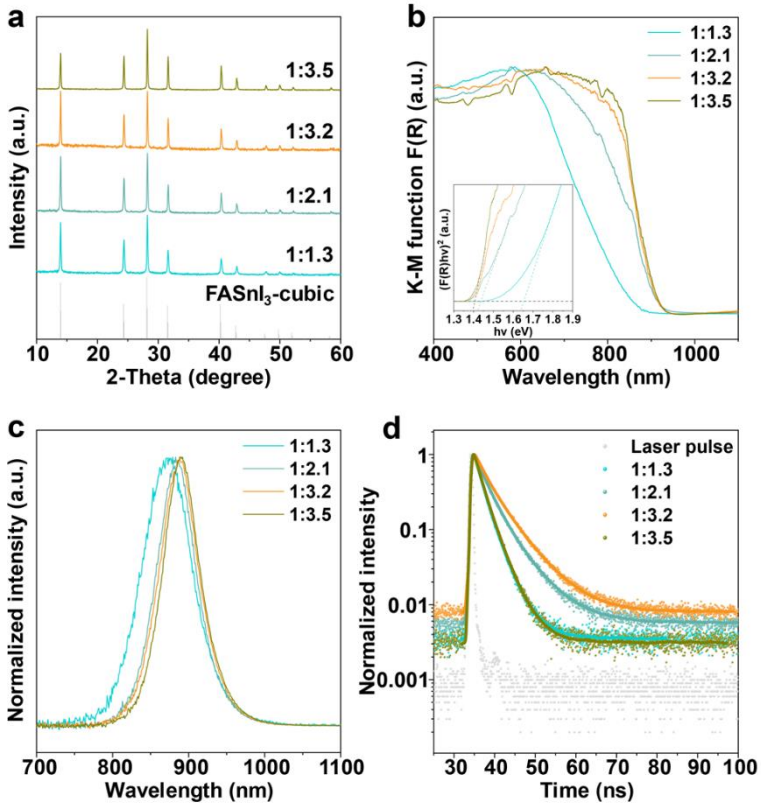

Figure 2.1. (a) Powder XRD patterns of $FASnI_3$ microcrystals synthesized under different FA: SnI_2 ratios. (b) Absorption spectra of $FASnI_3$ microcrystals synthesized under different FA: SnI_2 ratios. The data was collected in reflectance model and then converted to absorbance curves by the Kubelka-Munk function. Inset is the Tauc Plot spectra for the calculation of the bandgaps. (c) PL spectra of $FASnI_3$ microcrystals synthesized with different FA: SnI_2 ratios. (d) PL decay traces of $FASnI_3$ microcrystals synthesized with

different FA: SnI_2 ratios.

Next, I investigated the optical properties of $FASnI_3$ microcrystals. These samples demonstrate different optical absorption features (**Figure 2.1b)**: with increasing Sn ratio in the reaction, the absorption edge becomes sharp. Using the T*auc* Plot method,[35] I calculated the bandgaps of four samples (**inset of Figure 2.1b**), which are 1.64 eV for 1:1.3, 1.44 eV for 1:2.1, 1.41 eV for 1:3.2 and 1:3.5. **Figure 2.1c** displays the PL spectra of these microcrystals. Interestingly, I find that they show different PL behaviors: for 1:1.3, the PL peak position is at ~ 874 nm; with increasing the ratio of SnI_2, a distinct redshift of PL, 885 nm for 1:21, 888 nm for 1:3.2, and 890 nm for 1:3.5 occurs. In addition, the full width at half-maximum (fwhm) of PL for 1:1.3 (80 nm) is much larger than other three samples (65 nm for 1:2.1 and 1:3.2; 62 nm for 1:3.5). The PLQYs of four samples **(Table 2.1, Figure 2.3**), 3.8% for 1:1.3, 6.1% for 1:2.1, 8.0% for 1:3.2, and 4.2% for 1:3.5, suggest that the crystal quality can be tailored by the reactant ratio. I note that the maximum PLQY of $FASnI_3$ microcrystals is much higher than those of previously reported $FASnI_3$ NCs.[21, 36] I then carried out time-resolved PL decays to further examine the transient evolution of the photo-generated carriers. As shown in **Figure 2.1d**, all decays can be fitted well by a biexponential function, and the calculated average lifetimes are 2.29, 3.67, 4.31, and 2.35 ns for 1:1.3, 1:2.1, 1:3.2, and 1:3.5, respectively (**Table 2.1**). Using PLQYs and average lifetimes, I evaluated the radiative and nonradiative decay rates based on the following equations:

$$\Gamma_{rad} = \frac{\mathrm{PLQY}}{\tau_{ave}} \quad (1)$$

$$\Gamma_{non-rad} = \frac{1}{\tau_{ave}} - \Gamma_{rad} = \frac{1 - \mathrm{PLQY}}{\tau_{ave}} \quad (2)$$

where Γ_{rad} and $\Gamma_{non\text{-}rad}$ are the radiative and non-radiative recombination rates, respectively, and τ_{ave} is the average lifetime of the samples. I note that after changing the ratio of FA: SnI_2 from 1:1.3 to 1:3.2, the radiative recombination rate slightly increases from 16.59 μs^{-1} to 18.56 μs^{-1}, but the non-radiative recombination rate greatly decreases from 420.09 μs^{-1} to 213.46 μs^{-1} (**Table 2.1**), suggesting effective suppression of non-radiative recombination. Compared with the tin-poor reaction condition, rationally creating a tin-rich environment can suppress the formation of tin-related structural defects,

such as V_{Sn} and/or Sn^{4+} self-doping,[34] which leads to the increase in PLQY and suppression of non-radiative recombination when changing the ratio of FA: SnI_2 from 1:1.3 to 1:3.2. However, further increasing the ratio results in a larger nonradiative recombination rate, which could be attributed to the occurrence of other structural defects, such as V_{FA} that has a low defect formation energy.[33] My experimental results clearly indicate that increasing the Sn chemical potential favors a better quality of $FASnI_3$ crystal.

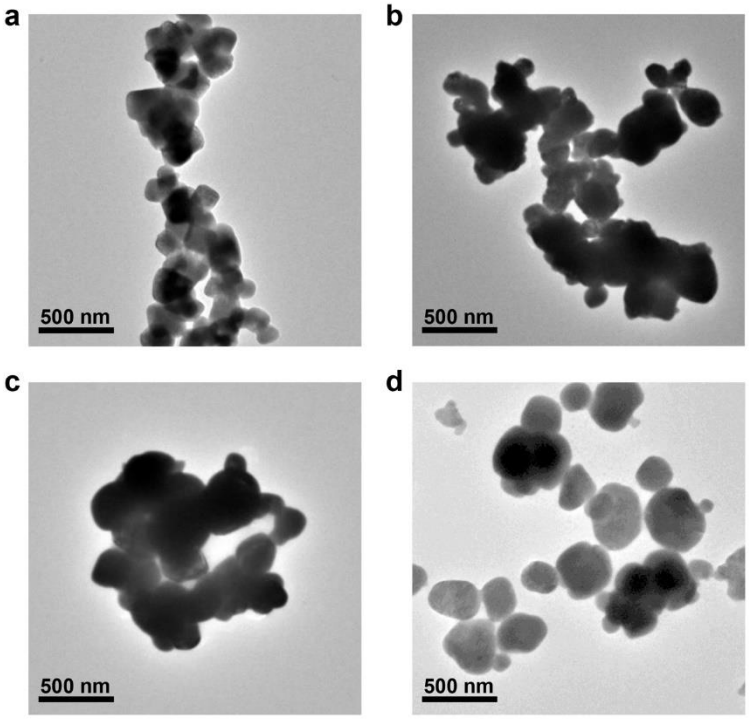

Figure 2.2. TEM images of $FASnI_3$ microcrystals synthesized under different FA: SnI_2 ratios of (a) 1: 1.3; (b) 1:2.1; (c) 1:3.2; (d) 1:3.5.

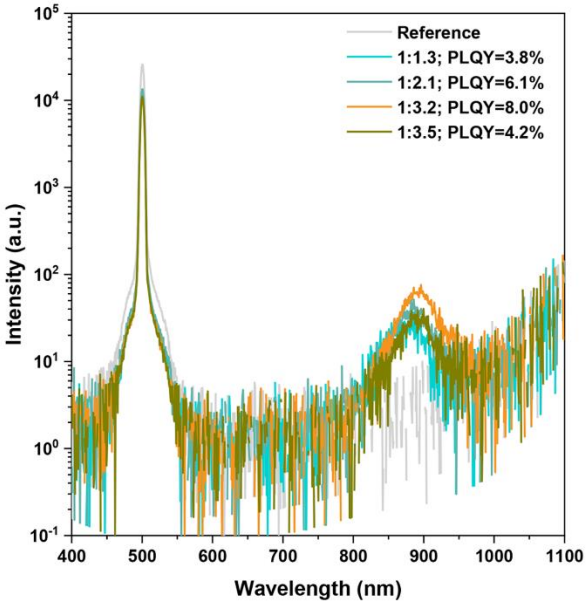

Figure 2.3. PLQY measurements of $FASnI_3$ microcrystals synthesized under different FA: SnI_2 ratios.

Table 2.2. Fitted lifetimes (τ_1, τ_2), average lifetimes (τ_{ave}) using a biexponential function, and PLQYs, calculated radiative (Γ_{rad}), nonradiative ($\Gamma_{non\text{-}rad}$) decay rates of $FASnI_3$ microcrystals synthesized under different FA: SnI_2 ratios.

FA:SnI_2	A_1	τ_1 (ns)	A_2	τ_2 (ns)	τ_{ave} (ns)	PLQY (%)	Γ_{rad} (μs^{-1})	$\Gamma_{non\text{-}rad}$ (μs^{-1})
1:1.3	0.73	1.99	0.27	3.85	2.29	3.8	16.59	420.09
1:2.1	0.59	2.86	0.41	6.19	3.67	6.1	16.62	255.86
1:3.2	0.33	2.69	0.67	6.11	4.31	8.0	18.56	213.46
1:3.5	0.65	1.98	0.35	3.60	2.35	4.2	17.87	407.66

As discussed above, sample 1:1.3 has a widened bandgap by ~0.23 eV compared with 1:3.2 (**Figure 2.1c**). Firstly, I exclude the possibility of quantum confinement because the particle size of $FASnI_3$ microcrystals is much larger than the exciton Bohr radius in $FASnI_3$ (3.5-4.4 nm).[36] Only when the particle size is close to the exciton Bohr radius of the crystals, the bandgap widening could be observed. Previous work suggests

that structural distortion, such as Sn^{2+} off-centering and/or I disorder, accounts for the bandgap widening in $FASnI_3$.[25, 36] To gain a deeper understanding of the structural nature of $FASnI_3$ microcrystals, I then conducted the XPS and ^{199}Sn solid-state NMR measurements. I particularly chose 1:1.3 and 1:3.2 for these measurements because they have notable difference in PLQY and bandgap. As shown in **Figure 2.4a**, the Sn 3d high-resolution XPS spectra of both samples are asymmetric, indicating the presence of more than one oxidation state of Sn. Four components in the fitted spectrum for 1:1.3 can be readily observed: the peaks located at 495.3 eV and 486.9 eV can be assigned to Sn $3d_{3/2}$ and Sn $3d_{5/2}$, which accords with the binding energies of Sn^{4+}, while those located at 494.2 eV and 485.8 eV to Sn $3d_{3/2}$ and Sn $3d_{5/2}$ from Sn^{2+};[37] the calculated concentration of Sn^{4+} in 1:1.3 is 23.2%. For 1:3.2 synthesized at the Sn-rich condition, Sn^{4+} signals appear at 494.9 eV and 486.6 eV for respective Sn $3d_{3/2}$ and Sn $3d_{5/2}$, while Sn^{2+} signals are at 494.1 eV and 485.7 eV. Importantly, the concentration of Sn^{4+} in 1:3.2 is distinctly reduced to 16.0%, suggesting that a Sn-rich reaction condition can alleviate the occurrence of Sn^{4+} during the crystal nucleation and growth. **Figure 2.5** shows the high-resolution I 3d spectra of two samples. We did not observe additional oxidation states of iodine; a peak shift of ~0.17 eV to higher binding energy in 1:3.2 compared to that in 1:1.3 is reasonable since less Sn^{4+} in 1:3.2 might impact the electronic density around I^-.

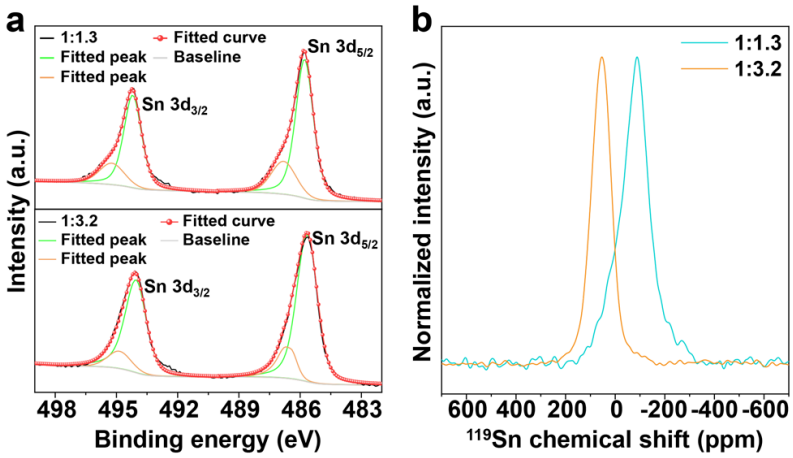

Figure 2.4. (a) High resolution XPS spectra of Sn 3d doublet for 1:1.3 and 1:3.2. The fitted peaks colored in organic and green originates from Sn^{4+} and Sn^{2+}, respectively. (b) ^{199}Sn solid-state NMR spectra for 1:1.3 and 1:3.2. The spectra were referenced to $SnMe_4$.

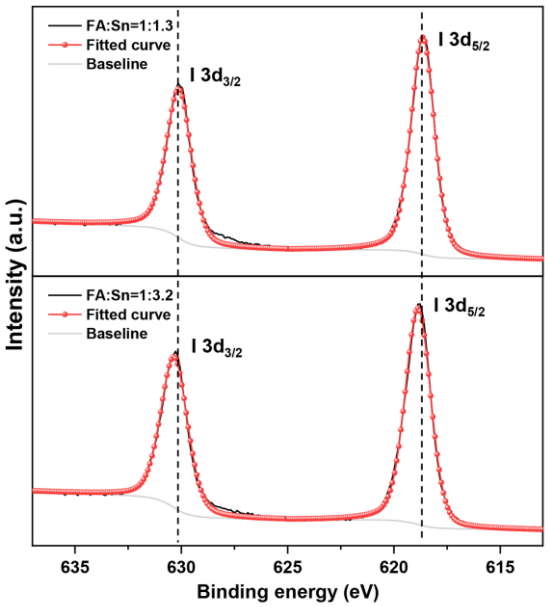

Figure 2.5. High resolution XPS spectra of I 3d doublet for 1: 1.3 and 1: 3.2.

Figure 2.4b exhibits ^{199}Sn solid-state NMR spectra that were calibrated by tetramethyltin ($SnMe_4$). The ^{199}Sn chemical shift in 1:1.3 (-88 ppm) is significantly upfield shift compared with that in 1:3.2 (53 ppm). Such a large shift indicates the different coordination environment of Sn. Previous study on the degraded tin halide perovskites shows that the presence of oxidized products leads to upfield shift signals.[38] We note that the signal at -88 ppm cannot be ascribed to the crystalline phase of FA_2SnI_6 that shows a chemical shift near -4800 ppm,[38] which is consistent with the absence of diffraction peaks of FA_2SnI_6 (**Figure 2.1a**). We consider that a high degree of Sn^{4+} self-doping in $FASnI_3$ could attract more I^- ions to coordinate with Sn ions, resulting in higher electronic density around Sn and thus enhanced the shielding effect. Owing to the cubic phase of $FASnI_3$ at room temperature, the ^{199}Sn NMR signal of 1:3.2 exhibits better symmetry without the presence of chemical shift anisotropy. However, for 1:1.3, a broader and asymmetric peak is observed. We surmise that the existence of more defects in 1:1.3 could induce lattice disordering, although it exbibits a (pseudo)cubic phase as suggested by XRD (**Figure 2.1a**). The structural disordering has multiple possibilities, for example, iodide-disorder-induced polymorphous instead of monomorphous nature of cubic halide perovskites,[36, 39] Sn off-centering,[25] and so on. However, this structural

disordering cannot result in obvious contractive or expanded lattice as seen in XRD (**Figure 2.1a**).

Degradation of tin halide perovskites in air is another process to generate structural defects. I then explored the bandgap variation during the degradation of $FASnI_3$ microcrystals under ambient environment. Firstly, I measured the PL spectra of two samples, 1:1.3 and 1:3.2, when they were exposed to air. As seen in **Figure 2.6a**, 1:1.3 shows a quick PL intensity drop after 5 min in air, accompanied by ~14 nm blueshift of PL peak to ~860 nm. An fwhm of PL for 1:1.3 exposed in air for 5 min is ~ 120 nm that is larger than the fresh one (~80 nm); after 20 min and 40 min, there is a further decrease in PL intensity. For 1:3.2, we can also observe the blueshift of its PL to ~870 nm after 40 min. With the degradation of $FASnI_3$ microcrystals, an increase in fwhm is also apparent: the fwhm of the PL after exposure in air for 40 min is 96 nm, greatly larger than 65 nm of the fresh one. My results indicate that the degradation of $FASnI_3$ is connected with its quality: the better the quality, the slower the degradation. Next, I measured the UV-vis-NIR absorption of two samples to gain the information of their bandgaps. I find slight bandgap widening during the degradation of $FASnI_3$ microcrystals in air. For 1:1.3, the bandgap broadens from 1.64 eV for fresh one to 1.67 eV after exposure to air for 40 min; for 1:3.2, the bandgap changes from 1.41 eV to 1.43 eV after 40 min (**Figure 2.6c, d**). Around 20-30 meV widening in bandgap accords with their PL blueshift (~22.3 meV for 1:1.3 and ~28.9 meV for 1:3.2). Previous work on the organic-inorganic tin halide perovskite polycrystalline films also revealed the bandgap widening during the oxidation upon exposure to ambient conditions.[27] It is noted that without exposure to air $FASnI_3$ microcrystals are stable as evidenced by unchanged PL properties after 24 h in an Ar-filled glovebox (**Figure 2.7**).

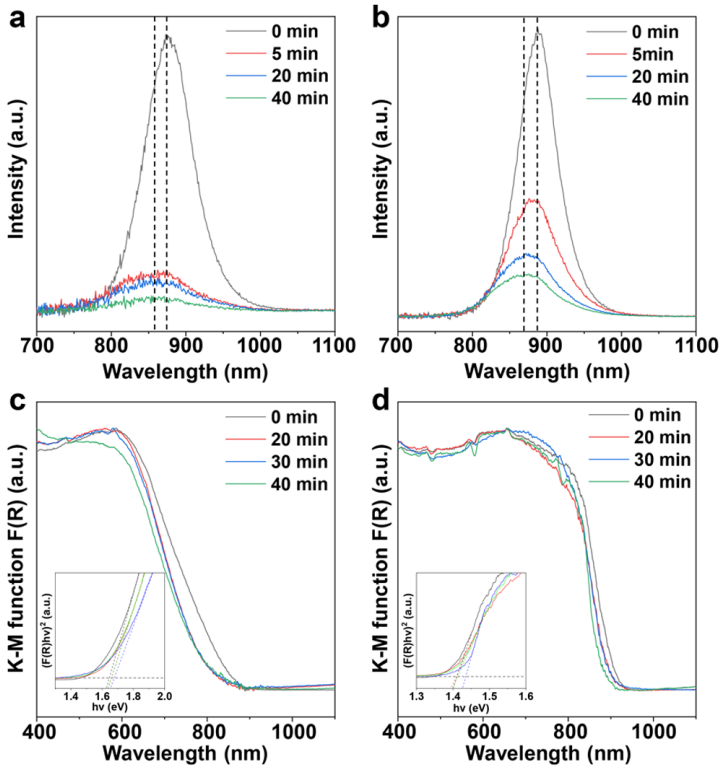

Figure 2.6. PL spectra of (a) 1:1.3 and (b) 1:3.2 after exposure to air for 0, 5, 20, and 40 min. The dotted lines are drawn to guide the eye. (c) Absorption spectra of 1:1.3 after exposure to air for 0, 20, 30, and 40 min. Inset is the T_{auc} Plot spectra for calculation of the bandgaps. The bandgaps are 1.64, 1.66, 1.66, 1.67 eV after exposure to air for 0, 20, 30, 40 min, respectively. (d) Absorption spectra of 1:3.2 after exposure to air for 0, 20, 30, and 40 min. Inset is the T_{auc} Plot spectra for calculation of their bandgaps. The bandgaps are 1.41, 1.41, 1.41, 1.43 eV after exposure to air for 0, 20, 30, 40 min, respectively.

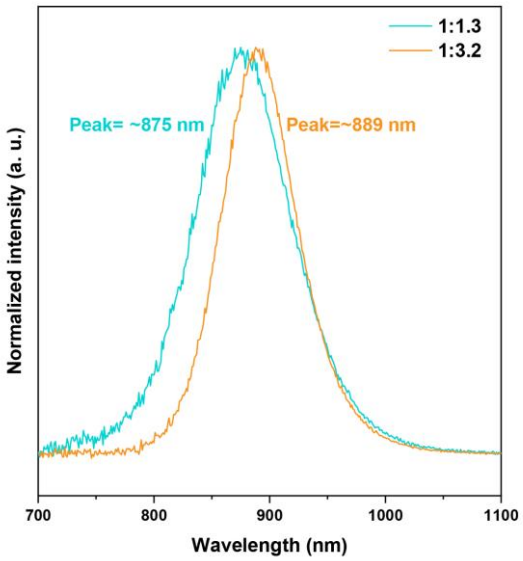

Figure 2.7. PL spectra of 1:1.3 and 1:3.2 after storing in the glovebox for 24 h.

To understand the structural properties of $FASnI_3$ microcrystals during the degradation process in air, I conducted XRD measurements. **Figure 2.8a** displays the XRD patterns of 1:1.3 after exposure to air for 10, 30, and 60 min. Within a short time (<10 min), the changes in the crystal structure are negligible (**Figure 2.1a, Figure 2.8a**). After 30 min, the intensity of diffraction peaks quickly declines, along with the broadening (**inset of Figure 2.8a**). An additional diffraction peak at ~12.3 degree after 60 min can be assigned to the FA_2SnI_6 phase. As a contrast, 1:3.2 has a better stability in air within 30 min (**inset of Figure 2.8b**), and a diffraction peak appears at ~12.3 degree, suggesting partial degradation of $FASnI_3$ into FA_2SnI_6. The decreased crystallinity in air for both samples indicates the augment of structural defects. I further took the XPS measurement to know the surface states of degraded $FASnI_3$ microcrystals. As shown in **Figure 2.8c**, the main peaks for both samples locate at ~495.5 eV and ~487.1 eV for Sn $3d_{3/2}$ and Sn $3d_{5/2}$, respectively, which originate from Sn^{4+}. The concentrations of Sn^{4+} are 94.6% and 91.3% for 1:1.3 and 1:3.2, respectively. This suggests that the surface is dominated by Sn^{4+} after exposure in air, which leads to reduced crystallinity as reflected in the XRD patterns (**Figure 2.8a, b**).

Volatile ionic lattices of organic-inorganic tin halide perovskites make the crystal structure be easily influenced by external stimulations. For example, an increasing temperature induces progressive emphatic Sn^{2+} off-centering and dynamic fluctuations of the perovskite lattice.[25] This distortion lowers the symmetry of $FASnI_3$ from a perfect cubic to local tetragonal or orthorhombic characters. Theoretical calculations show that low-symmetry structures influence the antibonding hybridization of Sn s and I p orbitals, resulting in lower positions of valence band maximum and thus larger bandgaps of $FASnI_3$.[26] In addition, the bending of Sn-I-Sn angle by ~10° can significantly modify the electronic structure of $FASnI_3$ and increase the bandgap by ~0.22 eV.[36] My work clearly establishes that defects can induce bandgap widening in $FASnI_3$ microcrystals. I surmise that the generation of structural defects could cause structural disordering that leads to bandgap widening, although $FASnI_3$ still possesses a pseudocubic phase as suggested by our XRD, XPS and ^{199}Sn solid-state NMR results (**Figure 2.1a, Figure 2.4, Figure 2.8**). Such disordering may be Sn^{2+} off-centering, iodide disorder, or their collective effect, all of which can impact the band structure and widen the bandgap of $FASnI_3$ microcrystals. However, the exact defects are hardly distinguished. They could be Sn^{4+} self-doping, Sn vacancies, FA/I-related defects, or collective defects.

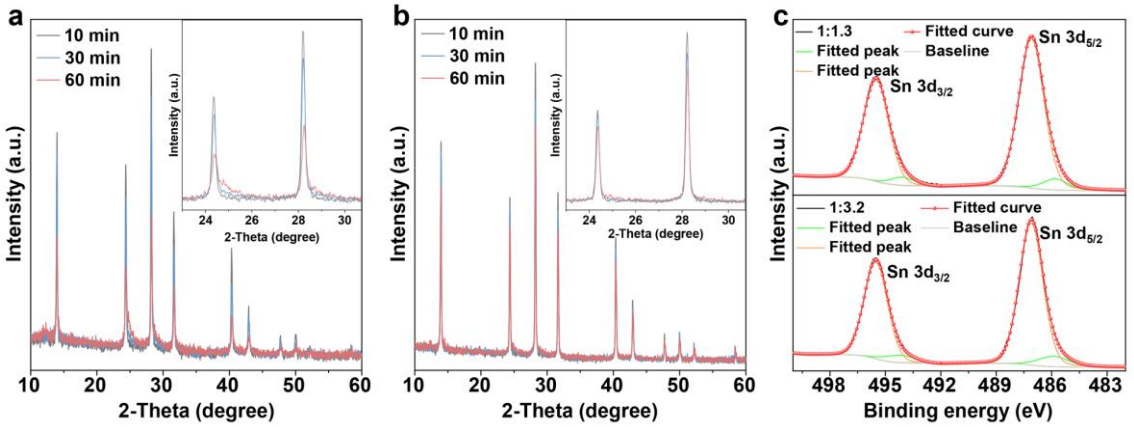

Figure 2.8. Powder XRD patterns of (a) sample 1:1.3 and (b) sample 1:3.2 after exposure to air for 10, 30, and 60 min. The insets show their intensity changes. An additional peak at ~12.3 degree reveals the presence of oxidated FA_2SnI_6. (c) High resolution XPS spectra of Sn 3d doublet for 1:1.3 and 1:3.2 after exposure to air for 20 min.

To further understand the impact of defects on the optical properties of $FASnI_3$ microcrystals, I carried out temperature-dependent PL measurements. I firstly compared the PL performance of 1:1.3 and 1:3.2 at 0.1 MPa and under vacuum (6×10^{-4} Pa) condition at room temperature. For both samples, I observed an obvious increased fwhm in PL under vacuum condition (**Figure 2.9**). Specifically, 1:1.3 in vacuum shows a ~10 nm PL redshift and a notable PL tail extending to ~1400 nm that is much weaker in 1:3.2, suggesting the occurrence of some mid-gap states. This gives an indication that $FASnI_3$ is not stable at high vacuum conditions, probably due to volatilization of some constituent elements. Coduri *et al*. studied the pressure-dependent photophysical properties of $FASnBr_3$, and they found the changes in Sn-Br bond length under different pressures.[40] My results unambiguously show that low-pressure conditions can also change the photophysical properties of $FASnI_3$ microcrystals and that more defects can be developed in poor-quality crystals. I note that the PL becomes absent under the same measurement condition after keeping 1:1.3 at the vacuum condition overnight, while the PL of 1:3.2 can be maintained. I thus chose 1:3.2 for the temperature-dependent PL measurement. **Figure 2.10** displays the PL spectra taken from 300 to 10 K, and their color plot is shown in **Figure 2.11a**. A gradual shift of PL peak from 888 to 1150 nm is observed as the temperature decreases from 300 to 10 K, which is consistent with the results of $FASnI_3$ thin film and single crystal.[26] The PL spectra taken from 10 to 300 K resembles that from 300 to 10 K (**Figure 2.12**), suggesting the stability of $FASnI_3$ microcrystals and the reversible temperature-dependent optical properties in the cooling-heating process.

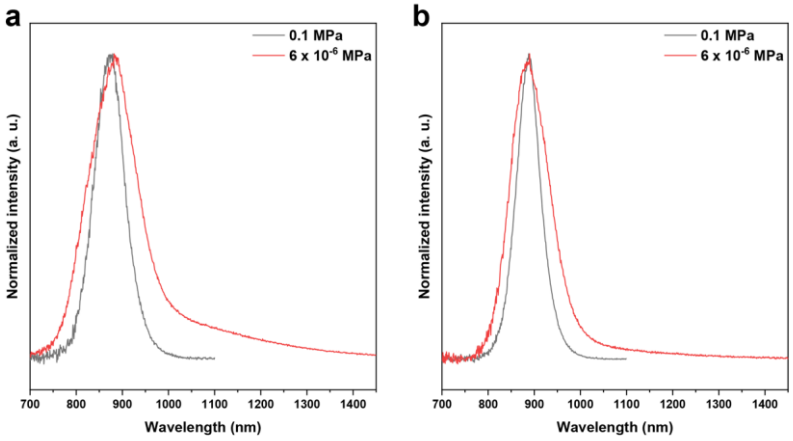

Figure 2.9. PL spectra of (a) 1:1.3 and (b) 1:3.2 at 0.1 MPa and under vacuum condition

at room temperature.

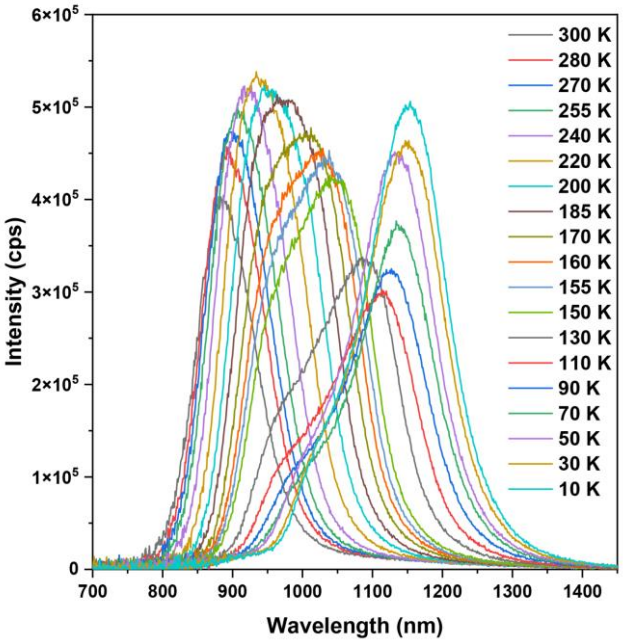

Figure 2.10. PL spectra of sample 1:3.2 upon cooling from 300 to 10 K.

Different from low-temperature PL of $FASnI_3$ films or single crystals,[26] I observe a new emission peak that is prominent below 185 K (**Figure 2.10**). **Figure 2.11b and 2.11c** exhibit two representative PL spectra at 185 K and 10 K, which were fitted by two Gaussian peaks. Compared with $FASnI_3$ intrinsic emission (peak 1), peak 2 has weaker emission intensity, which redshifts from 926 nm at 185 K to 1026 nm at 10 K (**Figure 2.11d**). Between 185 K and 150 K, two PL spectra significantly overlap each other (**Figure 2.11b, 2.10**). Two possible sources, phase transition-induced intrinsic emission and luminescent defect center may lead to the occurrence of this new PL band. As is known, $FASnI_3$ undergoes phase transition from cubic to tetragonal at 255 K and another tetragonal structure at 155 K.[26] I note that this new PL band occurs at ~185 K and survives till to 10 K, which signifies that it does not result from phase transition. I speculate that a certain structural defect may be luminescence-active at low temperatures, which becomes inactive at relatively high temperatures due to phonon-assisted non-radiative recombination. Similar emission was also observed in the $Ba_{1-x}Sr_xSnO_3$ series, which was tentatively assigned to Sn^{2+} ions situated roughly 1.4 eV above the valence-band edge.[41]

Although at present I cannot identify the exact nature of luminescent defect in our sample, I surmise that its occurrence is probably related to specific undercoordinated Sn^{2+} ion.

Another interesting finding is that both emissions show negative thermal quenching of PL (**Figure 2.11e**). For the intrinsic emission (peak 1), the integrated PL intensity reaches to the maximum at 200 K, while continually decreases up to ~ 55% of the maximum at 110 K. Further cooling can enhance the PL intensity. Kahmann et al. also observed this negative thermal quenching from 185 K to 150 K in $FASnI_3$ single crystal. The temperature range observed here is larger than that in the single crystal. For another possible defect emission, it reaches to the maximum at 110 K, while continually decreases between 110 K and 90 K. Below 90 K, the intensity nearly stabilizes at ~67% of the maximum. Upon cooling, suppressed exciton thermal dissociation is the reason for the increased radiative recombination and thus enhanced emission, which is commonly observed in semiconductor materials. However, defect states can trap photogenerated carriers that can be thermally activated and leads to radiative recombination. I underscore that the low-temperature PL results indicate the complexity of structural defects in $FASnI_3$ microcrystals. These defects not only could act as emission centers but also induce negative thermal quenching of PL.

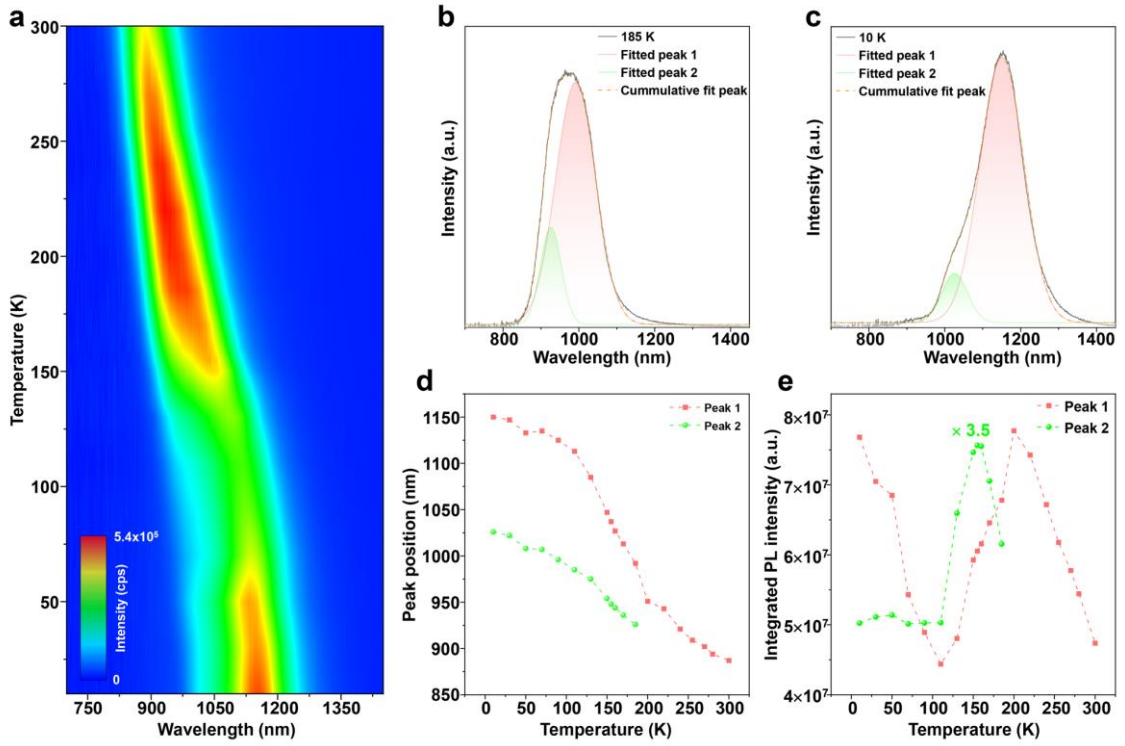

Figure 2.11. (a) Contour plot of the PL spectra of 1:3.2 upon cooling from 300 to 10 K. (b) PL spectrum and fitted bands at 185 K. (c) PL spectrum and fitted bands taken at 10 K. (d) Peak positions of two emission bands at different temperatures. (e) Temperature-dependent integrated PL intensity of two emission bands.

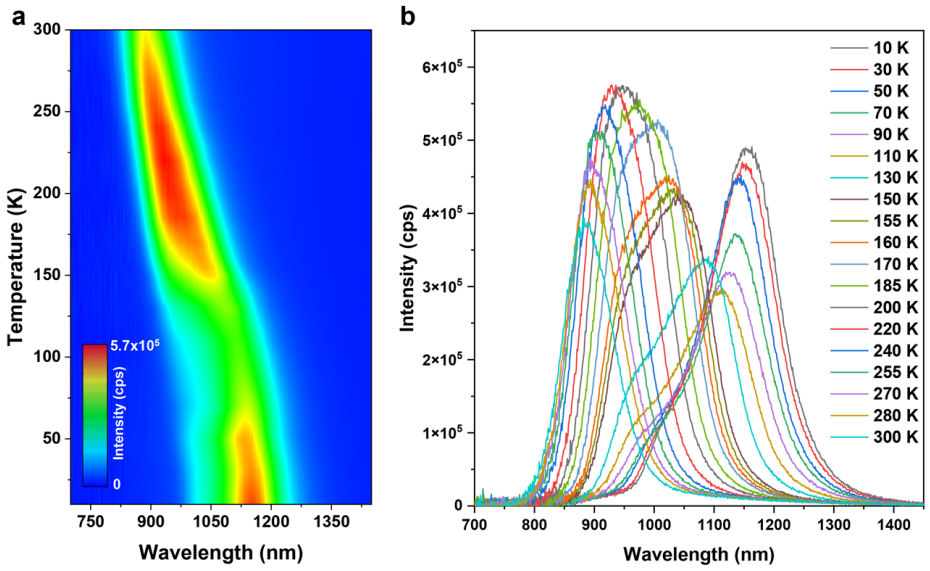

Figure 2.12. (a) Contour plot of the PL spectra of sample 1:3.2 upon heating from 10 K to 300 K. (b) PL spectra of sample 1:3.2 upon heating from 10 K to 300 K.

2.4 Conclusion

In summary, I have found defect-induced bandgap widening in $FASnI_3$ microcrystals synthesized by a well-controlled method. A large bandgap widening in defect-rich $FASnI_3$ microcrystals was discovered, which could be attributed to the deviation from the perfect cubic phase of $FASnI_3$ caused by structural defects. We demonstrated such bandgap widening also exists in degraded $FASnI_3$ microcrystals. Low-temperature PL measurements lead us to the finding of an unusual emission band that cannot be attributed to intrinsic emission of $FASnI_3$, which we tentatively assign to the structural defects such as undercoordinated Sn^{2+} ion. We also observed a broad temperature range corresponding to negative thermal quenching of PL in $FASnI_3$ microcrystals. Since certain applications such as solar cells and photodetectors are closely associated with the optical absorption of active layers, our work suggests the importance of developing methods that can avoid the defect formation as well as the oxidation of $FASnI_3$. Our work offers a facile synthesis route to improve the quality of organic-inorganic tin halide perovskite crystals, which

could guide further efforts on preparation of highly luminescent NCs or high-quality polycrystalline films for optoelectronic devices. The knowledge of defect-induced bandgap widening and abnormal PL gained here can help us deeply understand the structural-property relationship in organic-inorganic tin halide perovskites.

References:

1. Lee, M. M.; Teuscher, J.; Miyasaka, T.; Murakami, T. N.; Snaith, H. J. Efficient Hybrid Solar Cells Based on Meso-Superstructured Organometal Halide Perovskites. *Science* **2012,** *338*, 643-647.

2. Jeon, N. J.; Lee, J.; Noh, J. H.; Nazeeruddin, M. K.; Grätzel, M.; Seok, S. I. Efficient Inorganic–Organic Hybrid Perovskite Solar Cells Based on Pyrene Arylamine Derivatives as Hole-Transporting Materials. *Journal of the American Chemical Society* **2013,** *135*, 19087-19090.

3. Tan, Z.-K.; Moghaddam, R. S.; Lai, M. L.; Docampo, P.; Higler, R.; Deschler, F.; Price, M.; Sadhanala, A.; Pazos, L. M.; Credgington, D.; Hanusch, F.; Bein, T.; Snaith, H. J.; Friend, R. H. Bright light-emitting diodes based on organometal halide perovskite. *Nature Nanotechnology* **2014,** *9*, 687-692.

4. Yuan, M.; Quan, L. N.; Comin, R.; Walters, G.; Sabatini, R.; Voznyy, O.; Hoogland, S.; Zhao, Y.; Beauregard, E. M.; Kanjanaboos, P.; Lu, Z.; Kim, D. H.; Sargent, E. H. Perovskite energy funnels for efficient light-emitting diodes. *Nature Nanotechnology* **2016,** *11*, 872-877.

5. Saidaminov, M. I.; Adinolfi, V.; Comin, R.; Abdelhady, A. L.; Peng, W.; Dursun, I.; Yuan, M.; Hoogland, S.; Sargent, E. H.; Bakr, O. M. Planar-integrated single-crystalline perovskite photodetectors. *Nature Communications* **2015,** *6*, 8724.

6. T. Sanders; Y. Liu; V. Buchner; P.B. Tchounwou Neurotoxic Effects and Biomarkers of Lead Exposure: A Review. *Reviews on Environmental Health* **2009,** *24*, 15-46.

7. van der Stam, W.; Geuchies, J. J.; Altantzis, T.; van den Bos, K. H. W.; Meeldijk, J. D.; Van Aert, S.; Bals, S.; Vanmaekelbergh, D.; de Mello Donega, C. Highly Emissive Divalent-Ion-Doped Colloidal CsPb1–xMxBr3 Perovskite Nanocrystals through Cation Exchange. *Journal of the American Chemical Society* **2017,** *139*, 4087-4097.

8. Li, J.; Cao, H.-L.; Jiao, W.-B.; Wang, Q.; Wei, M.; Cantone, I.; Lü, J.; Abate, A.

Biological impact of lead from halide perovskites reveals the risk of introducing a safe threshold. *Nature Communications* **2020,** *11*, 310.

9. López-Fernández, I.; Valli, D.; Wang, C.-Y.; Samanta, S.; Okamoto, T.; Huang, Y.-T.; Sun, K.; Liu, Y.; Chirvony, V. S.; Patra, A.; Zito, J.; De Trizio, L.; Gaur, D.; Sun, H.-T.; Xia, Z.; Li, X.; Zeng, H.; Mora-Seró, I.; Pradhan, N.; Martínez-Pastor, J. P.; Müller-Buschbaum, P.; Biju, V.; Debnath, T.; Saliba, M.; Debroye, E.; Hoye, R. L. Z.; Infante, I.; Manna, L.; Polavarapu, L. Lead-Free Halide Perovskite Materials and Optoelectronic Devices: Progress and Prospective. *Advanced Functional Materials* **2024,** *34*, 2307896.

10. Diau, E. W.-G.; Jokar, E.; Rameez, M. Strategies To Improve Performance and Stability for Tin-Based Perovskite Solar Cells. *ACS Energy Letters* **2019,** *4*, 1930-1937.

11. Pitaro, M.; Tekelenburg, E. K.; Shao, S.; Loi, M. A. Tin Halide Perovskites: From Fundamental Properties to Solar Cells. *Advanced Materials* **2022,** *34*, 2105844.

12. Yuan, F.; Folpini, G.; Liu, T.; Singh, U.; Treglia, A.; Lim, J. W. M.; Klarbring, J.; Simak, S. I.; Abrikosov, I. A.; Sum, T. C.; Petrozza, A.; Gao, F. Bright and stable near-infrared lead-free perovskite light-emitting diodes. *Nature Photonics* **2024,** *18*, 170-176.

13. Lu, J.; Guan, X.; Li, Y.; Lin, K.; Feng, W.; Zhao, Y.; Yan, C.; Li, M.; Shen, Y.; Qin, X.; Wei, Z. Dendritic CsSnI3 for Efficient and Flexible Near-Infrared Perovskite Light-Emitting Diodes. *Advanced Materials* **2021,** *33*, 2104414.

14. Han, D.; Wang, J.; Agosta, L.; Zang, Z.; Zhao, B.; Kong, L.; Lu, H.; Mosquera-Lois, I.; Carnevali, V.; Dong, J.; Zhou, J.; Ji, H.; Pfeifer, L.; Zakeeruddin, S. M.; Yang, Y.; Wu, B.; Rothlisberger, U.; Yang, X.; Grätzel, M.; Wang, N. Tautomeric mixture coordination enables efficient lead-free perovskite LEDs. *Nature* **2023,** *622*, 493-498.

15.Jiang, X.; Li, H.; Zhou, Q.; Wei, Q.; Wei, M.; Jiang, L.; Wang, Z.; Peng, Z.; Wang, F.; Zang, Z.; Xu, K.; Hou, Y.; Teale, S.; Zhou, W.; Si, R.; Gao, X.; Sargent, E. H.; Ning, Z. One-Step Synthesis of SnI2·(DMSO)x Adducts for High-Performance Tin Perovskite Solar Cells. *Journal of the American Chemical Society* **2021,** *143*, 10970-10976.

16. Cui, D.; Liu, X.; Wu, T.; Lin, X.; Luo, X.; Wu, Y.; Segawa, H.; Yang, X.; Zhang, Y.; Wang, Y.; Han, L. Making Room for Growing Oriented FASnI3 with Large Grains via

Cold Precursor Solution. *Advanced Functional Materials* **2021,** *31*, 2100931.

17. Wang, S.; Wu, C.; Wu, T.; Yao, H.; Hua, Y.; Hao, F. π-Conjugated Lewis Base for Efficient Tin Halide Perovskite Solar Cells with Retarded Sn2+ Oxidation. *ACS Energy Letters* **2024,** *9*, 1168-1175.

18. Chan, P. F.; Qin, M.; Su, C.-J.; Ye, L.; Wang, X.; Wang, Y.; Guan, X.; Lu, Z.; Li, G.; Ngai, T.; Tsang, S. W.; Zhao, N.; Lu, X. iso-BAI Guided Surface Recrystallization for Over 14% Tin Halide Perovskite Solar Cells. *Advanced Science n/a*, 2309668.

19. Duan, C.; Zou, F.; Wen, Q.; Qin, M.; Li, J.; Chen, C.; Lu, X.; Ding, L.; Yan, K. A Bifunctional Carbazide Additive For Durable CsSnI3 Perovskite Solar Cells. *Advanced Materials* **2023,** *35*, 2300503.

20. Queisser, H. J. Detailed balance limit for solar cell efficiency. *Materials Science and Engineering: B* **2009,** *159-160*, 322-328.

21. Dai, L.; Deng, Z.; Auras, F.; Goodwin, H.; Zhang, Z.; Walmsley, J. C.; Bristowe, P. D.; Deschler, F.; Greenham, N. C. Slow carrier relaxation in tin-based perovskite nanocrystals. *Nature Photonics* **2021,** *15*, 696-702.

22. Ross, R. T.; Nozik, A. J. Efficiency of hot - carrier solar energy converters. *Journal of Applied Physics* **1982,** *53*, 3813-3818.

23. Chen, J.-K.; Zhang, B.-B.; Liu, Q.; Shirahata, N.; Mohammed, O. F.; Bakr, O. M.; Sun, H.-T. Advances and Challenges in Tin Halide Perovskite Nanocrystals. *ACS Materials Letters* **2021,** *3*, 1541-1557.

24. Fang, H.-H.; Adjokatse, S.; Shao, S.; Even, J.; Loi, M. A. Long-lived hot-carrier light emission and large blue shift in formamidinium tin triiodide perovskites. *Nature Communications* **2018,** *9*, 243.

25. Kontos, A. G.; Kaltzoglou, A.; Arfanis, M. K.; McCall, K. M.; Stoumpos, C. C.; Wessels, B. W.; Falaras, P.; Kanatzidis, M. G. Dynamic Disorder, Band Gap Widening, and Persistent Near-IR Photoluminescence up to At Least 523 K in ASnI3 Perovskites (A = Cs+, CH3NH3+ and NH2–CH═NH2+). *The Journal of Physical Chemistry C* **2018,**

122, 26353-26361.

26. Kahmann, S.; Nazarenko, O.; Shao, S.; Hordiichuk, O.; Kepenekian, M.; Even, J.; Kovalenko, M. V.; Blake, G. R.; Loi, M. A. Negative Thermal Quenching in FASnI3 Perovskite Single Crystals and Thin Films. *ACS Energy Letters* **2020,** *5*, 2512-2519.

27. Ozaki, M.; Katsuki, Y.; Liu, J.; Handa, T.; Nishikubo, R.; Yakumaru, S.; Hashikawa, Y.; Murata, Y.; Saito, T.; Shimakawa, Y.; Kanemitsu, Y.; Saeki, A.; Wakamiya, A. Solvent-Coordinated Tin Halide Complexes as Purified Precursors for Tin-Based Perovskites. *ACS Omega* **2017,** *2*, 7016-7021.

28. Treglia, A.; Ambrosio, F.; Martani, S.; Folpini, G.; Barker, A. J.; Albaqami, M. D.; De Angelis, F.; Poli, I.; Petrozza, A. Effect of electronic doping and traps on carrier dynamics in tin halide perovskites. *Materials Horizons* **2022,** *9*, 1763-1773.

29. Ma, J.-P.; Yin, J.; Chen, Y.-M.; Zhao, Q.; Zhou, Y.; Li, H.; Kuroiwa, Y.; Moriyoshi, C.; Li, Z.-Y.; Bakr, O. M.; Mohammed, O. F.; Sun, H.-T. Defect-Triggered Phase Transition in Cesium Lead Halide Perovskite Nanocrystals. *ACS Materials Letters* **2019,** *1*, 185-191.

30. Zhou, Y.; Poli, I.; Meggiolaro, D.; De Angelis, F.; Petrozza, A. Defect activity in metal halide perovskites with wide and narrow bandgap. *Nature Reviews Materials* **2021,** *6*, 986-1002.

31. Ran, C.; Xu, J.; Gao, W.; Huang, C.; Dou, S. Defects in metal triiodide perovskite materials towards high-performance solar cells: origin, impact, characterization, and engineering. *Chemical Society Reviews* **2018,** *47*, 4581-4610.

32. Li, B.; Chang, B.; Pan, L.; Li, Z.; Fu, L.; He, Z.; Yin, L. Tin-Based Defects and Passivation Strategies in Tin-Related Perovskite Solar Cells. *ACS Energy Letters* **2020,** *5*, 3752-3772.

33. Shi, T.; Zhang, H.-S.; Meng, W.; Teng, Q.; Liu, M.; Yang, X.; Yan, Y.; Yip, H.-L.; Zhao, Y.-J. Effects of organic cations on the defect physics of tin halide perovskites. *Journal of Materials Chemistry A* **2017,** *5*, 15124-15129.

34. Liu, Q.; Yin, J.; Zhang, B.-B.; Chen, J.-K.; Zhou, Y.; Zhang, L.-M.; Wang, L.-

M.; Zhao, Q.; Hou, J.; Shu, J.; Song, B.; Shirahata, N.; Bakr, O. M.; Mohammed, O. F.; Sun, H.-T. Theory-Guided Synthesis of Highly Luminescent Colloidal Cesium Tin Halide Perovskite Nanocrystals. *Journal of the American Chemical Society* **2021,** *143*, 5470-5480.

35. Tauc, J.; Grigorovici, R.; Vancu, A. Optical Properties and Electronic Structure of Amorphous Germanium. *physica status solidi (b)* **1966,** *15*, 627-637.

36. Dirin, D. N.; Vivani, A.; Zacharias, M.; Sekh, T. V.; Cherniukh, I.; Yakunin, S.; Bertolotti, F.; Aebli, M.; Schaller, R. D.; Wieczorek, A.; Siol, S.; Cancellieri, C.; Jeurgens, L. P. H.; Masciocchi, N.; Guagliardi, A.; Pedesseau, L.; Even, J.; Kovalenko, M. V.; Bodnarchuk, M. I. Intrinsic Formamidinium Tin Iodide Nanocrystals by Suppressing the Sn(IV) Impurities. *Nano Letters* **2023,** *23*, 1914-1923.

37. Kövér, L.; Kovács, Z.; Sanjinés, R.; Moretti, G.; Cserny, I.; Margaritondo, G.; Pálinkás, J.; Adachi, H. Electronic structure of tin oxides: High-resolution study of XPS and Auger spectra. *Surface and Interface Analysis* **1995,** *23*, 461-466.

38. Kubicki, D. J.; Prochowicz, D.; Salager, E.; Rakhmatullin, A.; Grey, C. P.; Emsley, L.; Stranks, S. D. Local Structure and Dynamics in Methylammonium, Formamidinium, and Cesium Tin(II) Mixed-Halide Perovskites from 119Sn Solid-State NMR. *Journal of the American Chemical Society* **2020,** *142*, 7813-7826.

39. Zhao, X.-G.; Dalpian, G. M.; Wang, Z.; Zunger, A. Polymorphous nature of cubic halide perovskites. *Physical Review B* **2020,** *101*, 155137.

40. Coduri, M.; Shiell, T. B.; Strobel, T. A.; Mahata, A.; Cova, F.; Mosconi, E.; De Angelis, F.; Malavasi, L. Origin of pressure-induced band gap tuning in tin halide perovskites. *Materials Advances* **2020,** *1*, 2840-2845.

41. Mizoguchi, H.; Woodward, P. M.; Park, C.-H.; Keszler, D. A. Strong Near-Infrared Luminescence in BaSnO3. *Journal of the American Chemical Society* **2004,** *126*, 9796-9800.

Chapter 3: Zwitterionic Phosphatidylcholine Ligand for Colloidal Synthesis of Stable Formamidinium Tin Iodide Perovskite Nanocrystals

3.1 Introduction

Over the past several years, metal halide perovskites have receiver tremendous scientific and technological interest because of their outstanding optoelectronic properties, including tunable band gaps, narrow emission bands, high absorption cross sections, and high carrier mobilities.[1-5] These merits make them excellent candidates for a variety of optoelectronic devices, such as high-efficiency solar cells, photodetectors, and light-emitting diodes (LEDs).[6-11] In particular, colloidal perovskite nanocrystals (NCs) are in the forefront of the current research owing to their attractive characteristics including direct and low-cost synthesis, structural flexibility, and remarkable photoluminescence quantum yield (PLQY) even without delicate shell passivation.[2, 12, 13] However, all highly luminescent perovskite NCs and related high-performance LEDs reported have thus far been limited to lead-containing system, which has become one of the most notable impediments on their way toward commercial and electronic equipment.[14, 15] To address this problem, tin halide perovskites NCs have raised researches concerns, since the similar ionic radius, valence electronic configuration of tin (Sn) with lead (Pb), as well as their low toxicity.[16-18]

Chemists, material scientists, and engineers recently have made some achievements on the tin halide perovskites in the form of polycrystalline films and on their related optoelectronic applications.[19-27] The external quantum efficiency of red LEDs based on tin halide perovskite has exceeded 20%,[28] and the tin halide perovskite based solar cells have attained a power conversion efficiency of over 14%.[29] Unfortunately, the synthetic chemistry, the understanding of intrinsic physical and chemical properties, and the device applications of the tin halide perovskite NCs significantly lag behind those of their Pb-based counterparts. At present, most studies are related to the synthesis of all-inorganic cesium (Cs) tin halide NCs, while organic-inorganic hybrid tin halide perovskite NCs, such as formamidinium (FA) tin iodide ($FASnI_3$), are rarely reported. A recent interesting finding reveals that when the size of $FASnI_3$ NCs is down to several nanometers, the relaxation of hot carriers could be effectively slowed down, leading to a higher theoretical

solar convention efficiency up to 66%.[30] This result shows the promising potential of organic-inorganic hybrid tin halide perovskite NCs.

The first synthesis of $FASnI_3$ NCs via solvent-thermal method was reported in 2021.[30] By varying the reaction temperature of the precursors, size-controlled (7.3-12.1 nm) $FASnI_3$ NCs were successfully achieved. The photoluminescence (PL) peaks can be changed from 666 nm to 763 nm due to the quantum size effect. Recently, Dirin et al. reported the synthesis of $FASnI_3$ NCs via traditional hot-injection method.[31] Uniform, cubic morphology of $FASnI_3$ NCs with an average of ~10 nm was achieved. However, their NCs show a PL peak at ~800 nm which is inconsistent with early reported results.[30] In addition, room temperature synthesis route was also developed, and small-sized (~7.1 nm) $FASnI_3$ NCs with a PL peak at ~ 825 nm were successfully achieved.[32] I note that the ever-reported $FASnI_3$ NCs do not show a consistent size-related optical properties. Amine ligands, like oleylamine (OAm), octylamine (OTAm), are commonly used for maintaining morphology and size, and passivating surface defects of colloidal perovskite NCs.[33-35] Nevertheless, amine-related two-dimensional (2D) perovskites, such as OAm_2SnI_4, easily crystallize along with the nucleation and growth of tin halide perovskite NCs.[36, 37] These byproducts exhibit a similar red emitting with a PL peak at ~700 nm. To avoid the formation of 2D perovskite crystals, and to better understand the photophysical properties of $FASnI_3$ NCs, developing amine-free synthesis route is necessary.

Traditional anionic and cationic surface ligands that attach to halide NC surfaces in an ionic manner, displacing surface ions with the ligand head groups also readily engage in adverse solubilization equilibria with the ions constituting the inorganic NC cores.[38, 39] This problem culminates with organic–inorganic hybrid perovskite compositions. Zwitterionic, hence charge-neutral, capping molecules offer a general mitigation strategy for avoiding these adverse ionic metathesis reactions with NC cores, and effectively enhance the structural stability of halide perovskite NCs.[38, 40, 41] Among them, eco-friendly phosphatidylcholines have been developed for not only regulating the growth kinetics but also improving the optical properties of halide perovskite NCs.[42, 43]

Here, I report a colloidal, amine-free synthetic approach for $FASnI_3$ perovskite NCs using zwitterionic long-chain molecules, phosphatidylcholines, as surfactants, avoiding the formation of possible 2D perovskite byproducts. Incorporating a small amount of phosphatidylcholines in the reaction can decrease the particle size of $FASnI_3$ NCs from

200-300 nm to ~30 nm. The obtained NCs exhibit a PLQY of 1.2% which is higher than ever reported results, and better colloidal stability in hexane as well as structural stability in glovebox even after 14 days. A range of experimental characterizations including Fourier transform infrared (FTIR), NMR spectroscopy, energy-dispersive X-ray spectroscopy (EDS) confirm the incorporation of phosphatidylcholine with $FASnI_3$ NCs. Importantly, I demonstrate that $FASnI_3$ NCs can be synthesized within a wide temperature range between 25°C to 150°C.

3.2 Experimental section

3.2.1 Chemicals

Formamidine acetate (FA-acetate, Sigma, 99%), tin 2-ethylhexanoate ($Sn(Oct)_2$, Sigma, 92.5-100.0%), tin(II) iodide (SnI_2, Sigma, 99.99% trace metals basis), 1-octadecene (ODE, Sigma, 95%), oleic acid (OA, Sigma, 90%), tri-n-octylphosphine (TOP, Thermo, 90%), 1,2-Didodecanoyl-sn-glycero-3-phosphocholine (C_{32}-PC, Sigma, >99%), 1,2-Dioleoyl-sn-glycero-3-phosphocholine (C_{44}-PC, TCI, >97%), 1,2-Dierucoyl-sn-glycero-3-phosphocholine (C_{52}-PC, TCI, >95%), n-hexane (Sigma, ≥99%), Toluene (Wako, 99%) were used without purification unless otherwise noted.

Table 3.1. List of the manufacturer, batch number, and purity from certificate of analysis (COA) of all used chemicals for synthesis.

Chemical	Manufacturer	Batch number	Purity from COA
FA-acetate	Sigma-Aldrich	BCBZ7461	100%
$Sn(Oct)_2$	Sigma-Aldrich	SLCM1306	96.9%
SnI_2	Sigma-Aldrich	0000303819	99.99%
ODE	Sigma-Aldrich	BCCH1566	98.9%
OA	Sigma-Aldrich	MKCR9052	94.9%
TOP	ThermoFisher	L15744	99.99%

C_{32}-PC	Sigma-Aldrich	SLBK8612V	100%
C_{44}-PC	TCI	TJLAN	99.8%
C_{52}-PC	TCI	BJH5O	99.4%
n-hexane	Sigma-Aldrich	STBL2142	99.3%
Toluene	FUJIFILM Wako	KSP2915	99.9%

3.2.2 Experiments

Preparation of FA-oleate solution. 0.2603 g FA-acetate was mixed with 20 ml 1-octadecene (ODE) and 3.39 ml oleic acid in 100 ml three-necked flask in an argon-filled glovebox. The mixture was then degassed for half hour at 80 ºC, then heated under nitrogen to 120 ºC for half hour, yielding a clear FA-oleate solution. After that, the as-prepared FA-oleate was cooled to room temperature, and transferred to glovebox for the further use.

Preparation of the SnI_2-TOP stock solution. The mixture of 0.1105 g SnI_2, 0.18 ml $Sn(Oct)_2$, and 0.3 ml TOP was vigorously stirred at 120 ºC on a hot plate for 20 min, yielding a yellow stock solution. Then, the solution was cooled to room temperature.

Preparation of the C_{44}-PC stock solution. 1,2-Dioleoyl-sn-glycero-3-phosphocholine (C44-PC) was dissolved in ODE at 120 ºC on a hot plate, yielding a clear solution of 0.1g/ml.

Synthesis of $FASnI_3$ NCs. 5 ml ODE, different amount of C_{44}-PC stock solution (30 μL; 60 μL; 90 μL; 120 μL for C44-PC-3 mg; 6 mg; 9 mg; 12 mg samples, respectively) were heated to a certain temperature in a 20 ml vial on a hot plate, followed by the addition of 0.12 ml SnI_2-TOP stock solution under vigorous stirring for 5 min. Then, 0.18 ml FA-oleate solution was swiftly injected into the reaction solution. After reaction for 10 s, the crude solution was taken off from the hot plate. The synthesis was conducted in an Ar-filled glovebox.

Purification of $FASnI_3$ NCs. The crude solution was centrifuged at 15000 r.p.m. for 5 min to remove the supernatant solution. The precipitate was redispersed in 1 ml toluene

and then centrifuged at 4000 r.p.m. for 5 min to remove aggregated NCs, resulting in the supernatant of long-term colloidally stable solution.

3.2.3 Characterizations

XRD, TEM, EDS measurements. Powder XRD data were recorded on a MiniFlex 600 diffractometer (Rigaku) with a Cu Kα X-ray source (λ = 1.5418 Å). The $FASnI_3$ microcrystals were dispersed in hexane to form a concentrated solution which was then dropped on a silicon substrate for XRD measurements. TEM images were collected by a JEM-2100F (JEOL) microscope operated at 200 kV. TEM samples were prepared by dropping a dilute microcrystals-hexane solution onto a TEM copper grid and dried in glovebox. Scanning transmission electron microscope (STEM) EDS elemental mapping was obtained on STEM mode operating at 200 kV. The dark-field image was acquired with a high-angle annular dark field (HAADF) detector.

Optical characterizations. PL spectra were measured by a TE-cooled micro spectrometer (Ootosky, ATP5020P) equipped with a 22 mW, 517 nm laser. Absolute PLQYs were measured by a standardized integrating sphere method using a C9920-03G system equipped with a 150-W xenon lamp (Hamamatsu Photonics). The absorption spectra were measured by a UV-vis-NIR spectrophotometer (V-770, JASCO).

FTIR and NMR characterizations. FTIR spectra were recorded using a Jasco 4100 FTIR spectrometer. NMR data were acquired on a JEOL ECS-400 spectrometer. For the NMR measurements, the samples were dispersed in chloroform-D.

3.3 Results and discussion

In the chapter 2, I successfully synthesized $FASnI_3$ microcrystals. Through changing the precursor ratios, I can modify the structural defects in $FASnI_3$. Here, to decrease the particle size, and get uniform-sized nanocrystals, I used zwitterionic phosphatidylcholine as a surfactant aimed at suppressing the growth of NCs. The synthesis route is shown in **Figure 3.1a**. In a typical synthesis, SnI_2 and $Sn(Oct)_2$ was mixed with tri-n-octylphosphine (TOP) at 120 ºC to form a Sn-I precursor. Then, this Sn-I precursor was mixed with 1-octadecene (ODE) at 120 ºC in a 20 ml vial on a hot plate, followed by introducing phosphatidylcholine. The FA-oleate solution was swiftly injected into the

reaction vial, triggering a rapid salt metathesis reaction and resulting in fast nucleation and growth of $FASnI_3$ NCs within 10 s. The precursor ratio of FA: Sn: I is 1: 6.3: 4.5. Keeping a tin-rich reaction condition is the key to get high-quality crystals, which has been confirmed in chapter 2.

I chose three phosphatidylcholines with different chain lengths, $C_{32}H_{64}NO_8P$ (C_{32}-PC), $C_{44}H_{84}NO_8P$ (C_{44}-PC), $C_{52}H_{100}NO_8P$ (C_{52}-PC), as ligands for colloidal synthesis of $FASnI_3$ NCs (**Figure 3.1b**). All of them are readily available commercially. The reason for me to choose phosphatidylcholine is 2-fold. Firstly, for typical anionic and cationic surface ligands, such as oleate (OA^-), oleylammonium (OAm^+), highly dynamic binding exists between the surface capping ligands and the oppositely charged NC surface ions, together with a mutual equilibrium between the ionized and molecular forms of these ligands.[39] These dynamics cause the rapid desorption of the protective ligand shell upon isolation and purification of NCs. Phosphatidylcholines as zwitterionic surfactant, is composed of a quaternary amine choline headgroup, a phosphate group, exhibiting tight binding with NC surface without dynamic interaction between ligand shell with NC surface ions. Secondly, OAm^+ is widely used for getting 2D tin perovskite crystals (OAm_2SnI_4), which have low formation energy. During the nucleation and growth of tin iodide perovskite, OAm_2SnI_4 easily appears as byproduct.[37] To avoid it, phosphatidylcholine instead of amine is used for the synthesis of $FASnI_3$ NCs.

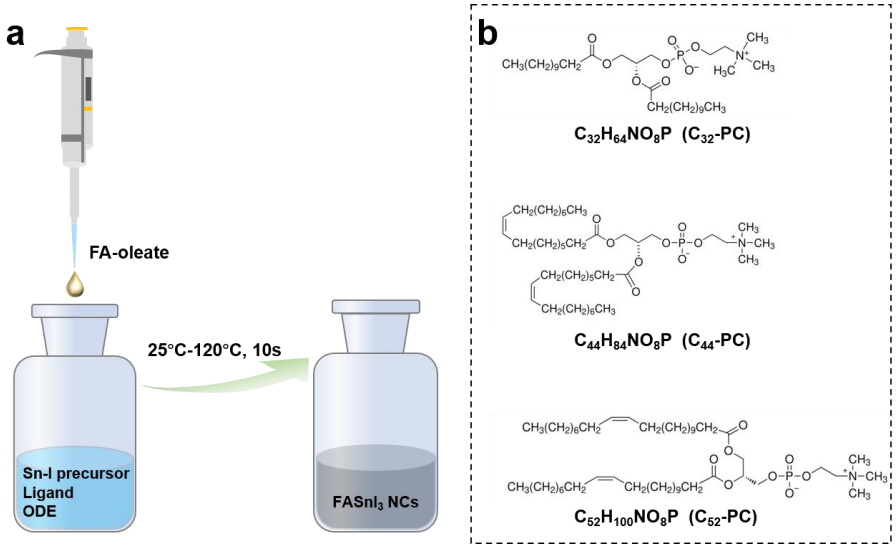

Figure 3.1. (a) Scheme of colloidal synthesis of $FASnI_3$ NCs. (b) Chemical structures of three phosphatidylcholines with different chain lengths.

I started with the synthesis of $FASnI_3$ NCs without the use of phosphatidylcholine as shown in **Figure 3.2**. Powder X-ray diffraction (XRD) patterns confirm the synthesis of pure cubic $FASnI_3$ crystals without additional crystalline phase (**Figure 3.2a**), and transmission electron microscopy (TEM) image show particle sized up to several hundred nanometers (nm) (**Figure 3.2b**). The results are consistent with my work in chapter 2. Next, I first used C_{44}-PC as a model surfactant that was introduced in the synthesis. I changed the mass amount of C_{44}-PC from 3 mg to 12 mg. The samples are denoted as C_{44}-PC-x mg, where x is the mass amount of the added C_{44}-PC. From the XRD patterns shown in **Figure 3.3a**, we can find that all the yielded products match the cubic structure of $FASnI_3$ perovskite, without any other additional crystalline phase. Interestingly, the TEM images in **Figure 3.3b-e** show that introducing C_{44}-PC greatly suppress the growth of $FASnI_3$ crystals, decreasing the particle size from several hundred nanometers (**Figure 3.2b**) to ~ 30 nm. C_{44}-PC capped $FASnI_3$ NCs have near-cubic morphology, and monodispersity in toluene solvent. The average size of $FASnI_3$ NCs are 32.2 nm, 30.7 nm, 29.4 nm, 30.3 nm, for C_{44}-PC-3 mg, C_{44}-PC-6 mg, C_{44}-PC-9 mg, C_{44}-PC-12 mg samples, respectively (**Figure 3.3b-e**). From 3 mg to 9 mg, we can observe the decrease trend of NC average size; further increasing the amount of C_{44}-PC can slightly increase the NC size.

According the classical nucleation theory, the whole crystallization of the $FASnI_3$ NCs is generally divided into two processes, namely nucleation process, and crystal growth.[44] The nucleation process originates from the supersaturated perovskite precursors when the perovskite solubility is much lower than the precursor concentration. With the increase of the nucleus concentration, perovskite monomers accumulated around formed nuclei, bursting the growth of crystals.[45] The whole growth process finishes when the concentration of perovskite precursors is lower than perovskite solubility in solvent. During the growth process, Ostwald ripening happens. When small particles dissolute, they will redeposit on the surface of larger particles, resulting in further growth of crystals.[46] The introduction of long-chain C_{44}-PC can effectively suppress the Ostwald ripening process, and slow down the growth rate, because of the steric effect. This is easily understanded from the TEM results: with C_{44}-PC, NCs hardly aggregated together (**Figure 3.2b; Figure 3.3b-e**). However, previous report confirmed the strong interaction of phosphatidylcholine with the tin halide perovskite precursors, resulting in better perovskite solubility in the solvent.[43] During the nucleation process, this strong interaction can lead to less perovskite nuclei, which explains the slight increase in particle size with more C_{44}-PC (**Figure 3.3e**).

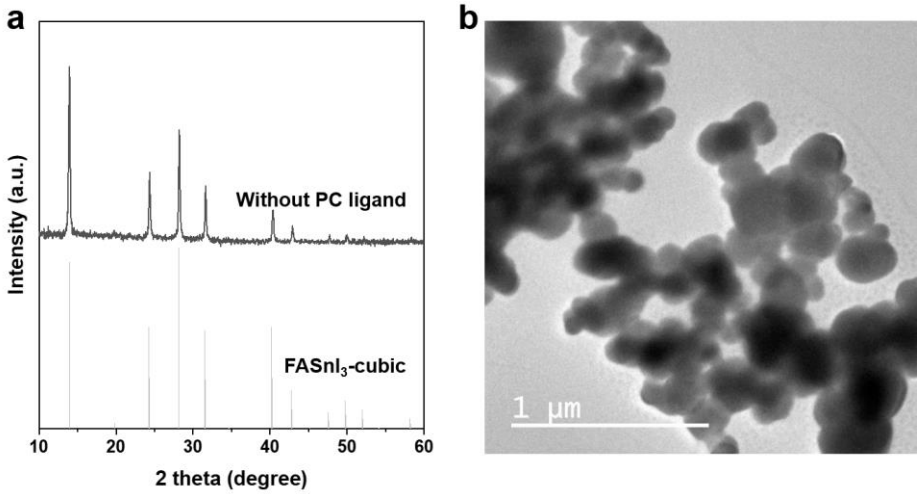

Figure 3.2. (a) Powder XRD pattern of $FASnI_3$ microcrystals synthesized without phosphatidylcholine. (b) TEM image $FASnI_3$ microcrystals synthesized without phosphatidylcholine.

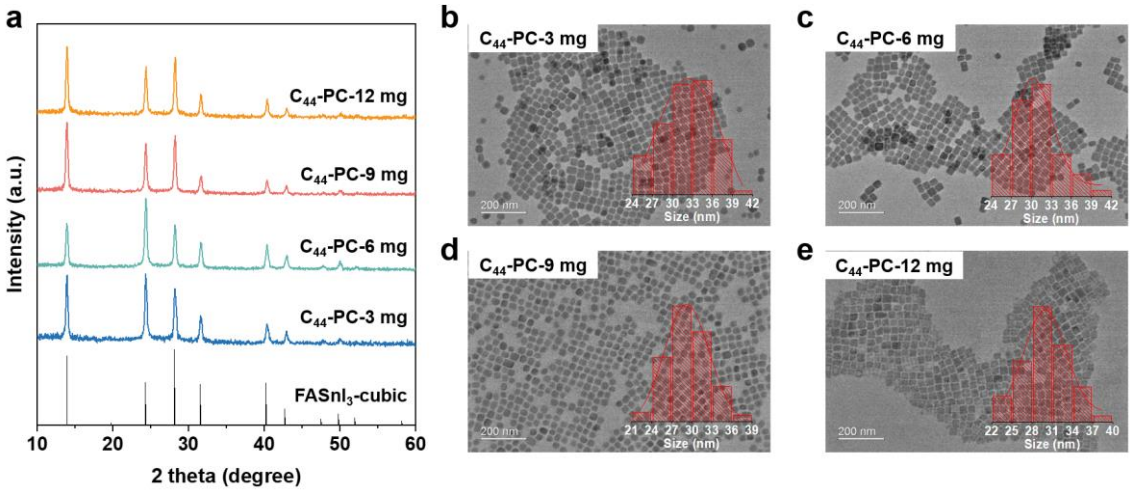

Figure 3.3. (a) Powder XRD patterns of $FASnI_3$ NCs synthesized with different amount of C_{44}-PC. (b) TEM image and corresponding size-distribution histograms of $FASnI_3$ NCs synthesized with different amount of C_{44}-PC.

Next, I investigated the optical properties of the $FASnI_3$ NCs synthesized with different amount of C_{44}-PC. All the samples demonstrate similar optical absorption and PL features **(Figure 3.4a**). Interestingly, using the Tauc Plot method,[47] the calculated bandgap of $FASnI_3$ NCs is ~2.31 eV, which is much larger than the large-sized $FASnI_3$ (1.41-1.64 eV) as I studied in Chapter 2. Dirin et al. studied the origin of bandgap widening for $FASnI_3$ NCs, and they considered that structural distortion, such as I disorder, contributes to the enlarged bandgap.[31] In Chapter 2, I also find that defect-induced structural distortion could induce bandgap widening. For small-sized $FASnI_3$ NCs, this effect is more outstanding since the more volatile lattices compared with microcrystals or larger-sized single crystal. From the PL spectra in **Figure 3.4a**, we can see that all samples have a PL peak position at ~868 nm. In addition, the full width at half-maximum (fwhm) of PL for 3 mg, 6 mg, 9 mg, 12 mg samples are 70 nm, 69 nm, 68 nm, 68nm, respectively. With more C_{44}-PC, we can observe slight decrease in fwhm, indicting the less defect states in $FASnI_3$ NCs, which also could be seen from their PLQY results: 0.7%; 0.8%, 1.2%; 1.1% for 3 mg, 6 mg, 9 mg, 12 mg samples, respectively (**Figure 3.4b**). Although the PLQY gotten here is larger than ever reported results, it is still unsatisfactory. For $FASnI_3$ NCs, how to suppress surface defects is of great importance, which will be discussed in the next Chapter.

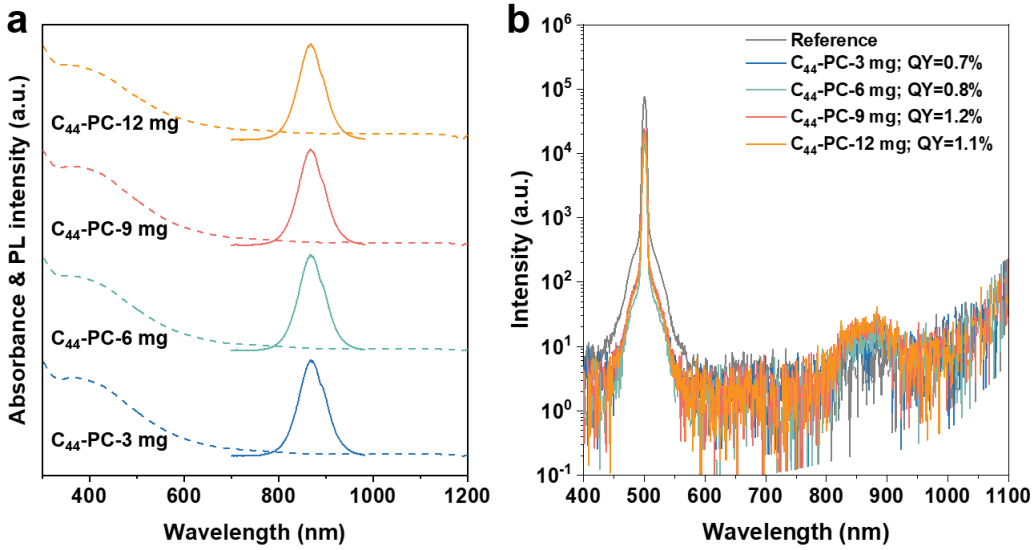

Figure 3.4. (a) Normalized PL (solid lines) and absorption (dashed lines) spectra of $FASnI_3$ NCs synthesized with different amount of C_{44}-PC. (b) PLQY measurements of $FASnI_3$ NCs synthesized with different amount of C_{44}-PC.

To know the function of hydrocarbon chains in phosphatidylcholine, I processed to synthesize $FASnI_3$ NCs using other phosphatidylcholines. The samples are denoted as C_y-PC, where y is the number of carbons in phosphatidylcholine. I find that using C_{32}-PC and C_{52}-PC can also produce $FASnI_3$ NCs without any other crystalline phase as seen in XRD patterns (**Figure 3.5a**). From the TEM images (**Figure 3.5, c**), we can see that both two samples have near-cubic morphology, and monodispersity in toluene solvent, which is as same as those using C_{44}-PC as ligand. The average particle sizes are ~29.2 nm and 30.3 nm for C_{32}-PC and C_{52}-PC. Specially, C_{52}-PC sample has wider size distribution that can be checked from their size-distribution histograms (**Figure 3.5, c**). These results confirm that the synthesis of $FASnI_3$ NCs doesn't rely on the fatty acid side-chain length of phosphatidylcholines. The optical properties in **Figure 3.6a** show that all obtain NCs have similar absorbance property with C_{44}-PC-x. However, they exhibit different PL behaviors: for C_{32}-PC sample, the PL peak position is at ~862 nm; for C_{52}-PC sample, the PL peak position is at ~866 nm. Both have slight blue-shift in PL spectra compared with C_{44}-PC-x, indicating intrinsic structural difference when using different phosphatidylcholines. **Figure 3.6b** is the PLQY measurements of C_{32}-PC and C_{52}-PC samples. They are 0.9% and 1.0% for C_{32}-PC and C_{52}-PC, slightly less than C_{44}-PC-9 mg

sample, indicting the effect of hydrocarbon-chain length on the crystal quality of $FASnI_3$ NCs.

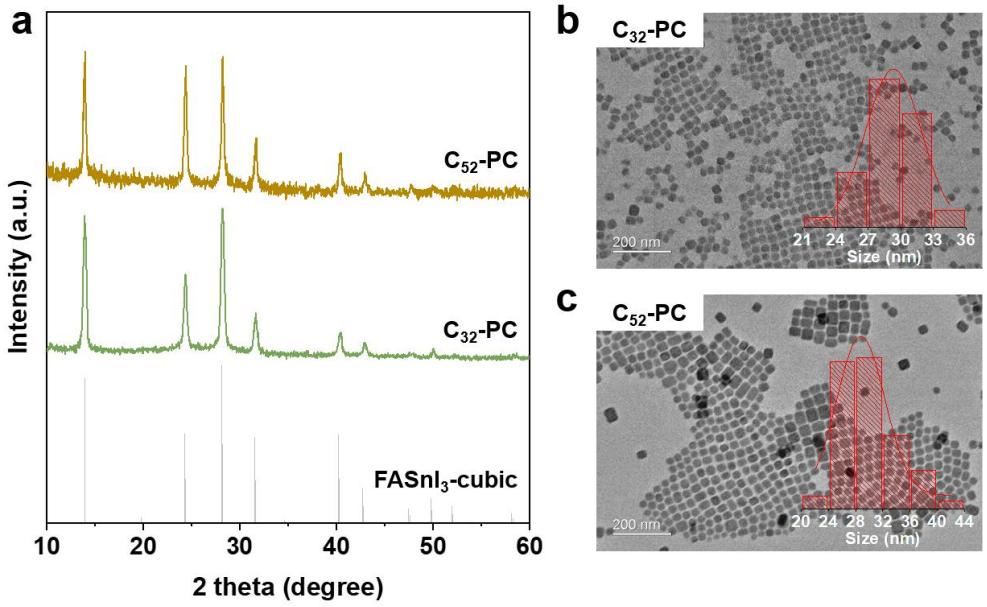

Figure 3.5. (a) Powder XRD patterns of $FASnI_3$ NCs synthesized with C_{32}-PC and C_{52}-PC. (b) TEM image and corresponding size-distribution histograms of $FASnI_3$ NCs synthesized C_{32}-PC and C_{52}-PC.

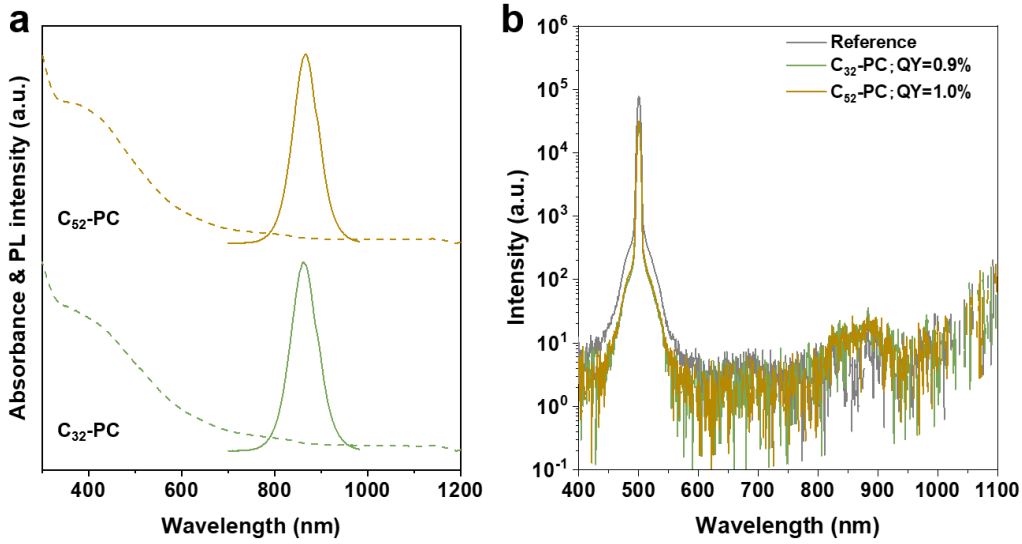

Figure 3.6. (a) Normalized PL (solid lines) and absorption (dashed lines) spectra of $FASnI_3$ NCs synthesized with C_{32}-PC and C_{52}-PC. (b) PLQY measurements of $FASnI_3$ NCs synthesized with C_{32}-PC and C_{52}-PC.

Next, I checked the stability of as prepared $FASnI_3$ NCs. I chose C_{44}-PC-9 mg as my research object since it has best optical properties among all products. I firstly investigated the colloidal stability of $FASnI_3$ without and with C_{44}-PC. As shown in **Figure 3.7a**, after 1day, sample without C_{44}-PC totally precipitated from hexane solution. But for sample with C_{44}-PC, even after 30 days, $FASnI_3$ NCs are will dispersed in the hexane solution (**Figure 3.7b**), indicating excellent colloidal stability of $FASnI_3$ NCs in hexane. The long-term colloidal stability indicates that C_{44}-PC can well bind with NC surface, without desorption of ligand shell even after 30 days. This character can also help to prepare a great NC film for potential optoelectronic applications. Secondly, I studied the structural stability of as-synthesized $FASnI_3$ NCs both in Ar and air atmosphere. As we can see in **Figure 3.8a**, C_{44}-PC capping $FASnI_3$ NCs have great structural stability in Ar-filled glovebox. Even after 13 days, they show no obvious changes in XRD patterns. In the air, $FASnI_3$ NCs can be easily oxidated into non-perovskite FA_2SnI_6 phase within 10 min (**Figure 3.8b**). In the future, choosing some appropriate ligands or conducting core-shell structure to protect fragile $FASnI_3$ NCs is the key point. A stable perovskite structure may promote intense efforts on constructing optoelectronic devices using $FASnI_3$ NCs.

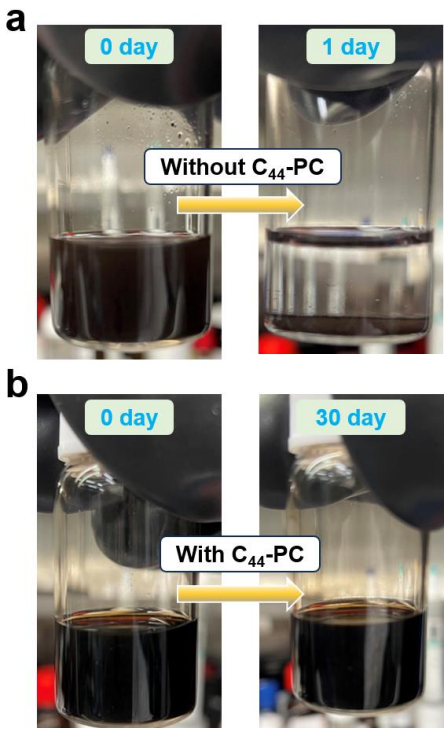

Figure 3.7. (a) Photos of NC-hexane solution of sample without C_{44}-PC stored in

glovebox after 0 and 1 day. (b) Photos of NC-hexane solution of sample without C_{44}-PC stored in glovebox after 0 and 30 days, showing excellent colloidal stability.

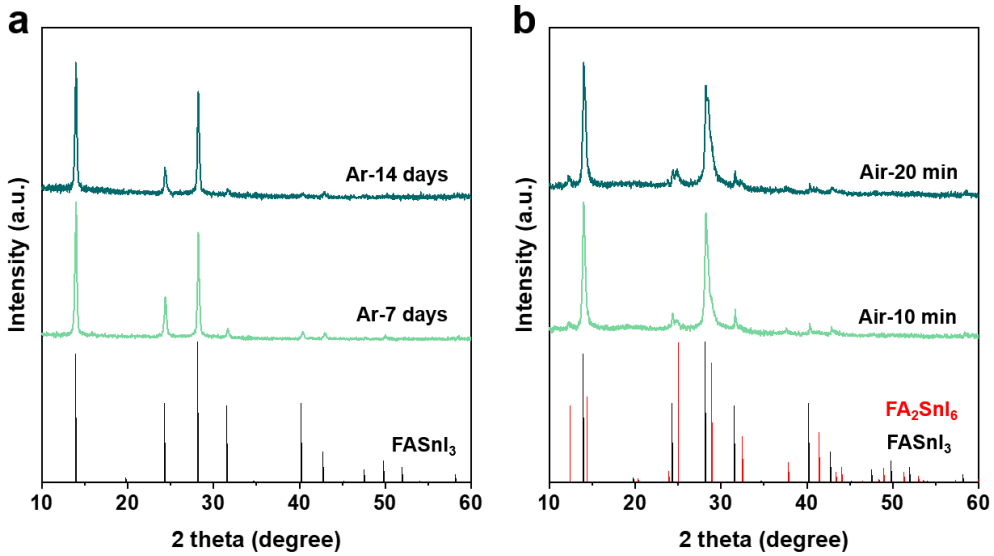

Figure 3.8. (a) XRD patterns of $FASnI_3$ NCs stored in Ar-filled glovebox for 7 and 14 days, respectively. (b) XRD patterns of $FASnI_3$ NCs stored in air for 10 and 20 min, respectively.

I then took Fourier transform infrared (FTIR) and ^1H nuclear magnetic resonance (NMR) measurements to glean information of the capping ligands on the surface of $FASnI_3$ NCs. I used C_{44}-PC-9 mg as an example system. As shown in **Figure 3.9a**, and **Table 3.1**, the vibrational bands at 2923 and 1458 cm^{-1} can be assigned to the C-H stretching and bending vibrations of the CH_2 group;[48, 49] the bands at 2856 and 1378 cm^{-1} instead result from the C-H stretching and bending vibrations of the CH_3 group.[48] In addition, the distinct vibrational band at 1647 cm^{-1} originates from the C=C stretching vibration of the C_{44}-PC or oleic acid (OA),[50] and the characteristic stretching vibration of the C=O at 1715 cm^{-1} is from the C_{44}-PC or OA.[48] Importantly, the vibrational band at 1061 cm^{-1} is the P-O-C stretching, confirming the presence of C_{44}-PC.[39] 1H NMR spectra is shown in **Figure 3.9b**. However, from the NMR spectra, we only can find distinct chemical shifts at 0.9 ppm and 1.2 ppm, which origin from methyl group (CH_3) and methylene group (CH_2).[51]

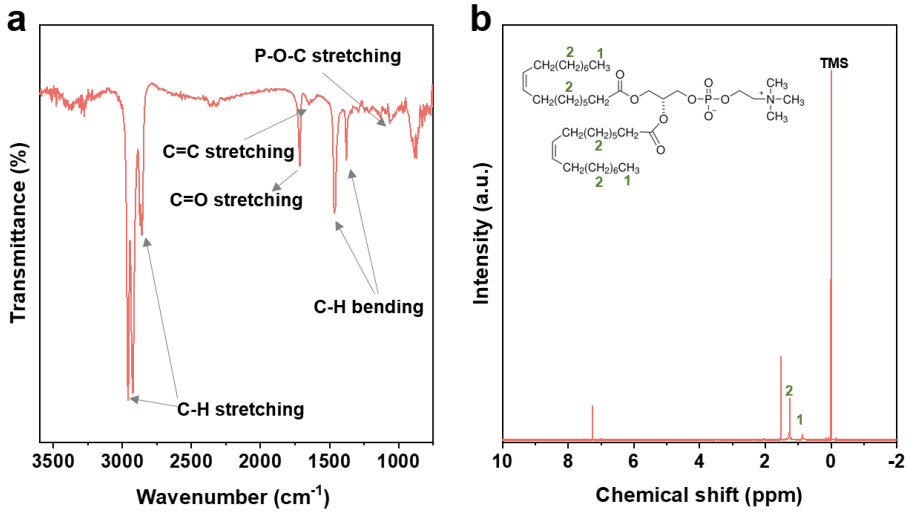

Figure 3.9. (a) FTIR spectra of sample C_{44}-PC-9 mg. (b) ^{1}H NMR spectra of C_{44}-PC-9 mg.

Table 3.2. FTIR vibrational modes and their assignments for $FASnI_3$ NCs using C_{44}-PC as ligand.

Frequency (cm^{-1})	Functional group assigned	References
2923	C-H stretching vibration of methylene group (CH_2)	48
2856	C-H stretching vibration of methylene group (CH_3)	48
1715	C=O stretching vibration	48
1647	C=C stretching vibration	50
1458	C-H bending vibration of methylene group (CH_2)	48
1378	C-H bending vibration of methyl group (CH_3)	48
1061	P-O-C stretching	39
869	C-H out-of-plane vibration or C-C stretching vibrations	52

To further confirm the presence of C_{44}-PC on the surface of $FASnI_3$ NCs, I then measured the scanning transmission electron microscopy (STEM) energy-dispersive X-

ray spectroscopy (EDS). The EDS-mapping images are shown in **Figure 3.10**. **Figure 3.10a and b** are the high angel annular dark field (HAADF)-STEM images of C_{44}-PC capping $FASnI_3$ NCs before and after EDS mapping, respectively. To avoid the rapid degradation of $FASnI_3$ NCs under electron beam, I chose a low magnification for analysis. However, even under low magnification, NCs also have some changes after long-time EDS mapping (**Figure 3.10b**). The corresponding mapping images of different elements are displayed in **Figure 3.10c-f**. We can observe the signals of N, Sn, I and P elements, wherein, N, Sn, I are from the $FASnI_3$, and P originates from C_{44}-PC ligand, confirming the successful coordination of phosphatidylcholine with NC surface. The element ratio of N: Sn: I: P is 2.7: 1: 2.0: 0.09. It is noted that the concentration of I is less than the normal value. The possible reason is that long-time EDS mapping may induce the loss of I element. Combined whit FTIR and NMR results, I proved the presence of C_{44}-PC as ligand on the surface of $FASnI_3$ NCs

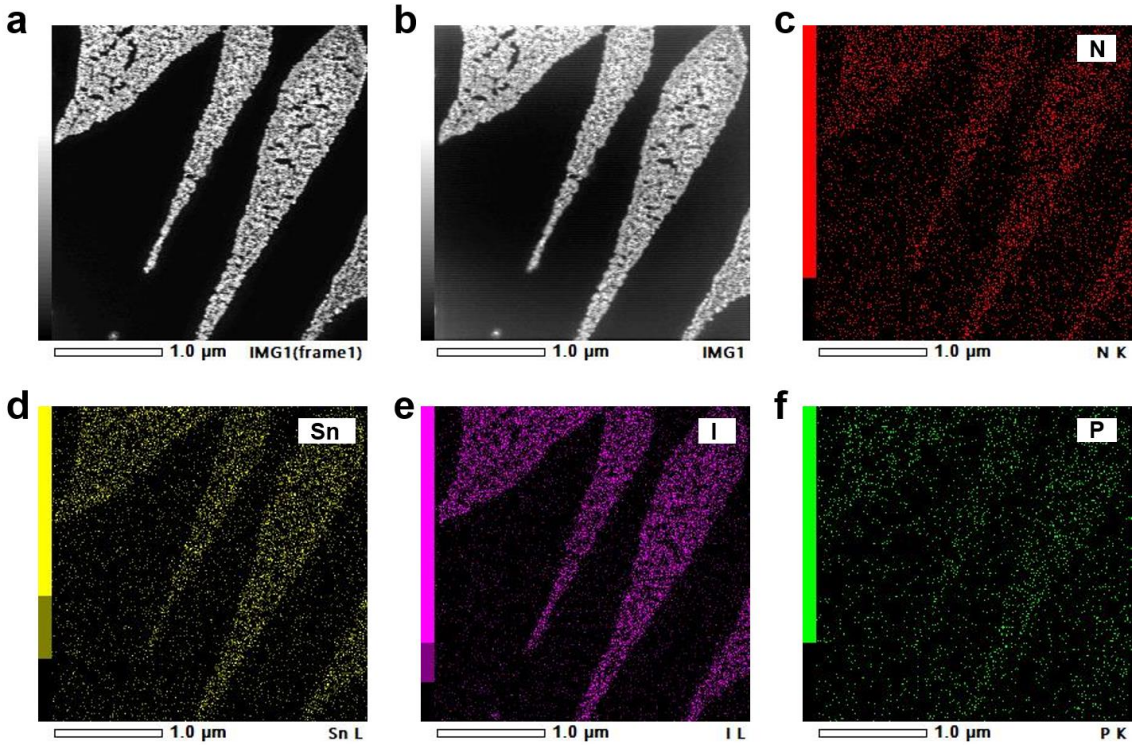

Figure 3.10. (a) HAADF-STEM image of $FASnI_3$ NCs before EDS mapping. (b) HAADF-STEM image of $FASnI_3$ NCs after EDS mapping. (c-f) STEM-EDS element mapping of N, Sn, I, and P.

Finally, I studied the photophysical properties of C_{44}-PC capped $FASnI_3$ NCs

synthesized under different reaction temperature. I changed the temperature from 25 ºC to 150 ºC. From the XRD patterns shown in **Figure 3.11a**, we can see that $FASnI_3$ NCs can be synthesized within the whole temperature range, without any other crystalline phase. However, at lower temperatures, especially for 25 ºC and 60 ºC, instead of (100) and (200) diffraction peaks, other peaks are too weak, indicating the oriented growth of $FASnI_3$ NCs along with (100) and (200) lattice planes. TEM images of as-prepared $FASnI_3$ NCs are shown in **Figure 3.11b-e**. At 25 ºC, some amorphous impurities can be found in the TEM image (**Figure 3.11b**), which is also reflected in the XRD pattern around 20 degree. These amorphous impurities may originate from the unreacted raw precursors since the low formation potential of $FASnI_3$ NCs at low temperature. Above 60 ºC, I can get near-cubic $FASnI_3$ NCs. But at 90 ºC, the as-synthesized $FASnI_3$ NCs have a poorer stability under electron beam (**Figure 3.11d**). The average particle sizes are 30.7 nm, 27.4 nm, 32.3 nm, and 33.0 nm for 25 ºC, 60 ºC, 90 ºC, and 150 ºC, respectively. I note that the particle size doesn't monotonously depend on the reaction temperature. With increasing the temperature, although the growth rate of NC is faster, the nucleation rate is also enhanced, resulting in more nucleus. Fast growth induces larger particle size, but more nucleus instead leads to more products and less size. These two effects can explain our temperature-depended particle size.

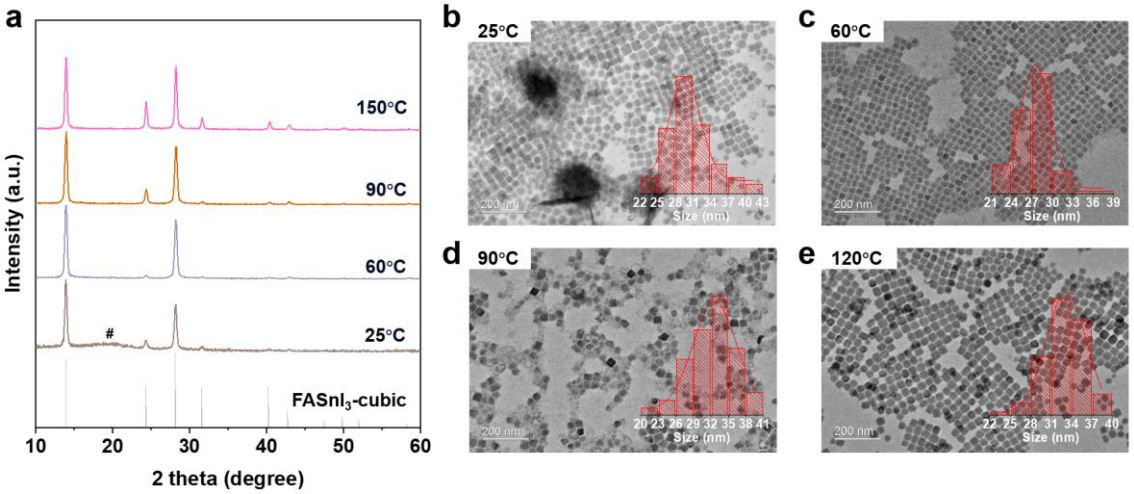

Figure 3.11. (a) Powder XRD patterns of $FASnI_3$ NCs synthesized at different temperatures. # reflects the diffraction peak from amorphous impurities. (b) TEM image and corresponding size-distribution histograms of $FASnI_3$ NCs synthesized with different amount of C_{44}-PC.

Figure 3.12 exhibits the optical properties of $FASnI_3$ NCs synthesized under different reaction temperature. Specially, the sample synthesized at 25 ºC show obvious blue-shift in absorption and PL spectra. This blue-shift doesn't result from the size-effect, because the size of sample synthesized at 25 ºC is larger than those at 25 ºC and 120 ºC (**Figure 3.3d, 3.11b, c**), and the exciton Bohr radius of $FASnI_3$ is only 3.5-4.4 nm.[31] Only when the particle size is close to the exciton Bohr radius of the crystals can the bandgap widening be observed. **Table 3.2** summarizes the average particle sizes, PL peaks, and PLQYs of all samples as-prepared here. We can find that the PL peaks of all samples do not rely on the NC size. At 25 ºC, the PL peak shifts to 845 nm, which may result from poor crystal quality and abundant structural defects in the lattice. **Figure 3.12c** is the PLQY measurements of $FASnI_3$ NCs synthesized under different reaction temperature, and the PLQYs are 0.7%, 0.8%, 1.0%, 0.9% for 25 ºC, 60 ºC, 90 ºC, 150 ºC, respectively. It is noted that 25 ºC sample has lowest PLQY, showing more defect states in this sample. Here, I stress that my synthesis route is temperature-independent. Evern at room temperature, I also can get luminescent colloidal $FASnI_3$ NCs, which is significant for the large-scale production.

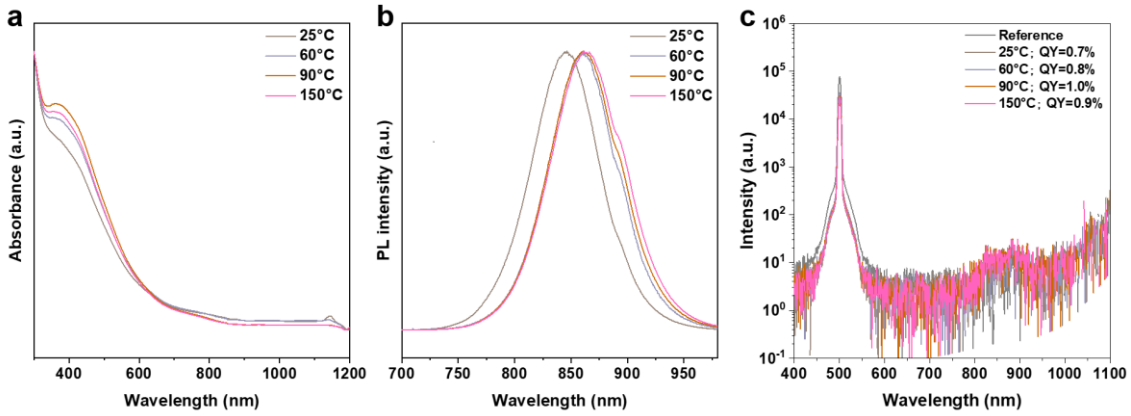

Figure 3.12. (a) Normalized absorption spectra of $FASnI_3$ NCs synthesized at different temperatures. (b) Normalized PL spectra of $FASnI_3$ NCs synthesized at different temperatures. (c) PLQY measurements of $FASnI_3$ NCs synthesized at different temperatures.

Table 3.3. Average particle sizes, PL peaks, and PLQYs of all samples prepared here.

Sample	Average particle size	PL peak	PLQY
C_{44}-PC-3 mg	32.2 nm	868 nm	0.7 %
C_{44}-PC-6 mg	30.7 nm	868 nm	0.8 %
C_{44}-PC-9 mg	29.4 nm	868 nm	1.2 %
C_{44}-PC-12 mg	30.3 nm	868 nm	1.1 %
C_{32}-PC	29.2 nm	862 nm	0.9 %
C_{52}-PC	30.3 nm	866 nm	1.0 %
25 ºC	30.7 nm	845 nm	0.7 %
60 ºC	27.4 nm	860 nm	0.8 %
90 ºC	32.3 nm	861 nm	1.0 %
120 ºC	33.0 nm	863 nm	0.9 %

3.4 Conclusion

In summary, I demonstrated a low-cost, amine-free synthesis approach for colloidal $FASnI_3$ perovskite NCs using zwitterionic phosphatidylcholine as surface capping ligand. The maximum PLQY of the yielded $FASnI_3$ NCs is 1.2%, larger than ever reported results. Different with typical amine ligand, phosphatidylcholine has one cation and one anion group, showing tightly binding with $FASnI_3$ surface without large quantities of excessive capping ligands. Even introducing a small amount of phosphatidylcholine can we get uniform-size and monodispersed $FASnI_3$ NCs. Under Ar atmosphere, phosphatidylcholine capped $FASnI_3$ NCs exhibit excellent colloidal and structural stability, which will serve as an ideal platform for further optoelectronic application of these NCs. At room temperature, my synthesis route also can produce colloidal $FASnI_3$ NC, indicating their great commercialized large-scale production. I envisage that my work here could inspire more research on high-quality tin-based perovskite NCs and speed up their use in high-performance optoelectronic devices such as solar cells, LEDs, lasers, and beyond.

Reference:

1. Sutherland, B. R.; Sargent, E. H. Perovskite photonic sources. *Nature Photonics* **2016,** *10*, 295-302.

2. Shamsi, J.; Urban, A. S.; Imran, M.; De Trizio, L.; Manna, L. Metal Halide Perovskite Nanocrystals: Synthesis, Post-Synthesis Modifications, and Their Optical Properties. *Chemical Reviews* **2019,** *119*, 3296-3348.

3. Kovalenko, M. V.; Protesescu, L.; Bodnarchuk, M. I. Properties and potential optoelectronic applications of lead halide perovskite nanocrystals. *Science* **2017,** *358*, 745-750.

4. Green, M. A.; Ho-Baillie, A.; Snaith, H. J. The emergence of perovskite solar cells. *Nature Photonics* **2014,** *8*, 506-514.

5. Shi, D.; Adinolfi, V.; Comin, R.; Yuan, M.; Alarousu, E.; Buin, A.; Chen, Y.; Hoogland, S.; Rothenberger, A.; Katsiev, K.; Losovyj, Y.; Zhang, X.; Dowben, P. A.; Mohammed, O. F.; Sargent, E. H.; Bakr, O. M. Low trap-state density and long carrier diffusion in organolead trihalide perovskite single crystals. *Science* **2015,** *347*, 519-522.

6. Lee, M. M.; Teuscher, J.; Miyasaka, T.; Murakami, T. N.; Snaith, H. J. Efficient Hybrid Solar Cells Based on Meso-Superstructured Organometal Halide Perovskites. *Science* **2012,** *338*, 643-647.

7. Jeon, N. J.; Lee, J.; Noh, J. H.; Nazeeruddin, M. K.; Grätzel, M.; Seok, S. I. Efficient Inorganic–Organic Hybrid Perovskite Solar Cells Based on Pyrene Arylamine Derivatives as Hole-Transporting Materials. *Journal of the American Chemical Society* **2013,** *135*, 19087-19090.

8. Saidaminov, M. I.; Adinolfi, V.; Comin, R.; Abdelhady, A. L.; Peng, W.; Dursun, I.; Yuan, M.; Hoogland, S.; Sargent, E. H.; Bakr, O. M. Planar-integrated single-crystalline perovskite photodetectors. *Nature Communications* **2015,** *6*, 8724.

9. Tan, Z.-K.; Moghaddam, R. S.; Lai, M. L.; Docampo, P.; Higler, R.; Deschler, F.; Price, M.; Sadhanala, A.; Pazos, L. M.; Credgington, D.; Hanusch, F.; Bein, T.; Snaith, H. J.; Friend, R. H. Bright light-emitting diodes based on organometal halide perovskite.

Nature Nanotechnology **2014,** *9*, 687-692.

10. Yuan, M.; Quan, L. N.; Comin, R.; Walters, G.; Sabatini, R.; Voznyy, O.; Hoogland, S.; Zhao, Y.; Beauregard, E. M.; Kanjanaboos, P.; Lu, Z.; Kim, D. H.; Sargent, E. H. Perovskite energy funnels for efficient light-emitting diodes. *Nature Nanotechnology* **2016,** *11*, 872-877.

11. Wang, N.; Cheng, L.; Ge, R.; Zhang, S.; Miao, Y.; Zou, W.; Yi, C.; Sun, Y.; Cao, Y.; Yang, R.; Wei, Y.; Guo, Q.; Ke, Y.; Yu, M.; Jin, Y.; Liu, Y.; Ding, Q.; Di, D.; Yang, L.; Xing, G.; Tian, H.; Jin, C.; Gao, F.; Friend, R. H.; Wang, J.; Huang, W. Perovskite light-emitting diodes based on solution-processed self-organized multiple quantum wells. *Nature Photonics* **2016,** *10*, 699-704.

12. Akkerman, Q. A.; Rainò, G.; Kovalenko, M. V.; Manna, L. Genesis, challenges and opportunities for colloidal lead halide perovskite nanocrystals. *Nature Materials* **2018,** *17*, 394-405.

13. Ghosh, S.; Manna, L. The Many "Facets" of Halide Ions in the Chemistry of Colloidal Inorganic Nanocrystals. *Chemical Reviews* **2018,** *118*, 7804-7864.

14. Infante, I.; Manna, L. Are There Good Alternatives to Lead Halide Perovskite Nanocrystals? *Nano Letters* **2021,** *21*, 6-9.

15. Fan, Q.; Biesold-McGee, G. V.; Ma, J.; Xu, Q.; Pan, S.; Peng, J.; Lin, Z. Lead-Free Halide Perovskite Nanocrystals: Crystal Structures, Synthesis, Stabilities, and Optical Properties. *Angewandte Chemie International Edition* **2020,** *59*, 1030-1046.

16. Chen, J.-K.; Zhang, B.-B.; Liu, Q.; Shirahata, N.; Mohammed, O. F.; Bakr, O. M.; Sun, H.-T. Advances and Challenges in Tin Halide Perovskite Nanocrystals. *ACS Materials Letters* **2021,** *3*, 1541-1557.

17. van der Stam, W.; Geuchies, J. J.; Altantzis, T.; van den Bos, K. H. W.; Meeldijk, J. D.; Van Aert, S.; Bals, S.; Vanmaekelbergh, D.; de Mello Donega, C. Highly Emissive Divalent-Ion-Doped Colloidal CsPb1–xMxBr3 Perovskite Nanocrystals through Cation Exchange. *Journal of the American Chemical Society* **2017,** *139*, 4087-4097.

18. Li, J.; Cao, H.-L.; Jiao, W.-B.; Wang, Q.; Wei, M.; Cantone, I.; Lü, J.; Abate, A.

Biological impact of lead from halide perovskites reveals the risk of introducing a safe threshold. *Nature Communications* **2020,** *11*, 310.

19. Marshall, K. P.; Walker, M.; Walton, R. I.; Hatton, R. A. Enhanced stability and efficiency in hole-transport-layer-free CsSnI3 perovskite photovoltaics. *Nature Energy* **2016,** *1*, 16178.

20. Song, T.-B.; Yokoyama, T.; Aramaki, S.; Kanatzidis, M. G. Performance Enhancement of Lead-Free Tin-Based Perovskite Solar Cells with Reducing Atmosphere-Assisted Dispersible Additive. *ACS Energy Letters* **2017,** *2*, 897-903.

21. Liang, H.; Yuan, F.; Johnston, A.; Gao, C.; Choubisa, H.; Gao, Y.; Wang, Y.-K.; Sagar, L. K.; Sun, B.; Li, P.; Bappi, G.; Chen, B.; Li, J.; Wang, Y.; Dong, Y.; Ma, D.; Gao, Y.; Liu, Y.; Yuan, M.; Saidaminov, M. I.; Hoogland, S.; Lu, Z.-H.; Sargent, E. H. High Color Purity Lead-Free Perovskite Light-Emitting Diodes via Sn Stabilization. *Advanced Science* **2020,** *7*, 1903213.

22. Hong, W.-L.; Huang, Y.-C.; Chang, C.-Y.; Zhang, Z.-C.; Tsai, H.-R.; Chang, N.-Y.; Chao, Y.-C. Efficient Low-Temperature Solution-Processed Lead-Free Perovskite Infrared Light-Emitting Diodes. *Advanced Materials* **2016,** *28*, 8029-8036.

23. Vegiraju, S.; Ke, W.; Priyanka, P.; Ni, J.-S.; Wu, Y.-C.; Spanopoulos, I.; Yau, S. L.; Marks, T. J.; Chen, M.-C.; Kanatzidis, M. G. Benzodithiophene Hole-Transporting Materials for Efficient Tin-Based Perovskite Solar Cells. *Advanced Functional Materials* **2019,** *29*, 1905393.

24. Nakamura, T.; Yakumaru, S.; Truong, M. A.; Kim, K.; Liu, J.; Hu, S.; Otsuka, K.; Hashimoto, R.; Murdey, R.; Sasamori, T.; Kim, H. D.; Ohkita, H.; Handa, T.; Kanemitsu, Y.; Wakamiya, A. Sn(IV)-free tin perovskite films realized by in situ Sn(0) nanoparticle treatment of the precursor solution. *Nature Communications* **2020,** *11*, 3008.

25. Ye, T.; Wang, X.; Wang, K.; Ma, S.; Yang, D.; Hou, Y.; Yoon, J.; Wang, K.; Priya, S. Localized Electron Density Engineering for Stabilized B-γ CsSnI3-Based Perovskite Solar Cells with Efficiencies >10%. *ACS Energy Letters* **2021,** *6*, 1480-1489.

26. Tai, Q.; Cao, J.; Wang, T.; Yan, F. Recent advances toward efficient and stable

tin-based perovskite solar cells. *EcoMat* **2019,** *1*, e12004.

27. Cui, D.; Liu, X.; Wu, T.; Lin, X.; Luo, X.; Wu, Y.; Segawa, H.; Yang, X.; Zhang, Y.; Wang, Y.; Han, L. Making Room for Growing Oriented FASnI3 with Large Grains via Cold Precursor Solution. *Advanced Functional Materials* **2021,** *31*, 2100931.

28. Han, D.; Wang, J.; Agosta, L.; Zang, Z.; Zhao, B.; Kong, L.; Lu, H.; Mosquera-Lois, I.; Carnevali, V.; Dong, J.; Zhou, J.; Ji, H.; Pfeifer, L.; Zakeeruddin, S. M.; Yang, Y.; Wu, B.; Rothlisberger, U.; Yang, X.; Grätzel, M.; Wang, N. Tautomeric mixture coordination enables efficient lead-free perovskite LEDs. *Nature* **2023,** *622*, 493-498.

29.Jiang, X.; Li, H.; Zhou, Q.; Wei, Q.; Wei, M.; Jiang, L.; Wang, Z.; Peng, Z.; Wang, F.; Zang, Z.; Xu, K.; Hou, Y.; Teale, S.; Zhou, W.; Si, R.; Gao, X.; Sargent, E. H.; Ning, Z. One-Step Synthesis of SnI2·(DMSO)x Adducts for High-Performance Tin Perovskite Solar Cells. *Journal of the American Chemical Society* **2021,** *143*, 10970-10976.

30. Dai, L.; Deng, Z.; Auras, F.; Goodwin, H.; Zhang, Z.; Walmsley, J. C.; Bristowe, P. D.; Deschler, F.; Greenham, N. C. Slow carrier relaxation in tin-based perovskite nanocrystals. *Nature Photonics* **2021,** *15*, 696-702.

31. Dirin, D. N.; Vivani, A.; Zacharias, M.; Sekh, T. V.; Cherniukh, I.; Yakunin, S.; Bertolotti, F.; Aebli, M.; Schaller, R. D.; Wieczorek, A.; Siol, S.; Cancellieri, C.; Jeurgens, L. P. H.; Masciocchi, N.; Guagliardi, A.; Pedesseau, L.; Even, J.; Kovalenko, M. V.; Bodnarchuk, M. I. Intrinsic Formamidinium Tin Iodide Nanocrystals by Suppressing the Sn(IV) Impurities. *Nano Letters* **2023,** *23*, 1914-1923.

32. Chen, Z.; Dhakal, T. P. Room temperature synthesis of lead-free FASnI3 perovskite nanocrystals with improved stability by SnF2 additive. *Applied Physics Reviews* **2023,** *10*.

33. De Trizio, L.; Infante, I.; Manna, L. Surface Chemistry of Lead Halide Perovskite Colloidal Nanocrystals. *Accounts of Chemical Research* **2023,** *56*, 1815-1825.

34. Li, H.; Dong, W.; Shen, X.; Ge, C.; Song, Y.; Wang, Z.; Wang, A.; Yang, Z.; Hao, M.; Zhang, Y.; Zheng, W.; Zhang, X.; Dong, Q. Enhancing the Efficiency and Stability of CsPbI3 Nanocrystal-Based Light-Emitting Diodes through Ligand Engineering with

Octylamine. *The Journal of Physical Chemistry C* **2022,** *126*, 1085-1093.

35. Sun, W.; Yun, R.; Liu, Y.; Zhang, X.; Yuan, M.; Zhang, L.; Li, X. Ligands in Lead Halide Perovskite Nanocrystals: From Synthesis to Optoelectronic Applications. *Small* **2023,** *19*, 2205950.

36. Li, Y.; Wang, D.; Yang, Y.; Ding, C.; Hu, Y.; Liu, F.; Wei, Y.; Liu, D.; Li, H.; Shi, G.; Chen, S.; Li, H.; Fuchimoto, A.; Tosa, K.; Hiroki, U.; Hayase, S.; Wei, H.; Shen, Q. Stable Inorganic Colloidal Tin and Tin–Lead Perovskite Nanocrystals with Ultralong Carrier Lifetime via Sn(IV) Control. *Journal of the American Chemical Society* **2024,** *146*, 3094-3101.

37. Gahlot, K.; de Graaf, S.; Duim, H.; Nedelcu, G.; Koushki, R. M.; Ahmadi, M.; Gavhane, D.; Lasorsa, A.; De Luca, O.; Rudolf, P.; van der Wel, P. C. A.; Loi, M. A.; Kooi, B. J.; Portale, G.; Calbo, J.; Protesescu, L. Structural Dynamics and Tunability for Colloidal Tin Halide Perovskite Nanostructures. *Advanced Materials* **2022,** *34*, 2201353.

38. Krieg, F.; Ochsenbein, S. T.; Yakunin, S.; ten Brinck, S.; Aellen, P.; Süess, A.; Clerc, B.; Guggisberg, D.; Nazarenko, O.; Shynkarenko, Y.; Kumar, S.; Shih, C.-J.; Infante, I.; Kovalenko, M. V. Colloidal CsPbX3 (X = Cl, Br, I) Nanocrystals 2.0: Zwitterionic Capping Ligands for Improved Durability and Stability. *ACS Energy Letters* **2018,** *3*, 641-646.

39. Morad, V.; Stelmakh, A.; Svyrydenko, M.; Feld, L. G.; Boehme, S. C.; Aebli, M.; Affolter, J.; Kaul, C. J.; Schrenker, N. J.; Bals, S.; Sahin, Y.; Dirin, D. N.; Cherniukh, I.; Raino, G.; Baumketner, A.; Kovalenko, M. V. Designer phospholipid capping ligands for soft metal halide nanocrystals. *Nature* **2024,** *626*, 542-548.

40. Krieg, F.; Ong, Q. K.; Burian, M.; Rainò, G.; Naumenko, D.; Amenitsch, H.; Süess, A.; Grotevent, M. J.; Krumeich, F.; Bodnarchuk, M. I.; Shorubalko, I.; Stellacci, F.; Kovalenko, M. V. Stable Ultraconcentrated and Ultradilute Colloids of CsPbX3 (X = Cl, Br) Nanocrystals Using Natural Lecithin as a Capping Ligand. *Journal of the American Chemical Society* **2019,** *141*, 19839-19849.

41. Krieg, F.; Sercel, P. C.; Burian, M.; Andrusiv, H.; Bodnarchuk, M. I.; Stöferle,

T.; Mahrt, R. F.; Naumenko, D.; Amenitsch, H.; Rainò, G.; Kovalenko, M. V. Monodisperse Long-Chain Sulfobetaine-Capped CsPbBr3 Nanocrystals and Their Superfluorescent Assemblies. *ACS Central Science* **2021,** *7*, 135-144.

42.Milanese, S.; Morello, G.; De Giorgi, M. L.; Cretì, A.; Andrusiv, H.; Bodnarchuk, M. I.; Qualtieri, A.; Lomascolo, M.; Kovalenko, M. V.; Anni, M. Air-sensitive amplified spontaneous emission in lecithin-capped CsPbBr3 nanocrystals thin films. *Materials Today Physics* **2023,** *35*, 101098.

43. Wang, L.-M.; Chen, J.-K.; Zhang, B.-B.; Liu, Q.; Zhou, Y.; Shu, J.; Wang, Z.; Shirahata, N.; Song, B.; Mohammed, O. F.; Bakr, O. M.; Sun, H.-T. Phosphatidylcholine-mediated regulation of growth kinetics for colloidal synthesis of cesium tin halide nanocrystals. *Nanoscale* **2021,** *13*, 16726-16733.

44. Kalikmanov, V. I., Classical Nucleation Theory. In *Nucleation Theory*, Kalikmanov, V. I., Ed. Springer Netherlands: Dordrecht, 2013; pp 17-41.

45. Jung, M.; Ji, S.-G.; Kim, G.; Seok, S. I. Perovskite precursor solution chemistry: from fundamentals to photovoltaic applications. *Chemical Society Reviews* **2019,** *48*, 2011-2038.

46. Baldan, A. Review Progress in Ostwald ripening theories and their applications to nickel-base superalloys Part I: Ostwald ripening theories. *Journal of Materials Science* **2002,** *37*, 2171-2202.

47. Tauc, J.; Grigorovici, R.; Vancu, A. Optical Properties and Electronic Structure of Amorphous Germanium. *physica status solidi (b)* **1966,** *15*, 627-637.

48. Chiba, T.; Hayashi, Y.; Ebe, H.; Hoshi, K.; Sato, J.; Sato, S.; Pu, Y.-J.; Ohisa, S.; Kido, J. Anion-exchange red perovskite quantum dots with ammonium iodine salts for highly efficient light-emitting devices. *Nature Photonics* **2018,** *12*, 681-687.

49. Pan, J.; Quan, L. N.; Zhao, Y.; Peng, W.; Murali, B.; Sarmah, S. P.; Yuan, M.; Sinatra, L.; Alyami, N. M.; Liu, J.; Yassitepe, E.; Yang, Z.; Voznyy, O.; Comin, R.; Hedhili, M. N.; Mohammed, O. F.; Lu, Z. H.; Kim, D. H.; Sargent, E. H.; Bakr, O. M. Highly Efficient Perovskite-Quantum-Dot Light-Emitting Diodes by Surface Engineering.

Advanced Materials **2016,** *28*, 8718-8725.

50. Hao, M.; Bai, Y.; Zeiske, S.; Ren, L.; Liu, J.; Yuan, Y.; Zarrabi, N.; Cheng, N.; Ghasemi, M.; Chen, P.; Lyu, M.; He, D.; Yun, J.-H.; Du, Y.; Wang, Y.; Ding, S.; Armin, A.; Meredith, P.; Liu, G.; Cheng, H.-M.; Wang, L. Ligand-assisted cation-exchange engineering for high-efficiency colloidal Cs1−xFAxPbI3 quantum dot solar cells with reduced phase segregation. *Nature Energy* **2020,** *5*, 79-88.

51. Liu, Q.; Yin, J.; Zhang, B.-B.; Chen, J.-K.; Zhou, Y.; Zhang, L.-M.; Wang, L.-M.; Zhao, Q.; Hou, J.; Shu, J.; Song, B.; Shirahata, N.; Bakr, O. M.; Mohammed, O. F.; Sun, H.-T. Theory-Guided Synthesis of Highly Luminescent Colloidal Cesium Tin Halide Perovskite Nanocrystals. *Journal of the American Chemical Society* **2021,** *143*, 5470-5480.

52. Pan, J.; Shang, Y.; Yin, J.; De Bastiani, M.; Peng, W.; Dursun, I.; Sinatra, L.; El-Zohry, A. M.; Hedhili, M. N.; Emwas, A.-H.; Mohammed, O. F.; Ning, Z.; Bakr, O. M. Bidentate Ligand-Passivated CsPbI3 Perovskite Nanocrystals for Stable Near-Unity Photoluminescence Quantum Yield and Efficient Red Light-Emitting Diodes. *Journal of the American Chemical Society* **2018,** *140*, 562-565.

Chapter 4: Regulating Surface Termination for Highly Luminescent Organic-inorganic Hybrid Tin Iodide Perovskite Nanocrystals

4.1 Introduction

In a decade, metal halide perovskites have paved their way aside from photovoltaics toward may eminently different applications, such as light-emitting diodes (LEDs),[1-3] photodetectors,[4-6] and lasers,[7, 8] because of outstanding optoelectronic properties, including low density of carrier trap states (10^9−10^{10} cm^{-3}),[9, 10] long electron−hole diffusion lengths (2−175 μm),[9, 11] high carrier mobilities (2.5−1000 cm^2 V^{-1} s^{-1}), long charge carrier lifetimes (0.08−450 μs),[9, 12] and high optical absorption coefficients at the absorption edge (2−7 × 10^4 cm^{-1}).[12] However, the present efficient perovskite optoelectronic devices are all based on lead-containing perovskites, which has become one of the most notable impediments on their way toward commercialization owing to the regulations on the use of lead in electrical and electronic equipment.[13-15] Recent years, chemists, material scientists, and engineers are devoting to developing lead-free perovskites and related optoelectronic devices.[16-19] The most ideal element replacing lead (Pb) is tin (Sn) since its similarity in ionic radius and valence electronic configuration with Pb.[20] Until now, the performance of Sn-based perovskite optoelectronic devices is gradually narrowing the gap with that of their lead counterpart.[21-23] For examples, the external quantum efficiency of red LEDs based on tin-halide perovskite has exceeded 20%,[24] and the powder conversion efficiency of tin halide perovskite-based solar cells has reached over 14%.[25] Within them, organic−inorganic hybrid tin-halide perovskites, especially formamidinium (FA) tin triiodide ($FASnI_3$), showing excellent potential in photovoltaics.[25-28]

Despite steady research progress in $FASnI_3$ polycrystalline films, $FASnI_3$ nanocrystals (NCs) are still in the preliminary stage of research development. Different with polycrystalline films, colloidal NCs have controlled particle size, and possible higher

photoluminescence quantum yield (PLQY), making them available for high-efficient LEDs, biological imaging, single photon source, and so on.[29-34] The first reported synthesis of $FASnI_3$ NCs dated back to 2021. Dai et al. provided a solvothermal method for getting size-tunable (7.3-12.1 nm) $FASnI_3$ NCs, and they found size-dependent carrier relaxation.[35] Small-size $FASnI_3$ NCs have slow carrier relaxation, which can alleviate the energy loss of hot carrier via phonon emission, leading to a higher theoretical solar conversion efficiency up to 66%.[36] Dirin et al. developed hot-injection method to get $FASnI_3$ NCs in 2023, and they found that 10 nm $FASnI_3$ NCs exhibit an unusually large band gap, which could be explained by the distortion of the lattice through the split of I-sites.[37] Notably, the present reported synthesis strategy cannot provide high-quality $FASnI_3$ NCs with satisfactory optical properties. The PLQYs of pure $FASnI_3$ NCs are all below to 0.3%. Even after doping some bifunctional organic cations, such as ethylenediammonium, the PLQY is still below 1%.[37]

Different with lead halide perovskites, tin halide perovskites have low defect-tolerance. Some studies have confirmed that Sn vacancies is the main defect that can introduce deep transition level, inducing the nonradiative recombination.[38, 39] In Chapter 2, I also found that Sn-related defects can influence the crystal quality of $FASnI_3$. To suppress the formation of Sn vacancies, creating a Sn-rich reaction condition is necessary, which have been confirmed by Liu et al,[38] and my work in Chapter 2 also show the possibility of this precursor strategy in improving the quality of $FASnI_3$. Although a tin-rich reaction condition can suppress some intrinsic structural defects in $FASnI_3$, NC surface condition cannot be modified. This is why in Chapter 3, the PLQY of my $FASnI_3$ NC is only 1.2% even under Sn-rich reaction environment. When the size of $FASnI_3$ is down to nanometer level, larger specific surface area of NCs make the surface condition become crucial.

The traditional wisdom about modifying NC surface is ligand strategy, including choosing appropriate organic or inorganic ligands.[40, 41] Instead of widely used oleylamine and oleic acid, zwitterionic ligands are used as another alternative for getting stable

colloidal perovskite NCs.[42, 43] Bidentate ligand, 2,2′-iminodibenzoic acid has higher surface binding energy compared with carboxylic ligands, which resulting in near-unity PLQY of $CsPbI_3$ NCs and efficient red LEDs.[44] Some inorganic ions, such as alkaline-earth metals (Ca^{2+}, Sr^{2+}) have been proposed to be able to substitute surface Pb^{2+} in $CsPbCl_3$ NCs, creating a Ca^{2+}/Sr^{2+} involved passivation layer, which results in the increase in PLQY from 0.8% to 77.1%.[45] Inspired by the previous studies, I hypothesized that, for $FASnI_3$ NCs, based on tin-rich reaction condition, if I find one or two appropriate ligands to passivate the surface defects, I may get highly luminescent $FASnI_3$ NCs.

Here, we start with detailed theoretical calculations of $FASnI_3$, in terms of the formation energy and thermodynamical charge-transition levels of typical point defects. The lowest formation energy of tin vacancies (V_{Sn}) shows that V_{Sn} is the main intrinsic structural defects, and tin-rich reaction condition is necessary. Further calculations on the surface state of $FASnI_3$ NCs inspire us to establish a quasi-AI-terminated surface, which has more stable surface condition. Guided by the calculations, I then provide a synthetic concept for highly luminescent colloidal $FASnI_3$ NCs, involving the organic cation, 2-thiopheneethylammonium (TEA^+), and inorganic cation, sodium (Na^+), surface passivation. The PLQY of near-infrared-emitting $FASnI_3$ NCs can be boosted to 36.9± 0.7%, which is much higher than that synthesized without TEA^+ and Na^+. Detailed experimental analyses by X-ray photoelectron spectra, inductively coupled plasma optical emission spectrometry, energy-dispersive X-ray spectroscopy, electrospray ionization mass spectrometry (ESI-MS), and ζ-potential, lead me to conclude that TEA^+ and Na^+ are present on the surface of $FASnI_3$ NCs, and resulting in possible TEAI and NaI-terminated surface, which is consistent with our theoretical calculations. Importantly, I demonstrate that this concept is sufficiently general and can be used for FA/Cs alloying tin halide perovskite NCs. My work thus paves the way for the design and synthesis of high-quality organic-inorganic hybrid tin halide perovskite NCs for optoelectronic applications.

4.2 Experimental section

4.2.1 Chemicals

Formamidine acetate (FA-acetate, Sigma, 99%), tin 2-ethylhexanoate ($Sn(Oct)_2$, Sigma, 92.5-100.0%), tin(II) iodide (SnI_2, Sigma, 99.99% trace metals basis), tin(II) iodide (SnI_2, Strem, 99%), 1-octadecene (ODE, Sigma, 95%), 1-octadecene (ODE, Kanto, >90%), oleic acid (OA, Sigma, 90%), tri-n-octylphosphine (TOP, Thermo, 90%), 1,2-Dioleoyl-sn-glycero-3-phosphocholine (C_{44}-PC, TCI, >97%), 2-phenylethylamine hydroiodide (PEAI, TCI, >98%), 2-thiopheneethylammonium iodide (TEAI, Greatcell Solar Materials, >99%), 2-thiophenemethylammonium iodide (TMAI, Greatcell Solar Materials), potassium 2-ethylhexanoate (KOct, TCI, >95%), sodium 2-ethylhexanoate (NaOct, TCI, >98%), sodium oleate (Na-oleate, Sigma, ≥99%), rubidium carbonate (Rb_2CO_3, Alfa, 99%), cesium carbonate (Cs_2CO_3, Sigma, 99.995% trace metals basis), n-hexane (Sigma, ≥99%), methanol (Wako, Guaranteed Reagent) were used without purification unless otherwise noted.

Table 4.1. List of the manufacturer, batch number, and purity from certificate of analysis (COA) of all used chemicals for synthesis.

Chemical	Manufacturer	Batch number	Purity from COA
FA-acetate	Sigma-Aldrich	BCBZ7461	100%
$Sn(Oct)_2$	Sigma-Aldrich	SLCM1306	96.9%
SnI_2	Sigma-Aldrich	0000303819	99.99%
SnI_2	Strem	L02142201	99%
ODE	Sigma-Aldrich	BCCH1566	98.9%
ODE	Kanto	409Y2186	95.5%
OA	Sigma-Aldrich	MKCR9052	94.9%
TOP	ThermoFisher	L15744	99.99%
C_{44}-PC	TCI	TJLAN	99.8%

TEAI	Greatcellsolar Materials	226451	>99.8%
TMAI	Greatcellsolar Materials	323942	>99.8%
PEAI	TCI	UY6HI	99.3%
Cs_2CO_3	Sigma-Aldrich	0000087555	99.6%
KOct	TCI	2YJLJ	99.6%
NaOct	TCI	OQ7AC	98.4%
Rb_2CO_3	Alfa Aesar	N14F029	99.28%
Na-oleate	Sigma-Aldrich	SLCM3152	99%
n-hexane	Sigma-Aldrich	STBL2142	99.3%
Toluene	FUJIFILM Wako	KSP2915	99.9%

4.2.2 Experiments

Preparation of FA-oleate solution. 0.2603 g FA-acetate was mixed with 10 mL 1-octadecene (ODE, Sigma) and 3.39 mL oleic acid in 100 mL three-necked flask in an argon-filled glovebox. The mixture was then degassed for half hour at 80 ºC, then heated under nitrogen to 120 ºC for half hour, yielding a clear FA-oleate solution. After that, the as-prepared FA-oleate was cooled to room temperature, and transferred to glovebox for the further use.

Preparation of Cs-oleate solution. 0.4073 g Cs_2CO_3 was mixed with 10 mL 1-octadecene (ODE, Sigma) and 3.39 mL oleic acid in 100 mL three-necked flask in an argon-filled glovebox. The mixture was then degassed for half hour at 80 ºC, then heated under nitrogen to 120 ºC for half hour, yielding a clear Cs-oleate solution. After that, the as-prepared Cs-oleate was cooled to room temperature, and transferred to glovebox for the further use. Before using, Cs-oleate was pre-heated at 120 ºC on a hot plate.

Preparation of Rb-oleate powder. 0.4619 g Rb_2CO_3 was mixed with 10 mL 1-octadecene (ODE, Sigma) and 2 mL oleic acid in 100 ml three-necked flask in an argon-filled glovebox. The mixture was then degassed for one hour at 120 ºC, then heated under nitrogen to 150 ºC for 15 min, and then heated to 180 ºC for 45 min, yielding a clear Rb-oleate solution. The as-prepared Rb-oleate solution was centrifugated at 12000 r.p.m. for 10 min to remove the supernatant solution. The precipitate was redispersed in 4 mL hexane and then centrifuged at 12000 r.p.m. for 5 min to get Rb-oleate powder. This process was repeated twice. The final powder was dried under vacuum for half hour, and then was transferred to glovebox for the further use.

Preparation of the SnI_2-TOP stock solution. The mixture of 0.1105 g SnI_2 (Sigma), 0.18 ml $Sn(Oct)_2$, PEAI/TEAI/TMAI, and 0.3 ml TOP was vigorously stirred in a 7 mL vial at 120 ºC on a hot plate for 20 min, yielding a yellow stock solution. For control NCs, PEAI/TEAI/TMAI was not added in the solution. For PEA-0.25, TMA-0.25 NCs, the amount of PEAI and TMAI are 0.0085 g and 0.0081 g, respectively. For the samples that TEA: FA is 0.05, 0.15, 0.25, and 0.3, the mounts of TEAI are 0.0017g, 0.0052 g, 0.0087 g, and 0.0104 g, respectively. For sample that TEA: FA=0.35, the mount of TEAI is 0.0121 g, but yielding insoluble precursor. For the samples that Sn: I=1.2: 1 and 1: 1, the amount of $Sn(Oct)_2$ are 0.135 mL and 0.090 mL, respectively. Then, the solution was cooled to room temperature. All processes were conducted in an Ar-filled glovebox. To study the influence the reagent from different manufacturer, SnI_2 (Sigma) was changed to SnI_2 (Strem).

Preparation of the C_{44}-PC stock solution. 1,2-Dioleoyl-sn-glycero-3-phosphocholine (C_{44}-PC) was dissolved in ODE (Sigma) in a 7 mL vial at 120 ºC on a hot plate, yielding a clear solution of 0.1g/mL. All processes were conducted in an Ar-filled glovebox.

Preparation of (FA+Na), (FA+K), and (FA+Rb) stock solution. NaOct, KOct, or Rb-oleate was dissolved in 1 mL FA-oleate in a 20 ml vial at 120 ºC on a hot plate for 10 min yielding a clear solution. For the samples that Na: FA=0.5, 1.5, 2.5, and 3.5, the amounts of NaOct are 0.016 g, 0.048 g, 0.08 g, and 0.112 g, respectively. For the samples that K: FA and Rb: FA=2.5, the amount of KOct is 0.0895 g, and that of Rb-oleate is

0.1711 g. Before synthesis, (FA+Na), (FA+K), and (FA+Rb) stock solutions were pre-heated at 120 ºC on a hot plate for 5 min.

Synthesis of $FASnI_3$, $FA_{0.9}Cs_{0.1}SnI_3$, and $FA_{0.8}Cs_{0.2}SnI_3$ NCs. 5 mL ODE (Sigma), 110 μL C_{44}-PC stock solution were heated to 120 ºC in a 20 ml vial on a hot plate, followed by the addition of 0.12 mL SnI_2-TOP stock solution under vigorous stirring for 10 min. Then, 0.18 mL FA-oleate solution was swiftly injected into the reaction solution. After reaction for 10 s, the crude solution was taken off from the hot plate, and naturally cooled down to room temperature. The synthesis was conducted in an Ar-filled glovebox. For the sample with Na or K or Rb passivation, 0.18 mL FA-oleate solution was changed to 0.18 mL (FA+Na) or (FA+K) or (FA+Rb) stock solution. For the synthesis of $FA_{0.9}Cs_{0.1}SnI_3$ and $FA_{0.8}Cs_{0.2}SnI_3$ NCs, 0.18 mL FA-oleate solution was changed to 0.18 mL FA-oleate, Cs-oleate, and NaOct mixed solution. For $FA_{0.9}Cs_{0.1}SnI_3$ NCs, the volume ratio of FA-oleate to Cs-oleate is 9:1; for $FA_{0.8}Cs_{0.2}SnI_3$ NCs, the volume ratio of FA-oleate to Cs-oleate is 8:2. The amount of NaOct in this mixed 1 mL FA-oleate and Cs-oleate solution is 0.08 g. To study the influence the reagent from different manufacturer, ODE (Sigma) was changed to ODE (Kanto).

Isolation and purification of perovskite NCs. The crude solution was centrifuged at 10000 r.p.m. for 5 min. Then the precipitate was discarded, and the supernatant was centrifuged again at 15000 r.p.m. for 5 min. Finally, the resultant precipitates were collected as the final product. To wash the NCs, NCs were redispersed into 50 μL hexane, and then centrifuged at 12000 r.p.m. for 5 min. This process was repeated by once and twice. Instead of the centrifugation processes in centrifuge, other all processes were conducted in an Ar-filled glovebox.

Post-synthetic treatments of $FASnI_3$ NCs. 9 mg Na-oleate was dissolved in 0.9 mL hexane and 45 μL OA in a 7 mL vial under vigorous stirring for 3 hours at room temperature, yielding a clear solution. OA was used for dissolving Na-oleate in hexane. $FASnI_3$ NCs were dispersed in 0.1 ml hexane, and then 20 μL NC-hexane solution was diluted into 2.5 mL hexane, following by the injection of Na-oleate solution for direct PLQY measurements. For control and TEA-0.25 NCs, the amounts of Na-oleate solution were 5 μL, 10 μL, and 20 μL; for TEA-0.25/Na-2.5 NCs, the amounts of Na-oleate solution were 2 μL, 5 μL, and 10 μL.

4.2.3 Characterizations

Optical characterizations. PL spectra were measured by a NanoLog Horiba Jovin Yvon spectrofluorometer with a continuous 450 W xenon lamp. Absolute PLQYs were measured by a standardized integrating sphere method using a C9920-03G system equipped with a 150-W xenon lamp (Hamamatsu Photonics). The absorption spectra were measured by a UV-vis-NIR spectrophotometer (V-770, JASCO). The PL decays were obtained with a time-correlated single photon counting lifetime spectroscopy system (NanoLog, Horiba Jovin Ybon), equipped with a pulse laser (λem = 726 nm). For all optical characterizations, $FASnI_3$ NCs were dispersed into 50 μL hexane, and then 15 μL NC-hexane solution was diluted into 2.5 mL hexane in cuvette. The calculated average PLQYs of all samples from three parallel experiments.

Structure and morphology characterizations. Powder XRD data were recorded on a MiniFlex 600 diffractometer (Rigaku) with a Cu Kα X-ray source (λ = 1.5418 Å). The perovskite NCs were dispersed in hexane to form a concentrated solution which was then dropped on an anaerobic sample holder for XRD measurements. For getting enough sample, multifold synthesis is necessary. TEM images were collected by a JEM-2100F (JEOL) microscope operated at 200 kV. TEM samples were prepared by dropping a dilute NC-hexane solution onto a TEM copper grid and dried in glovebox. Scanning transmission electron microscope (STEM) EDS elemental mapping was obtained on STEM mode operating at 200 kV. High-resolution TEM images were collected by a Themis Z (Thermo Fisher Scientific) microscope using a K2 (Gatan Inc.) detector in electron counting mode, operating at 300 K. To avoid the degradation of NCs, dose density was controlled to ~ 375 e^-/nm^2 every flame, and 25 flames were collected for the final image.

Composition analysis of $FASnI_3$ NCs. The actual ion concentrations of tin and sodium were taken by inductively coupled plasma optical emission spectrometry (ICP-OES) (Shimadzu Corporation). $FASnI_3$ NCs were transferred to a quartz beaker with 10 mL of HNO_3 and Milli Q water. The volume ratio of HNO_3/water is 1:1. 10 mL of H_2SO_4 was added, and heating was continued until white smoke was occured to decompose the sample. The acid decomposition solution was transferred to a 100 mL of PP volumetric flask using HCl aqueous solution and diluted by HCl solution to the marked line. The

reported values are average of two sample's analytical results. ESI-MS spectra were measured by a Q-Exactive Plus mass spectrometer (ThermoFisher Scientific) with an electrospray ion source. This was used for the detection of TEA^+. For the measurement, TEAI and NCs were dissolved in methanol.

ζ-potential, and XPS characterizations. ζ-potential data were collected using a Zetasizer Nano-Z system (Malvern Instruments). Colloidal QD solutions were put into quartz cuvettes with dip cell electrodes and then inserted into the instrument stage. All measurements included 50 scans and were repeated for three times to get an average value. To avoid the degradation of NCs, all measurements were conducted in N_2-filled glovebox. XPS spectra were measured using a dual scanning X-ray photoelectron microprobe equipped with hard X-ray photoelectron spectroscopy (HAX-PES/XPS; ULVAC-PHI, Inc., Japan). A concentrated NC-hexane solution was dropped on the Si substrate. To avoid the oxidation in the air, an anaerobic transfer vessel was used in the Ar-filled glovebox.

4.2.4 Density Functional Theory (DFT) Calculations

Formation energy calculations. The formation energy of the point defects of both bulk $FASnI_3$ supercell and slab structure were performed based on density functional theory (DFT) calculations using Vienna ab initio simulation package (VASP) code with standard frozen-core projector augmented-wave (PAW) method. The exchange-correlation potential utilized is generalized gradient approximation (GGA) of Perdew–Burke–Ernzerhof (PBE) functional. The energy cut-off for geometry optimization and self-consistent calculations for basis functions is 450eV and the force convergence criterion used for geometry optimization is 0.02 eV/Å. Defects calculations are based on a (3×3×3) supercell model and (3×3×5) slab model with reasonable vacuum thickness of with a single G point. The formation energy calculation of six different types of point defects (I_{FA}, I_i, Sn_i, V_{Sn}, V_I, V_{FA}) in $FASnI_3$ supercell, in-plane Sn vacancy (V_{Sn}), in-plane Iodine vacancy (V_I) on SnI_2-rich surface, in-plane FA vacancy (V_{FA}), in-plane Iodine vacancy (V_I) on FAI-rich surface of $FASnI_3$ slab structure and out-of-plane Iodine vacancy on TEA and Na adsorbed SnI_2-rich surface were performed using the following formula:

$$\Delta H_{defect} = E_{defect} - E_{pristine} + \sum_i n_i (\mu_i + E_i) \quad (1)$$

where ΔH_{defect} is the defect formation energy, E_{defect} and $E_{pristine}$ are the total energies of the defected and pristine structure, respectively. n_i is the number of species i removed from the crystal structure ($n_i > 0$). μ_i and E_i are the chemical potential and elemental solid energy of specie *i*, respectively. To determine the feasible chemical potential regions for thermal equilibrium growth of the $FASnI_3$ perovskite crystals, the chemical potential of Sn, FA and I should satisfy the following requirements, ensuring that the thermal equilibrium growth of the target crystal and preventing the formation of the secondary compounds such as FAI, SnI_2, SnI_4 and FA_2SnI_6.

$$\mu_{FA} + \mu_{Sn} + 3\mu_I = \Delta H(FASnI_3) = -3.63eV \quad (2)$$

$$\mu_{Sn} + 2\mu_I < \Delta H(SnI_2) = -1.30eV \quad (3)$$

$$\mu_{Sn} + 4\mu_I < \Delta H(SnI_4) = -1.43eV \quad (4)$$

$$2\mu_{FA} + \mu_{Sn} + 6\mu_I < \Delta H(FASnI_6) = -5.43eV \quad (5)$$

$$\mu_{FA} + \mu_I < \Delta H(FAI) = -2.16eV \quad (6)$$

Defects charge transition level. The charge transition level calculation for the defects in the $FASnI_3$ supercell and surface model were performed. The charge transition level of a defect α from charge state q to charge state q' is ε(q,q') is defined is the fermi energy at which the formation energy of the defect at two charge state equals to each other.

$$\varepsilon(q, q') = \frac{E(\alpha, q) - E(\alpha, q') + (q - q')(E_{VBM} + \Delta V)}{q' - q} \quad (7)$$

where E(α, q) and E(α, q') correspond to the total energy of the system containing the defect with charge state q and q' respectively. E_{VBM} is the VBM energy of the pristine structure and ΔV is a correction term for alignment of the VBM energy in structures with different charged states.

Ab initio molecular dynamics simulation. Ab initio molecular dynamics (AIMD) simulations were conducted to investigate FA-I rich (100) surface supercell structures

adsorbed by tetraethylammonium ions (TEA^+) and sodium ions (Na^+) at varying concentrations of 2, 4, and 6 Na^+ ions per structure. These simulations were performed at two distinct temperatures, 300 K and 400 K, within the NPT ensemble framework. The computational approach utilized the CP2K package, which implements the hybrid Gaussian and plane wave method (GPW) through its Quickstep module. To effectively control temperature and manage the ionic degrees of freedom, a Nose-Hoover thermostat was employed. In terms of computational parameters, the DZVP-MOLOPT-GTH basis set and PBE-GTH pseudopotentials were utilized for the elements involved, specifically tin (Sn), iodine (I), carbon (C), nitrogen (N), hydrogen (H), sulfur (S), and sodium (Na). An energy cutoff of 600 Ry was established for the auxiliary plane wave basis set to ensure adequate representation of the system's electronic structure. The total simulation time for the AIMD was set to 5 ps, with a time step of 1 fs for the integration of the dynamic equations.

4.3 Results and discussion

We began by carrying out theoretical calculations aimed at understanding the nature of defects in $FASnI_3$ and their effect on the photophysical properties. The generalized gradient approximation (GGA) with the Perdew-Burke-Ernzerhof (PBE) exchange-correlation functional was first used for the calculations. As illustrated in **Figure 4.1a**, I note that the calculated chemical potential region in which $FASnI_3$ is stable under the equilibrium growth condition is extremely narrow. Three chemical potential conditions C1, C2, and C3 corresponding to the Sn-rich, moderate, and I-rich conditions are samples. I then performed DFT calculations on the point defect formation energy in $FASnI_3$ (see details in the **Experimental Section**). Three vacancies (V_{FA}, V_{Sn}, and V_I), one antisite (I_{FA}), and two interstitials (I_i, Sn_i) were considered in our calculations. As illustrated in **Figure 4.1b**, under I-rich/Sn-poor condition, V_{Sn} has lowest formation energy (~-0.10 eV) and is the dominant defect, while Sn_i, I_{FA} have high formation energies (~3.63 eV, ~2.40 eV, respectively) than other studied defects. In the moderate condition, V_{Sn} is still the dominant defect since its formation energy is ~ 0.48 eV that is the lowest than other defects. As the chemical potential point shifts to Sn-rich/I-poor side, the formation energy

of V_{Sn} increases to ~1.07 eV, and V_I (~0.77 eV) becomes the dominant defect. In both three points, Sn_i, I_{FA} have high formation energies, indicating the hard formation trend of these two defects. We underscore that, with increasing Sn chemical potential, the defect formation energies of V_{Sn}, I_i, V_{FA}, I_{FA} monotonically increase, while those of Sn_i, V_I slightly decrease, signifying that Sn-rich condition is significant for getting low defect-density $FASnI_3$. My work in Chapter 1 is well consistent with these theoretical calculations. To screen out the most detrimental point defect for the radiative recombination of charge carriers in $FASnI_3$, we next calculated the thermodynamical charge-transition levels of defects aforementioned. As shown in **Figure 4.1c**, in bulk $FASnI_3$, almost all point defects can introduce deep defect levels between conduction band minimum (CBM) and valance band maximum (VBM). Different with lead perovskites, $FASnI_3$ is quiet defect-intolerant, indicating the difficulty in getting highly luminescent crystals. From **Figure 4.1b**, under Sn-rich reaction condition, V_I becomes crucial, since its low formation energy, indicating the importance for suppressing the formation of V_I.

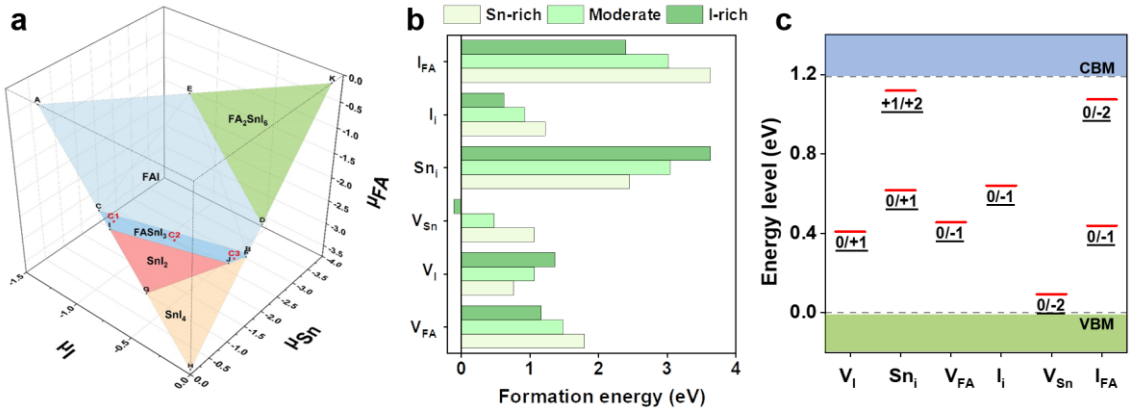

Figure 4.1. (a) The allowed chemical potential region for the thermal equilibrium growth of $FASnI_3$ marked by the blue polyhedral region, in which three chemical potential conditions are sampled: Sn-rich (C1), Moderate (C2) and I-rich (C3). (b) Calculated defect formation energies for the point defects in the bulk $FASnI_3$. (c) Defect charge transition levels for point defects in the bulk $FASnI_3$.

Considering the larger specific surface area of NCs, surface condition is crucial. Then, we calculated the defect formation energies for the point defects on the FAI-rich and SnI_2-rich surfaces at different growth conditions. As seen in **Figure 4.2a**, on the SnI_2-

rich surface, the formation energies of both V_I and V_{Sn} are negative under three different growth conditions. The optimized crystal structures for calculations and total density of states (TDOS) are displayed in **Figure 4.3a**. Tuning the chemical potential from tin-poor/I-rich to Sn-rich/I poor, the formation energies of V_I decreases and that of V_{Sn} increases (**Figure 4.2a**). However, the negative formation energies of V_I and V_{Sn} indicating that SnI_2-rich termination surface can induce a lot of surface defects no matter in Sn-rich/I-poor or Sn-poor/I-rich conditions, indicating much unstable SnI_2-rich termination surface. For FAI-rich termination surface, the formation energies of both V_I and V_{FA} are high. Form I-rich to Sn-rich, the formation energy of V_I decreases from ~2.00 eV to ~1.40 eV, while that of V_{FA} increased from 1.27 eV to 1.90 eV (**Figure 4.2a**). The related optimized crystal structures and total density of states (TDOS) are shown in **Figure 4.3b**. From the calculations, we can conclude that FAI-termination can result in a low-defect-density NC surface. However, on the FAI-rich surface, V_I is detrimental, because it can introduce deep defect level as shown in **Figure 4.2b**, further indicating the importance of suppression the formation of V_I for highly luminescent $FASnI_3$ NCs. On the SnI_2-rich surface, V_{Sn} and V_I cannot induce deep defect level (**Figure 4.2c**), but their low formation energies may induce unstable surface structure, and thus may induce the degradation of NCs. Form all DFT calculations, I note that three factors are important for the attainment of highly luminescent $FASnI_3$ NCs: 1). Creating a Sn-rich reaction condition; 2). Constructing a FAI-rich surface termination; 3) suppressing the formation of surface V_I.

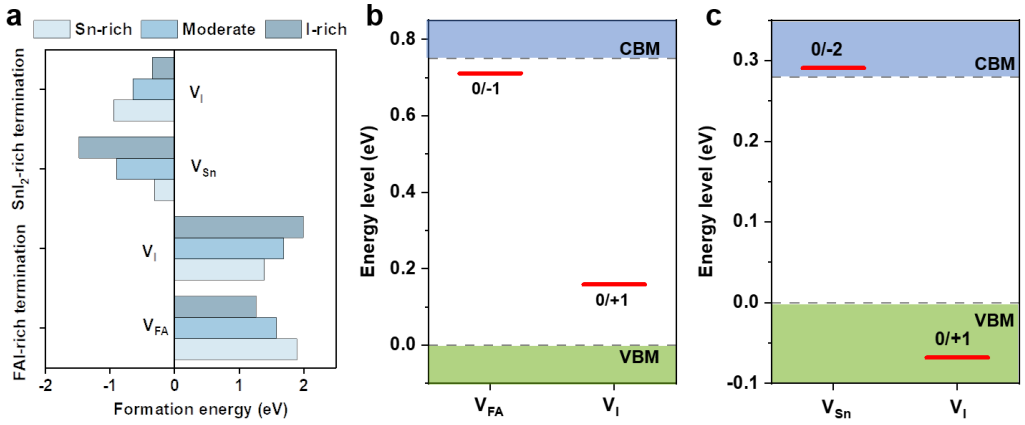

Figure 4.2. (a) Calculated defect formation energies for the point defects on the FAI-rich and SnI_2-fich surface of $FASnI_3$. (b) Defect charge transition levels on the FAI-rich

surface. (c) Defect charge transition levels on the SnI_2-rich surface.

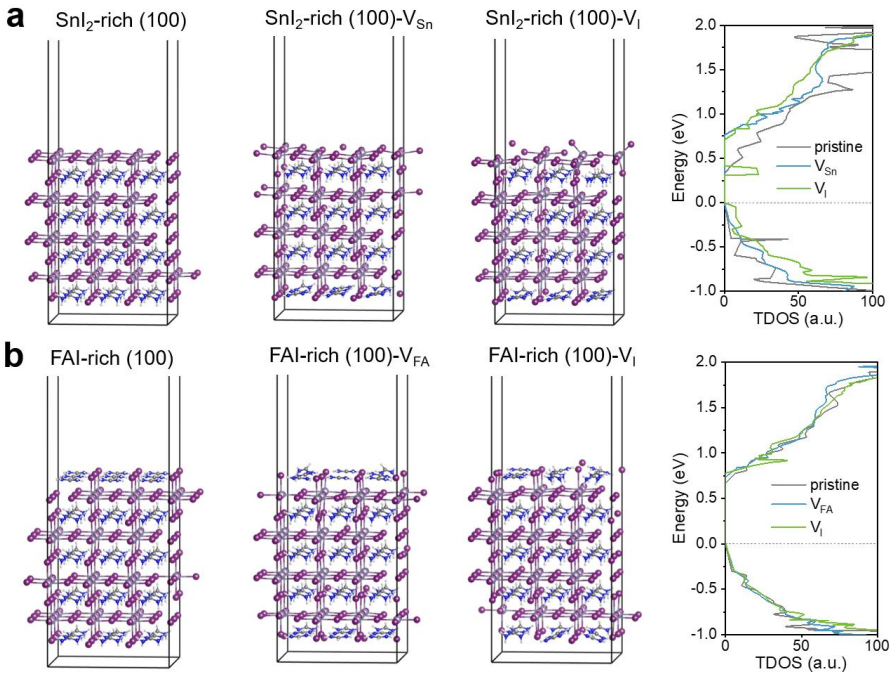

Figure 4.3. Optimized crystal structures and total density of states (TDOS) for (a) SnI_2-rich (100) supercell without and with a surface defect (V_{FA} and V_I), and for (b) FAI-rich (100) supercell without and with a surface defect (V_{Sn} and V_I). The DFT calculations were performed at GGA/PBE+vdW level.

Importantly, if we create a Sn-rich reaction condition, $FASnI_3$ NCs more tend to form a SnI_2-rich termination. From **Figure 4.4**, we can see that for FAI-rich termination, the total atom ration of I/Sn in one $FASnI_3$ crystal is higher than 3, and the ratio of I/FA is lower than 3. When the particle size is down to several nanometers, to form a FAI-rich termination, the amount of FA is very high. Otherwise, SnI_2-rich termination is more possible. To break this deadlock, a tin-rich reaction condition that can avoid the SnI_2 termination could be the key. Considering that I cannot provide a FA-rich reaction condition, I thus proposed the use of exogenous cation that can act as a quasi-A-site cation to establish an AI-terminated surface. I then focus on some organic and inorganic cations with one plus oxidation states. For organic cations, I chose phenylethylamine (PEA^+), 2-thiophenemethylammonium (TMA^+), and 2-thiopheneethylammonium (TEA^+), all of which tend to form RP 2D perovskites, and they are generally used to passivate 3D perovskites.[46-50] For inorganic cations, I chose alkali metal ions, K^+, Na^+, Rb^+. Li^+ is

excluded here, because it has very small ionic radius. Firstly, we conducted theoretical calculations to confirm the possibility of incorporating these one plus cations on the surface of $FASnI_3$ NCs. As shown in **Figure 4.5a**, the binding energies of three organic cations, PEA^+, TMA^+, and TEA^+ are -3.768 eV, -3.746 eV, and -3.867 eV. TEA^+ shows highest binding energy. **Figure 4.5b** shows the optimized crystal structures with K^+, Na^+, Rb^+ replacement, and the binding energies are -2.970 eV, -2.426 eV, and -2.998 eV, respectively. Among metal ions, Na^+ shows smaller binding energy than K^+ and Rb^+. The TDOS calculations are also displayed in **Figure 4.5**. I note that all these cations do not introduce deep traps. The DFT calculations indicate that all these cations possibly bind with NC surface forming a quasi-AI-termination without introducing other defects.

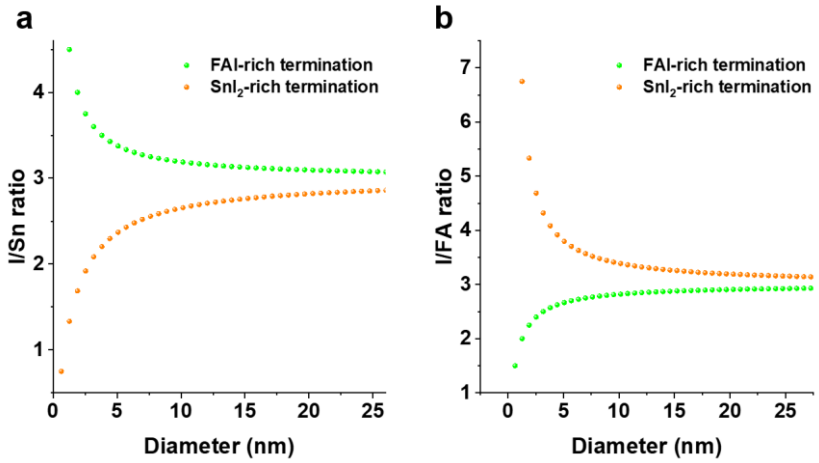

Figure 4.4. Size-dependent (a) I/Sn ratio and (b) I/FA ratio of a cubic $FASnI_3$ NC with FAI-rich (green circles) and SnI_2-rich (orange circles) terminations. Unlike in the bulk, in a NC, the I/Sn and I/FA ratios deviate from three.

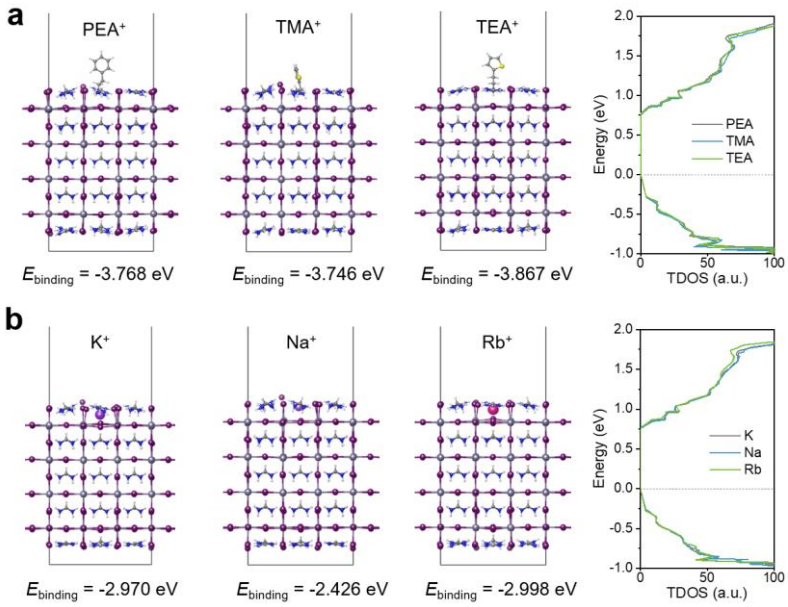

Figure 4.5. Optimized crystal structures, calculated binding energies ($E_{binding}$), and total density of states (TDOS) for FAI-rich (100) supercell (a) with a metal cation replacement (K^+, Na^+, and Rb^+), and (b) with an organic cation replacement (PEA^+, TMA^+, and TEA^+). The DFT calculations were performed at GGA/PBE+vdW level.

I then sought to challenge my hypothesis experimentally by devising a colloidal synthesis strategy that ensues a Sn-rich reaction condition but realize a quasi-AI-termination surface for $FASnI_3$ NCs. I judiciously employed FA-oleate, SnI_2, and tin (II) 2-ethylhexanoate ($Sn(Oct)_2$) as precursors, and 1,2-Dioleoyl-sn-glycero-3-phosphocholine (C_{44}-PC) as ligand for the synthesis of $FASnI_3$ NCs, which is as same as that in Chapter 3. The reason why choose C_{44}-PC as ligand is also discussed in Chapter 3. To achieve surface modification, PEAI/TMAI/TEAI were introduced in Sn-I precursors, and KOct/NaOct/Rb-oleate were introduced in FA-oleate solution (**Figure 4.6**). In a typical synthesis, I firstly prepared two precursor solutions. FA-oleate was mixed with KOct/NaOct/Rb-oleate at 120 ºC on a hot plate as FA-oleate precursor solution; SnI_2, $Sn(Oct)_2$, and PEAI/TMAI/TEAI were dissolved in TOP at 120 ºC on a hot plate as Sn-I-TOP precursor solution. Then, Sn-I-TOP precursor solution was injected in to 5 ml ODE, followed by introducing C_{44}-PC at 120 ºC. FA-oleate was then swiftly injected into the reaction vial at 120 ºC, triggering a rapid salt metathesis reaction and resulting in fast nucleation and growth of $FASnI_3$ NCs within 10 s. The mole ratio of FA:

Sn: I was kept at 0.2: 1.4: 1.

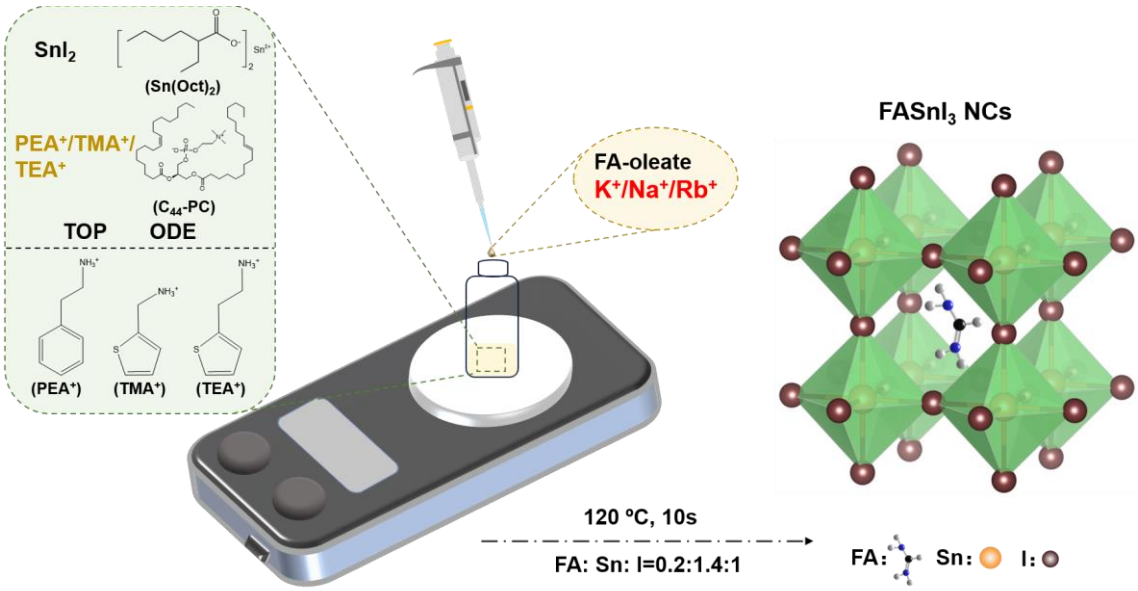

Figure 4.6 Scheme illustration of colloidal synthesis for $FASnI_3$ NCs.

I firstly synthesized $FASnI_3$ NCs without any cation passivation, denoted as control, and the PLQY is only 0.9±0.1% (**Figure 4.7a**). Here, in this work, all the samples were repeated three times for measuring PLQYs, and the average PLQYs as well as error bar were calculated. Then, I tried the surface passivation by PEA^+ and TMA^+. The effect of TEA^+ will be discussed later. The mole ratio of PEA/TMA: FA is 0.25: 1. Hence, the two samples were denoted as PEA-0.25 and TMA-0.25, respectively. For PEA-0.25, the PLQY is slightly increased to 2.0±0.2% (**Figure 4.7b**), while the PLQY of TMA-0.25 is only 0.8±0.1% (**Figure 4.7c**), close to that of control. The powder X ray diffraction (PXRD) patterns of PEA-0.25, TMA-0.25 nicely match the cubic $FASnI_3$ structure, and no secondary crystalline phase detected (**Figure 4.8a**). The bright-field transmission electron microscopy (TEM) images of the products are also shown in **Figure 4.8b, c**. I note that the morphology of two samples is not perfect cubic. They are cuboids. The average width and length for PEA-0.25 are 18.8 nm and 20.6 nm; and those for TMA-0.25 are 19.2 nm and 21.8 nm, respectively. The histograms of edge widths and lengths of corresponding $FASnI_3$ NCs are also shown in **Figure 4.8b, c**.

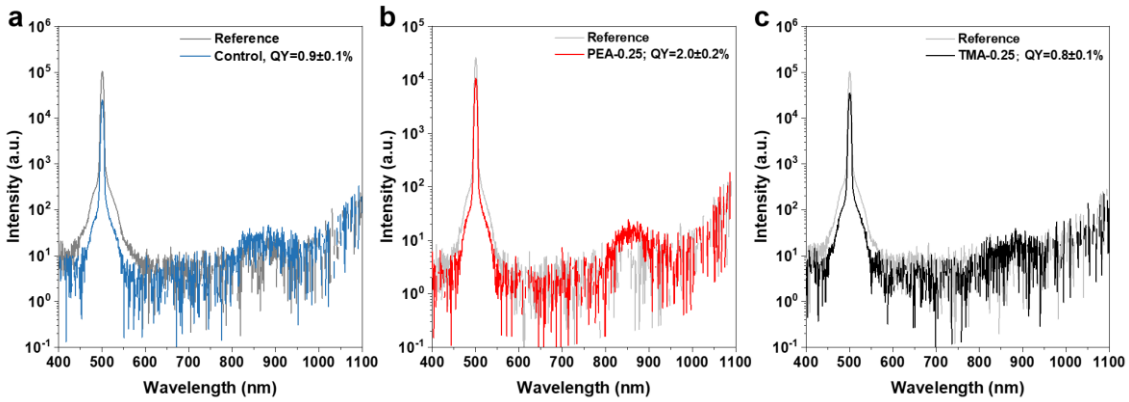

Figure 4.7 PLQY measurements of (a) control; (b) PEA-0.25; (c) TMA-0.25, respectively.

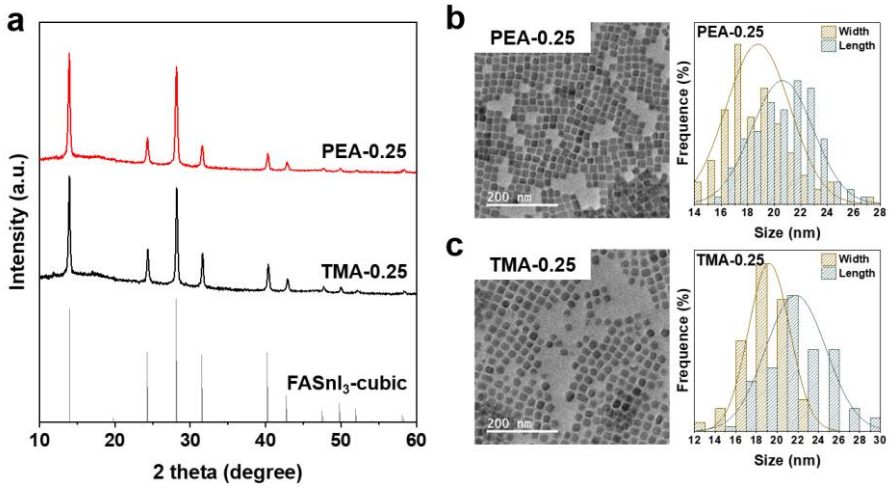

Figure 4.8 (a) XRD patterns of PEA-0.25 and TMA-0.25. (b, c) TEM images of PEA-0.25 and TMA-0.25. The histograms of edge widths as well as lengths of corresponding $FASnI_3$ NCs are shown in the right.

I further tried the passivation effect of alkali metal ions, K^+ and Rb^+. The effect of Na^+ will be discussed later. The molar ratio of K or Rb: FA is 2.5: 1. Hence, the samples are denoted as K-2.5 or Rb-2.5. However, after introduction of K^+, the color of the final produce is dark yellow, not black (**Figure 4.9a**), indicating that K^+ can suppress the nucleation and growth of $FASnI_3$ NCs. After introducing Rb^+, the color of the final product is black (**Figure 4.9a**), and the main structure phase of the product is cubic $FASnI_3$, as shown in **Figure 4.9b**. Notably, a small amount of RbI byproduct was also crystallized in the final product, which is confirmed in XRD pattern (The diffraction peak of RbI is marked by # in **Figure 4.9b**). The TEM image of Rb-2.5 is displayed in **Figure**

4.9c. Some particles exhibit quasi-cubic morphology, while some particles exhibit quasi-sphere morphology, indicating that alkali metal ions can affect the morphology of $FASnI_3$ NCs. The mean particle size of Rb-2.5 is 26.2 nm. The PLQY result is shown in **Figure 4.10**. After the passivation by Rb, the PLQY can be slightly increased to 2.0±0.1%.

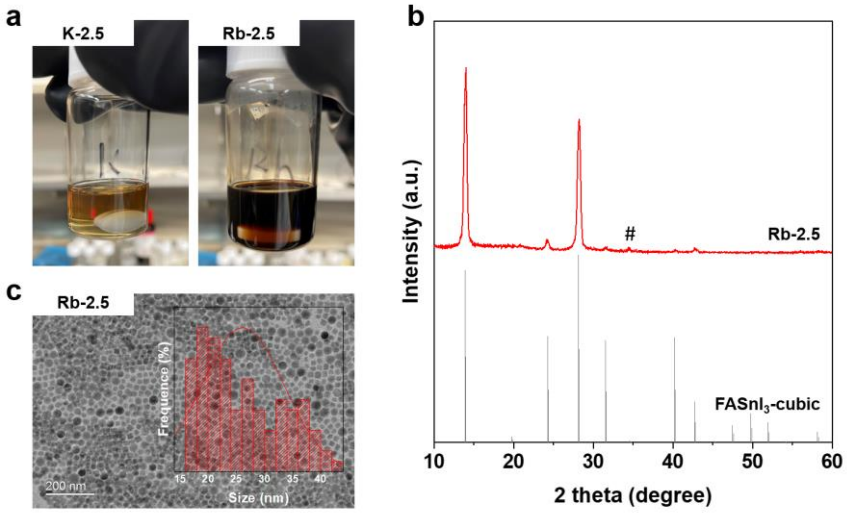

Figure 4.9 (a) Photos of the final product of K-2.5 and Rb-2.5. (b) XRD pattern of Rb-2.5. The diffraction peak marked by # comes from RbI. (c) TEM images of Rb-2.5. The inset the histogram of its edge length.

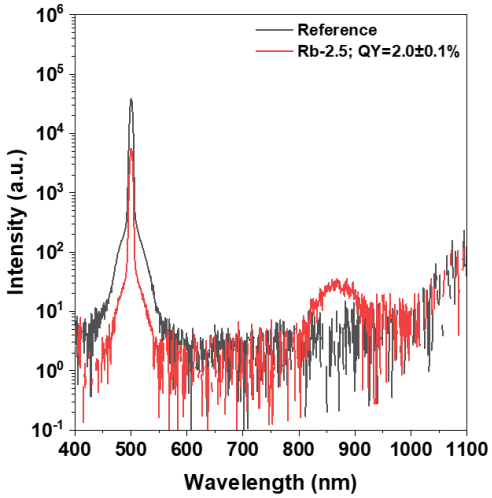

Figure 4.10 PLQY measurement of Rb-2.5.

In the following, I focus on the discussion about TEA^+ and Na^+ passivation effect. Four typical samples are discussed here: without cations (Control); with TEA (TEA:

FA=0.2:1; denoted as TEA-0.25); with Na (Na: FA=2.5:1; denoted as Na-2.5); with both TEA and Na (TEA: FA=0.25:1; Na: FA=2.5:1; denoted as TEA-0.25/Na-2.5). **Figure 4.11a** shows the XRD patterns of as-prepared four products, and all of them match nice with cubic $FASnI_3$ structure without any other crystalline phase. From the XRD patterns, I do not observe the shift in their diffraction peaks. The TEM images of four samples are displayed in **Figure 4.11b** and their histograms of width and length are exhibited in **Figure 4.11c**. I note that control sample have an average width of 25.8 nm and length of 27.7 nm. After introduction of TEA, the average width slightly decreases to 22.1 nm and length decreases to 26.2 nm. Both control and TEA-0.25 have quasi-cubic morphology. However, introduction of Na can induce larger particles. Some particles show nanosheet morphology. The average width and length are 30.6 nm and 40.5 nm, respectively. Interestingly, introducing both TEA and Na results in cuboid morphology. The average width and length are 22.4 nm and 34.2 nm, respectively. The TEM images indicate that alkali metal ions can affect the morphology of $FASnI_3$ NCs, and TEA can reduce the edge size of $FASnI_3$ NCs.

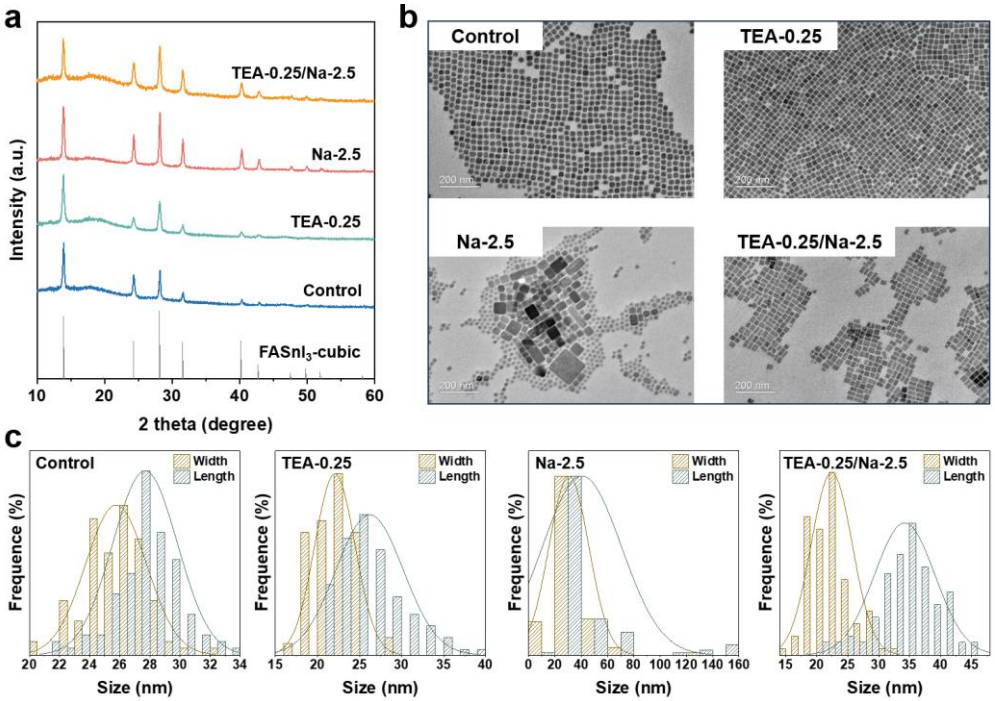

Figure 4.11 (a) XRD patterns of control; TEA-0.25; Na-2.5; TEA-0.25/Na-2.5 NCs, respectively. (b) TEM images of control; TEA-0.25; Na-2.5; TEA-0.25/Na-2.5 NCs, respectively. control; TEA-0.25; Na-2.5; TEA-0.25/Na-2.5 NCs, respectively. (c) The histograms of edge widths as well as lengths of corresponding $FASnI_3$ NCs.

Next, I investigated the lattice of two typical samples: control and TEA-0.25/Na-2.5 NCs. $FASnI_3$ NCs show extremely poor stability under electron beam. To avoid the degradation of NCs, dose density was controlled to ~ 375 e^-/nm^2 every flame, and 25 flames were collected for the final image. **Figure 12a** shows high-resolution TEM (HRTME) images of control sample. The left is low-magnification image, and the right is the high-magnification image. We can clearly see that the control sample is octahedral, and the lattice constant is 6.40 Å**,** which is in consistent with (100) plane. Compared with bulk $FASnI_3$, 6.34 Å for (100) plane,[51] my NCs exhibit slightly lower lattice constant. The corresponding selected area electron diffraction (SAED) pattern is shown in **Figure 4.12b**, which also confirms the cubic structure of $FASnI_3$ NCs. The HRTEM images of TEA-0.25/Na-2.5 NCs are displayed in **Figure 4.12c**. From them, we can find the lattice constant of TEA-0.25/Na-2.5 is also 6.40 Å, as same as control, indicating that TEA and Na do not enter the lattice of $FASnI_3$ NCs. The SAED pattern in **Figure 4.12d** also confirms the cubic structure of as-prepared NCs.

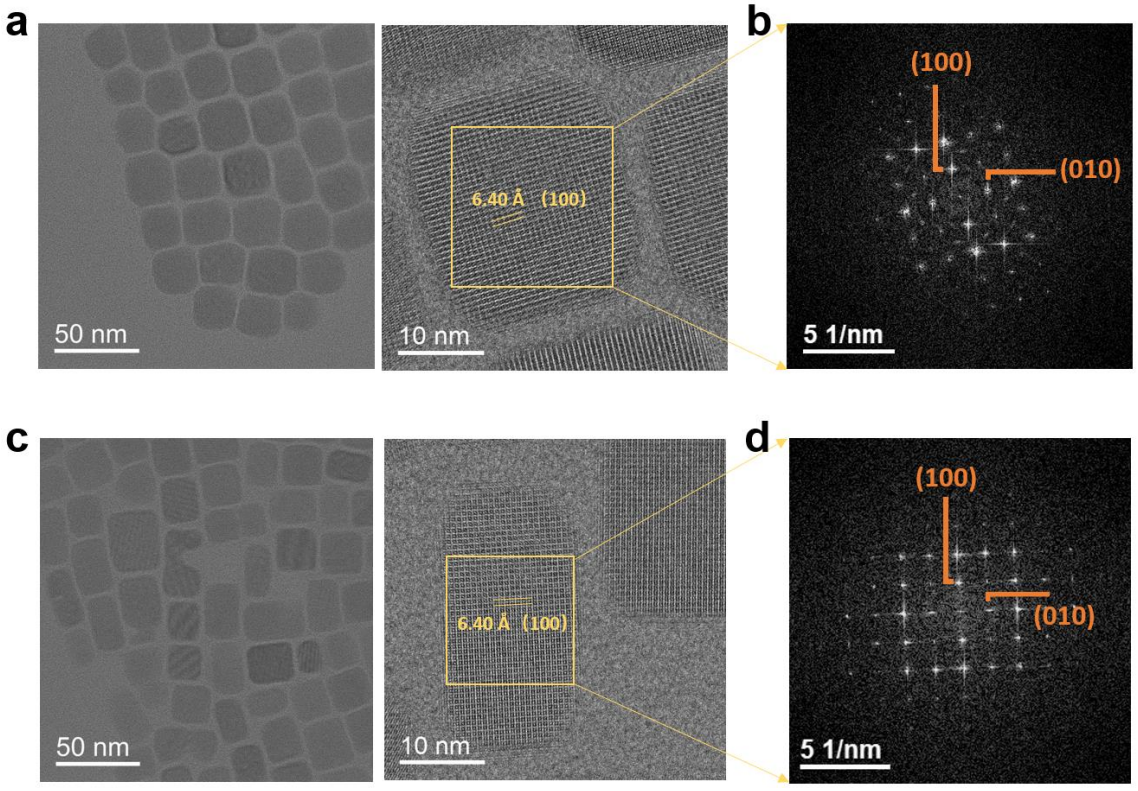

Figure 4.12. (a) High-resolution TEM image of control NCs. The left is low-magnification image and the right is high-magnification image. (b) Corresponding

selected area electron diffraction pattern of control NCs. (c) High-resolution TEM image of TEA-0.25/Na-2.5 NCs. The left is low-magnification image and the right is high-magnification image. (d) Corresponding selected area electron diffraction pattern of TEA-0.25/Na-2.5 NCs.

I then proceeded to investigate the photophysical properties of as-prepared four $FASnI_3$ NCs. **Figure 4.13a** displays the absorption and PL spectra of these NCs. All NCs show similar absorption characteristic. However, they have different PL peaks: 860 nm, 854 nm, 867 nm, and 854 nm for control, TEA-0.25, Na-2.5 and TEA-0.25/Na-2.5, respectively. Although the particle sizes of these NCs are different (**Figure 4.11b**), it cannot be explained by size effect since the Bohr radius in $FASnI_3$ is quite small (3.5-4.4 nm).[37] Previous work confirmed that structural distortion can induce the bandgap widening in $FASnI_3$.[37] Here, I speculate that the shift in PL peaks may originate from different structural distortion induced by TEA and Na. Importantly, the PLQYs of theses NCs are 0.9±0.2%, 4.0±0.7%, 13.6±0.2%, and 36.9±0.7% for control, TEA-0.25, Na-2.5 and TEA-0.25/Na-2.5, respectively (**Figure 4.13b, d**). Compared with PEA^+ and TMA^+, TEA^+ shows better passivation effect, which can be explained by higher binding energy of TEA^+ (**Figure 4.5a**). In addition, during all alkali metal ions, Na^+ passivated NCs show better PLQY compared with K^+ or Rb^+ (**Figure 4.10**). Interesting, combining TEA^+ with Na^+, the as-prepared NCs show maximum PLQY, 36.9±0.7%, that is an record value compared with all previously reported tin halide perovskite NCs.[16, 35, 37, 38]

I then carried out time-resolved PL measurements to glean information on the transient evolution of the photogenerated carriers. **Figure 4.13c** displays the decay curves of yielded four $FASnI_3$ NCs. I note that control sample has much fast decay that is close to the laser pulse. With the passivation by TEA or/and Na, the PL decay becomes slower. I fitted all decay curves by a biexponential function (**Figure 4.13c, Table 4.2**), from which the average lifetimes are obtained. The average lifetime of control is only 0.28 ns. TEA-0.25, and Na-2.5 have a lifetime of 20.94 ns, 90.30 ns, respectively. Specially, TEA-0.25/Na-2.5 sample has a much long lifetime of 132.52 ns, suggesting significantly suppressed non-radiative recombination.

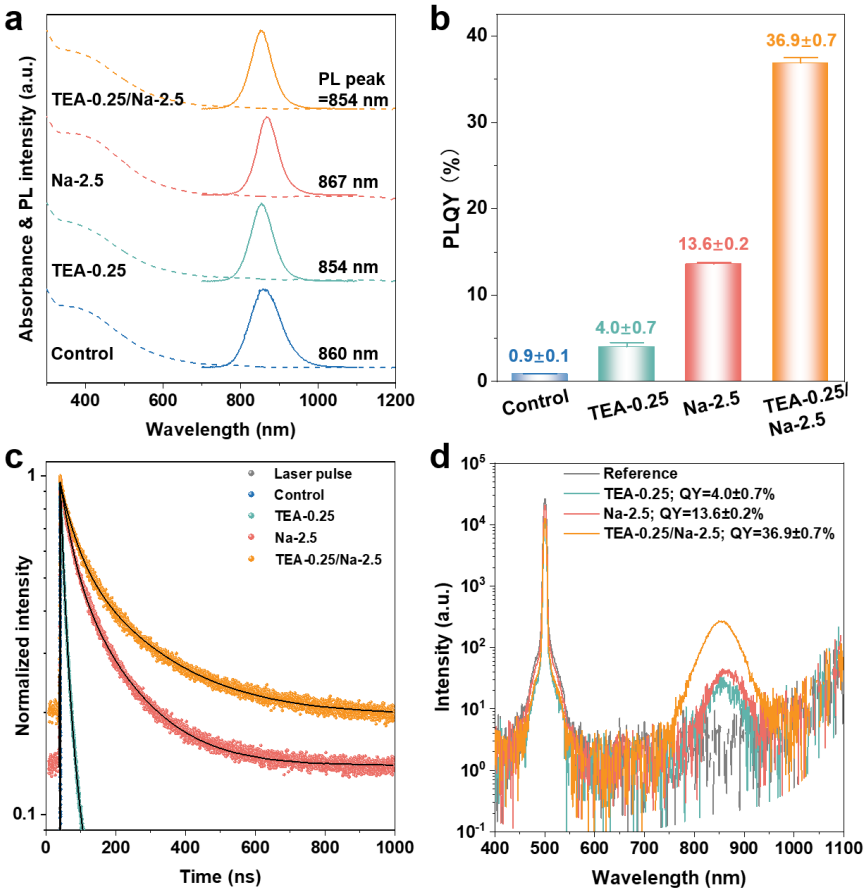

Figure 4.13 (a) Normalized PL (solid lines) spectra and optical absorption (dashed lines) of control; TEA-0.25; Na-2.5; TEA-0.25/Na-2.5 NCs. (b) Histograms of the PLQYs for control; TEA-0.25; Na-2.5; TEA-0.25/Na-2.5 NCs. The average PLQY and error bar were obtained by three parallel experiments. (c) PL decay traces of $FASnI_3$ NCs. The black curves are their fitting curves. (d) PLQY measurements of TEA-0.25; Na-2.5; TEA-0.25/Na-2.5 NCs.

Table 4.2. Fitted lifetimes (τ_1, τ_2), average lifetimes (τ_{ave}) using a biexponential function, and PLQYs of $FASnI_3$ NCs.

Samples	A_1	τ_1 (ns)	A_2	τ_2 (ns)	τ_{ave} (ns)	PLQY (%)
Control	0.50	0.28	0.50	0.49	0.38	0.9

TEA-0.25	0.71	11.81	0.29	43.12	20.94	4.0
Na-2.5	0.49	33.81	0.51	145.21	90.30	13.6
TEA-0.25/ Na-2.5	0.49	45.37	0.51	215.18	132.52	36.9

It is known that tin halide perovskite NCs commonly show poor stability. Previously results revealed that exposure of tin halide perovskite NCs in air for a short duration leads to significant degradation since the fast oxidization of Sn^{2+} into Sn^{4+}, leading to structural deformation.[52, 53] My NCs also exhibit poor stability in the air. Within 10 min, $FASnI_3$ NCs totally degraded into white salts. But in the Ar-filled glovebox (H_2O<0.6 ppm; O_2<0.1 ppm), after 24 hours, control and TEA-0.25/Na-2.5 NCs still maintained 88% and 91% of their initial PLQYs (**Figure 4.14**). I note that, how to further improve the stability of $FASnI_3$ NCs is highly desirable to explore in the future.

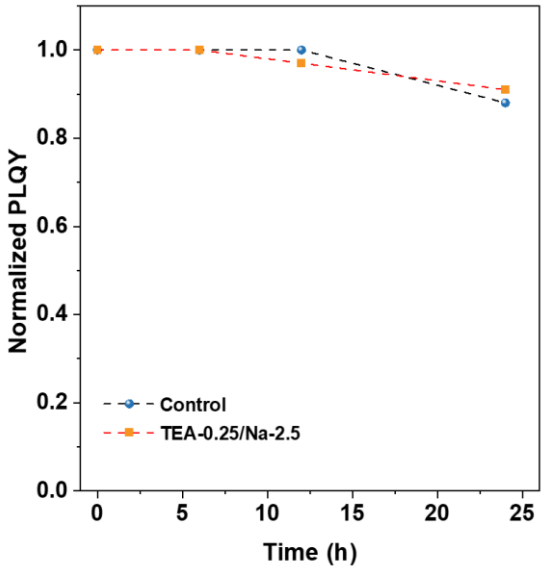

Figure 4.14 Temporal evolution of PLQYs of control and TEA-0.25/Na-2.5 NCs dispersed in hexane in glovebox (H_2O<0.6 ppm; O_2<0.1 ppm).

I then turned to studying the impact of the amount of TEA and Na. Firstly, I kept the amount of Na (Na: FA=2.5: 1), while change the amount of TEA. The molar ratios of

TEA: FA=0.05:1, 0.15:1, and 0.3:1, and the corresponding products are denoted as TEA-0.05/Na-2.5; TEA-0.15/Na-2.5; TEA-0.3/Na-2.5. Further increase the molar ratio of TEA: FA to 0.35: 1 induced the insoluble Sn-I precursor solution. The XRD patterns of as-prepared products are displayed in **Figure 4.15a**. All three samples match well with cubic $FASnI_3$ structure. Their TEM images and corresponding size-distribution histograms are shown in **Figure 4.15b-d**. The average width and length for TEA-0.05/Na-2.5 are 22.0 nm and 33.6 nm; those for TEA-0.15/Na-2.5 are 18.6 nm and 31.2 nm; those for TEA-0.3/Na-2.5 are 21.0 nm and 30.0 nm. Their morphology and particle size have no distinct difference. **Figure 4.16a** displays their absorption and PL properties. All three samples have almost same absorption and PL spectra, while their PLQYs are quite different: 15.2 ±0.6%; 28.0±1.4%; and 31.8±1.4% for TEA-0.05/Na-2.5; TEA-0.15/Na-2.5; and TEA-0.3/Na-2.5, respectively (**Figure 4.16b**). The best ratio of TEA: FA is 0.25:1 that have been discussed above (**Figure 4.13**). With increasing the amount of TEA, we can see the increase in PLQYs until TEA: FA=0.25:1. Further increase the amount of TEA can induce slight decrease in PLQY.

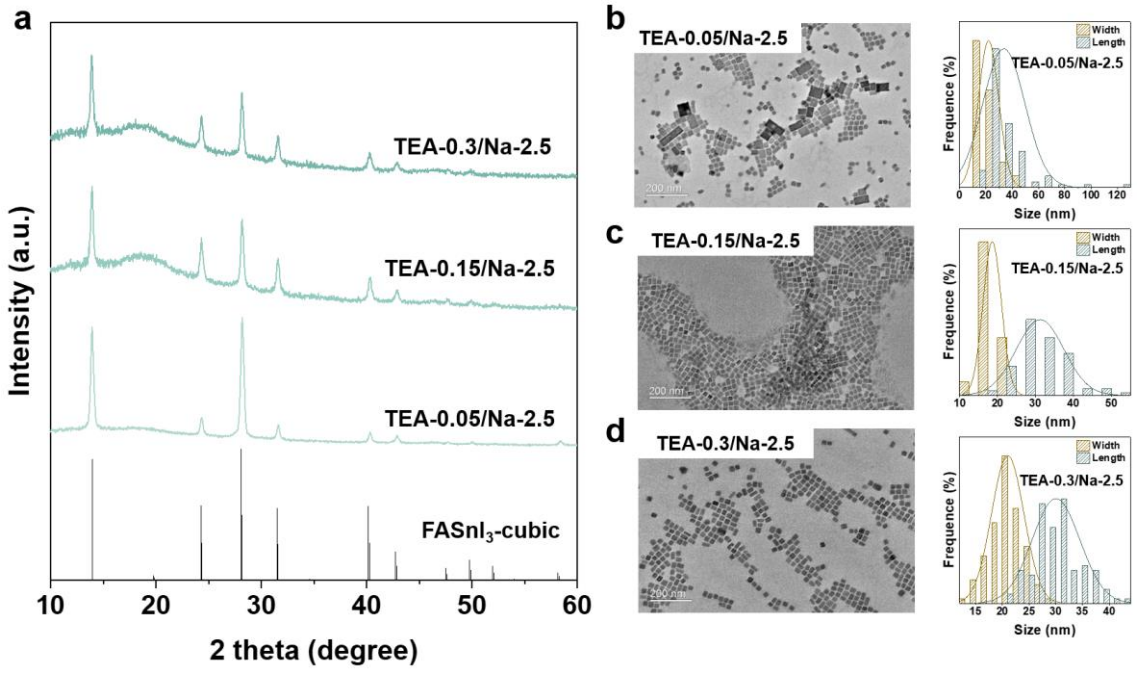

Figure 4.15 (a) XRD patterns of TEA-0.05/Na-2.5; TEA-0.15/Na-2.5; and TEA-0.3/Na-2.5 NCs. (b-d) TEM images (left) and their histograms of edge widths as well as lengths (right) of TEA-0.05/Na-2.5 (b); TEA-0.15/Na-2.5 (c); and TEA-0.3/Na-2.5 (d) NCs.

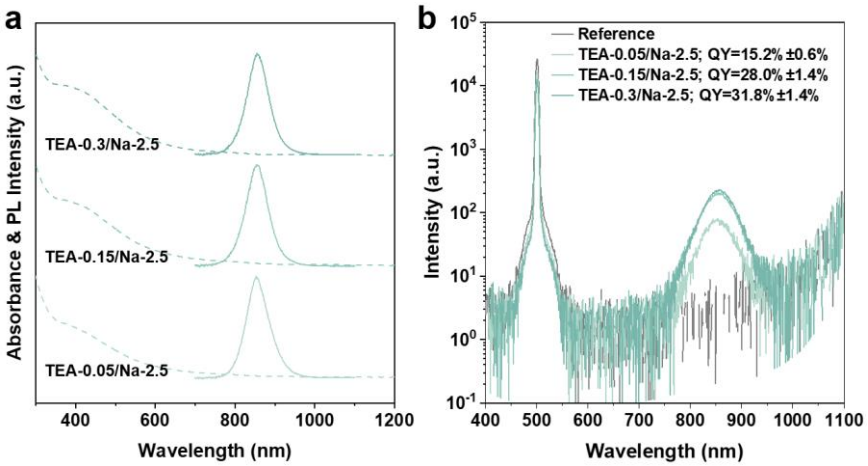

Figure 4.16 (a) Normalized PL (solid lines) spectra and optical absorption (dashed lines) of TEA-0.05/Na-2.5; TEA-0.15/Na-2.5; and TEA-0.3/Na-2.5 NCs. (c) PLQY measurements of TEA-0.05/Na-2.5; TEA-0.15/Na-2.5; and TEA-0.3/Na-2.5 NCs.

Secondly, I kept the amount of TEA (TEA: FA=0.25: 1), while change the amount of Na. The molar ratios of Na: FA=0.5:1, 1.5:1, and 3.5:1, and the corresponding products are denoted as TEA-0.25/Na-0.5; TEA-0.25/Na-1.5; TEA-0.25/Na-3.5. The XRD patterns of as-prepared products are displayed in **Figure 4.17a**. All three samples match well with cubic $FASnI_3$ structure. Their TEM images and corresponding size-distribution histograms are shown in **Figure 4.17b-d**. The average width and length for TEA-0.25/Na-0.5 are 22.7 nm and 24.2 nm; those for TEA-0.25/Na-1.5 are 19.1 nm and 27.3 nm; those for TEA-0.25/Na-3.5 are 20.4 nm and 32.5 nm. I note that, with increasing the amount of Na, the average width has no obvious different but the length becomes longer, indicating that Na can promote the growth of $FASnI_3$ NCs along [100] direction (**Figure 4.12c**). **Figure 4.18a** displays their absorption and PL properties. All three samples have almost same absorption and PL spectra, while their PLQYs are quite different: 6.0±0.3%; 19.7± 1.4%; and 33.9±0.6% for TEA-0.25/Na-0.5; TEA-0.25/Na-1.5; and TEA-0.25/Na-3.5, respectively (**Figure 4.18b**). The best ratio of Na: FA is 2.5:1 that have been discussed above (**Figure 4.13**). With increasing the amount of Na, we can see the increase in PLQYs until Na: FA=2.5:1. Further increase the amount of Na can induce slight decrease in PLQY.

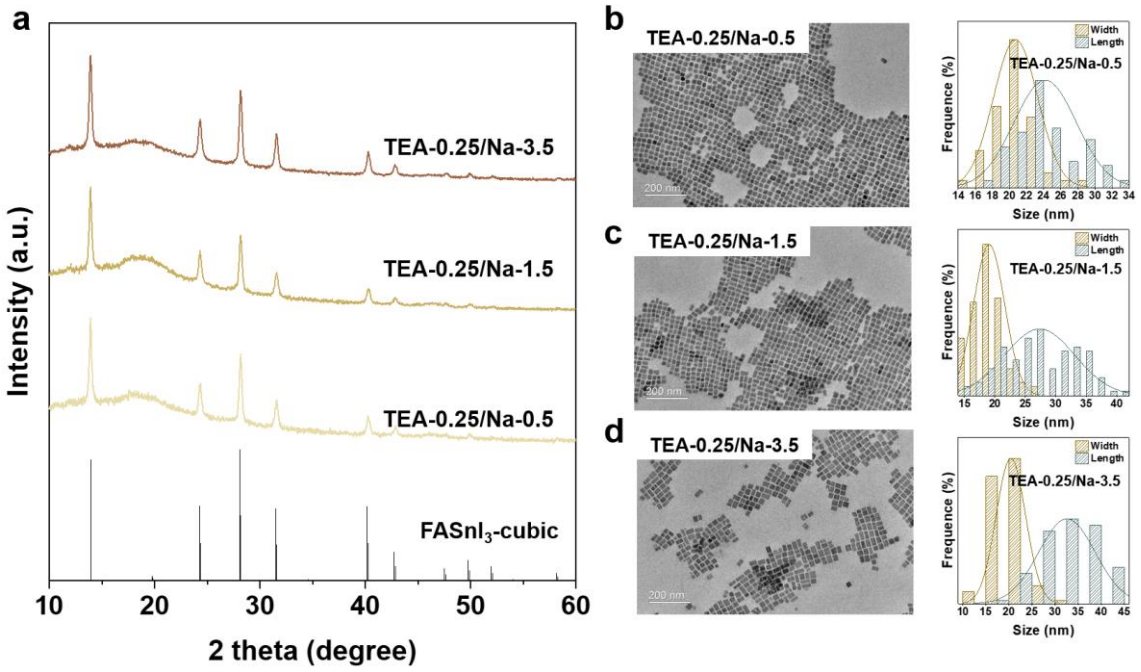

Figure 4.17 (a) XRD patterns of TEA-0.25/Na-0.5; TEA-0.25/Na-1.5; and TEA-0.25/Na-3.5 NCs. (b-d) TEM images (left) and their histograms of edge widths as well as lengths (right) of TEA-0.25/Na-0.5 (b); TEA-0.25/Na-1.5 (c); and TEA-0.25/Na-3.5 (d) NCs.

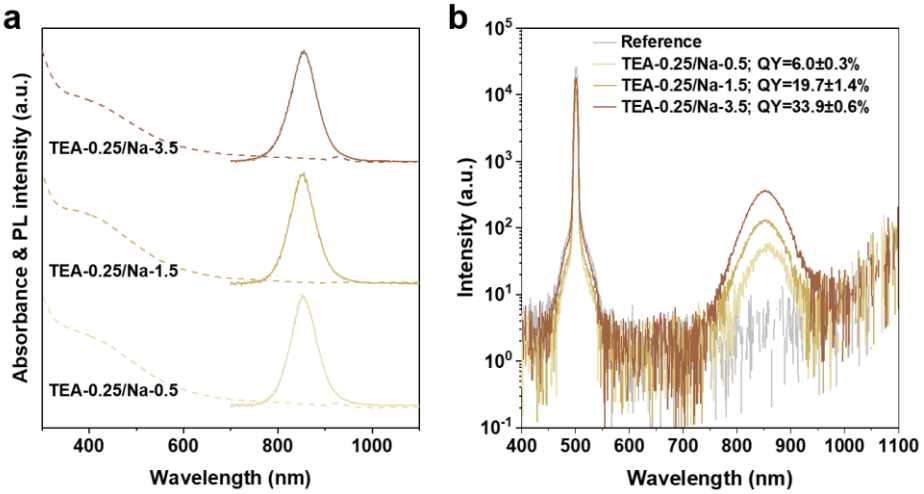

Figure 4.18 (a) Normalized PL (solid lines) spectra and optical absorption (dashed lines) of TEA-0.25/Na-0.5; TEA-0.25/Na-1.5; and TEA-0.25/Na-3.5 NCs. (c) PLQY measurements of TEA-0.25/Na-0.5; TEA-0.25/Na-1.5; and TEA-0.25/Na-3.5 NCs.

My synthesis route was conducted under Sn-rich reaction condition: FA: Sn: I=0.2: 1.4: 1 (See **Figure 4.6** and **Experiment section**) that is guided by DFT calculations

(**Figure 4.1**). To further confirm that Sn-rich reaction condition is necessary for getting highly luminescent $FASnI_3$ NCs, I then studied the photophysical properties of $FASnI_3$ NCs with reducing amount of Sn. The amount of Sn: I was reduced to 1.2:1 and 1:1, and the as-prepared products are denoted as Sn: I=1.2:1 and Sn: I=1:1. **Figure 4.19** displays the structural and optical properties of as-prepared NCs. The XRD patterns confirm the pure phase of cubic $FASnI_3$ NCs (**Figure 4.19a**). From **Figure 4.19b, c**, we can see that the average width and length for Sn:1=1.2:1 are 19.4 nm and 30.7 nm, respectively; those for Sn: I=1:1 are 27.6 nm and 36.8 nm, respectively. With decreasing the amount of Sn, both width and length of particles are larger. PLQY results in **Figure 4.19d** confirms that reducing Sn amount leads to decreased PLQYs: $19.2 \pm 0.9\%$ and $11.9 \pm 0.6\%$ for Sn:1=1.2:1 and Sn: I=1:1, respectively, suggesting that Sn-rich reaction condition is essential, well in agreement with DFT calculations as discussed above.

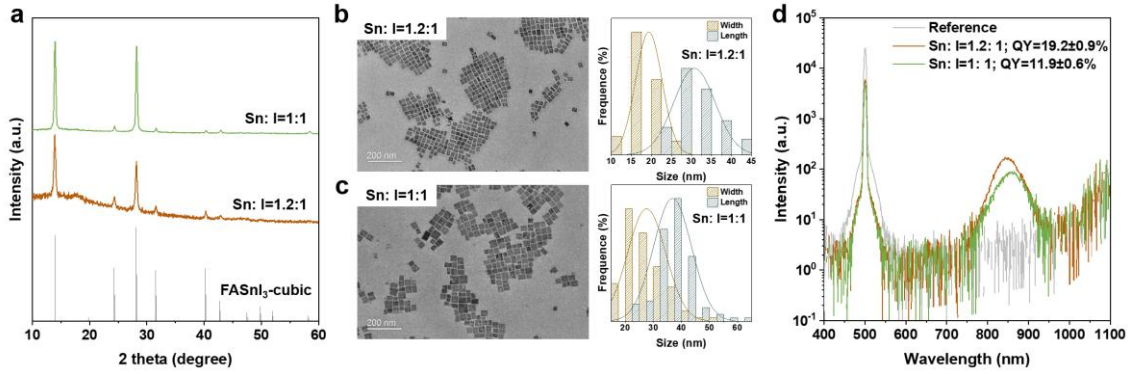

Figure 4.19 (a) XRD patterns of $FASnI_3$ NCs synthesized with different ratios of Sn: I. (b, c) TEM images (left) and their histograms of edge widths as well as lengths (right) of $FASnI_3$ NCs synthesized with different ratios of Sn: I. (d) PLQY measurements of $FASnI_3$ NCs synthesized with different ratios of Sn: I.

The synthesis of perovskite NCs is normally strict with the manufacturer and purity of reagents. To study this effect, I tried to synthesize TEA-0.25/Na-2.5 NCs using different ODE and SnI_2 from other manufacturers. As displayed in **Figure 4.20**, using ODE from Kanto (purity is 95.5% from COA, see **Table 4.1**)), the PLQY slightly decreased to 34.8%; while using SnI_2 from Strem (purity is 99%, see **Table 4.1**), the PLQY largely decreased to 23.1%, possible since the lower purity of these reagents. To

help others better reproduce highly luminescent $FASnI_3$ NCs, the manufacturers, batch numbers, and purities from COA of all the reagents used here are listed in **Table 4.1**.

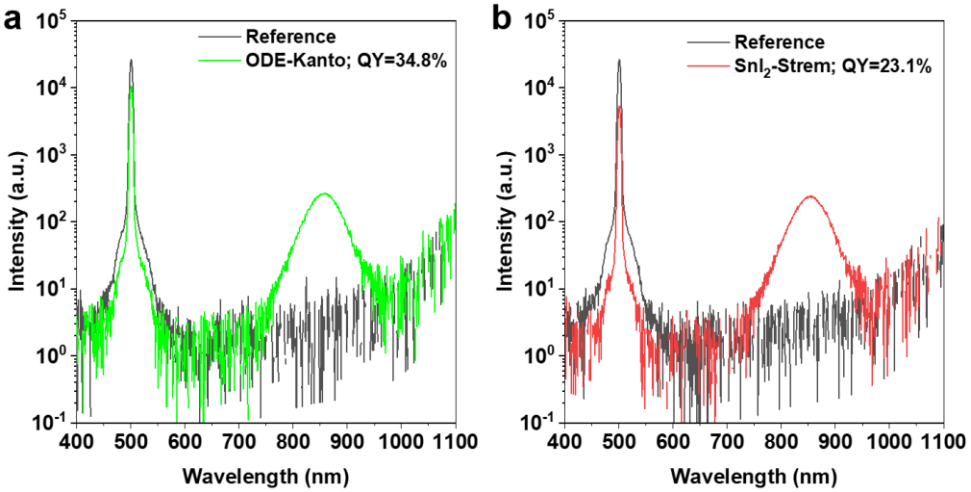

Figure 4.20 PLQY measurements of TEA-0.25/Na-2.5 NCs using (a) ODE from Kanto and (b) SnI_2 from Strem.

Experimental observations confirm that introduction TEA^+ and Na^+ in the reaction system can produce high-quality $FASnI_3$ NCs with great PLQY. To take an insight into the effect of TEA^+ and Na^+, I firstly studied the presence and distribution of these cations. Elemental mapping was performed on TEA-0.25, Na-2.5 NCs, as shown in **Figure 4.21**. All the corresponding mapping images of N, Sn, I, Na, S, P are overlapping with the TEM image, illustrating the existence of Na and TEA in the TEA-0.25, Na-2.5 NCs. In addition, P comes from C_{44}-PC ligand. The element ratio of Na: S: N: Sn: I: P is 0.38: 0.04: 2.4: 1: 1.67: 0.42, showing extremely high concentration of Na and small amount of TEA. It is noted that the concentration of I is less than the normal value. The possible reason is that long-time EDS mapping may induce the loss of I element. From the STEM images before and after EDS mapping, we also can see the partial damage of $FASnI_3$ NCs upon X-ray irradiation.

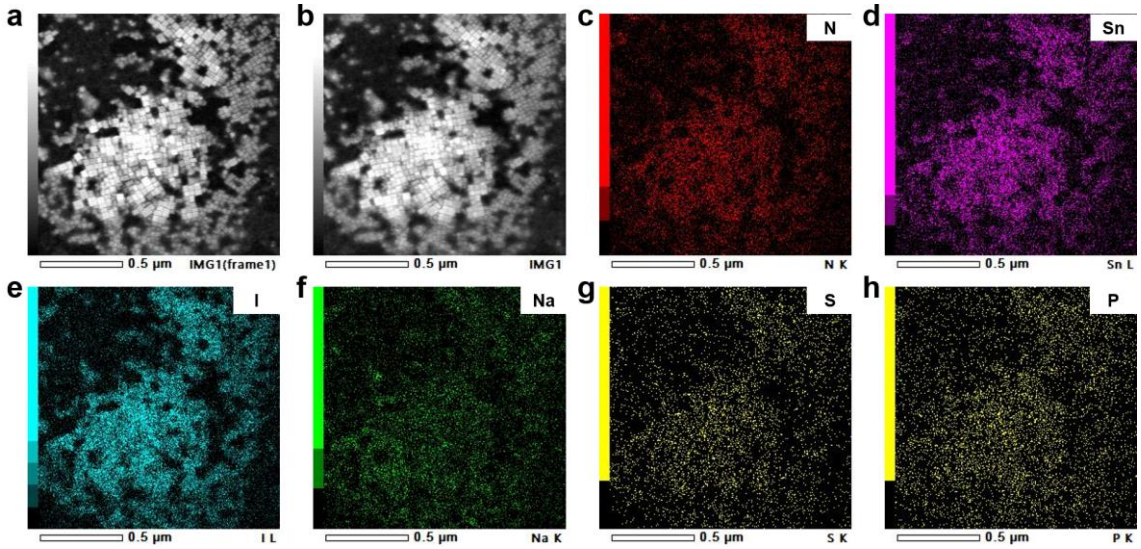

Figure 4.21. (a) HAADF-STEM image of TEA-0.25/Na-2.5 NCs before EDS mapping. (b) HAADF-STEM image of TEA-0.25/Na-2.5 NCs after EDS mapping. (c-h) STEM-EDS element mapping of N, Sn, I, Na, S, and P.

Then, I used ICP to confirm the actual concentration of Na. ICP result shows that Na/Sn is 48.0% for TEA-0.25/Na-2.5 (**Figure 4.22a, Table 4.2**). **Table 4.2** also lists the molar ratio of Na: Sn of other samples. All of them show a high Na concentration. From the HRTEM as discussed above, TEA-0.25/Na-2.5 NCs have same lattice constant with that of control NCs, indicating Na^+ ions do not enter the lattice of NCs (**Figure 4.12**). In addition, such a large amount of Na^+ ions cannot be all on the surface of NCs, since that even all surface FA^+ ions are replaced by Na^+, the ratio of Na/Sn for a $FASnI_3$ NC with ~30 nm particle size is only ~10%. Based on these, I speculate that there are some Na^+-related complexes mixed with $FASnI_3$ NCs, because there are some oily organic in the final product. To confirm it, I washed $FASnI_3$ NCs by hexane once and twice to remove the oily organic. The ICP results show that the concentration of Na largely decreased after wash: Na/Sn=7.7% and 3.6% for wash once and twice NCs (**Figure 4.22a, Table 4.2**), suggesting that some Na^+-related complexes are mixed with the final $FASnI_3$ NCs. Interestingly, I find that structure and morphology of NCs after wash had no obviously changes (**Figure 4.23 a-c**), but their PLQY decreased a lot: 15.2±1.6% and 10.0±0.4% for wash once and twice NCs (**Figure 4.22a, 23d**), compared with the highly luminescent unwashed NCs (**Figure 4.22a**), indicating that these Na^+-related complexes have surface

passivation effect. **Figure 4.22b** displays the high-resolution ESI-MS spectra of TEAI and TEA-0.25, Na-2.5 NCs dissolved in methanol. Two distinct peaks at m/z of 111.03 and 128.05 were detected for both TEAI reactant and NCs. The peak of 128.05 is from the signal of TEA^+, and the peak of 111.03 is from the split fraction of TEA^+. Both confirm the presence of TEA^+ in the final product.

To understand the surface passivation effect of TEA^+ and Na^+, I then conducted electrokinetic potential (ζ-potential) measurements for four main samples, which are displayed in **Figure 4.22b**. The ζ-potentials were obtained by using Henry's equation and the Hückel approximation for non-polar systems:

$$\frac{U}{E} = \frac{2\varepsilon\zeta F(\kappa a)}{3\eta} \tag{10}$$

where U/E is the electrophoretic mobility obtained using the instrument, ζ is the ζ potential, ε is the solvent dielectric permittivity, η is the viscosity and F(κa) is the dimensionless Henry function. For non-polar systems, the Hückel approximation is applied and the value of Henry's function is close to 1. To avoid the degradation, all measurements were conducted in N_2-filled glovebox (See **Experimental section**). Control NCs have a negative ζ potential of ~-15.0 eV, indicating the negative charge surface, due to the abundant presence of FA vacancies on the surface or subsurface of $FASnI_3$ NCs. TEA-0.25 NCs have a ζ potential of ~-3.1 eV. TEA^+ can lead to a TEAI-termination surface, reduce the surface FA vacancies, and thus increase the surface ζ potential. Interestingly, Na-2.5 and TEA-0.25/Na-2.5 NCs have a positive ζ potential of 14.5 mV and 27.0 mV. It is noted that abundant Na ions (38.4% of Na/Sn and 48.0% of Na/Sn for Na-2.5 and TEA-0.25/Na-2.5 NCs, See **Figure 4.22a** and **Table 4.3**) as ligand-shell are present on the surface area of $FASnI_3$ NCs, which could result in a bipolar-shell surface. Na^+-enriched outer shell thus can promote a positive ζ potential. Dong et al. also found the similar passivation mechanism in $CsPbBr_3$ NCs.[54]

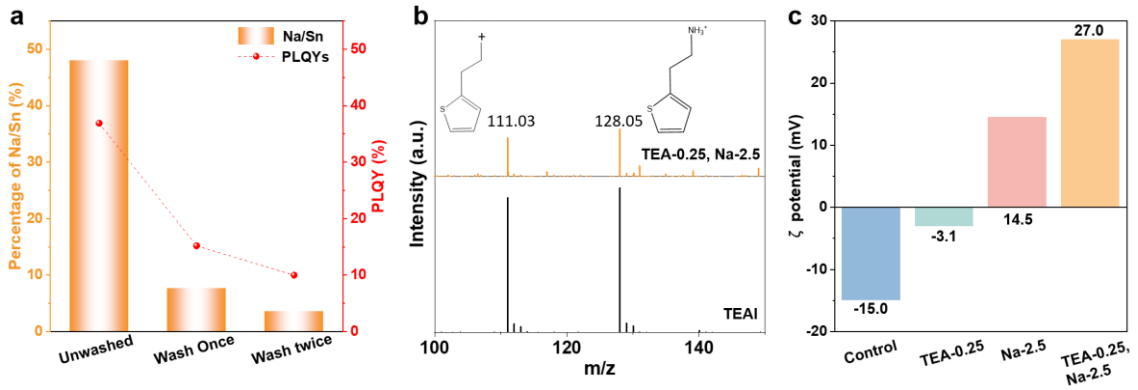

Figure 4.22 (a) The percentage of Na/Sn tested from ICP, and PLQYs of unwashed, wash once, and wash twice TEA-0.25/Na-2.5 NCs. (b) ESI-MS peaks of TEAI and TEA-0.25/Na-2.5 NCs dissolved in methanol. (c) ζ potentials of control; TEA-0.25; Na-2.5; TEA-0.25/Na-2.5 NCs.

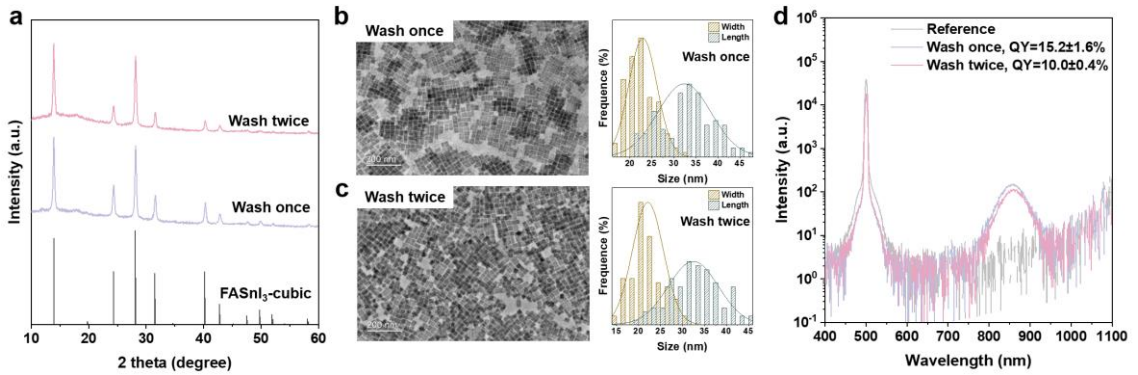

Figure 4.23 (a) XRD patterns of $FASnI_3$ NCs after wash once and twice. (b, c) TEM images (left) and their histograms of edge widths as well as lengths (right) of $FASnI_3$ NCs after wash once and twice. (d) PLQY measurements of $FASnI_3$ NCs after wash once and twice.

Table 4.3. ICP results and calculated molar ratio of Na/Sn of $FASnI_3$ NCs

Sample	Na (mass%)	Sn (mass%)	Molar ratio of Na/Sn
Na-2.5	0.067	0.90	38.4%
TEA-0.25/Na-0.5	0.015	0.45	17.2%
TEA-0.25/Na-1.5	0.034	0.59	29.7%
TEA-0.25/Na-2.5	0.053	0.57	48.0%

TEA-0.25/Na-3.5	0.063	0.68	47.8%
Wash once	0.15	10	7.7%
Wash twice	0.12	17	3.6%

X-ray photoelectron spectroscopy (XPS) was also used for understanding the surface condition of $FASnI_3$ NCs. As display in **Figure 4.24a**, high-resolution Sn 3d XPS spectra for TEA-0.25/Na-2.5 NCs are highly asymmetric indicating the presence of more than one oxidation of Sn. Six components in the fitted spectrum can be readily observed: the peaks located at 493.08 eV and 484.67 eV can be assigned to Sn $3d_{3/2}$ and Sn $3d_{5/2}$, which aligns with the binding energies of Sn^0; the peaks located at 494.12 eV and 485.71 eV can be assigned to Sn $3d_{3/2}$ and Sn $3d_{5/2}$ from Sn^{2+}; those located at 495.19 eV and 486.78 eV comes from the Sn $3d_{3/2}$ and Sn $3d_{5/2}$ of Sn^{4+}.[55] Additionally, I also can observe Na KLL auger peak located at 497.91 eV in **Figure 2.24a**.[56] Here, Sn^0, Sn^{2+}, and Sn^{4+} signals are all detected, and their contents are 62.15%, 24.43%, and 13.42% for Sn^0, Sn^{2+}, and Sn^{4+}, respectively. I could be well-fitted by one curve as shown in **Figure 4.24b**. Then I turned to observer the signal of S and Na of TEA-0.25/Na-2.5 NCs. As shown in **Figure 4.25a**, S 2p spectrum can be fitted by four components. The peaks located at 165.85 eV and 164.67 eV comes from S $2P_{1/2}$ and $2P_{3/2}$ of natural thiophene for TEA.[57] However, the peaks at 169.34 eV and 168.16 eV originates from a higher oxidation of S $2P_{1/2}$ and $2P_{3/2}$,[58] which may be resulted from the coordination between TEA and Sn.

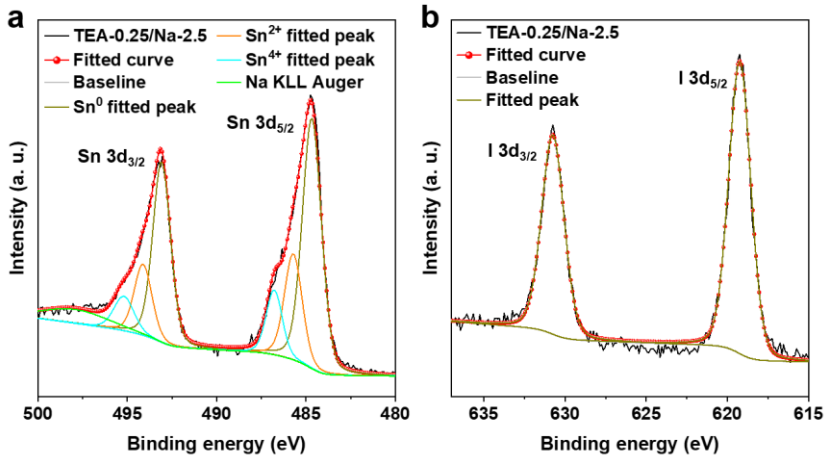

Figure 4.24. (a) High-resolution XPS spectra of Sn 3d doublet for TEA-0.25/Na-2.5 NCs. (b) High-resolution XPS spectra of I 3d doublet for TEA-0.25/Na-2.5 NCs.

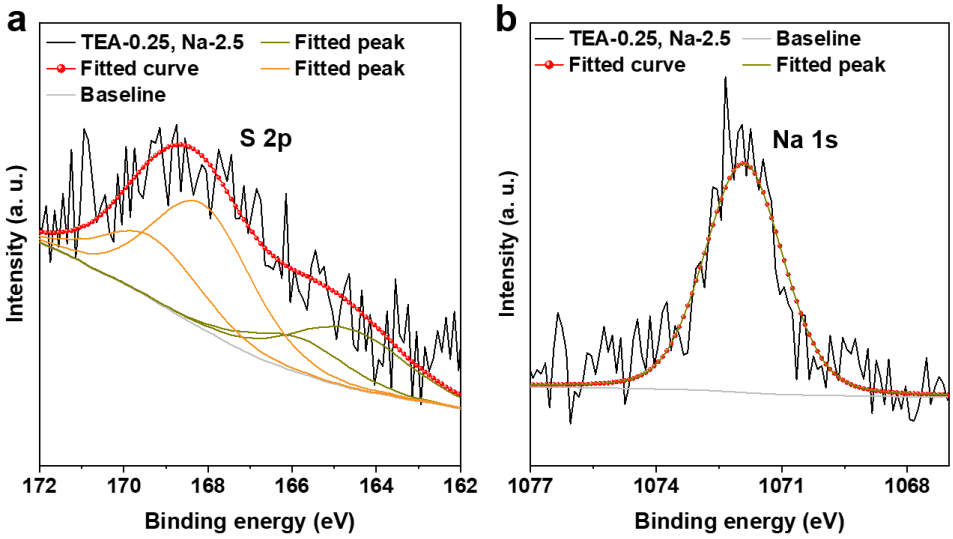

Figure 4.25. (a) High-resolution XPS spectra of S 2p doublet for TEA-0.25/Na-2.5 NCs. The fitted peaks colored by dark yellow originate from neutral thiophene, while those colored by orange may originate from the oxidated thiophene. (b) High-resolution XPS spectra of Na 1s for TEA-0.25/Na-2.5 NCs.

To further understand the surface reconstruction by TEA^+ and Na^+, we then did the DFT calculations. Surface defect transition levels shown in **Figure 4.2b** lets me know that V_I is the dominate defect that can induce the nonradiative recombination in $FASnI_3$ NCs. So, we did the DFT calculation for the formation energies of V_I on the NC surface. As display in **Figure 26a-c**, we constructed three different surface conditions: 1) TEA^++ 2 Na^+; 2) TEA^++ 4 Na^+; 3) TEA^++6 Na^+. The provided three conditions are based on our experimental results that abundant Na^+ ions are in the final product. The calculated formation energies are shown in **Figure 4.26d**. Under Sn-rich reaction condition, the formation energies of V_I are -0.81 eV, 0.70 eV, 1.30 eV, for TEA^++ 2 Na^+, TEA^++ 4 Na^+, and TEA^++6 Na^+ surfaces, respectively, indicting the increase formation energy with more Na^+ ions absorbing on the NC surface, in agreement with our above experimental results. Under I-rich reaction condition, although the defect formation energies of surface V_I are higher than Sn-rich and moderate conditions for all three surface states (**Figure 4.26d**), some other point defects in bulk, such as V_{Sn}, I_i, V_{FA} will have lower formation energies (**Figure 4.1b**), which induces more defect states inside $FASnI_3$ lattice.

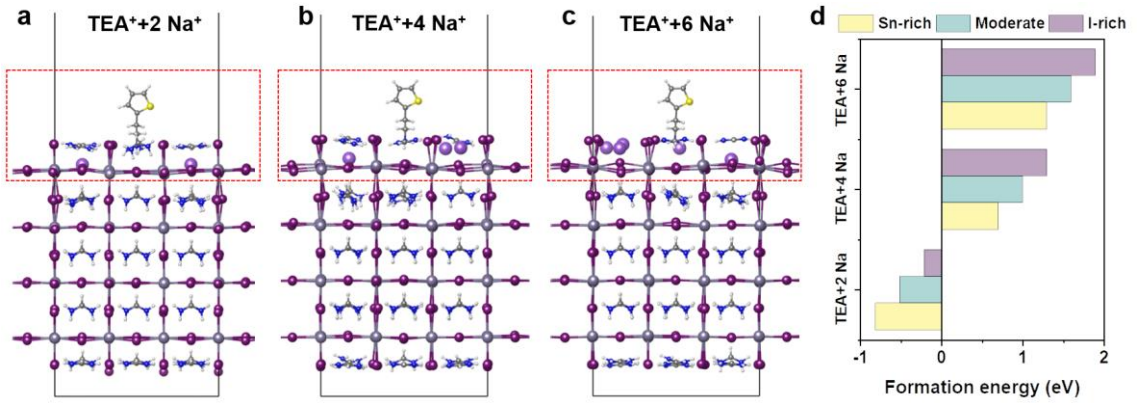

Figure 4.26. Optimized crystal structures for FAI-rich (100) supercell with surface (a) TEA^++2 Na^+, (b) TEA^++4 Na^+, and (c) TEA^++6 Na^+. (d) Calculated defect formation energies of V_I for three different surfaces under Sn-rich, moderate, and I-rich reaction conditions. The DFT calculations were performed at GGA/PBE+vdW level.

To elucidate the synergistic effect of TEA^+ and Na^+ in enhancing the luminescence of $FASnI_3$ NCs, we performed Ab Initio Molecular Dynamics (AIMD) simulations to generate Radial Distribution Function (RDF) plots for Na-I and S-I pairs both at 300 K and 400 K. These RDF plots serve as a powerful tool to probe the atomic-level stability of adsorbed TEA^+ and Na^+ (**Figure 4.27, 4.28, 4.29**). **Figure 4.27 a and b** display diagrammatic representation of S atom and four near I atoms for RDF calculations. The temperatures as a function of time in AIMD both at 300 K and 400 K for three different surface conditions are shown in **Figure 4.28**. In **Figure 4.29**, the presence of distinct RDF peaks indicates preferred interatomic distances, shedding light on the underlying atomic structure. In the Na-I RDF, a prominent peak near 3 Å suggests that Na^+ ions remain tightly bound to I^- ions, consistent with the Na-I bond length in DFT-optimized structures, indicating minimal atomic displacement. The RDF for the S-I pair displays two peaks at approximately 6 Å and 11 Å, corresponding to the distances between S and two distinct I atoms, signifying that TEA^+ remains adsorbed on the NC surface during the AIMD simulations. (**Figure 4.29**). Additionally, the first peak's FWHM in the Na-I RDF narrows with increasing Na^+ concentration, particularly at 300 K, suggesting that higher Na^+ levels contribute to greater surface stabilization (**Figure 4.27c**).

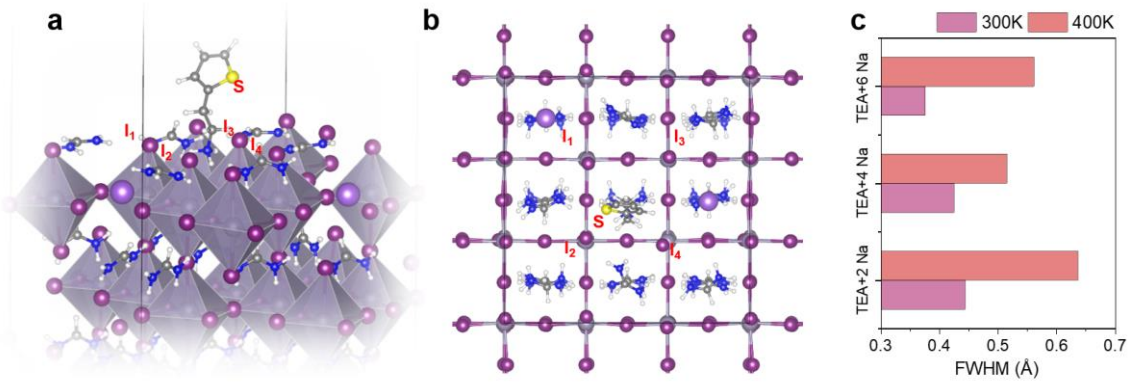

Figure 4.27. (a, b) Diagrammatic representation of S atom and four near I atoms for RDF calculations. (c) Full-width at half-maximum (FWHM) of the Gaussian function fitted first peak in radial distribution function obtained from the MD simulations for FAI-rich surface with $TEA^+ + 2\ Na^+$, $TEA^+ + 4\ NA^+$, and $TEA^+ + 6\ Na^+$, at 300K and 400K.

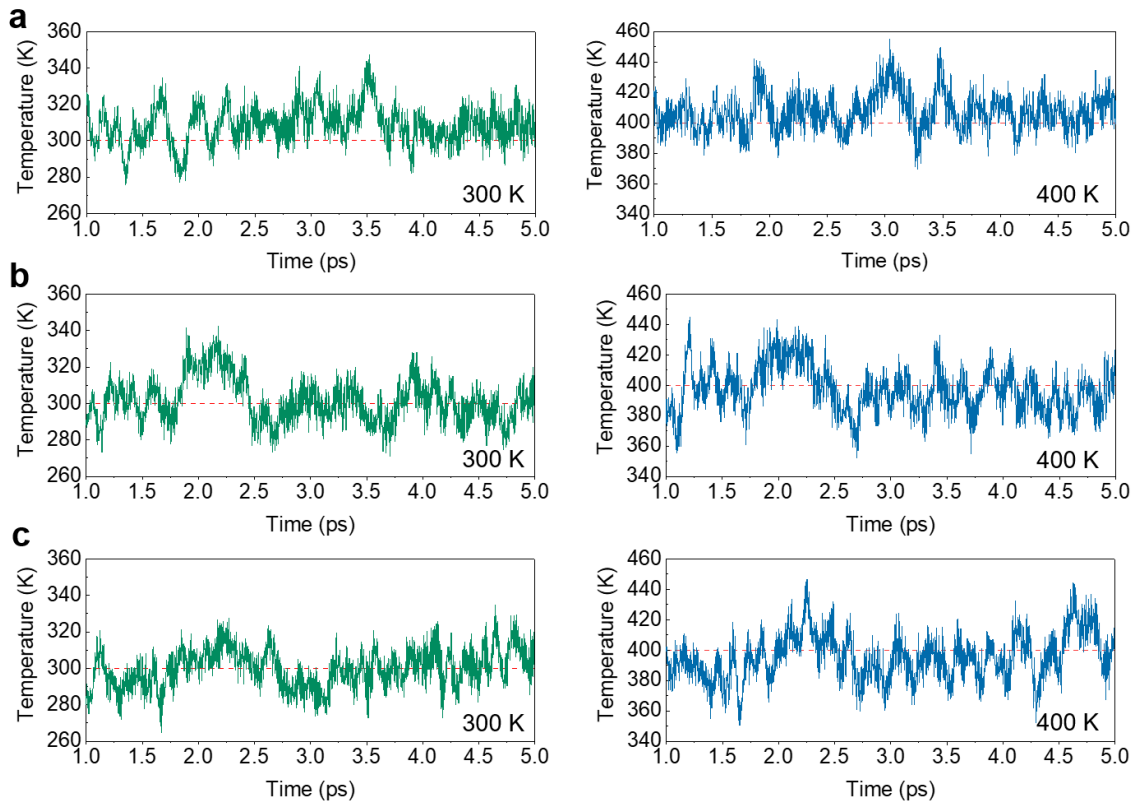

Figure 4.28. The temperature as a function of time in molecular dynamic simulations for (a) $TEA^+ + 2\ Na^+$, (b) $TEA^+ + 4\ NA^+$, (c) $TEA^+ + 6\ Na^+$ absorbed on the FAI rich surface at 300 K (left) and at 400 K (right).

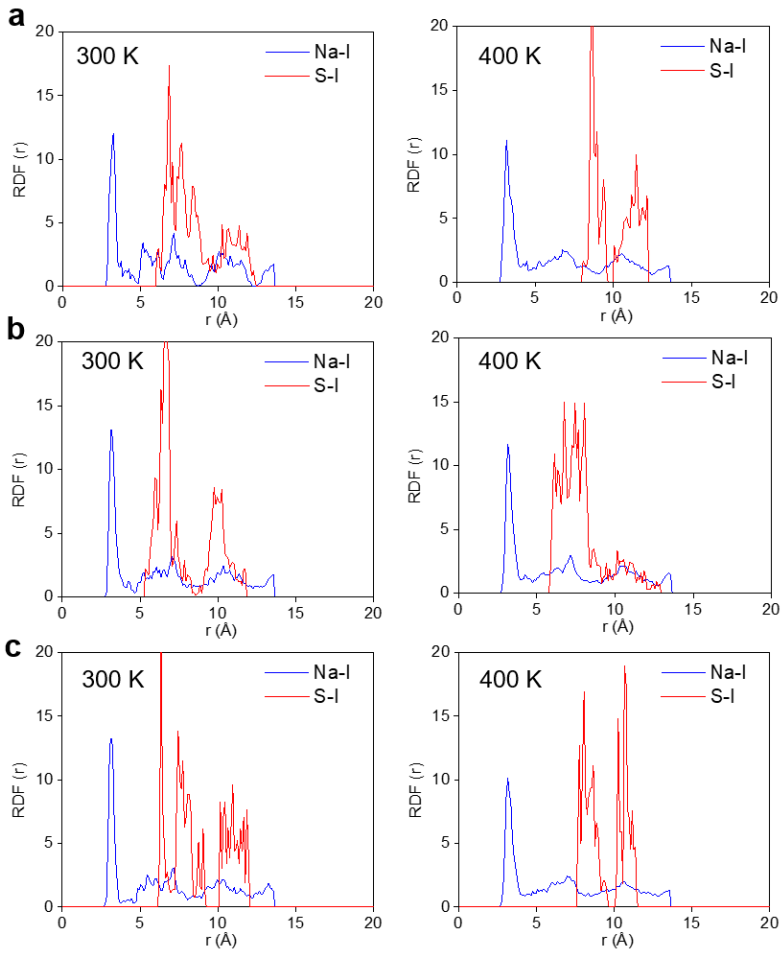

Figure 4.29. RDF plots obtained from the MD simulations for (a) TEA^+ + 2 Na^+, (b) TEA^+ + 4 NA^+, (c) TEA^+ + 6 Na^+ absorbed on the FAI rich surface at 300 K (left) and at 400 K (right).

Based on all experimental fact, I propose a plausible mechanism for the surface reconstruction by TEA^+ and Na^+ in $FASnI_3$ NCs (**Figure 4.30**). Firstly, without TEA^+ and Na^+, the $FASnI_3$ surface is terminated by SnI_2, since the reaction was conducted under Sn-rich condition. However, SnI_2-terminated surface is unstable, because of the much low defect formation energies of V_{Sn} and V_I. The defective SnI_2-terminated surface is illustrated in **Figure 4.30a**. Although our calculation results do not find that surface V_{Sn} and V_I defects can introduce deep defect levels between CBM and VBM (**Figure 4.2c**), this unstable surface may induce the degradation of NCs and thus may generate other defects both on the NC surface and inside NC lattice. The modified surface by TEA^+ and Na^+ is displayed in **Figure 4.30b**. After the introduction of TEA^+ and Na^+, NC surface is

terminated by TEAI/NaI. A small amount of TEA^+ cations and a large amount of Na^+ cations absorb on NC surface as organic and inorganic ligand-shell, not only reducing the surface V_{FA}, but only stabilizing the surface I^- ions that circled by red (**Figure 4.30b**). The modified TEAI/NaI-terminated surface has low defect density, contributing to the enhancement in PLQY (**Figure 4.13**).

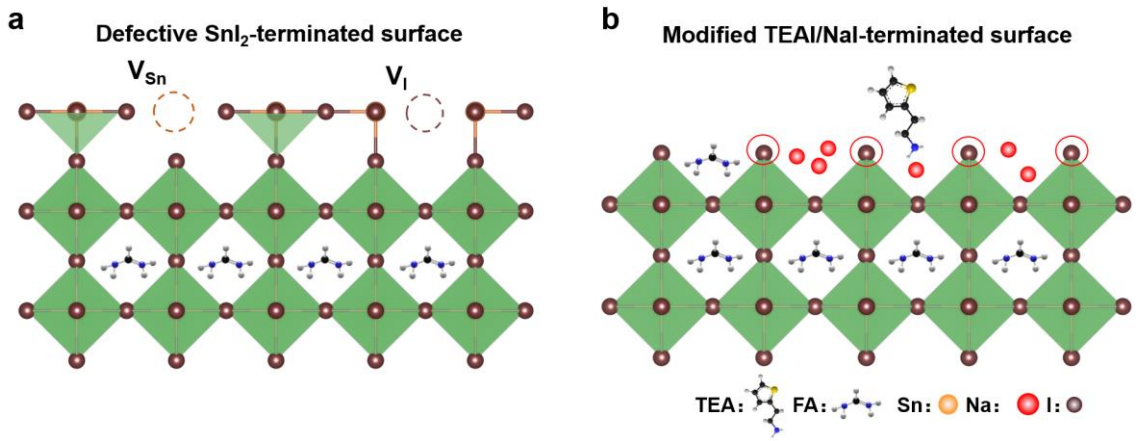

Figure 4.30. Schematic illustration of the proposed surface modification. (a) Defective SnI2-terminated surface without TEA^+ and Na^+. (b) Modified TEAI/NaI-terminated surface after introduction of TEA^+ and Na^+.

Post-synthesis treatment is another possible strategy for achieving surface reconstruction. To verify this possibility. I then used Na-oleate as ligand to treat $FASnI_3$ NCs. Due to the poor solubleness of TEA-related reagents in non-polar solvent, I only tried Na post-treatment instead of TEA. Na-oleate was firstly dissolved in hexane, and then Na-oleate solution was injected into NC-hexane solution for PLQY measurement (See **Experiment section**). The PLQY results are listed in **Table 4.4**. We can see that, after Na-oleate post-treatment, the PLQY of control NCs was increased to 3.2±0.3%, and that of TEA-0.25 NCs was increased to 12.2±0.8%, indicating the feasibility of post-synthetic surface reconstruction. But for TEA-0.25/Na-2.5 NCs, the additional Na-oleate induced the decrease in PLQY, possibly because of the already passivated NC surface. This post-treatment here provides another flexible route to getting highly luminescent $FASnI_3$ NCs.

Table 4.4. PLQYs of control; TEA-0.25; TEA-0.25/Na-2.5 NCs after post-synthetic treatment by different amount of Na-oleate.

Sample	Control			TEA-0.25			TEA-0.25/Na-2.5		
Amount of Na-oleate (μL)	5	10	20	5	10	20	2	5	10
PLQY (%)	2.4± 0.2	3.1± 0.3	3.2± 0.3	9.4± 0.6	12.2 ±0.8	11.4 ±1.5	36.7 ±1.1	33.1 ±0.6	20.1 ±1.8

I finally demonstrate that my synthetic concept is sufficiently general and can be extended for the synthesis of FA/Cs alloying tin halide perovskite NCs. By partially replacing FA-oleate with Cs-oleate, I can produce $FA_{0.9}Cs_{0.1}SnI_3$ and $FA_{0.8}Cs_{0.2}SnI_3$ perovskite NCs (**Figure 4.31a, b**). The calculated element ratios from STEM-EDS are displayed in **Figure 4.32**. Interestingly, from TEM images, we can see that the morphology of FA/Cs alloying NCs tends to become nanowires. The average width and length for $FA_{0.9}Cs_{0.1}SnI_3$ NCs are 18.6 nm and 32.1 nm; while those for $FA_{0.8}Cs_{0.2}SnI_3$ NCs are 14.6 nm and 81.5 nm. With more Cs, NC exhibits shorter width and longer length. HRTEM image (**Figure 4.33**) shows that $FA_{0.8}Cs_{0.2}SnI_3$ nanowires have the property of orthorhombic phase, indicating Cs^+-induced phase transition. Possibly, due to different surface energy of (001) and (100) planes, $FA_{0.8}Cs_{0.2}SnI_3$ has a trend to grow along [001] direction, and finally forms nanowire.

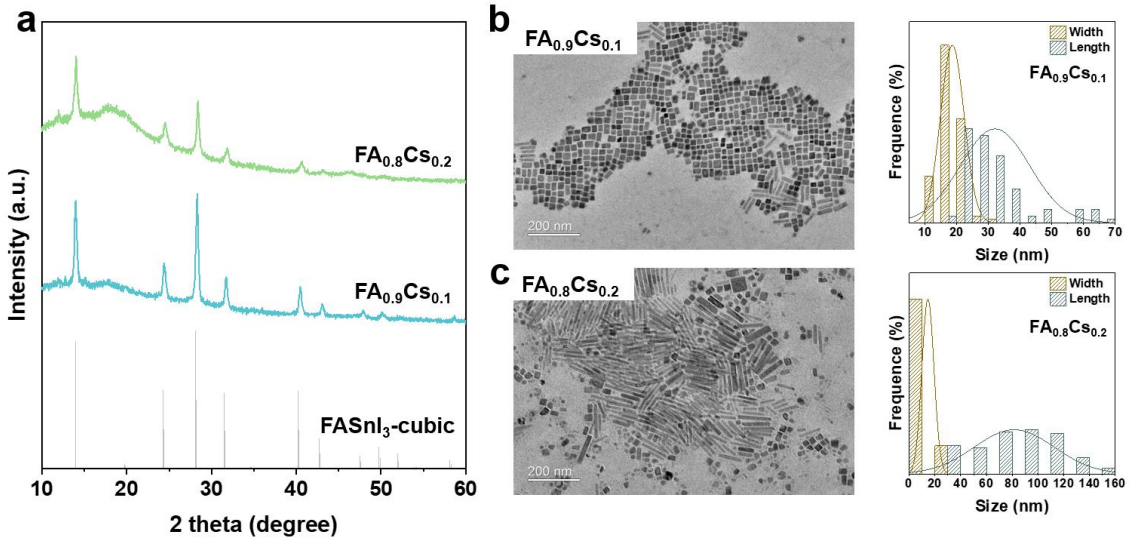

Figure 4.31. (a) XRD patterns of $FA_{0.9}Cs_{0.1}SnI_3$ and $FA_{0.8}Cs_{0.2}SnI_3$ NCs. (b, c) TEM images (left) and their histograms of edge widths as well as lengths (right) of $FA_{0.9}Cs_{0.1}SnI_3$ and $FA_{0.8}Cs_{0.2}SnI_3$ NCs.

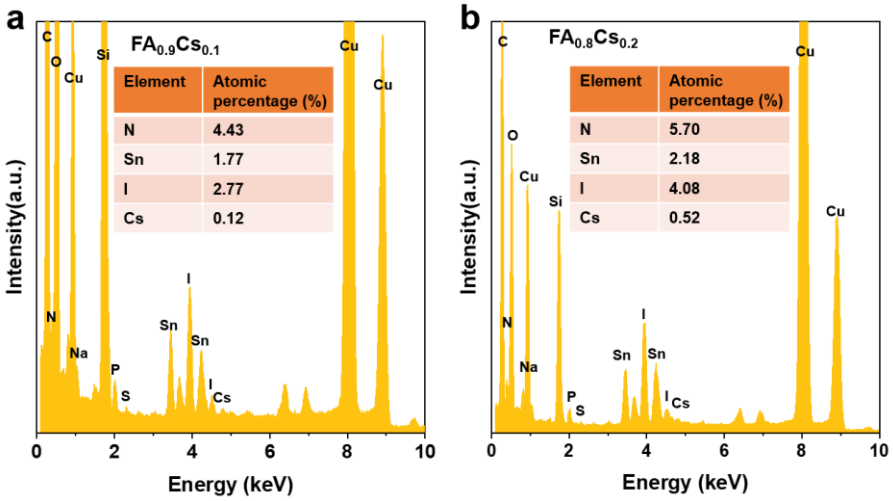

Figure 4.32. STEM-EDS spectra and calculated atomic ratios of $FA_{0.9}Cs_{0.1}SnI_3$ NCs (a) and $FA_{0.8}Cs_{0.2}SnI_3$ NCs (b).

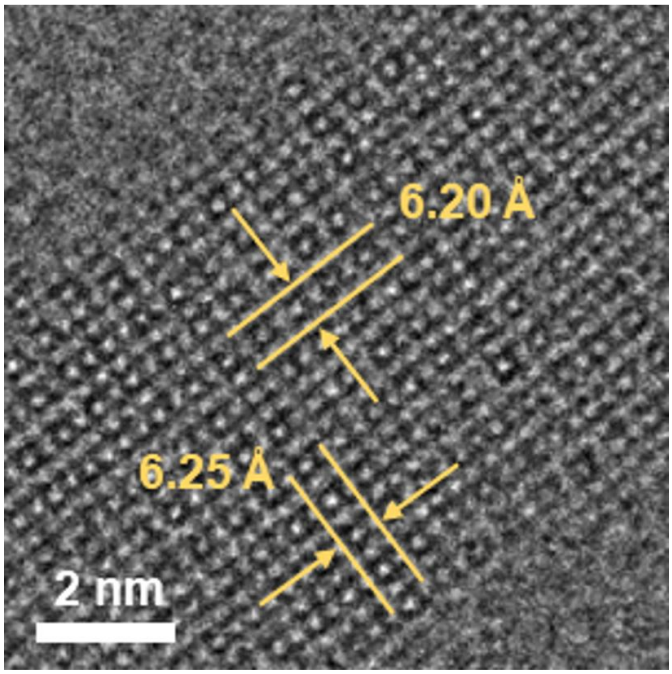

Figure 4.33. HRTEM image of $FA_{0.8}Cs_{0.2}SnI_3$ nanowires.

Figure 4.34a displays the absorption and PL spectra of as-prepared NCs. As expected, with increasing Cs content, the absorption and PL spectra red-shift owing to the

narrowing of the band gap. The $FA_{0.9}Cs_{0.1}SnI_3$ and $FA_{0.8}Cs_{0.2}SnI_3$ NCs show emission peaks at 881 nm and 898 nm , with PLQYs of 26.7±1.2% and 21.1±1.2%, respectively (**Figure 4.34a, b**). The $FA_{0.9}Cs_{0.1}SnI_3$ and $FA_{0.8}Cs_{0.2}SnI_3$ NCs demonstrate average PL decays of 97.48 ns and 59.76 ns, respectively (**Figure 4.34c, Table 4.5**). Although the PLQYs of these NCs are still lower than those of lead-based cousins, they represent the record values among those of FA/Cs alloying tin halide perovskite NCs. I believe that further fine-tuning of other synthetic parameters, such as synthetic temperatures, the relative ratios of precursors, and the amount of capping agents, could result in higher PLQYs.

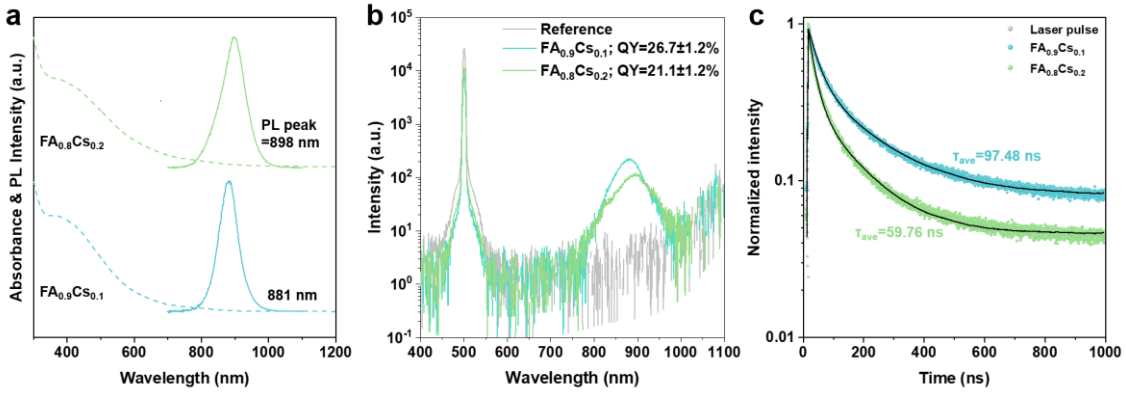

Figure 4.34. (a) Normalized PL (solid lines) spectra and optical absorption (dashed lines) of $FA_{0.9}Cs_{0.1}SnI_3$ and $FA_{0.8}Cs_{0.2}SnI_3$ NCs. (b) PLQY measurements of $FA_{0.9}Cs_{0.1}SnI_3$ and $FA_{0.8}Cs_{0.2}SnI_3$ NCs. (c) PL decay traces of $FASnI_3$ NCs. The black curves are their fitting curves.

Table 4.5. Fitted lifetimes (τ_1, τ_2), average lifetimes (τ_{ave}) using a biexponential function, and PLQYs of $FA_{0.9}Cs_{0.1}SnI_3$ and $FA_{0.8}Cs_{0.2}SnI_3$ NCs.

Samples	A_1	τ_1 (ns)	A_2	τ_2 (ns)	τ_{ave} (ns)	PLQY (%)
$FA_{0.9}Cs_{0.1}$	0.60	36.03	0.40	189.75	97.48	26.7

$FA_{0.8}Cs_{0.2}$	0.69	23.95	0.31	140.89	59.76	21.1

4.4 Conclusion

In summary, I have successfully developed a one-pot surface modification strategy for the synthesis of highly luminescent $FASnI_3$ perovskite NCs by regulating NC surface termination. DFT calculations of the formation energies and transition levels of several point defects both in the bulk and on the surface of $FASnI_3$ predicted that obtaining highly luminescent $FASnI_3$ NCs should meet following three factors: 1). Creating a Sn-rich reaction condition that reduces intrinsic structural defects; 2). Constructing a quasi-AI surface termination instead of defective and unstable SnI_2 surface termination; 3). Suppressing the formation of V_I on the quasi-AI-terminated surface. Under Sn-rich reaction condition, by judiciously choosing TEA^+ and Na^+ as surface-terminated ions, I obtained colloidal $FASnI_3$ NCs with a record PLQY of 36.9±0.7%, which is over 50 times larger than those previously reported. The combined optical and structural characterizations show that TEA^+ and Na^+ absorb on the NC surface instead of entering the NC lattice, regulating the surface condition from SnI_2 termination to TEAI/NaI termination. Such a created surface can reduce surface atomic vacancies, thus suppressing the nonradiative recombination pathways in NCs. Further DFT calculations revealed that a small amount of TEA^+ ions and a large amount of Na^+ ions can strengthen surface I^- binding, thus suppressing the formation of surface V_I. Finally, the scalability and adaptability of my approach have been validated by its successful application to highly luminescent FA/Cs alloyed $FA_xCs_{1-x}SnI_3$ NCs. My findings have not only broken the long-time obstacle in the synthesis of high-quality tin halide perovskite NCs but also laid the foundation for future high-performance optoelectronic devices such as solar cells, LEDs, lasers, and beyond.

Reference:

1. Lin, K.; Xing, J.; Quan, L. N.; de Arquer, F. P. G.; Gong, X.; Lu, J.; Xie, L.; Zhao, W.; Zhang, D.; Yan, C.; Li, W.; Liu, X.; Lu, Y.; Kirman, J.; Sargent, E. H.; Xiong, Q.; Wei, Z. Perovskite light-emitting diodes with external quantum efficiency exceeding 20 per cent. *Nature* **2018,** *562*, 245-248.

2. Fakharuddin, A.; Gangishetty, M. K.; Abdi-Jalebi, M.; Chin, S.-H.; bin Mohd Yusoff, A. R.; Congreve, D. N.; Tress, W.; Deschler, F.; Vasilopoulou, M.; Bolink, H. J. Perovskite light-emitting diodes. *Nature Electronics* **2022,** *5*, 203-216.

3. Pacchioni, G. Highly efficient perovskite LEDs. *Nature Reviews Materials* **2021,** *6*, 108-108.

4. Wang, H.; Kim, D. H. Perovskite-based photodetectors: materials and devices. *Chemical Society Reviews* **2017,** *46*, 5204-5236.

5. Dou, L.; Yang, Y.; You, J.; Hong, Z.; Chang, W.-H.; Li, G.; Yang, Y. Solution-processed hybrid perovskite photodetectors with high detectivity. *Nature Communications* **2014,** *5*, 5404.

6. Zheng, D.; Pauporté, T. Advances in Optical Imaging and Optical Communications Based on High-Quality Halide Perovskite Photodetectors. *Advanced Functional Materials* **2024,** *34*, 2311205.

7. Zhang, Q.; Shang, Q.; Su, R.; Do, T. T. H.; Xiong, Q. Halide Perovskite Semiconductor Lasers: Materials, Cavity Design, and Low Threshold. *Nano Letters* **2021,** *21*, 1903-1914.

8. Lei, L.; Dong, Q.; Gundogdu, K.; So, F. Metal Halide Perovskites for Laser Applications. *Advanced Functional Materials* **2021,** *31*, 2010144.

9. Shi, D.; Adinolfi, V.; Comin, R.; Yuan, M.; Alarousu, E.; Buin, A.; Chen, Y.; Hoogland, S.; Rothenberger, A.; Katsiev, K.; Losovyj, Y.; Zhang, X.; Dowben, P. A.; Mohammed, O. F.; Sargent, E. H.; Bakr, O. M. Low trap-state density and long carrier diffusion in organolead trihalide perovskite single crystals. *Science* **2015,** *347*, 519-522.

10. Fang, H.-H.; Adjokatse, S.; Wei, H.; Yang, J.; Blake, G. R.; Huang, J.; Even, J.;

Loi, M. A. Ultrahigh sensitivity of methylammonium lead tribromide perovskite single crystals to environmental gases. *Science Advances* **2016,** *2*, e1600534.

11. Saidaminov, M. I.; Abdelhady, A. L.; Murali, B.; Alarousu, E.; Burlakov, V. M.; Peng, W.; Dursun, I.; Wang, L.; He, Y.; Maculan, G.; Goriely, A.; Wu, T.; Mohammed, O. F.; Bakr, O. M. High-quality bulk hybrid perovskite single crystals within minutes by inverse temperature crystallization. *Nature Communications* **2015,** *6*, 7586.

12. Manser, J. S.; Christians, J. A.; Kamat, P. V. Intriguing Optoelectronic Properties of Metal Halide Perovskites. *Chemical Reviews* **2016,** *116*, 12956-13008.

13. Akkerman, Q. A.; Rainò, G.; Kovalenko, M. V.; Manna, L. Genesis, challenges and opportunities for colloidal lead halide perovskite nanocrystals. *Nature Materials* **2018,** *17*, 394-405.

14. Infante, I.; Manna, L. Are There Good Alternatives to Lead Halide Perovskite Nanocrystals? *Nano Letters* **2021,** *21*, 6-9.

15. Fan, Q.; Biesold-McGee, G. V.; Ma, J.; Xu, Q.; Pan, S.; Peng, J.; Lin, Z. Lead-Free Halide Perovskite Nanocrystals: Crystal Structures, Synthesis, Stabilities, and Optical Properties. *Angewandte Chemie International Edition* **2020,** *59*, 1030-1046.

16. Chen, J.-K.; Zhang, B.-B.; Liu, Q.; Shirahata, N.; Mohammed, O. F.; Bakr, O. M.; Sun, H.-T. Advances and Challenges in Tin Halide Perovskite Nanocrystals. *ACS Materials Letters* **2021,** *3*, 1541-1557.

17. Zhang, Y.; Ma, Y.; Wang, Y.; Zhang, X.; Zuo, C.; Shen, L.; Ding, L. Lead-Free Perovskite Photodetectors: Progress, Challenges, and Opportunities. *Advanced Materials* **2021,** *33*, 2006691.

18. Ke, W.; Kanatzidis, M. G. Prospects for low-toxicity lead-free perovskite solar cells. *Nature Communications* **2019,** *10*, 965.

19. De Angelis, F. The Prospect of Lead-Free Perovskite Photovoltaics. *ACS Energy Letters* **2021,** *6*, 1586-1587.

20. van der Stam, W.; Geuchies, J. J.; Altantzis, T.; van den Bos, K. H. W.; Meeldijk, J. D.; Van Aert, S.; Bals, S.; Vanmaekelbergh, D.; de Mello Donega, C. Highly Emissive

Divalent-Ion-Doped Colloidal CsPb1–xMxBr3 Perovskite Nanocrystals through Cation Exchange. *Journal of the American Chemical Society* **2017,** *139*, 4087-4097.

21. Konstantakou, M.; Stergiopoulos, T. A critical review on tin halide perovskite solar cells. *Journal of Materials Chemistry A* **2017,** *5*, 11518-11549.

22. Yu, B.-B.; Chen, Z.; Zhu, Y.; Wang, Y.; Han, B.; Chen, G.; Zhang, X.; Du, Z.; He, Z. Heterogeneous 2D/3D Tin-Halides Perovskite Solar Cells with Certified Conversion Efficiency Breaking 14%. *Advanced Materials* **2021,** *33*, 2102055.

23. Zhang, F.; Min, H.; Zhang, Y.; Kuang, Z.; Wang, J.; Feng, Z.; Wen, K.; Xu, L.; Yang, C.; Shi, H.; Zhuo, C.; Wang, N.; Chang, J.; Huang, W.; Wang, J. Vapor-Assisted In Situ Recrystallization for Efficient Tin-Based Perovskite Light-Emitting Diodes. *Advanced Materials* **2022,** *34*, 2203180.

24. Han, D.; Wang, J.; Agosta, L.; Zang, Z.; Zhao, B.; Kong, L.; Lu, H.; Mosquera-Lois, I.; Carnevali, V.; Dong, J.; Zhou, J.; Ji, H.; Pfeifer, L.; Zakeeruddin, S. M.; Yang, Y.; Wu, B.; Rothlisberger, U.; Yang, X.; Grätzel, M.; Wang, N. Tautomeric mixture coordination enables efficient lead-free perovskite LEDs. *Nature* **2023,** *622*, 493-498.

25.Jiang, X.; Li, H.; Zhou, Q.; Wei, Q.; Wei, M.; Jiang, L.; Wang, Z.; Peng, Z.; Wang, F.; Zang, Z.; Xu, K.; Hou, Y.; Teale, S.; Zhou, W.; Si, R.; Gao, X.; Sargent, E. H.; Ning, Z. One-Step Synthesis of SnI2·(DMSO)x Adducts for High-Performance Tin Perovskite Solar Cells. *Journal of the American Chemical Society* **2021,** *143*, 10970-10976.

26. Cui, D.; Liu, X.; Wu, T.; Lin, X.; Luo, X.; Wu, Y.; Segawa, H.; Yang, X.; Zhang, Y.; Wang, Y.; Han, L. Making Room for Growing Oriented FASnI3 with Large Grains via Cold Precursor Solution. *Advanced Functional Materials* **2021,** *31*, 2100931.

27. Wang, S.; Wu, C.; Wu, T.; Yao, H.; Hua, Y.; Hao, F. π-Conjugated Lewis Base for Efficient Tin Halide Perovskite Solar Cells with Retarded Sn2+ Oxidation. *ACS Energy Letters* **2024,** *9*, 1168-1175.

28. Chan, P. F.; Qin, M.; Su, C.-J.; Ye, L.; Wang, X.; Wang, Y.; Guan, X.; Lu, Z.; Li, G.; Ngai, T.; Tsang, S. W.; Zhao, N.; Lu, X. iso-BAI Guided Surface Recrystallization for Over 14% Tin Halide Perovskite Solar Cells. *Advanced Science* **2024,** *11*, 2309668.

29. Kovalenko, M. V.; Protesescu, L.; Bodnarchuk, M. I. Properties and potential optoelectronic applications of lead halide perovskite nanocrystals. *Science* **2017,** *358*, 745-750.

30. Quan, L. N.; Rand, B. P.; Friend, R. H.; Mhaisalkar, S. G.; Lee, T.-W.; Sargent, E. H. Perovskites for Next-Generation Optical Sources. *Chemical Reviews* **2019,** *119*, 7444-7477.

31. Song, J.; Li, J.; Li, X.; Xu, L.; Dong, Y.; Zeng, H. Quantum Dot Light-Emitting Diodes Based on Inorganic Perovskite Cesium Lead Halides (CsPbX3). *Advanced Materials* **2015,** *27*, 7162-7167.

32. Zhang, H.; Wang, X.; Liao, Q.; Xu, Z.; Li, H.; Zheng, L.; Fu, H. Embedding Perovskite Nanocrystals into a Polymer Matrix for Tunable Luminescence Probes in Cell Imaging. *Advanced Functional Materials* **2017,** *27*, 1604382.

33. Pramanik, A.; Gates, K.; Patibandla, S.; Davis, D.; Begum, S.; Iftekhar, R.; Alamgir, S.; Paige, S.; Porter, M. M.; Ray, P. C. Water-Soluble and Bright Luminescent Cesium–Lead–Bromide Perovskite Quantum Dot–Polymer Composites for Tumor-Derived Exosome Imaging. *ACS Applied Bio Materials* **2019,** *2*, 5872-5879.

34. Zhu, C.; Marczak, M.; Feld, L.; Boehme, S. C.; Bernasconi, C.; Moskalenko, A.; Cherniukh, I.; Dirin, D.; Bodnarchuk, M. I.; Kovalenko, M. V.; Rainò, G. Room-Temperature, Highly Pure Single-Photon Sources from All-Inorganic Lead Halide Perovskite Quantum Dots. *Nano Letters* **2022,** *22*, 3751-3760.

35. Dai, L.; Deng, Z.; Auras, F.; Goodwin, H.; Zhang, Z.; Walmsley, J. C.; Bristowe, P. D.; Deschler, F.; Greenham, N. C. Slow carrier relaxation in tin-based perovskite nanocrystals. *Nature Photonics* **2021,** *15*, 696-702.

36. Ross, R. T.; Nozik, A. J. Efficiency of hot - carrier solar energy converters. *Journal of Applied Physics* **1982,** *53*, 3813-3818.

37. Dirin, D. N.; Vivani, A.; Zacharias, M.; Sekh, T. V.; Cherniukh, I.; Yakunin, S.; Bertolotti, F.; Aebli, M.; Schaller, R. D.; Wieczorek, A.; Siol, S.; Cancellieri, C.; Jeurgens,

L. P. H.; Masciocchi, N.; Guagliardi, A.; Pedesseau, L.; Even, J.; Kovalenko, M. V.; Bodnarchuk, M. I. Intrinsic Formamidinium Tin Iodide Nanocrystals by Suppressing the Sn(IV) Impurities. *Nano Letters* **2023,** *23*, 1914-1923.

38. Liu, Q.; Yin, J.; Zhang, B.-B.; Chen, J.-K.; Zhou, Y.; Zhang, L.-M.; Wang, L.-M.; Zhao, Q.; Hou, J.; Shu, J.; Song, B.; Shirahata, N.; Bakr, O. M.; Mohammed, O. F.; Sun, H.-T. Theory-Guided Synthesis of Highly Luminescent Colloidal Cesium Tin Halide Perovskite Nanocrystals. *Journal of the American Chemical Society* **2021,** *143*, 5470-5480.

39. Wong, A. B.; Bekenstein, Y.; Kang, J.; Kley, C. S.; Kim, D.; Gibson, N. A.; Zhang, D.; Yu, Y.; Leone, S. R.; Wang, L.-W.; Alivisatos, A. P.; Yang, P. Strongly Quantum Confined Colloidal Cesium Tin Iodide Perovskite Nanoplates: Lessons for Reducing Defect Density and Improving Stability. *Nano Letters* **2018,** *18*, 2060-2066.

40. Fiuza-Maneiro, N.; Sun, K.; López-Fernández, I.; Gómez-Graña, S.; Müller-Buschbaum, P.; Polavarapu, L. Ligand Chemistry of Inorganic Lead Halide Perovskite Nanocrystals. *ACS Energy Letters* **2023,** *8*, 1152-1191.

41. Hills-Kimball, K.; Yang, H.; Cai, T.; Wang, J.; Chen, O. Recent Advances in Ligand Design and Engineering in Lead Halide Perovskite Nanocrystals. *Advanced Science* **2021,** *8*, 2100214.

42. Krieg, F.; Ochsenbein, S. T.; Yakunin, S.; ten Brinck, S.; Aellen, P.; Süess, A.; Clerc, B.; Guggisberg, D.; Nazarenko, O.; Shynkarenko, Y.; Kumar, S.; Shih, C.-J.; Infante, I.; Kovalenko, M. V. Colloidal CsPbX3 (X = Cl, Br, I) Nanocrystals 2.0: Zwitterionic Capping Ligands for Improved Durability and Stability. *ACS Energy Letters* **2018,** *3*, 641-646.

43. Morad, V.; Stelmakh, A.; Svyrydenko, M.; Feld, L. G.; Boehme, S. C.; Aebli, M.; Affolter, J.; Kaul, C. J.; Schrenker, N. J.; Bals, S.; Sahin, Y.; Dirin, D. N.; Cherniukh, I.; Raino, G.; Baumketner, A.; Kovalenko, M. V. Designer phospholipid capping ligands for soft metal halide nanocrystals. *Nature* **2024,** *626*, 542-548.

44. Pan, J.; Shang, Y.; Yin, J.; De Bastiani, M.; Peng, W.; Dursun, I.; Sinatra, L.; El-

Zohry, A. M.; Hedhili, M. N.; Emwas, A.-H.; Mohammed, O. F.; Ning, Z.; Bakr, O. M. Bidentate Ligand-Passivated CsPbI3 Perovskite Nanocrystals for Stable Near-Unity Photoluminescence Quantum Yield and Efficient Red Light-Emitting Diodes. *Journal of the American Chemical Society* **2018,** *140*, 562-565.

45. Chen, J.-K.; Ma, J.-P.; Guo, S.-Q.; Chen, Y.-M.; Zhao, Q.; Zhang, B.-B.; Li, Z.-Y.; Zhou, Y.; Hou, J.; Kuroiwa, Y.; Moriyoshi, C.; Bakr, O. M.; Zhang, J.; Sun, H.-T. High-Efficiency Violet-Emitting All-Inorganic Perovskite Nanocrystals Enabled by Alkaline-Earth Metal Passivation. *Chemistry of Materials* **2019,** *31*, 3974-3983.

46. Zhuang, J.; Mao, P.; Luan, Y.; Yi, X.; Tu, Z.; Zhang, Y.; Yi, Y.; Wei, Y.; Chen, N.; Lin, T.; Wang, F.; Li, C.; Wang, J. Interfacial Passivation for Perovskite Solar Cells: The Effects of the Functional Group in Phenethylammonium Iodide. *ACS Energy Letters* **2019,** *4*, 2913-2921.

47. Teale, S.; Degani, M.; Chen, B.; Sargent, E. H.; Grancini, G. Molecular cation and low-dimensional perovskite surface passivation in perovskite solar cells. *Nature Energy* **2024,** *9*, 779-792.

48. Pica, G.; Montecucco, R.; Zanetta, A.; Oranskaia, A.; Faini, F.; Pancini, L.; Mrkyvkova, N.; Siffalovic, P.; Dally, P.; Pirota, V.; Ledinsky, M.; De Bastiani, M.; De Wolf, S.; Doria, F.; Schwingenschlögl, U.; Grancini, G. Unraveling Bulk versus Surface Passivation Effects in Highly Efficient p–i–n Perovskite Solar Cells Using Thiophene-Based Cations. *Solar RRL* **2024,** *8*, 2300681.

49. Kodalle, T.; Moral, R. F.; Scalon, L.; Szostak, R.; Abdelsamie, M.; Marchezi, P. E.; Nogueira, A. F.; Sutter-Fella, C. M. Revealing the Transient Formation Dynamics and Optoelectronic Properties of 2D Ruddlesden-Popper Phases on 3D Perovskites. *Advanced Energy Materials* **2023,** *13*, 2201490.

50. Lin, J.-T.; Hu, Y.-K.; Hou, C.-H.; Liao, C.-C.; Chuang, W.-T.; Chiu, C.-W.; Tsai, M.-K.; Shyue, J.-J.; Chou, P.-T. Superior Stability and Emission Quantum Yield (23% ± 3%) of Single-Layer 2D Tin Perovskite TEA2SnI4 via Thiocyanate Passivation. *Small* **2020,** *16*, 2000903.

51. Kahmann, S.; Nazarenko, O.; Shao, S.; Hordiichuk, O.; Kepenekian, M.; Even, J.; Kovalenko, M. V.; Blake, G. R.; Loi, M. A. Negative Thermal Quenching in FASnI3 Perovskite Single Crystals and Thin Films. *ACS Energy Letters* **2020,** *5*, 2512-2519.

52. Jellicoe, T. C.; Richter, J. M.; Glass, H. F. J.; Tabachnyk, M.; Brady, R.; Dutton, S. E.; Rao, A.; Friend, R. H.; Credgington, D.; Greenham, N. C.; Böhm, M. L. Synthesis and Optical Properties of Lead-Free Cesium Tin Halide Perovskite Nanocrystals. *Journal of the American Chemical Society* **2016,** *138*, 2941-2944.

53. Kang, C.; Rao, H.; Fang, Y.; Zeng, J.; Pan, Z.; Zhong, X. Antioxidative Stannous Oxalate Derived Lead-Free Stable CsSnX3 (X=Cl, Br, and I) Perovskite Nanocrystals. *Angewandte Chemie International Edition* **2021,** *60*, 660-665.

54.Dong, Y.; Wang, Y.-K.; Yuan, F.; Johnston, A.; Liu, Y.; Ma, D.; Choi, M.-J.; Chen, B.; Chekini, M.; Baek, S.-W.; Sagar, L. K.; Fan, J.; Hou, Y.; Wu, M.; Lee, S.; Sun, B.; Hoogland, S.; Quintero-Bermudez, R.; Ebe, H.; Todorovic, P.; Dinic, F.; Li, P.; Kung, H. T.; Saidaminov, M. I.; Kumacheva, E.; Spiecker, E.; Liao, L.-S.; Voznyy, O.; Lu, Z.-H.; Sargent, E. H. Bipolar-shell resurfacing for blue LEDs based on strongly confined perovskite quantum dots. *Nature Nanotechnology* **2020,** *15*, 668-674.

55. Kövér, L.; Kovács, Z.; Sanjinés, R.; Moretti, G.; Cserny, I.; Margaritondo, G.; Pálinkás, J.; Adachi, H. Electronic structure of tin oxides: High-resolution study of XPS and Auger spectra. *Surface and Interface Analysis* **1995,** *23*, 461-466.

56. Kishi, K.; Kirimura, H.; Fujimoto, Y. XPS studies for NaCl deposited on the Ni(111) surface. *Surface Science* **1987,** *181*, 586-595.

57. Peng, H.; Montes-García, V.; Raya, J.; Wang, H.; Guo, H.; Richard, F.; Samorì, P.; Ciesielski, A. Supramolecular engineering of cathode materials for aqueous zinc-ion hybrid supercapacitors: novel thiophene-bridged donor–acceptor sp2 carbon-linked polymers. *Journal of Materials Chemistry A* **2023,** *11*, 2718-2725.

58. Lin, F.; Wang, D.; Jiang, Z.; Ma, Y.; Li, J.; Li, R.; Li, C. Photocatalytic oxidation of thiophene on BiVO4 with dual co-catalysts Pt and RuO2 under visible light irradiation using molecular oxygen as oxidant. *Energy & Environmental Science* **2012,** *5*, 6400-6406.

Chapter 5: Conclusions and future prospects

5.1 General conclusions

Tin halide perovskites have been proved as ideal substitution for lead halide perovskites in various optoelectronic devices since their low-toxicity and similar outstanding optoelectronic properties with those of their lead-based cousins. During them, formamidinium tin iodide ($FASnI_3$) is an ideal light-absorb material in solar cells because its bandgap is ~1.41 eV close to the optimum bandgap (1.34 eV) of single junction solar cell that can approach the Shockley-Queisser efficient limit. Based on the $FASnI_3$ solar cells have achieved great progresses, and the power conversion efficiencies have reached over 14%, gradually shortening the gap with that of lead halide perovskite solar cells. Recent researches are mainly focused on the $FASnI_3$ polycrystalline films, while those on their micro/nano crystals are still limited. Some interesting photophysical properties of $FASnI_3$ polycrystalline films, single crystals, and nanocrystals were observed, such as bandgap widening by structural distortion; negative thermal quenching of PL under low temperatures; slow carrier relaxation for quantum-confined NCs. Considering that their study objects featuring massive defect concentrations that lead to extremely low PLQYs, their observed structural-photophysical property relationships are deficient. Colloidal NCs have some excellent photophysical properties that contribute to some special applications, such as QLED, biological imaging, and single-quantum source. Unfortunately, present researches on $FASnI_3$ NCs just started in 2021, and still have no great improvement until now. How to get stable and highly luminescent $FASnI_3$ NCs is the main obstacle at present.

In this thesis, I started with the research on $FASnI_3$ microcrystals, uncovering defect-induced unconventional photophysical properties in $FASnI_3$, and discovering the significance of Sn-rich reaction condition during the nucleation and growth of high-quality $FASnI_3$ crystals. Furthermore, I turned my researches to $FASnI_3$ NCs, and developed a new kind of capping ligand, phosphatidylcholine, for stable $FASnI_3$ NCs. Finally, focused on the surface modification of $FASnI_3$ NCs, and improved their PLQY to $36.9\pm0.7\%$ that is a record value during all reported tin halide perovskite NCs. Herein, I present the detailed findings of my researches:

In Chapter 2, I found that by simply tuning the reactant ratios of FA-oleate to SnI_2, different-quality $FASnI_3$ microcrystals were synthesized, and the best PLQY of 8.0% was achieved under Sn-rich reaction conditions. This is the first time to confirm that Sn-rich reaction condition can suppress the formation of some structural defects, such as tin vacancies, Sn^{4+} self-doping in $FASnI_3$ microcrystals. For the low-quality $FASnI_3$ microcrystals, I observed a larger bandgap. X-ray photoelectron spectroscopy shows higher Sn^{4+} content in low-quality microcrystals, and ^{119}Sn solid-state nuclear magnetic resonance shows structural distortion in low-quality microcrystals. Thus, I provided my understanding that defect-induced structural distortion contributes to the widening bandgap in $FASnI_3$. This is the first time to discover the defect-dependent structural-photophysical property relationship in $FASnI_3$ microcrystals. Air-degradation is another progress for generating structural defects that also induced bandgap widening. However, the specific defects are still unknown. I speculate that they are Sn vacancies or Sn^{4+}-related defects. In addition, what kind of structural distortion is also still unknow, which needs to be discovered in the future. Low-temperature PL measurements lead me to the finding of an unusual near-infrared emission band, and negative thermal quenching in a broad range of 110-200 K. Both could be on account of structural defects in $FASnI_3$ microcrystals.

In Chapter 3, based on the Sn-rich synthesis method discovered in Chapter 2, I introduced a zwitterionic ligand, phosphatidylcholine, for the preparation of small-sized $FASnI_3$ NCs. Phosphatidylcholine is composed of a quaternary amine choline headgroup, a phosphate group, and two branched fatty acid side-chains. Two functional groups help the strong binding of ligand with NC surface, and long-chain side-chains provide steric hindrance for suppressing the fast growth of $FASnI_3$ NCs. Even introducing a small amount of phosphatidylcholine, small-sized $FASnI_3$ NCs with a mean particle size of ~30 nm and a PLQY of 1.2% could be achieved. Different phosphatidylcholines with different chain lengths were also studied, and all of them could produce small-sized $FASnI_3$ NCs. Detailed characterizations confirm the presence of phosphatidylcholine on the NC surface. Stability tests confirm that phosphatidylcholine-capped $FASnI_3$ NCs exhibit long-term colloidal stability and structural stability in Ar-filled glovebox, which are benefited by strong binding of phosphatidylcholine capping ligand. Interestingly, I note that $FASnI_3$ NCs also could be produced even under room temperature, showing the potential in

industrialized large-scale production.

In Chapter 4, I focused on how to improve the optical properties of $FASnI_3$ NCs. Though theoretical calculations, I noted that three factors are necessary for getting highly luminescent $FASnI_3$ NCs: the first is creating a Sn-rich reaction condition; the second is achieving FAI-terminated surface; the third is suppressing the surface iodine vacancies. First one has been proved in Chapter 2. However, for the second one, Sn-rich reaction condition and FAI-terminated surface are contradictory, because Sn-rich reaction condition usually leads to a SnI_2-terminated surface. To address this problem, I thus proposed the use of exogenous cation that can act as a quasi-A-site cation to establish an AI-terminated surface. I found that combing the use of 2-thiophenemethylammonium (TEA^+) and sodium (Na^+) can result in a record PLQY of 36.9±0.7%. Through detailed characterizations, such as X-ray photoelectron spectra (XPS), inductively coupled plasma optical emission spectrometry, energy-dispersive X-ray spectroscopy, and ζ-potential, I provided an ideal passivation model, in which, TEA^+ locates at the surface FA position, forming a local TEAI-terminated surface, Na^+ ions gather in the surface A sites, forming a bio-polar ligand shell. Whole surface condition exhibits a quasi-AI termination characteristic, resulting in low defect-density. In this work, I found that $FASnI_3$ NCs are strongly unstable upon the X-ray exposure, with the appearance of Sn^0 and Sn^{4+} XPS signals, extremely influencing our analysis on the surface conditions of $FASnI_3$ NCs. In addition, high-resolution transmission electron microscopy (TEM) with well controlled dose density was firstly used for observing the lattice of electron-sensitive $FASnI_3$ NC, benefiting the future works on the structures of tin halide perovskite NCs. Finally, I demonstrate that my synthesis concept was also used for highly luminescent FA/Cs alloying tin iodide perovskite NCs. FA/Cs alloying structures show better tolerance factors for stable perovskite structures, which pays the way for future high-efficiency and stable tin halide perovskite optoelectronic devices.

5.2 Future prospects

Although I discovered the defect-induce bandgap widening and abnormal PL in $FASnI_3$ microcrystals, the specific kind of defects is still unknow. To better understand the defect effect, more detailed researches are necessary. For examples, positron annihilation lifetime studies could be conducted for analyzing the defects in $FASnI_3$;

synchrotron radiation X-ray diffraction technology could be considered for investigating the defect-induced structural distortion in $FASnI_3$. All of them could further deepen our understanding on the relationship between defects and photophysical properties of tin-based perovskites. Different with microcrystals or polycrystalline films, $FASnI_3$ NCs may feature other interesting photophysical properties needed to be discovered since their smaller particle size and larger specific surface area.

The stability of $FASnI_3$ NCs is always a tough challenge. Although I discovered a new ligand for long-term stability in glovebox, the air stability is still poor, which is resulted from the easy oxidation of Sn^{2+}. The trace amount of Sn^{4+} may cause the self-doping of Sn^{4+} into the lattice of $FASnI_3$ NCs and then destroy the perovskite structure. Instead of oxygen, $FASnI_3$ NCs are also poorly tolerant of heat, light, and humidity. Some traditional wisdoms, such as using antioxidant ligands, constructing core-shell structures, could be considered in the future.

Compared with lead halide perovskite NCs, the PLQYs of tin halide perovskite NCs are still not satisfactory. In my research, I improved the PLQY of $FASnI_3$ NCs to 36.9±0.7%, still far from nearly 100% as demonstrated in the lead-based perovskites. To construct high-efficiency NC-based LEDs, high PLQY is essential. Considering that $FASnI_3$ are quiet defect-intolerant, to further improve their PLQY is difficult. One possible route is that, synthesizing small-sized $FASnI_3$ quantum dots and then achieving better surface modifications. Furthermore, instead of $FASnI_3$ NCs, Br- or Cl- based, and all-inorganic tin perovskite NCs are seldom studied. Achieving highly luminescent tin halide perovskite NCs with all visible to near-infrared emitting region is also a challenge in the future researches.

Finally, realization of NC-based optoelectronic applications is also important. The applications could be solar cells, LEDs, biological image, photodetectors, and so on. Notable, optoelectronic devices need great conductivity of NCs. The ligand I used, phosphatidylcholine, is a long-chain molecule that will affect the charge transfer in devices. Future work could be focused on the ligand exchange with short-chain and conductive ligands.

In conclusion, I believe that, more and more efforts will be devoted to the tin halide perovskite NCs and the potential applications in a range of high-performance optoelectronic devices will be achieved soon.

Acknowledgements

In November, 2020, with excitements and curiousness, I firstly left from my own country and started my overseas study. Time flies, four years have already gone. Looking back on these years, there are loneliness, tears, happiness, and pleasures filling in my Ph.D. study, which will be my most valuable and meaningful experience in my life. As a Hokkaido University's student and NIMS Junior researcher, I am grateful since that I can work with so many kind, excellent students and professors. Here, I would like to acknowledge all those who have already played important roles in my life.

First and foremost, I would like to express my deepest gratitude to Prof. Naoto Shirahata and Dr. Hong-Tao Sun for their patient guidance and encouragement. During my whole Ph.D. study, they taught me a lot of knowledge, and guided my whole research direction. As teachers, they not only taught me how to conduct scientific researches, but also taught me how to be a well person.

I also would like to thank Prof. Jun Yin for the cooperations on the theoretical calculations and Prof. Jun Kikkawa for the cooperations on the high-resolution TEM observations. Their works help me complete my scientific researches.

Secondly, I sincerely thank my former and current laboratory colleagues: Ms. Hiromi Kobayashi, Ms. Fumie Takazawa, Ms. Masami Soga, Dr. Subhashri Chatterjee, Dr. Shilaj Roy, Dr. Hiroyuki Yamada, Dr. Kazuhiro Nemoto, and Dr. Bloyet Clarisse Florence. Thank them for their collaborative efforts, kind helps, and technical assistance.

Next, I would like to thank my dear friends and classmates: Dr. Binbin Zhang, Mr. Cong Zhang, Dr. Xiaoyu Huang, Dr. Qing Zhao, Dr. Tingting Deng, Dr. Hong Ming, Mr. Dongxun Chen, and Ms. Zhibo Chen. Thank you for the opportunity to know all of them. During the whole four years, their accompany and supports give me a lot of happiness, and make my Ph.D. life rich and colorful.

Finally, I am forever grateful to my parents and grandparents for their loves and supports. Whenever I am feeling down, they always provide the best comforts. Without them, it's hard for me to complete my Ph.D. study. Specially, I want to express my heartfelt gratitude to my grandmother. Her love supports my whole 30 years. On 15th May, 2024, she passed away. I deeply regret that I was not being able to spend more time with her during my Ph.D. study. In my future life, I will keep on going always with her

love. Grandmom, may you rest in peace!

Jiakai Chen
Tsukuba, Japan
September 2024